Thèse
de doctorat
de l'UTT

Hui CHEN

Influence of Residual Stress and Work Hardening on the Tensile and Cyclic Behavior of Shot-peened Inconel 625

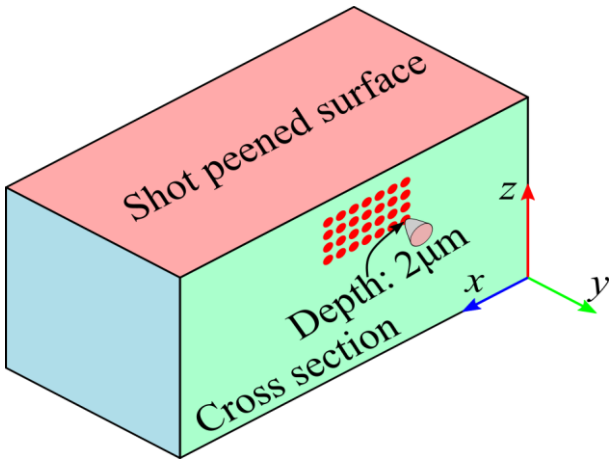

Champ disciplinaire :
Sciences pour l'Ingénieur

2024TROY0045

Année 2024

utt
UNIVERSITÉ DE TECHNOLOGIE
TROYES

THESE

pour l'obtention du grade de

DOCTEUR
de l'UNIVERSITE DE TECHNOLOGIE DE TROYES

en SCIENCES POUR L'INGENIEUR

Spécialité : MATERIAUX, MECANIQUE, OPTIQUE ET NANOTECHNOLOGIE

présentée et soutenue par

Hui CHEN

le 16 décembre 2024

Influence of Residual Stress and Work Hardening on the Tensile and Cyclic Behavior of Shot-peened Inconel 625

JURY

Mme Salima BOUVIER	PROFESSEURE DES UNIVERSITES	Présidente
M. David GLOAGUEN	PROFESSEUR DES UNIVERSITES	Rapporteur
M. Guillaume KERMOUCHE	PROFESSEUR MINES SAINT-ETIENNE – HDR	Rapporteur
M. Mario GUAGLIANO	PROFESSORE ORDINARIO	Examinateur
M. Régis KUBLER	MAITRE DE CONFERENCES	Examinateur
M. Manuel FRANÇOIS	PROFESSEUR DES UNIVERSITES	Directeur de thèse
Mme Pascale KANOUTÉ	INGENIEURE DE RECHERCHE ONERA	Directrice de thèse

Acknowledgment

It has been four years since I began my doctoral journey in France. The completion of this thesis is an important time in my life, and I would like to take this opportunity to express my heartfelt gratitude to those who have supported and guided me throughout this process.

First, I would like to express my deepest appreciation to my kind supervisors, Manuel François and Pascale Kanouté. I was not familiar with the research field at the beginning. However, they provided patient guidance and explanations, even for the simple questions I proposed. In this way, they lead me step by step into the gate of the scientific field on materials and engineering. Their unwavering support, insightful guidance, and invaluable feedback throughout the duration of my research are invaluable.

I am also deeply grateful to Mr. Guillaume Kermouche, Mr. David Gloaguen, Mrs. Salima Bouvier, Mr. Régis Kubler, and Mr. Mario Guagliano, who served as jury members on my defense committee. I thank them for their time, constructive criticism and valuable suggestions, which greatly improved the quality of this work.

This thesis is carried within the Laboratory of Mechanical & Material Engineering (LASMIS). I would like to express my gratitude to all the colleagues in LASMIS for their contributions to the creation of a stimulating and enjoyable environment. I would like to extend my gratitude to Mr. Bruno Guelorget and Mr. Matthieu Strub for their invaluable guidance and assistance in the areas of polishing and nanoindentation. I would like to express my most sincere gratitude to Mr. Mahmoud Naim and Mr. Mahdi Chemkhi for their advises on additive manufacturing samples. Thanks also to Mr. Zhidan Sun for his training on the shot peening machine and his insights on the PhD experience. I am also grateful to Mr. Pierre-Antoine Adragna for his training on the coordinate measurement machine. Finally, I would like to thank Mr. Carl Labergère and Mr. Houssem Badreddine for their assistance with the simulation.

I owe a great deal of gratitude to the administrative and technical staff of doctoral school, whose help and support have been crucial in the completion of this thesis.

I am deeply indebted to my family for their unwavering support and encouragement. To my parents, who have always believed in me and provided me with the foundation to pursue my dreams; to my siblings, for their constant encouragement; and to my friends, for their understanding and patience during the many phases of my research.

I am deeply indebted to my parents and little sister for their support and encouragement. Thanks to my friends for their help in daily life. Thanks to my girlfriend Xiao Liu for the support, understanding and tolerance.

Lastly, I would like to thank UTT and LASMIS for providing the office, the laboratory facilities, and the administrative supports. I would also like to thank China scholarship council (CSC) for providing the financial support that made this research possible.

Content

Abstract I
Résumé II
General introduction III
Chapter 1 1
Introduction to the techniques used and research background 1
1.1. The key concepts 1
1.1.1. Fatigue failure 1
1.1.2. Residual stress 2
1.1.3. Work hardening 2
1.1.4. The constitutive behavior 3
1.1.5. Shot peening 4
1.2. Parameters evolution during cyclic loading 5
1.2.1. The relaxation of residual stress 5
1.2.2. The relaxation of mean stress 6
1.2.3. The evolution of work hardening 6
1.3. Characterization of residual stress and work hardening 7
1.3.1. Characterization of residual stresses 7
1.3.2. Characterization of work hardening 10
1.4. Instrument indentation technique 14
1.4.1. The key parameters 14
1.4.2. Characterization of residual stress with indentation technique 16
1.4.3. Influence of work hardening on indentation responses 17
1.5. Our target material: Nickel-based alloys 19
1.6. The aims and technique approaches 19
Chapter 2 21
Numerical characterization of work hardening and residual stress with indentation 21
2.1. Technical background in simulation 21
2.1.1. Material constitutive behavior 21
2.1.2. Nanoindentation simulation model 22
2.2. Analysis of shot peening backstress effect on nanoindentation 26
2.2.1. Shot peening simulation 26
2.2.2. The shot peening backstress distribution 29
2.2.3. The equivalent backstress 30

2.2.4. The effect of shot peening backstress 31
2.3. Characterization of residual stress and cumulative plastic strain 40
2.3.1. The Response Surface Function method 40
2.3.2. Application of the method with a pure simulation view 42
2.4. The relaxation of residual stress during cutting process 51
2.4.1. Define a residual stress profile 52
2.4.2. Finite element simulation of the residual stress relaxation 54
2.5. Conclusion 55
Chapter 3 57
Experimental characterization of work hardening and residual stress 57
3.1. Material and sample condition 57
3.1.1. Received material 57
3.1.2. Samples for mechanical tests 57
3.2. Shot peening 58
3.3. X-ray diffraction measurement 59
3.4. Calibration of peak width and cumulative plastic strain 61
3.5. Instrumented indentation tests 62
3.5.1. Sample preparation 62
3.5.2. Spherical indentation tests 64
3.5.3. The correction of edge effect 66
3.6. Material behavior parameters identification 67
3.6.1. Isotropic hardening parameters identification 67
3.6.2. Combined hardening parameters identification 67
3.6.3. Indentation simulation with identified behavior parameters 70
3.7. Optimizing the simulation parameters 71
3.7.1. The possible reasons for the difference between simulation and experiment 71
3.7.2. The constitutive behavior model selection strategy 72
3.7.3. Inverse analysis technique 73
3.7.4. The examination and analysis on rationality of the optimal parameters 76
3.8. Application of the Response surface function method in practice 78
3.8.1. The indentation simulations with the optimized parameters 78
3.8.2. Application of Response surface function method 80
3.9. Conclusion 86
Chapter 4 88
Mechanical properties characterization under cyclic and monotonic tensile test 88
4.1. Material and sample condition 88
4.1.1. The printed material 88

4.1.2. Tensile properties comparison 90
4.2. Shot peening treatment 90
4.3. Monotonic tensile test 92
4.3.1. Selection of the strain level 92
4.3.2. The tensile stress-strain curves 92
4.3.3. Analysis of the surface properties by X-Ray diffraction 94
4.3.4. Analysis of EBSD results at longitudinal section 101
4.3.5. Analysis of nanoindentation on longitudinal section 107
4.4. Cyclic test 114
4.4.1. The cyclic curves and key parameters 114
4.4.2. Analysis of the surface mechanical state by X-Ray diffraction 117
4.4.3. Analysis of dislocation evolution at longitudinal section 119
4.4.4. Analysis of nanoindentation on longitudinal section 121
4.5. Conclusion 127
Chapter 5 130
Conclusions and perspectives 130
5.1. Overview of the thesis 130
5.2. The major conclusions of the thesis 133
5.3. Perspectives 134
Appendix 136
Résumé en français 139
References 144

Abstract

Shot peening is a mechanical surface treatment that can improve the fatigue performance of a material as it introduces compressive residual stress and work hardening simultaneously. To study the influence of shot peening during fatigue cycles, the method of characterizing residual stress and work hardening, as well as their evolution during monotonic and cyclic tests is investigated in this thesis.

The Response Surface Function method is proposed to characterize residual stress and work hardening simultaneously using instrumented indentation technique. The effects of shot peening backstress on indentation response are investigated. Results indicate that, compared to the effect of residual stress and cumulative plastic strain, the effect of backstress can be neglected. Therefore, the work hardening is represented by cumulative plastic strain in the proposed method. The response surface function can be built through a series of finite element simulations. By solving two response surface functions, the residual stress and cumulative plastic strain values can be obtained.

The evolution of residual stress and work hardening on two kinds of shot peened Inconel 625 alloy are investigated in this thesis. One is a cold rolled alloy, and another one is an additively manufactured alloy. Monotonic tensile tests and 10 cycles cyclic tests are conducted on the samples, which are shot peened by two treatment times. X-ray diffraction, nanoindentation and Electron backscattered diffraction are employed to characterize the evolution of residual stress and work hardening.

Keywords: Shot peening; Residual stresses; Strain hardening; X-ray-Diffraction; Nanoindentation; Finite element method;

Résumé

Le grenaillage est un traitement de surface qui améliore la performance en fatigue d'un matériau en introduisant simultanément des contraintes résiduelles de compression et un écrouissage. Afin d'étudier l'influence du grenaillage pendant les cycles de fatigue, la caractérisation des contraintes résiduelles et de l'écrouissage, ainsi que leur évolution lors des essais monotones et cycliques sont étudiées.

La méthode des surfaces de réponse est proposée pour caractériser simultanément les contraintes résiduelles et l'écrouissage en utilisant la technique de nanoindentation. L'effet de l'écrouissage cinématique induit par le grenaillage sur l'indentation est étudié. Les résultats indiquent que, par rapport à l'effet des contraintes résiduelles et de la déformation plastique cumulée, l'effet de l'écrouissage cinématique peut être négligé. Par conséquent, l'écrouissage est représenté par la déformation plastique cumulée. Les surfaces de réponses peuvent être construites à travers une série de simulations. En utilisant deux surfaces, les valeurs de contraintes résiduelles et de déformation plastique cumulée peuvent être obtenues.

L'évolution des contraintes résiduelles et de l'écrouissage sur deux types d'Inconel 625 grenaillés est étudiée. Un essai de traction monotone et un essai cyclique de 10 cycles sont réalisés sur les échantillons, grenaillés pour deux durées de traitement. La diffraction des rayons X, la nanoindentation et l'EBSD sont employées pour caractériser l'évolution des contraintes résiduelles et de l'écrouissage.

Mots-clés: Grenaillage de précontrainte; Contraintes résiduelles; Écrouissage; Rayons X -- Diffraction; Nanoindentation; Éléments finis, Méthode des;

General introduction

Fatigue is a major research focus in the field of mechanical materials due to its potential to cause failure in common components such as gears, wings, landing gears, and engines. The goal of improving the fatigue life of materials is constantly pursued. Research has shown that the presence of residual compressive stresses and work hardening can effectively slow the expansion of fatigue cracks and significantly improve fatigue properties. Although many processes are capable of introducing residual stresses and work hardening into materials, in most cases, these stresses and hardening cannot be estimated or controlled. Therefore, they are not a reliable means of improving fatigue life. Shot peening has become a well-established method of surface treatment for materials over the centuries. During the shot peening process, the component surface is impacted by high-velocity shots, resulting in the formation of stable plastic deformation layers on the surface and to a certain depth. This process produces a series of plastic deformation layers that cause a high residual compressive stress in the component due to the incompatibility between the layers. Furthermore, shot peening can potentially close pre-existing micro-cracks [1], thereby impeding the formation of macro-fatigue cracks. The fatigue resistance performance of shot peened components can be significantly improved by these factors, which is reflected in a higher fatigue limit and longer fatigue life.

However, when studying the effect of shot peening on material fatigue properties, it is important to note that residual stresses and work hardening introduced by shot peening are always coupled and jointly affect material properties during cycling loading. This coupling can make it difficult to conduct an in-depth study. Therefore, two issues should be considered when studying the effect of shot peening on the fatigue life of materials. One issue is how to characterize residual stresses and work hardening simultaneously. The second issue is the evolution of residual stresses and work hardening on shot peened material under different types of loading, such as monotonic loading or cyclic loading.

The development of a method to characterize residual stress and work hardening simultaneously is meaningful for the study of their effects during fatigue cycles. Therefore, this thesis focuses on proposing an innovative method using nanoindentation. Previous studies have proposed various relevant methods, but they only provide information on either residual stress or work hardening. X-ray diffraction has been known as a method can both characterize residual stress and work hardening. However, no matter the calibration way or the Williamson-Hall method [48], it is an empirical approach for estimating work hardening. In addition, the estimation can only be used for isotropic hardening. Furthermore, one practical troublesome issue of the X-ray diffraction method is that it requires layer removal through electropolishing and depth measurement. However, nanoindentation can be conducted along the depth away from the shot-peened surface, thus enabling the information introduced by shot peening to be obtained through a single sample preparation process. Instrument indentation technique is

sensitive to both residual stress and work hardening [74] which can be seen as a trouble but, if handled appropriately, it can provide a mean to characterize both phenomena. Therefore, this thesis employs nanoindentation to characterize residual stress and work hardening for shot peened samples. The indentation responses can be calibrated with both isotropic hardening and kinematic hardening using finite element simulations, which show the potential of the indentation technique to characterize residual stress, isotropic hardening and kinematic hardening.

Meanwhile, both residual stress and work hardening can affect the performance, thus it is crucial to characterize them separately to gain a better understanding of their role in loading. This understanding can help improve surface treatment technology and enhance the mechanical fatigue properties of materials. The evolution of residual stress and work hardening on shot peened material under monotonic tensile loading and cyclic loading is also addressed in this thesis. After shot peening, residual stress and work hardening are introduced experimentally in the material, which then undergoes evolution under mechanical loadings.. The evolution of residual stress and work hardening for the shot peened sample is observed by nanoindentation, electron backscatter diffraction and X-ray diffraction technique.

The content of each chapter is listed below.

In Chapter 1, a systematic review of the critical concepts involved in this thesis are presented. In addition, the main objectives and the techniques used in the thesis are introduced.

In Chapter 2, a method is proposed to characterize residual stress and work hardening simultaneously. Simulation results indicate that the effect of shot peening backstress on indentation responses can be neglected compared with the effect of residual stress and work hardening. Thus, only residual stress and cumulative plastic strain was considered in the proposed method. The proposed method, called Response Surface Function method, aims to construct the functions of normalized responses and to solve them in order to obtain the value of residual stress and cumulative plastic strain. The method was verified numerically.

In Chapter 3, the proposed method was applied experimentally. Two samples were shot peened with one being prepared for indentation and another one being measured with X-ray diffraction as a reference. A significant difference was found between the simulated *P-h* curve using the material behavior parameters identified from the mechanical tests and the experimental *P-h* curve. To reduce the difference, an inverse technique was applied to find the best optimal material behavior parameters. With the optimized parameters, the Response surface function method was applied in practice. However, a gap was observed between the residual stress and cumulative plastic strain profile obtained from proposed method and measured by X-ray diffraction. One potential explanation for this gap may be related to the sample preparation process. The residual stress relaxation and surface hardening may have occurred during the sample preparation process, which can lead to the observed differences. The stress redistribution due to the sample preparation is studied through the finite element simulations.

In Chapter 4, the evolution of residual stress and work hardening on cyclic test and monotonic tensile test was investigated. The thesis focused on two kinds of Inconel: a commercial cold rolled Inconel 625 and an additively manufactured Inconel 625. High and low strain level of monotonic tensile tests and cyclic tests were conducted for both these two kinds of materials. Observing with X-ray diffraction, Electron backscatter diffraction (EBSD) and nanoindentation, the residual stress and work hardening are quantified. Additionally, the relaxation of residual stress and work hardening was observed after the mechanical tests.

In the final chapter, we present a comprehensive overview of the thesis and give several perspectives for related research in the future.

Chapter 1
Introduction to the techniques used and research background

This chapter introduces the key concepts that are researched and focused on in the thesis, discusses the current state of research in related technologies, proposes the research aims and finally develops the approach used in the thesis.

1.1. The key concepts

1.1.1. Fatigue failure

Fatigue is related to a type of material failure under repeated or cyclic loading conditions, which leads to cracks initiation and fracture propagation [2]. Fatigue failure differs from sudden failures caused by a single, high-stress event in that it tends to progress gradually over time due to the repeated application of stress. It is estimated that almost 90% of engineering component failures are caused by fatigue [3].

Fatigue can be classified into high cycle fatigue and low cycle fatigue. The high cycle fatigue (HCF) life is characterized by a large number of cycles and a stress in the elastic range; the low cycle fatigue (LCF) life is characterized by a small number of cycles to failure however with significant plastic deformations [4]. Similarly, fatigue tests can be divided into stress-controlled test and strain-controlled tests to meet the different requirements.

Fatigue failures typically occur in three stages. The first stage is crack initiation, where cracks due to cyclic loading occur on the material surface or internally but do not propagate to a degree that could cause damage. The second stage is crack propagation, where the small cracks gradually aggregate and then form a macroscopic crack. The third stage is rapid failure. After cracks propagate to a certain extent, the structural performance of the material rapidly decreases, leading to sudden fracture. Therefore, to improve fatigue performance, it is important to prevent crack initiation or propagation in the component.

Two factors, residual stress and work hardening, can influence the initiation and propagation of cracks, thereby affecting the fatigue performance of a material. Therefore, a number of strengthening techniques have been developed to introduce compressive residual stress or work hardening to the material in order to improve the material fatigue performance. Of these, shot peening is a popular and mature strengthening method, which is chosen in the present study.

1.1.2. Residual stress

Residual stress is a type of self-equilibrium stress that is stored in the material during the manufacturing process. It exists in the material without any applied external force. Residual stress can be classified into three types based on the scale of inhomogeneity, as shown in Fig.1-1.

The 1st type of residual stress exists over a relatively large range, larger than the grain size, and evolves at macroscopic scales. The internal forces or moments related to the 1st type of residual stress are in equilibrium through any cross-section. When the equilibrium is disrupted, macroscopic dimensional changes will occur. The 2nd type of residual stress varies from one grain to another and are homogenous over one grain. The 3rd type of residual stress exists within a grain, especially as a result of the presence of dislocations, which is inhomogeneous. Generally, the total residual stresses at a specific position of the component are typically determined by superimposing the 1st, 2nd, and 3rd types of residual stresses.

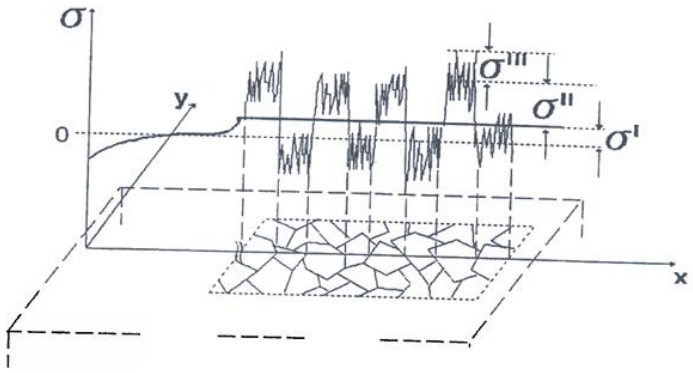

Fig.1-1 The schematic diagram of three types of residual stress, in which σ^{I}, σ^{II} and σ^{III} represents the 1st, 2nd and 3rd type of residual stress respectively [5]

The 1st type of residual stress typically refers to macroscopic residual stress, while the 2nd and 3rd types refer to microscopic residual stress. In engineering disciplines, discussions of problems and effects related to residual stresses typically only consider the macroscopic residual stress, i.e. 1st type of residual stress.

The origins of the macro residual stress could be to many phenomena: nonhomogeneous plastic flow, nonhomogeneous cooling rates and nonhomogeneous phase transformation, etc. In fact, all the ways of inducing residual stresses result in the permanent incompatibilities of deformation in the material, which leads to residual stresses [6].

Residual stress can significantly affect the material fatigue performance in practice. Tensile residual stress can have a negative effect on fatigue life, while compressive residual stress can improve fatigue performance by slowing crack initiation and propagation.

1.1.3. Work hardening

Work hardening, also known as strain hardening, is a phenomenon where the stress required to induce plastic deformation of a metal increases with increasing strain [7]. This

occurs when a metal is plastically deformed. The work hardening can easily be observed from the stress-strain curve of a monotonic tensile test. Fig.1-2 shows a typical monotonic stress-strain curve for a ductile metal. Loading starts at point A and continues to point B, where the stress reaches the yield stress σ_y, causing the material to plastify. When the material is unloaded from point C, the elastic strain ε_e will be recovered, while the plastic strain ε_p will remain. If the material is reloaded after that, it will not plastify until the stress reaches σ_{y1}, which is greater than the initial yield stress.. This phenomenon is called work hardening. It usually happens in the forming process of metal at room temperature. For fatigue loading, softening can also be observed during some stages in certain materials.

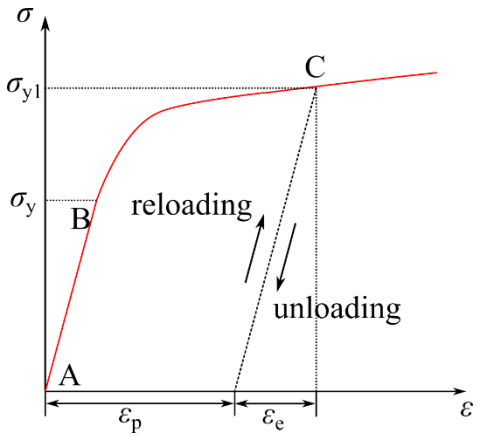

Fig.1-2 The work hardening in monotonic tension

The phenomenon of work hardening is closely linked to dislocations, which appear during plastic deformation and form at grain boundaries, free surfaces, or interfaces between the lattice matrix and second phase particles. These dislocations interact with each other and impede each other movement, producing resistance to further motion. As dislocation motion becomes more restricted, a larger stress must be applied, resulting in higher strength and flow stress. However, the ductility, or the rate of elongation or reduction of area, decreases at the same time [8][9]. Literature shows that work hardening does have an effect on the plasticity-induced crack opening or closure stress intensities, fatigue crack growth rates (FCGR) and the threshold of resistance to crack propagation. The effect is a complex function of material, crack length and applied load. It was found that work hardening could increase FCGR, and decrease crack opening stress for Al2024 [10]. However, no significant effect was found on Al7475 [11]. Klumpp et.al [12] investigate the effect of work hardening on Inconel 718 alloy. The results indicate that work hardening can decrease the impact of roughness on crack closure, resulting in a smoother fracture surface. However, excessive degrees of work hardening can significantly increase FCGR at the applied ratios (R = 0.2, 0.5, 0.7).

1.1.4. The constitutive behavior

Constitutive behavior describes the mechanical behavior of a material and consists of a set of mathematical idealizations of its observed behavior [13]. For instance, Hooke's Law is a well-known set of equations that describes the behavior of materials within their elastic range.

However, practical material behaviors are complex and cannot be described by only one or two mathematical equations. Therefore, it is important to select the appropriate range or type of behavior to meet the requirements of the problem at hand. In the case of metallic alloys, it is crucial to characterize their elastic-plastic behaviors under loading. The plastic behavior, also known as work hardening behavior, introduced earlier, should be carefully considered.

In engineering research, the hardening behavior of metallic materials is frequently characterized by both kinematic hardening and isotropic hardening, referred to as combined hardening when they are simultaneously present. The schematic diagram illustrating combined hardening under a uniaxial stress state is presented in Fig.1-3. The combined hardening yield surface in principal stress space is derived from both the isotropic hardening and kinematic hardening components. The kinematic hardening part, represented as backstress, shifts the center of the yield surface, while the isotropic hardening, represented as a function of the cumulative plastic strain, changes the dimensions of the yield surface. For practical problems in a monotonic loading state, isotropic hardening is sufficient. However, for more complex issues such as fatigue or shot peening, combined hardening should be selected.

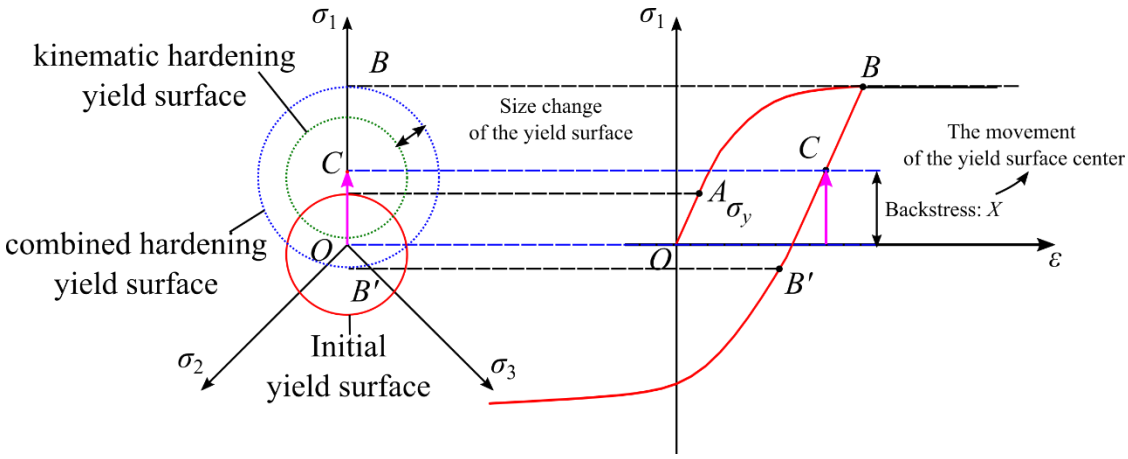

Fig.1-3 Schematic diagram of combined hardening under uniaxial stress state

1.1.5. Shot peening

Shot peening is a conventional surface treatment technique that could enhance the mechanical properties by introducing a compressive residual stress layer. It has been used in industry since the 1940s [14].

Shot peening process is shown in Fig.1-4. In this process, the shots, generally round balls made with metal or ceramic, are accelerated to a high velocity (80-110 m/s for compressed air shot-peening, or 2-10 m/s for ultrasonic shot-peening, use in the present work) to impact the material surface, creating a dimple with each impact. Elastic deformation occurs around the dimple, which is locally plastically deformed. The plastic deformation tends to expand while the adjacent elastic deformation prevents this trend, resulting in a compressive residual stress state. Repeated impacts create overlapped dimples that result in a compressive residual stress layer, while the core region contains tensile residual stress for equilibrium. Meanwhile, work hardening is also introduced to the material due to the strong plastic deformations on the surface

caused by the impacts. Since the crack of fatigue failure generally occurs at the surface, the compressive residual stress layer introduced by shot peening could effectively slow the crack initiation and propagation.

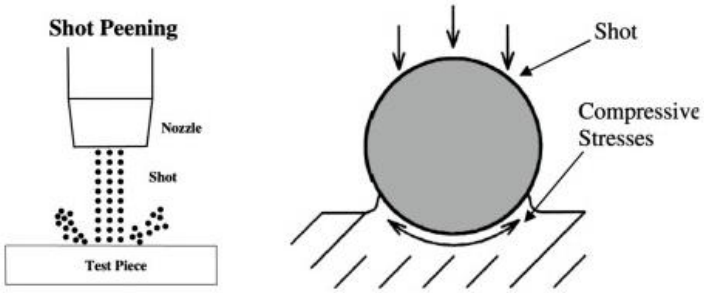

Fig.1-4 Shot peening process [15]

1.2. Parameters evolution during cyclic loading

1.2.1. The relaxation of residual stress

Compressive residual stresses can improve the fatigue performance. However, this improvement depends on the residual stress distribution and stability. Any relaxation could decrease the benefits. Mattson and Coleman [16] observed the relaxation of residual stress after cyclic loading a long time ago. Although relaxation occurs, the remaining compressive residual stress can still contribute to fatigue life. Zhuang and Halford [17] proposed that the cyclic relaxation of residual stress is mainly affected by three factors: (1) the loading parameters, such as stress amplitude, mean stress ratio or cycle numbers; (2) the initial residual stress magnitude and degree of work hardening; and (3) the cyclic behavior of the material. In which, the stress amplitude, mean stress ratio or cycle numbers are closely related to the fatigue performance. Leguinagoicoa et.al [18], Maleki et.al [19] and Kim et.al [20] investigated the shot peening residual stress relaxation during the low cycle fatigue process. Their results lead to the similar conclusion that the rate of residual relaxation increases with the applied stress amplitude, as shown in Fig.1-5. Moreover, the relaxation is significant at the first few cycles.

Besides, Leguinagoicoa et.al [18] also investigate the relaxation under quasi-static loading. The results show that the relaxation is positively related to the magnitude of applied stress, which is the same as the cyclic loading. Additionally, it is found that when a tensile stress is applied, relaxation occurs when the applied stress is higher or equal to the monotonic yield stress. When the applied stress is lower than the yield stress, no relaxation occurs or even the compressive residual stress increases.

As mentioned above, the residual stress occurs because of the incompatibilities of deformation in the material. The relaxation during cyclic loading could be due to the redistribution of the plastic deformation or dislocation, which changes the incompatibility state, thus make the residual stress relax and redistribute.

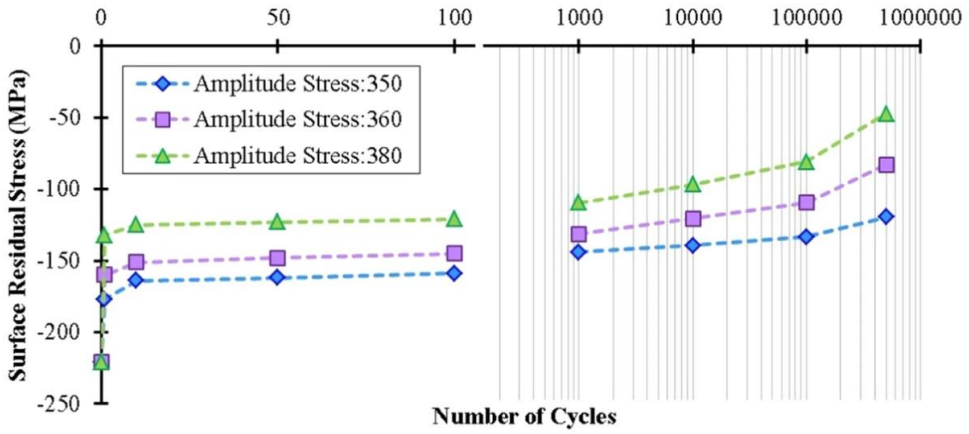

Fig.1-5 Surface residual stress in different cycles for conventionally treated specimen S171-100 [19]

1.2.2. The relaxation of mean stress

Mean stress was focused on because of its significant effect on fatigue life for engineering materials [21]. For the bulk material, it is shown that a compressive mean stress is beneficial to fatigue performance while a positive mean stress gives an opposite effect [22]. Both tensile and compressive mean stresses tend to evolve during cyclic loading [23].

Previous experimental studies under strain controlled cyclic tests for different strain ratios show that the mean stress relaxation only occurs for a strain ratio $R_\varepsilon \neq -1$ [21][22]. The mean stress then tends to relax to zero for large strain amplitudes when large plastification occurs, or to an intermediate value depending on the degree of plastification (See the figures shown in Chapter 4). The relaxation rate increases with increasing strain amplitude and decreases with increasing strain ratio. Moreover, the mean stress is sensitive to the material cyclic behavior. Generally, mean stress relaxation occurs more easily for cyclically softening materials [24].

In addition, for the shot peened samples, mean stress relaxation during cyclic loading can cause surface residual stress relaxation, which can affect fatigue performance [23]. Observing residual stress relaxation on a cycle-by-cycle basis is difficult, whereas mean stress relaxation is easier. It would be interesting to investigate the coupling effect between residual stress relaxation and mean stress relaxation, which could bridge the gap between the two phenomena.

1.2.3. The evolution of work hardening

For mechanical components subject to cyclic loading under strain control, metallic materials exhibit either cyclic hardening, cyclic softening or cyclic hardening followed by cyclic softening. As shown in Fig.1-6.

Some possible reasons for cyclic behaviors can be explained by the evolution of dislocation patterns during cyclic loading. For instance, the carbide precipitation on dislocations [27] and the accumulation of dislocations [28] may cause cyclic hardening. In contrast, the grain growth during cyclic loading at high temperatures [29], the formation of planar dislocation structures [30], and the growth of precipitates [31] will lead to cyclic softening. The evolution

of dislocation density and distribution, i.e. work hardening, can influence the cyclic behaviors of the material, resulting in varying fatigue performance. Therefore, investigating the evolution of work hardening can lead to a better understanding of the deformation mechanisms under cyclic loading.

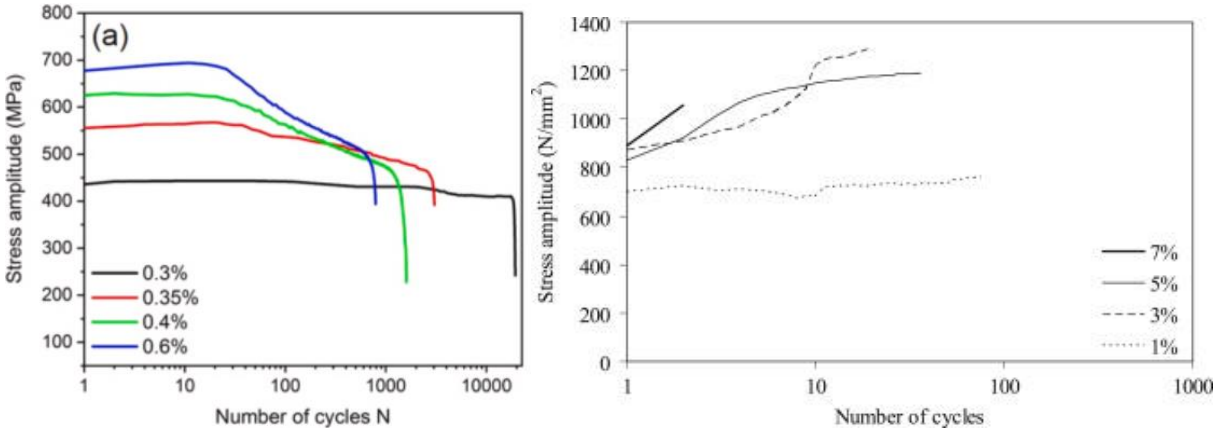

Fig.1-6 Cyclic behaviors of (a) Inconel 750H under different strain amplitudes [25], the alloy exhibits a continuous cyclic softening after the initial hardening (b) Cold-formed stainless steel, the alloy exhibits a cyclic hardening [26]

1.3. Characterization of residual stress and work hardening

1.3.1. Characterization of residual stresses

Currently, the techniques for measuring residual stresses are well established and the discrepancies between different measurement methods are not large. According to the measurement principle, these methods can be mainly divided into mechanical relaxation methods, diffraction methods and methods based on a correlation with physical properties (ultrasound velocity, Barkhausen noise…).

Due to the self-equilibrium of residual stress, it is predicted that the redistribution of residual stress may cause strains or displacements in a component. If perturbed in a controlled manner, the residual stress state can be determined by measuring the strain or displacement, based on the principles of elastic mechanics. This is called mechanical relaxation method. According to the different ways of residual stress relaxation, these methods are called hole drilling method [32], ring-core method [33], layer removal method [34] and contour method [35]. The accuracy of first two methods can be improved by using advanced techniques to measure the displacement or strain. The layer removal method assume that the residual stress is uniformly distributed in each layer. When the layers are removed, the residual stress can be obtained from the deformation. The contour method is widely used in welding residual stress measurement. The schematic diagram of contour method is shown in Fig.1-7.

Samples are cut along the section where residual stresses are to be measured. The cutting surface is assumed to be an ideal plane, and there exists an unknown residual stress σ_A in the sample. Due to stress relaxation and redistribution, the contour of the cutting surface is deformed. If an external reverse stress σ_C is applied to the surface, its planar state prior to

cutting can be restored. According to Bueckner's superposition principle, the external stresses applied are residual stresses. In practice, contour data is collected and fitted using a measuring device. This data is then loaded into a stress-free finite element model in the opposite direction to obtain the stress distribution in the cross-section.

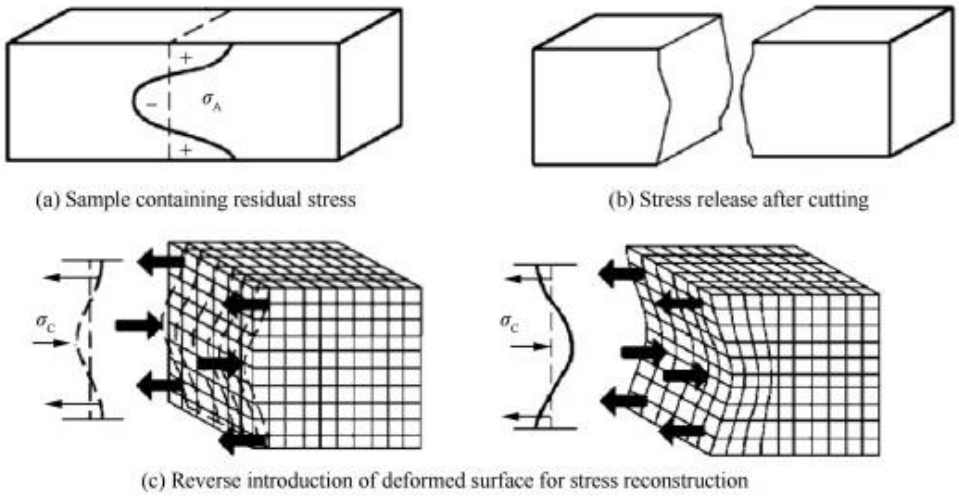

Fig.1-7 The schematic diagram of contour method [36]

The fundamental mechanical principle of these mechanical relaxation methods necessitates the destruction of the specimen in order to achieve residual stress measurement, which may not be desirable in some cases. Diffraction is the most widely used of the non-destructive methods, which include X-ray diffraction [37], neutron diffraction [38] and so on. These methods can achieve non-destructive residual stress measurement at the penetration depth of the diffraction source. In which, X-ray diffraction is most popular for measuring residual stresses and has been used in many fields.

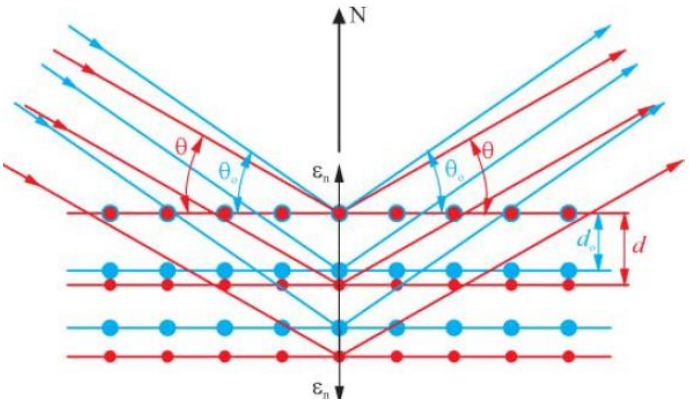

Fig.1-8 Strain measurement with Bragg's law [37]

X-ray stress measurement is based on two fundamental theories: the theory of elasticity, which defines the relationship between stresses and strains, and X-ray diffraction theory, which describes the relationship between the atomic arrangement in a solid and its diffraction pattern [37]. The strain is measured with Bragg's law, as shown in Fig.1-8.

Bragg's law is given by:

$$\lambda = 2d_0 \sin\theta_0 \qquad (1-1)$$

Where λ is the wavelength of X-ray beam, θ_0 is the Bragg angle and d_0 is the space between adjacent crystal planes. The subscript 0 means the interplanar spacing of strain free crystal, shown as blue lines or dots in Fig.1-8. A standard method called the $\sin^2\psi$ method is often used for residual stress measurement. By using this method, the sample is tilted with two rotations, described by angles ψ and ϕ. The angles refer to the sample coordinates shown Fig.1-9.

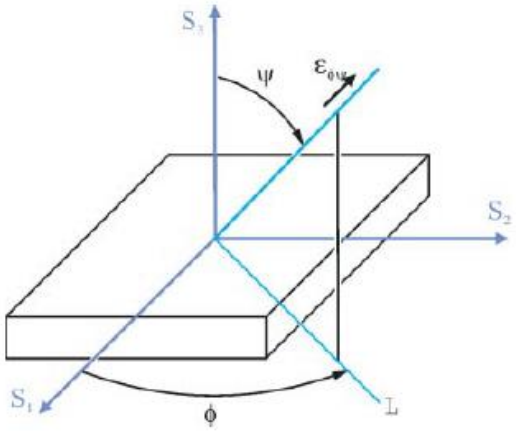

Fig.1-9 The sample coordinate system for X-ray diffraction [37]

The strain measured under sample coordinate system $\varepsilon_{\phi\psi}$ is given by:

$$\varepsilon_{\phi\psi} = \frac{d_{\phi\psi} - d_0}{d_0} = \varepsilon_{11}\cos^2\phi\sin^2\psi + \varepsilon_{22}\sin^2\phi\sin^2\psi + \varepsilon_{33}\cos^2\psi + \varepsilon_{12}\sin 2\phi\sin^2\psi + \varepsilon_{13}\cos\phi\sin 2\psi + \varepsilon_{23}\sin\phi\sin 2\psi \qquad (1-2)$$

In which $d_{\phi\psi}$ is the interplanar spacing. The stress is determined from Eq.1-2 with Hooke's law, shown as:

$$\varepsilon_{\phi\psi}^{\{hkl\}} = S_1^{\{hkl\}}(\sigma_{11} + \sigma_{22} + \sigma_{33}) + \frac{1}{2}S_2^{\{hkl\}}\sin^2\psi\,(\sigma_{11}\cos^2\phi + \sigma_{12}\sin 2\phi + \sigma_{22}\sin^2\phi) + \frac{1}{2}S_2^{\{hkl\}}\sin 2\psi\,(\sigma_{13}\cos\phi + \sigma_{23}\sin\phi) + \frac{1}{2}S_2^{\{hkl\}}\sigma_{33}\cos^2\psi \qquad (1-3)$$

Where $\varepsilon_{\phi\psi}^{\{hkl\}}$ is the strain measured under sample coordinate system from the lattice planes $\{hkl\}$, $S_1^{\{hkl\}}$ and $\frac{1}{2}S_2^{\{hkl\}}$ are the diffraction elastic constants.

For a biaxial stress state, Eq.1-3 can be simplified as:

$$\varepsilon_{\phi\psi}^{\{hkl\}} = S_1^{\{hkl\}}(\sigma_{11} + \sigma_{22}) + \frac{1}{2}S_2^{\{hkl\}}\sigma_\phi\sin^2\psi + \frac{1}{2}S_2^{\{hkl\}}\tau_\phi\sin 2\psi \qquad (1-4)$$

In which, σ_ϕ is normal stress and τ_ϕ is the shear stress along L direction:

$$\sigma_\phi = \sigma_{11}\cos^2\phi + \sigma_{12}\sin 2\phi + \sigma_{22}\sin^2\phi$$
$$\tau_\phi = \sigma_{13}\cos\phi + \sigma_{23}\sin\phi$$

As the sample is tilted with a series of ψ, a series of $\varepsilon_{\phi\psi}^{\{hkl\}}$ can be measured. If the measured strain is plotted versus $\sin^2\psi$, there should be a linear relationship. Thus, the normal stress can be obtained with the slope *m*:

$$\sigma_\phi = \frac{m}{\frac{1}{2}S_2^{\{hkl\}}} \qquad (1-5)$$

X-ray diffraction and the $\sin^2\psi$ method is applied in this thesis in order to obtain the residual stress information. However, it should be noted that X-ray diffraction also has some disadvantages. One of which is the large measurement area. The beam size of X-rays becomes smaller as the technology advances, but it still remains around several square millimeters. This presents challenges when applying X-ray diffraction to small samples. Another disadvantage is the sample geometry effect. The curvature of the sample will introduce geometric effects, translation and rotation, thus reduce the quality of the diffraction patterns, which in turn affects the accuracy of the extracted stress values [39].

1.3.2. Characterization of work hardening

Characterizing work hardening is a complex process. As previously stated, work hardening involves the dislocations density and distribution, the precipitates growth or disordering, the misorientation of grains and other factors. No single indicator can fully represent work hardening. Therefore, different characterization methods can be chosen for different indicators, in a semi-quantitative way.

The storage of dislocation can result in work hardening. Dislocations may be stored for two reasons: they may accumulate in a random way, or they may be required for the compatible deformation of various parts of the material [40]. The first type is referred as statistically stored dislocations (SSD) and the second type is referred as geometrically necessary dislocation (GND). Electron backscatter diffraction (EBSD) can be used to characterize the GND. The system can be attached to a Scanning Electron Microscope (SEM) and is commonly used in material science field to gather information on sample microstructure. The schematic diagram of EBSD is shown in Fig.1-10.

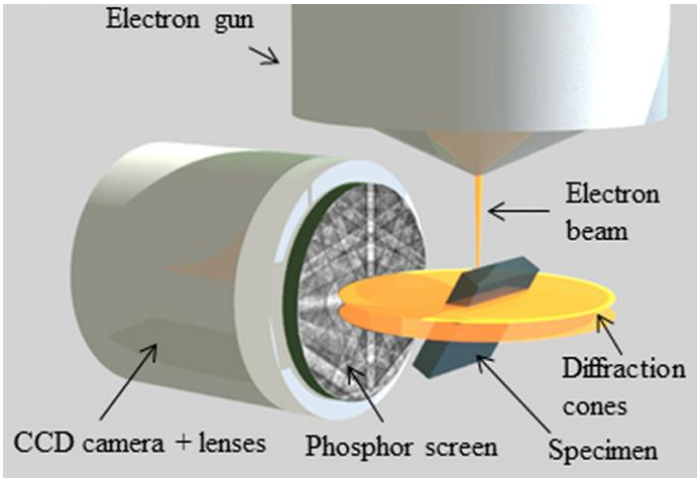

Fig.1-10 The schematic diagram of EBSD system [41]

The sample is typically tilted at an angle of approximately 70° relatively to the incident electron beam. Because of the interaction between the backscattered electrons and the atoms, the electrons are both elastically diffracted and lose energy, causing them to scatter at various

angles. The resulting Kikuchi patterns are formed when the electrons reach the phosphor screen. These patterns can be indexed to provide information about the grain structure, grain orientation, and phase of the material. The misorientation within a given area (the kernel) can be characterized as Kernel Average Misorientation (KAM) or within each grain as Grain Average Misorientation (GAM).

For instance, KAM is based on the kernel area (scanning pixel pattern). It is calculated by the misorientation angles between each pixel and its neighbors, as shown in Fig.1-11.

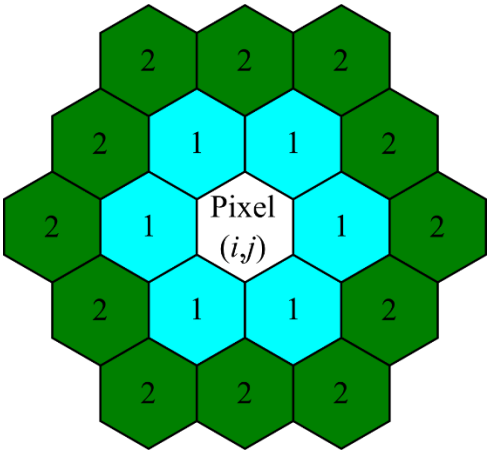

Fig.1-11 KAM calculation

For a pixel at position (i,j), the $\mathrm{KAM}_{i,j}$ can be calculated with:

$$\mathrm{KAM}_{i,j} = \frac{1}{N_{i,j}} \sum_{(k,l)\in N_{i,j}} \mathrm{mis}\left(o_{i,j}, o_{k,l}\right) \qquad (1-6)$$

In which, $N_{i,j}$ means the number of the neighboring pixels taken into account, $o_{i,j}$ is the orientation of the pixel at position (i,j), $o_{k,l}$ is the orientation of the pixel at position (k,l), $\mathrm{mis}(o_{i,j}, o_{k,l})$ is the disorientation angle between the pixel at position (i,j) and its neighboring pixels at position (k,l). The number of the neighboring pixels could be defined by different orders. For instance, in Fig.1-11, the blue pixels mean the 1st order neighboring while the green pixels mean the 2nd order neighboring. GAM uses a similar calculation method, but it is based on the grain rather than the pixel. It determines the orientation of the grain first and then calculates the average disorientation angle between all the pixels in this grain.

Two approaches can be used to calculate GND densities. The first one follows Kubin and Mortensen [42], for which the GND density ρ_{GND} can be described as:

$$\rho_{\mathrm{GND}} = \frac{2\vartheta}{ub_v} \qquad (1-7)$$

Where u is the scanning step, b_v is the magnitude of Burger's vector and ϑ is the kernel average misorientation obtained with Eq.1-6. The second approach is based on Nye's dislocation tensor [43]. The dislocation density tensor α_d can be related to the dislocations present in the neighborhood by the relation [44]:

$$\alpha_d = \sum_{i=1}^{K} \rho^i \left(b_v^i \otimes z^i\right) \qquad (1-8)$$

Where $b^i \otimes z^i$ represents a geometrical definition of dislocation having Burger's vector b_v^i and slip plane normal direction z^i. The sum is over all the dislocations present and ρ^i is the scalar dislocation density of dislocation. With a linear simplex method and a normal equation lower bound method, for FCC materials (Such as the target alloy in this thesis), Eq.1-8 can be reduced to:

$$\alpha_{d-l} = A^{lk}\rho^k, k = 1{,}36 \text{ and } l = 1{,}9 \qquad (1-9)$$

Where the matrix A is a component of the dislocation dyadic. With L^2 minimization method, the densities of all 36 dislocations can be computed as:

$$\rho_{\mathrm{GND}} = A^T(AA^T)^{-1}\alpha_d \qquad (1-10)$$

In general, both calculation methods yield very consistent results. Thus, according to the first approach, KAM with a constant scanning step can be used to represent the GND density. With this technique, it is possible to show the work hardening introduced by treatment methods. Fig.1-12 shows the KAM map of the additively manufactured nickel base alloy under different shot peening intensities. The different depth of affected layers (hardening layers) can be observed clearly.

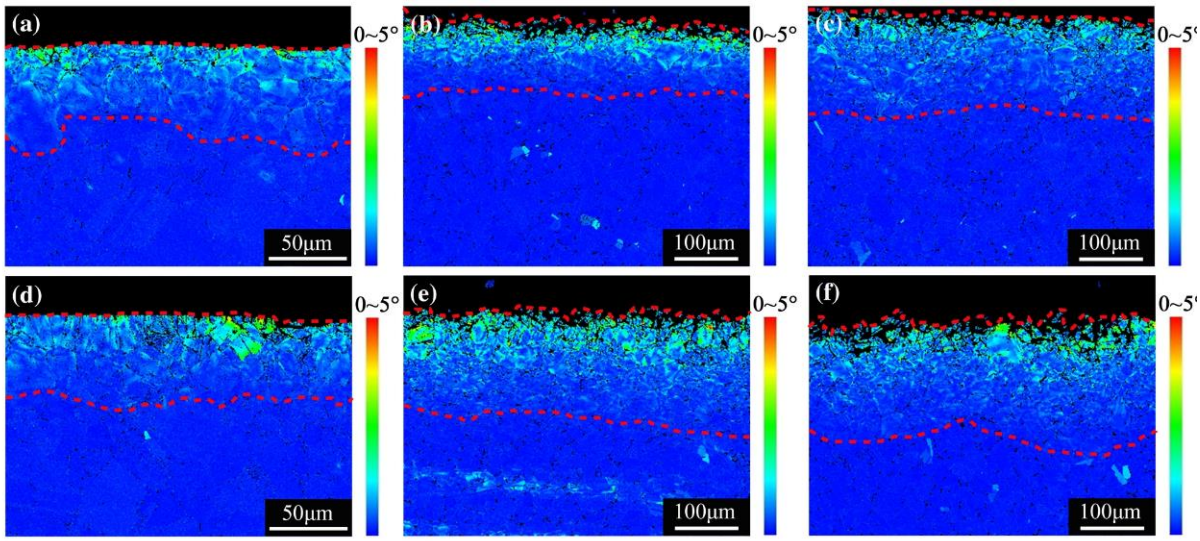

Fig.1-12 KAM map of FGH4113A Ni-based powder metallurgy super alloy under different shot peening intensities, the red line in the figure shows the layer affected by shot peening [45]

However, the quantitative measurement of the amount of the work hardening through EBSD is not perfect. Although misorientation angles can represent the amount of work hardening to some degree, it is important to note that areas with strong work hardening, generally occur with high plastic deformation, and thus cannot be accurately indexed. The image quality in these areas is poor, making characterization impossible. In addition, the sample preparation for EBSD is complex. Samples must be well polished with no deformation introduced, which adds to the difficulty of the measurement. Furthermore, as mentioned above, GNDs, together with SSDs, represent the degree of work hardening. However, only the GNDs can be observed through EBSD technique.

The peak broadening of X-ray diffraction lines is related to lattice strain heterogeneities, which is mostly caused by dislocation density [46]. Therefore, X-ray diffraction is a useful technique for characterizing work hardening.

The dislocation density ρ_d can be calculated with [47]:

$$\rho_d = \sqrt{\rho_D \rho_\varepsilon} \qquad (1-7)$$

In which:

$$\rho_D = \frac{3}{D^2} \qquad \rho_\varepsilon = \frac{k\,\langle\varepsilon\rangle^2}{b_v^2}$$

Where D is the crystallite size, k is a material constant, $\langle\varepsilon\rangle$ is the RMS (root mean square) micro strain and b_v is the magnitude of Burger's vector. The RMS micro strain could be obtained, for instance, from Williamson-Hall function [48]:

$$B\cos\theta = \frac{K\,\lambda}{D} + 4\,\langle\varepsilon\rangle \sin\theta \qquad (1-8)$$

Where B is the peak width, K is the crystallite shape factor, close to one (Scherrer's constant) and θ is the diffraction angle. For a quantitative approach, B should be corrected from instrumental broadening.

Previous literature [49] compared the dislocation density measured by EBSD and X-ray diffraction. For EBSD, they calculated GNDs with the second approach while for X-ray diffraction they used the method mentioned above. Results show that the density measured by X-ray diffraction is always high and not accurate for low dislocation density. Besides, RMS micro strain is obtained from the slope on the plot of $B\cos\theta$ *vs* $\sin\theta$. Therefore, it is necessary to have a sufficient number of diffraction peaks. This limitation applies to certain materials that do not have an abundance of diffraction peaks. Other methods such as Warren-Averbach or Krivoglaz methods can also be used but they have their limitations and can be complex to implement.

An empirical relationship between the cumulative plastic strain and the diffraction peak width can be established through a series of tests, an example is shown in Fig.1-13. The samples are first annealed or treated to obtain an optimal initial state, and then deformed to a known amount. The peak width is measured for all samples.

This method allows for easy quantitative characterization of work hardening. However, it is only useful for materials where the cumulative plastic strain is independent of the mode of deformation. Otherwise, if the deformation mode of the measured sample differs from that of the known deformed sample, the correlation may not be entirely suitable. Thus, it can be seen above that X-ray diffraction is an empirical approach to estimated work hardening, and it can only characterize isotropic hardening. Even when only isotropic hardening is present, a dislocation rearrangement at microscale (dislocation dipoles, dislocation cells, subgrain boundaries, etc.) can affect diffraction peak widths in a non-monotonic way.

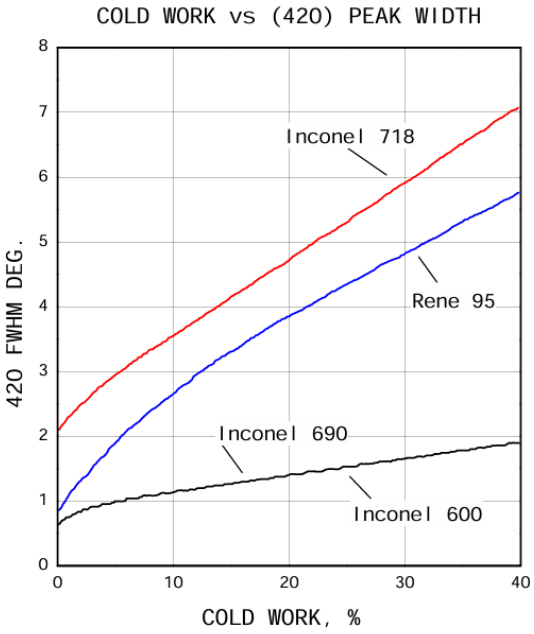

Fig.1-13 Empirical curves of diffraction peak width to percent work for four nickel base alloys [50]

1.4. Instrument indentation technique

1.4.1. The key parameters

Nanoindentation test can be used to determine some mechanical properties of materials with the help of the load-depth (*P*-*h*) curve. The maximum load P_{max}, the indentation depth h and contact stiffness S are the key parameters usually extracted from *P*-*h* curve, as shown in Fig.1-14. In which, the contact stiffness S can be described as:

$$S = \frac{\mathrm{d}P}{\mathrm{d}h}_{h=h_{\max}} \qquad (1-9)$$

Oliver and Pharr [51] proposed that the unloading curve could be fitted by a power law relating the indentation load P to the difference between the indentation depth h and the residual indentation depth:

$$P = B_{\mathrm{iit}}\left(h - h_f\right)^m \qquad (1-10)$$

Where B_{iit}, h_f and m are the best fit parameters. Similar to the selection of data for the experimental unloading curves, in this paper, the data in the range 40–95% of the maximum load are used for the fit. Thus, S could be obtained from the following equation:

$$S = \frac{\mathrm{d}P}{\mathrm{d}h}_{h=h_{\max}} = m\,B_{\mathrm{iit}}\left(h_{\max} - h_f\right)^{m-1} \qquad (1-11)$$

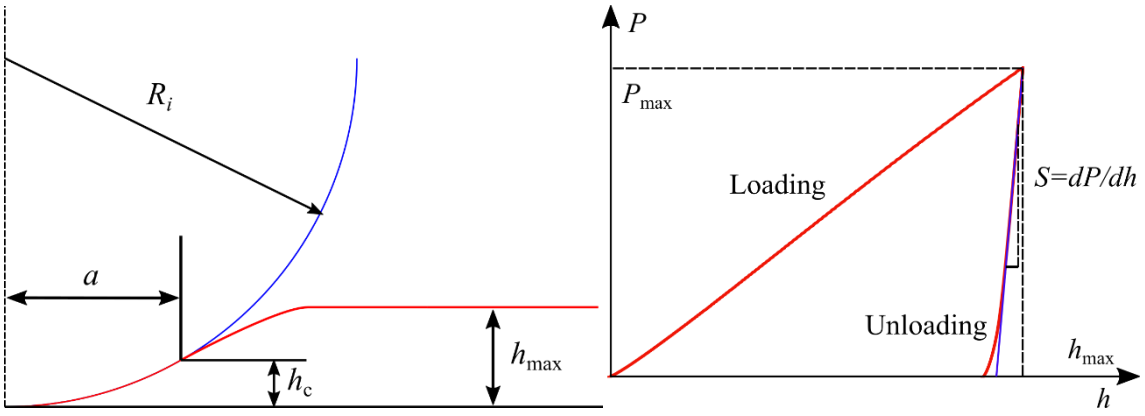

Fig.1-14 The key parameters in nanoindentation test

For a spherical indenter, R_i is the radius of the indenter and a is the contact radius of indentation. The contact area A_c can be obtained from

$$A_c = \pi a^2 \qquad (1-12)$$

The contact hardening H is calculated from

$$H = \frac{P_{max}}{A_c} \qquad (1-13)$$

In practice, the contact radius a could be calculated with:

$$a = \sqrt{2R_i h_c - h_c^2} \qquad (1-14)$$

Where h_c is the contact depth, which is described as:

$$h_c = \alpha_p \left(h_{max} - \varepsilon \frac{P}{S} \right) \qquad (1-15)$$

Where α_p is a factor of pile up taken generally equal to 1.2, ε is a indenter factor which is equal to 0.75 for a spherical indenter.

For a Berkovich indenter, the ideal contact area is:

$$A_c = 24.5 h_c^2 \qquad (1-16)$$

Considering the bluntness and other imperfections of the indenter, the area function could be described as:

$$A_c = C_0 h_c^2 + C_1 h_c + C_2 h_c^{\frac{1}{2}} + C_3 h_c^{\frac{1}{4}} + \cdots + C_8 h_c^{\frac{1}{128}} \qquad (1-17)$$

Where C_0~C_8 are constants calibrated from a standard reference material (i.e. fused silica). The first term represents the global indenter shape, the others describe the correction of the geometry due to the blunting and other imperfections.

The reduced modulus E^* could then be calculated from indentation as:

$$E^* = \frac{1}{\beta} \frac{\sqrt{\pi}}{2} \frac{S}{\sqrt{A_c}} \qquad (1-18)$$

Where β is the indenter geometry shape factor, which is equal to 1 for conical or spherical indenter and 0.75 for Berkovich indenter. Then, we can obtain the modulus of the material from the following equation:

$$\frac{1}{E^*} = \frac{1-\nu^2}{E} + \frac{1-\nu_i^2}{E_i} \qquad (1-19)$$

Where E_i and ν_i are the Young's Modulus and Poisson's ratio of the indenter, E and ν are the Young's Modulus and Poisson's ratio of the material.

Unlike the quasi-static indentation test mentioned earlier, the continuous stiffness method (CSM) has become a popular indentation measurement method in recent years. The method involves superimposing a high-frequency oscillation (>40 Hz) onto the main loading signal and measuring the magnitude of the resulting partial unloading using a lock-in amplifier [52], as shown in Fig.1-15. This enables the continuous determination of the *S*, *H*, and *E* of the material at different depths of indentation. In which, contact stiffness *S* is obtained from the dynamic response of the indentation system [53], not the *P-h* curve, which is different with the traditional indentation method.

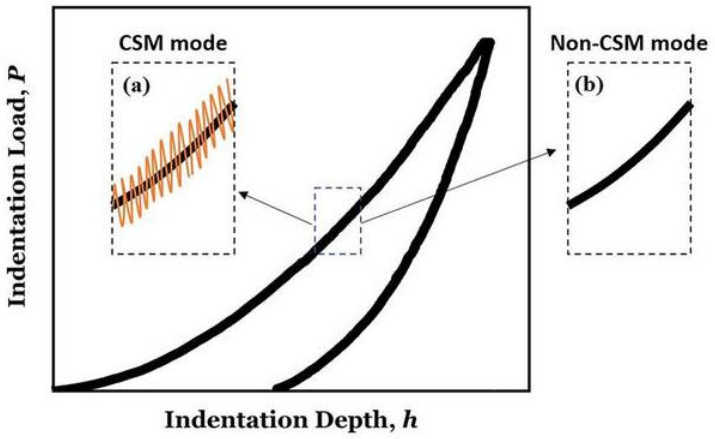

Fig.1-15 The indentation loading with or without CSM [52]

1.4.2. Characterization of residual stress with indentation technique

Instrumented indentation technique has been an efficient new measurement method in recent years due to its sensitivity to residual stress. The effect of residual stress on indentation load-depth (*P-h*) curve was investigated by Tsui et al. [54] with experiments in a purely elastic regime and by Bolshakov et al.[55] using the finite element analysis. The influence of residual stress on *P-h* curve is shown in Fig.1-16. The compressive residual stress moves up the *P-h* loading curve while the positive residual stress moves it down.

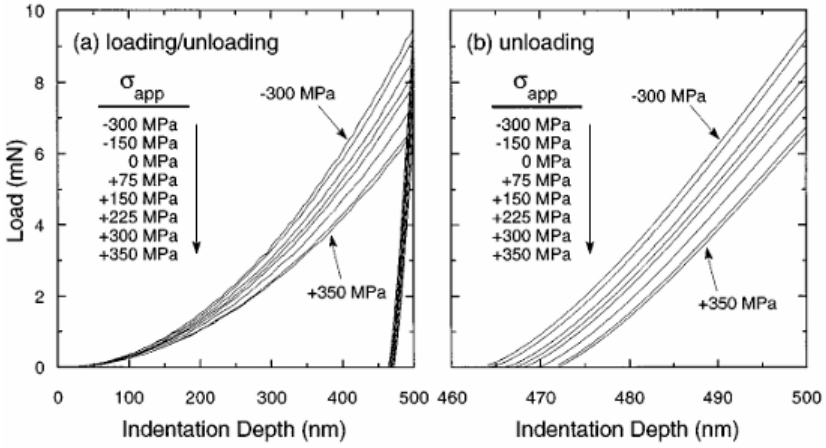

Fig.1-16 Simulated indentation *P-h* curves for several different applied biaxial stresses [55]

Subsequently, Giannakopoulos and Suresh [56][57] suggested that the contact area could be affected by residual stress and proposed a method to estimate an equibiaxial residual stress state using instrumented sharp indentation. Carlsson and Larsson [58][59] recognized that residual stress is correlated with the size of the contact area. In addition to the contact area, many other responses, such as the curvature of loading curve [60][61], and indentation load [62]-[68], could also be affected by the residual stress, and thus these parameters can potentially be used to estimate them. In the case of a spherical indenter, residual stress also affects the elastic-plastic transition regime [69]. The yield onset [70][71] also can be used for residual stress characterization. Furthermore, Wang et al. [72][73] developed iterative equations using dimensional analysis based on the representative strain to determine the residual stress and elastic-plastic properties of materials. However, the abundance of methods and of fitting parameters makes it highly sensitive to experimental errors, which can lead to challenges such as solution uniqueness and difficulties in practical application.

The methods proposed by the previous literature does give a better view on residual stress characterization with indentation technique. However, none of them takes into account the presence of work hardening, which may also have an influence on the induced responses. This is a key issue as, in most practical cases (shot peening, laser shock peening, stamping, cold-rolling, drawing, etc.) the manufacturing process induces both residual stress and work-hardening. The present work is addressing this issue, in the line of a previous thesis at LASMIS [91].

1.4.3. Influence of work hardening on indentation responses

Instrument indentation technique is also sensitive to the work hardening, which show the potential to characterize the work hardening. With finite element simulations, Li et al. [74] found that, for any given value of the compressive residual stress, a corresponding cumulative plastic strain level can be found that has almost the same indentation response curve, which means that cumulative plastic strain and residual stress may produce a similar effect on the indentation responses, as shown in Fig.1-17. This result indicates that the indentation responses are influenced by the combination of residual stress and work hardening.

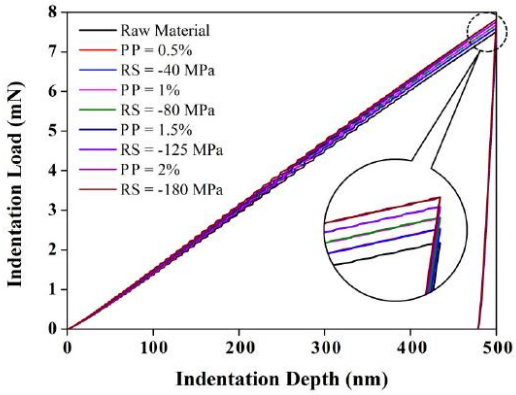

Fig.1-17 *P-h* curves for various combinations of cumulative plastic strain and residual stress for a spherical indenter [74]

In addition, the work hardening is described by cumulative plastic strain in the simulation. However, as mentioned above in Section 1.1.4, work hardening can be described by combined isotropic and kinematic hardenings to model the material behaviors. Isotropic hardening can then be defined as a function of the cumulative plastic strain while the variable for kinematic hardening is a set of tensors called backstress tensors.

For the kinematic hardening, Idriss et al [75] carried out phenomenological simulation studies to investigate the influence of the type of hardening on the *P-h* curves. Their results indicate that kinematic hardening softens the *P-h* curve because some regions in the indented zone undergo different load paths during loading, which means the kinematic hardening should be considered in indentation, as shown in Fig.1-18. Thom et al. [76] developed a nanoindentation load-drop method using the self-similar Berkovich tip to accomplish backstress measurements in single crystals of olivine, quartz, and plagioclase feldspar. However, their study does not provide a clear explanation regarding the effect of backstress on indentation responses. Consequently, the effect of backstress tensors on indentation responses is still not clear.

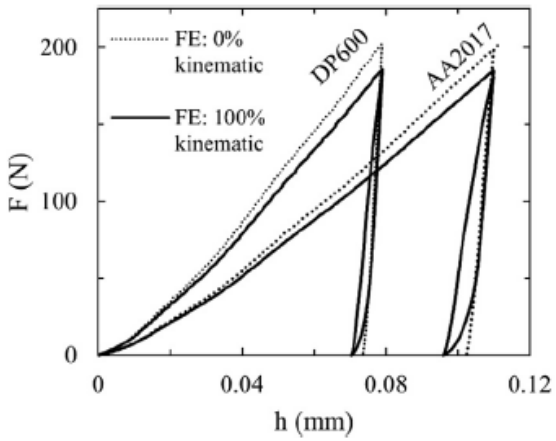

Fig.1-18 *P-h* curves for 0% kinematic hardening and 100% kinematic hardening of DP600 and AA2017 [75]

For a solid that is perfectly plastic-rigid, the ratio of indentation hardness to the yield stress is a constant factor [77][78]. When using a Knoop or Vickers diamond indenter, this factor is very close to 3. Work hardening is directly represented as the change of yield stress, thus the change of hardness. Gale et al. [79] observed that for a given indentation load, the pile-up height decreases, and the indentation depth increases as the amount of work hardening decreases, with both changes following a power law relationship. This result also explains the reason for the change in hardness. Hardness can be easily obtained through indentation tests. However, in most cases, residual stresses are induced along with work hardening. The parameters used to determine hardness, P_{max} and contact area, are affected by residual stress, which can limit the accuracy of hardness measurements for work hardening determination.

All in all, previous research has demonstrated that residual stress and work hardening can be characterized using instrument indentation techniques. However, it is important to note

that they may have similar effects on *P-h* curves or hardness. A suitable method should be proposed to separate them, thus completing the characterization.

1.5. Our target material: Nickel-based alloys

Nickel-based alloys are extensively used in various fields, including space vehicles, rocket engines, nuclear reactors, and submarines, due to their exceptional strength, oxidation resistance, corrosion resistance, and high-temperature performance. They constitute around 50% of the total material requirement of advanced aircraft engines [80].

The gamma phase is a nickel-base phase that typically contains a high percentage of solid-solution elements, including Co, Fe, Cr, Mo, and W. It serves as the matrix for all nickel-based alloys, and is a face-centered cubic (FCC) structure. In addition, gamma prime γ' phase and gamma double prime γ'' phase also exist as precipitates in nickel-based alloys. Gamma double prime, γ'', is a phase in which Ni and Nb combine with iron to form body-centered tetragonal (BCT) Ni3Nb. This phase offers high strength at low to intermediate temperatures but is unstable at temperatures above approximately 650°C. This phase exists in nickel-iron alloys, which is the main source of the precipitate strengthening [81]. Secondary precipitate strengthening comes from gamma prime γ' precipitates, which is formed by adding Al and Ti in precise amounts to precipitate FCC γ' (Ni3Al, Ti). This phase is essential for achieving high-temperature strength and creep resistance.

Inconel 625 is a solid-solution hardening nickel-based alloy with excellent corrosion resistance. It contains solid solution strengthening elements such as Cr, Mo, Fe, and Nb. Cr and Mo enhance the alloy corrosion resistance, Fe reduces cost, and Nb facilitates precipitation hardening [82].

Two kinds of Inconel 625 alloy are investigated in this thesis, one is a cold rolled commercial Inconel 625 and another one is an additively manufactured Inconel 625 by a Markforged® equipment, with the process called Atomic Diffusion Additive Manufacturing (ADAM). This process combines metal injection molding (MIM) and fused filament fabrication (FFF) technologies into Bound Powder Extrusion (BPE) [83], which provides a fast and convenient method for printing metal materials. Previous literature [84-86] has extensively researched the performance of commercial Inconel 625. However, there are few works that present the performance of the printed Inconel 625 using ADAM process.

1.6. The aims and technique approaches

Residual stress and work hardening can have a significant impact on material fatigue performance. However, in most situations, their effects are combined. To study the role of residual stress or work hardening during fatigue, it is necessary to characterize them separately. This allows their evolution to be investigated, and fatigue specimens can be specifically designed to improve fatigue performance based on their respective characteristics. Currently widely used characterization methods can only measure either residual stress or work hardening, and there are few methods for quantitative characterization of work hardening. Instrumented

indentation technique is sensitive to both residual stress, which provides the possibility to characterize them simultaneously.

There are mainly two aims in this thesis. The first aim is to propose a method to characterize the residual stress and work hardening with nanoindentation technique. Finite element simulation is a straightforward method for investigating and calibrate the new method. As our final characterization is applied to fatigue analysis, we will use the combined hardening behavior in the simulation. The cumulative plastic strain (representing isotropic hardening) and backstress (representing kinematic hardening) can serve as indicators of work hardening. The effect of work hardening on indentation response will be investigated using finite element analysis due to its low cost and visualization. Furthermore, the feasibility and accuracy of the proposed method can also be verified and examined through numerical view. This part will be presented in Chapter 2.

When the proposed characterizing method has been proven reliable with the simulation approach, the next step is to apply it in practice for the commercial alloy Inconel 625. Two samples will be shot peened. One of them will be cut, embedded, and polished in order to perform indentation tests. The proposed method will then be applied to the experimental data. The characterization results will be compared to the conventional methods, with X-ray diffraction being a suitable approach for comparison. Thus, X-ray diffraction will be used to measure the residual stress and work hardening on another sample. Analyzing the difference between the two methods could lead to a better evaluation and improvement of the proposed method. This part will be presented in Chapter 3.

Inconel 625 alloy has been known as having good high temperature performance and is widely used in many fields. However, the performance of printed Inconel 625 using the ADAM process has not been well investigated. Therefore, this thesis also focuses on comparing the tensile and cyclic behavior of both cold rolled and printed Inconel 625 under different intensities of shot peening. X-ray diffraction, EBSD, and instrument indentation technique will be used to provide a comprehensive understanding of the evolution of residual stress and work hardening in both types of samples. This is the main content of Chapter 4.

Chapter 2

Numerical characterization of work hardening and residual stress with indentation

Residual stress and work hardening, also known as strain hardening, can affect material behavior during cyclic loading and, therefore, affect the fatigue performance. In order to better understand their effects on material behaviors, it is necessary to characterize them. The instrumented indentation technique is sensitive to both residual stress and work hardening, making it possible to characterize these two parameters.

The finite element method (FEM) is a cost-effective way to simulate experimental processes, making it particularly useful for exploring new experimental methods in the early stages. In this chapter, we will use FEM to investigate the effect of kinematic hardening on indentation responses, which has seldom (and not completely) been previously presented in the literature. Furthermore, FEM is used to investigate the method of characterizing residual stress and work hardening simultaneously using the instrumented indentation technique.

2.1. Technical background in simulation

2.1.1. Material constitutive behavior

Many constitutive models can be used to describe the material behavior. For nanoindentation, an isotropic hardening model is generally used in the simulation, such as Holloman's power law. In this work, nanoindentation is performed on a shot peened sample. The cyclic loading path is observed under the shot peening area, so the Chaboche combined hardening model, which is a classical and widely used model, is used in this thesis.

For metallic materials with combined hardening mechanisms, a yield function using the von-Mises criterion will be described as:

$$f = J_2\left(\bar{\bar{\sigma}} - \bar{\bar{X}}\right) - R - \sigma_y \qquad (2-1)$$

Where, $\bar{\bar{\sigma}}$ is the stress tensor, $\bar{\bar{X}}$ is the backstress tensor, R is a variable describing the effect of the isotropic hardening, σ_y is the initial yield stress, $J_2\left(\bar{\bar{\sigma}} - \bar{\bar{X}}\right)$ is the equivalent von Mises stress, which is defined as:

$$J_2\left(\bar{\bar{\sigma}} - \bar{\bar{X}}\right) = \sqrt{\frac{3}{2}\left(\bar{\bar{S}} - \bar{\bar{X}}'\right) : \left(\bar{\bar{S}} - \bar{\bar{X}}'\right)} \qquad (2-2)$$

Where, $\bar{\bar{S}}$ is the deviatoric stress tensor, and $\bar{\bar{X}}'$ is the deviatoric part of the backstress tensor.

The Armstrong and Frederick formulation [87] is currently used for the backstress evolution rule:

$$\dot{\bar{\bar{X}}}_k = \frac{2}{3} C_k \dot{\bar{\bar{\varepsilon}}}_p - \gamma_k \bar{\bar{X}}_k \dot{\varepsilon}_p^{eq} \qquad (2-3)$$

In which $\bar{\bar{X}}_k$ is the *k*-th backstress component, C_k and γ_k are *k*-th kinematic parameters, $\dot{\bar{\bar{\varepsilon}}}_p$ is the plastic strain rate tensor, and $\dot{\varepsilon}_p^{eq}$ is the equivalent plastic strain rate, which can be defined as:

$$\dot{\varepsilon}_p^{eq} = \sqrt{\frac{2}{3} \dot{\bar{\bar{\varepsilon}}}_p : \dot{\bar{\bar{\varepsilon}}}_p} \qquad (2-4)$$

The total backstress tensor can be calculated by superimposing several backstress tensors to cover a wide range of deformations [88]:

$$\bar{\bar{X}} = \sum_{k=1}^{N} \bar{\bar{X}}_k \qquad (2-5)$$

The chosen isotropic hardening evolution rule was proposed by Voce [89]:

$$\dot{R} = b(Q - R)\dot{\varepsilon}_p^{eq} \qquad (2-6)$$

Where Q and b are the isotropic hardening parameters.

For a monotonic uniaxial tensile loading, once the previous equations are integrated, the scalar stress σ (in a uniaxial state) can be described as:

$$\sigma = \sigma_y + X + R \qquad (2-7)$$

Where the kinematic hardening part *X* is the sum of each backstress components, which can be described as:

$$X = \sum_{k=1}^{N} \frac{C_k}{\gamma_k} \left(1 - \exp(-\gamma_k p)\right) \qquad (2-8)$$

Where the isotropic hardening part *R* is given as follows:

$$R = Q\left(1 - \exp\left(-b\varepsilon_p\right)\right) \qquad (2-9)$$

In which, ε_p is the plastic strain in uniaxial tensile loading.

2.1.2. Nanoindentation simulation model

Nanoindentation should be performed on the cross section, in order to characterize the residual stress and work hardening of a shot peened material. The procedure of indentation in our test is shown in Fig.2-1.

We take a cylindrical representative volume element (RVE) on the cross section for the simulation, and assume that the residual stress and work hardening are homogenous in the RVE. The simulations in our work are performed on software ABAQUS (Version 2020). The indenter was represented by an analytical rigid surface due to the significant difference in elastic modulus between the indenter and the material. According to the literature, the friction coefficient between diamond and metal materials typically ranges from 0.1 to 0.15 [90]. Therefore, we assume that the interaction between the indenter and the target material is finite

sliding and surface-to-surface, with a friction coefficient of 0.15. The normal contact behavior is defined as a 'HARD' pressure-overclosure relationship. The shot peening stress field and hardening (cumulative plastic strain, backstress) field can be introduced in the model by the ABAQUS option **Predefined field*.

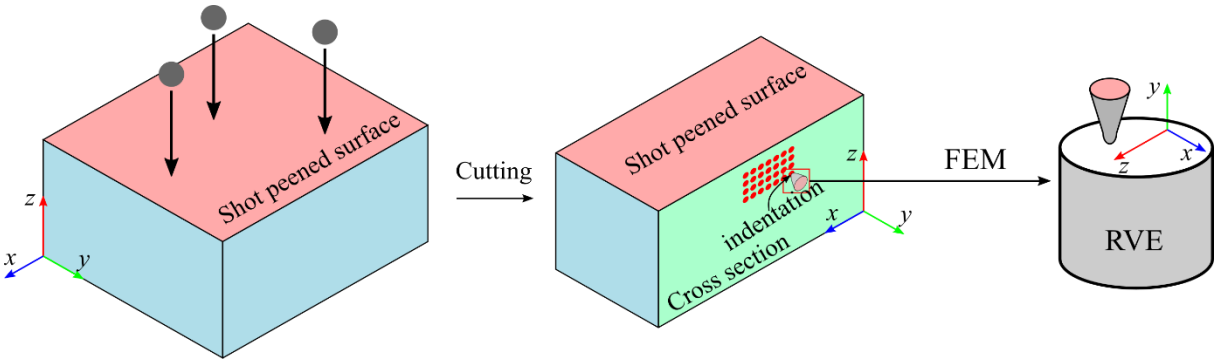

Fig.2-1 Nanoindentation on the cross section

2.1.2.1. Two-dimensional axisymmetric finite element model

Firstly, Li [91] employed the Berkovich indenter in an attempt to develop a characterization method. However, due to the self-similarity of the Berkovich indenter, it provides less information than the spherical indenter, for which the representative strain varies with the penetration depth. In this thesis, a spherical indenter is employed for the development of methods. Considering that the model of indentation using spherical indenter is axisymmetric that the material is isotropic and that the mechanical state is equibiaxial, a 2D axisymmetric finite element model is built to simulate the nanoindentation test. The target is modeled as an elastic-plastic body, with C4X4R elements, which are using the stiffness hourglass control. The target width and height are 200 μm, which is large enough to represent a semi-infinite body for penetration depth. The mesh in the zone beneath the indenter (42.5 μm×42.5 μm) was refined to guarantee the precision of the model, as shown in Fig.2-2. The mesh size was 0.0391 μm at the surface contact with indenter. The number of elements is 23910 in our model. The mesh used here is inspired by Li's model [91], and the sensitivity to mesh size has been validated in his thesis.

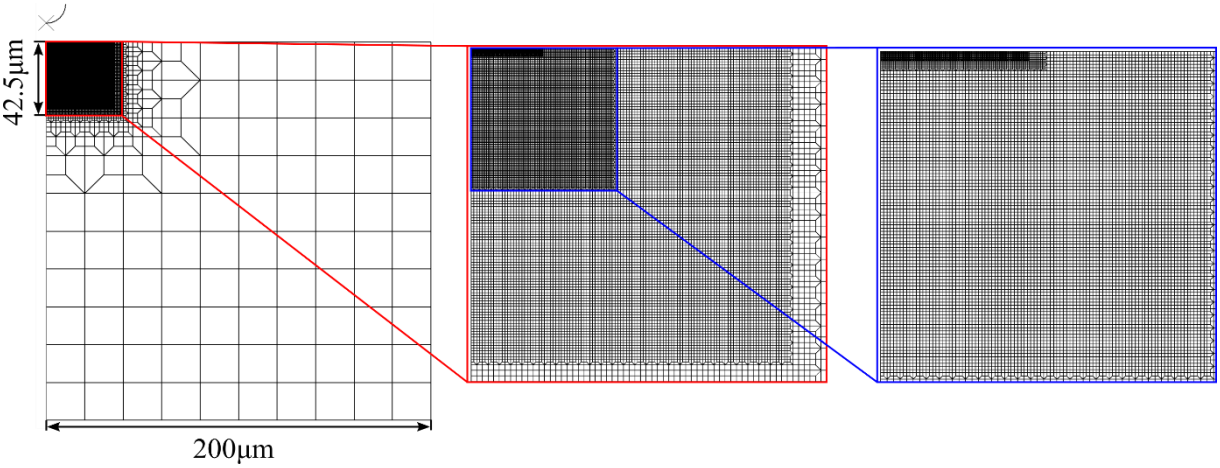

Fig.2-2 2D axisymmetric finite element model

2.1.2.2. Three-dimensional finite element model

As the profile of backstress and residual stress may not be axisymmetric (See in Section 2.2.2), the indentation is no longer an axisymmetric case when residual stress and backstress field are introduced. Thus the 2D axisymmetric model can no longer be used for simulation. Therefore, a 3D finite element model is constructed. The 3D finite element model with C3D8R mesh was rotated by the 2D axisymmetric model along the symmetry axis as shown in Fig.2-3. Only a quarter of the cylindrical target is used to reduce the computation time.

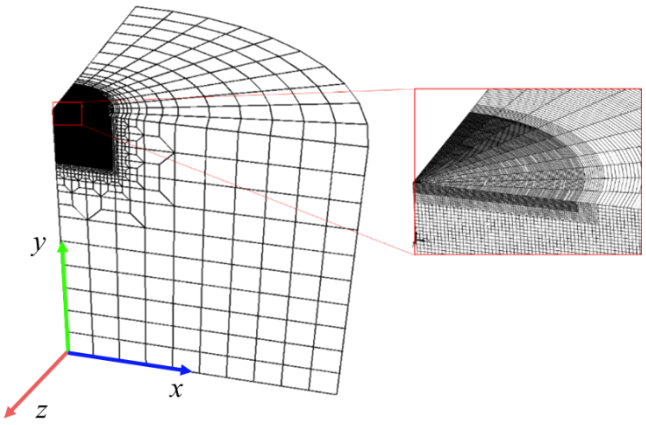

Fig.2-3 3D finite element model

2.1.2.3. Validation of the simplification of the residual stress introduced in the model

Several previous studies indicate that during Berkovich indenter or Vickers indenter indentation processes involving residual stresses, the critical parameter influencing the responses is the hydrostatic stress in the region beneath the indenter, rather than each individual component of the residual stress tensor [56][57]. Therefore, similar to the coordinate system in Fig.2-1, the residual stresses introduced in our work can be transformed into an equibiaxial stress state, as shown in Fig.2-4. The 2D model can then still be used.

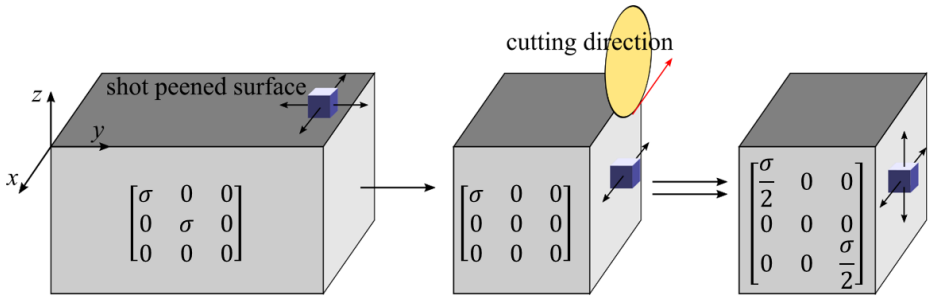

Fig.2-4 Residual stress tensor transformation

However, it has not been validated whether this statement could be extended to a spherical indenter. We therefore carried out simulations to verify this point, using a virtual material shown in Tab.2-1. A spherical indenter is considered with a radius of 2.2 μm.

Tab.2-1: Constitutive parameters of virtual material

E = 200000 MPa, ν = 0.3
σ_y = 850 MPa
C_1 = 5000 MPa, γ_1 = 10

Firstly, an indentation simulation is conducted using the 2D and the 3D finite element model respectively without any residual stress state and the result are shown in Fig.2-5(a). It can be seen that the curve of 2D and 3D model are identical, which means both models (2D and 3D) can represent the indentation responses.

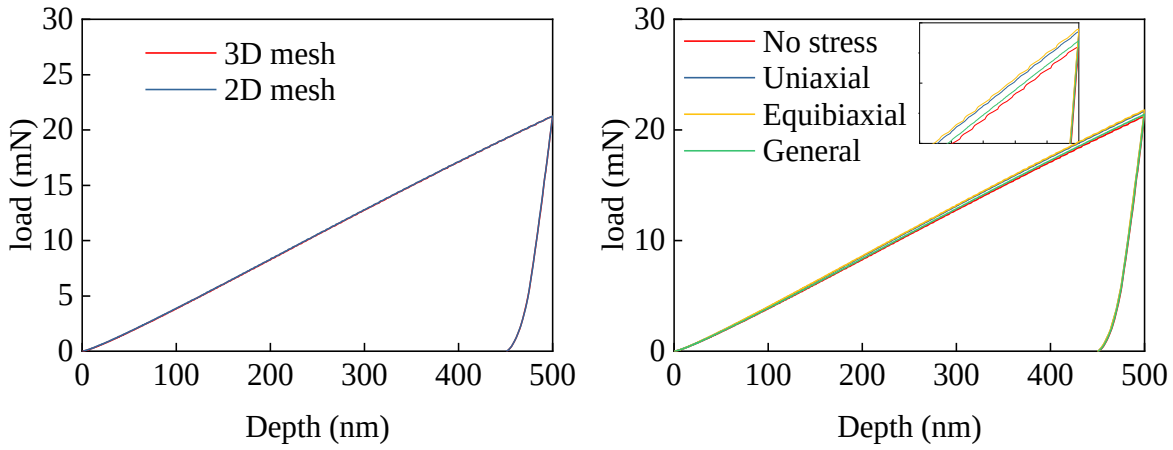

(a) (b)

Fig.2-5 The *P-h* curves of (a)2D and 3D model (b) different residual stress state in 3D model

Fig.2-5(b) shows the *P-h* curves under different residual stress state using 3D model. In which no stress means the simulation without residual stress, uniaxial, equibiaxial and general means:

$$\text{Uniaxial} = \begin{bmatrix} -400 & 0 & 0 \\ 0 & 0 & 0 \\ 0 & 0 & 0 \end{bmatrix}, \text{Equibiaxial} = \begin{bmatrix} -200 & 0 & 0 \\ 0 & 0 & 0 \\ 0 & 0 & -200 \end{bmatrix}, \text{General} = \begin{bmatrix} 200 & 0 & 0 \\ 0 & 0 & 0 \\ 0 & 0 & -600 \end{bmatrix}$$

As we use the cross-section to perform the indentation, the uniaxial state represents the actual condition of our experiment. The equivalent equibiaxial state is derived from the uniaxial state, as depicted in Fig.2-4, while the general state refers to an arbitrary state with the same hydrostatic stress as the uniaxial and equibiaxial states.

The curve of the general state differs significantly from that of the uniaxial and equibiaxial states. The curves of the uniaxial, equibiaxial, and general states are not identical, indicating that the conclusion from the literature is not entirely applicable for spherical indenter. However, the difference between the curves of the uniaxial and equibiaxial states is not substantial, although they are not identical. The differences in indentation responses are 0.4% for P_{max} and 0.01% for stiffness, which are considered insignificant. Therefore, if an equibiaxial residual stress state and a cumulative plastic strain can be used, a 2D axisymmetric finite element model can still be consistent enough for the simulations.

Please note that the loading direction for the nanoindentation test is along y direction, as shown in Fig.2-1. During the cutting process, a release of backstress may occur. However, it is believed that the backstresses primarily arise from the interactions between the dislocations and the precipitates. As a result, the relaxation of backstress throughout the thickness should be on the same scale as the spacing of the precipitates or the mean free path of the dislocations [92]. Compared to the nanoindentation penetration depth in our work, the relaxation can thus be considered as negligible, which means that it is possible to perform the nanoindentation tests on cross section to characterize the backstresses, whether in simulation or in practice. On the other hand, the relaxation of residual stress could be a factor that affects the indentation responses. More details about the relaxation during the cutting process will be discussed in the following section.

2.2. Analysis of shot peening backstress effect on nanoindentation

Previous literature has demonstrated the effect of isotropic hardening and residual stress on indentation responses [74]. However, it is unclear how backstress affects the response of nanoindentation. The backstress state is defined by a second order tensor. A general study of all the possibilities of variations is beyond the scope of the present work. Our aim is to focus on shot peening as a way to introduce compressive residual stresses and work hardening in a component. However, the profile of the backstress after shot peening is also unknown. In order to understand how the components of the backstress tensor are related and how they evolve with depth, simulations of the shot-peening process have been performed. This section describes the finite element model set up to obtain the backstress profile after shot peening.

The backstress induced by shot peening is then introduced into the nanoindentation model to study its effect on the corresponding responses. It should be clarified that only the effect of kinematic hardening is investigated in this section, so, only the backstress is introduced into the indentation model, without any cumulative plastic strain or residual stress, as we assume that their effects on indentation responses are already known.

2.2.1. Shot peening simulation

A 3D finite element model is built to simulate the shot peening process. The commercial finite element software ABAQUS (Version 2020) is used, with the **Dynamic/Explicit* analysis method. The constitutive behavior of the material used in the simulation, Inconel 718, is based on the combined hardening theory described in Section 2.1. A *VUMAT* subroutine is then considered in order to obtain the profile of each backstress component (The preset construction in ABAQUS cannot provide this information in *Explicit analysis). The constitutive behavior parameters of the material are shown in Tab.2-2 [93]. The yield stress σ_y is equal to 850MPa. Three backstress components are taken in order to describe accurately the cyclic evolution of the material.

Tab.2-2: Constitutive parameters of Inconel 718

E = 200000 MPa, ν = 0.3
Q= -215 MPa, b = 3
C_1 = 470000 MPa, γ_1 = 1000, C_2 = 9000 MPa, γ_2 = 100, C_3 = 2400 MPa, γ_3 = 10

The dimension of the impacted area is 3 mm × 3 mm. In order to ensure that the simulation results are not sensitive to the applied boundary conditions far away from the impacted area, and to control the computing time, the dimension of the target model is set to 15 mm×15 mm×10.2 mm, as shown in Fig.2-6. The shots are considered as rigid bodies. The component, modelled as an elastic-plastic body, is meshed using two types of elements: CIN3D8 (*infinite element*), used in the outer layer, to prevent the elastic wave reflections from the boundary; C3D8R, used in the rest of the component. On the surface, the element size was set to be about 0.002 mm in the impact area.

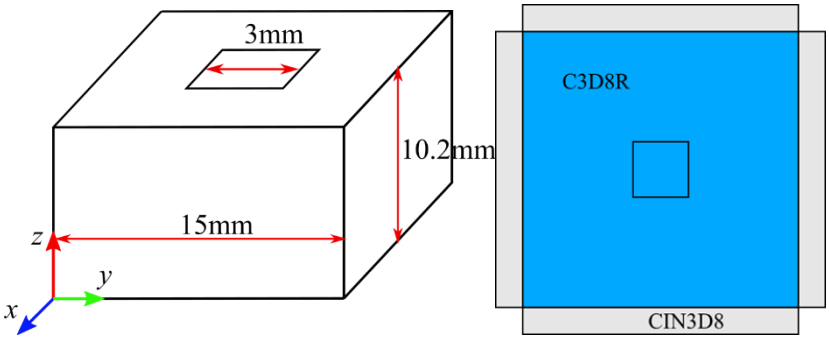

Fig.2-6 The target model

The impact radius r_s can be estimated by the equation [94]:

$$r_s = D_s \left(\frac{K\pi\rho_s V^2}{4\sqrt{2}E^*} \right)^{\frac{1}{5}} \qquad (2-10)$$

The distance between the centers of adjacent impacts e was given as [94]:

$$e = 10\, r_s \sqrt{\frac{2\pi}{\sqrt{3}N}} \qquad (2-11)$$

Where D_s is the shot diameter, which is equal to 2 mm in our work (corresponding to ultrasonic shot peening as used in our laboratory); K is the impact efficiency ratio, which is defined as the ratio between the elasto-plastic energy and the total kinetic energy. It can be taken as 0.8 [94][95]; ρ_s is the shot density which is equal to 7800 kg/m^3, V is the shot velocity; and E^* is the reduced Young's modulus of the target and the shot. As the shot is assumed as a rigid body, E^* can be calculated using the following equation:

$$\frac{1}{E^*} = \frac{1-\nu^2}{E} \qquad (2-12)$$

Where E and ν are the material parameters shown in Tab.2-2.

The coverage rate N can then be increased by lowering the distance e. Once the chosen coverage rate and shot speed have been selected, the number and distribution of shots are

determined, as shown in Fig.2-7. The movement of the shots from the initial position under different shot peening conditions can be executed by a Python script, and the impact order is set to be random.

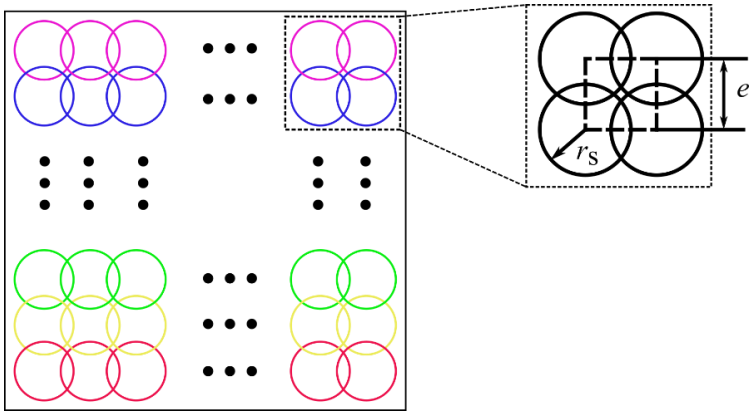

Fig.2-7 Impact distribution, order of arrival is random

In the affected layer, the mechanical fields are strongly heterogeneous due to the finite number of impacts [93][96]. However, the mechanical state is measured in practice at a certain depth on an area that is an average result of several impacts. For instance, the diameter of X-ray beam generally used is 1 mm or 2 mm. Considering the dimension of the impacted area (3 mm×3 mm), in this research, we use the average values for each layer to ensure consistency with reality.

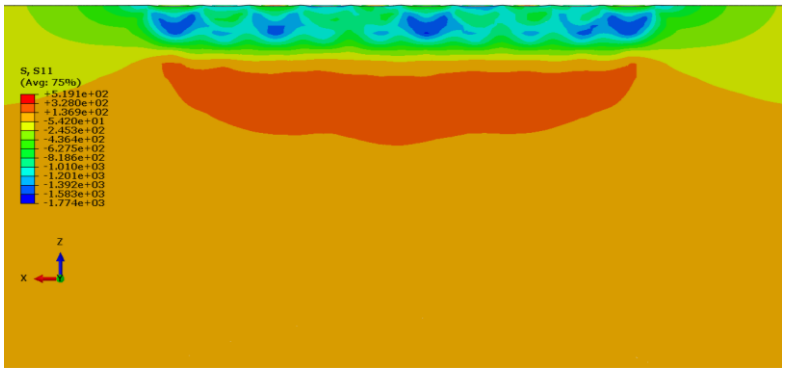

(a)

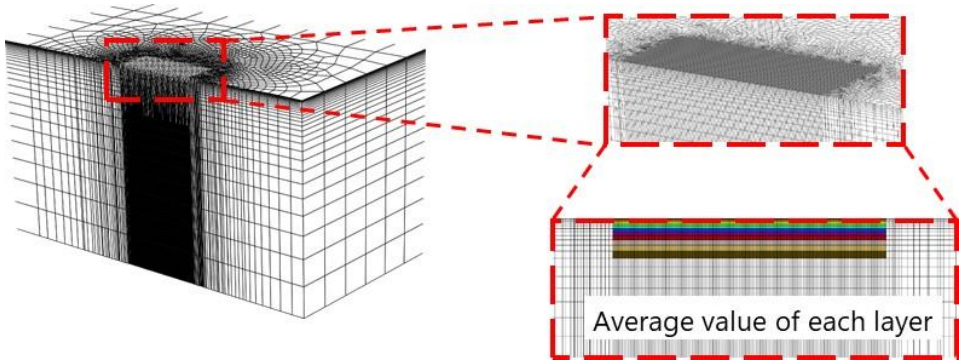

(b)

Fig.2-8 (a) The heterogeneous of stress field after shot peening at each layer (b) The strategy of average value

Residual stress, cumulative plastic strain, and backstresses have been averaged across all the integration points within a layer at a specified depth, as illustrated in Fig.2-8.

The shot diameter is equal to 2 mm. Besides, it could be noted that we aim to obtain information about the distribution of the profile of backstress along depth, so the strain rate dependency of the constitutive behavior is not so important. If we wanted a quantitative comparison between simulations and experiments, this dependency could play a significant role.

2.2.2. The shot peening backstress distribution

A simulation with a shot speed of 10m/s and coverage rate of 100% is carried out. The shot peening backstress distribution along the distance to the surface is shown in Fig.2-9. A component is noted X_{i-jk}, where i is the index specifying the kinematic hardening number and jk are the indices of the tensor component.

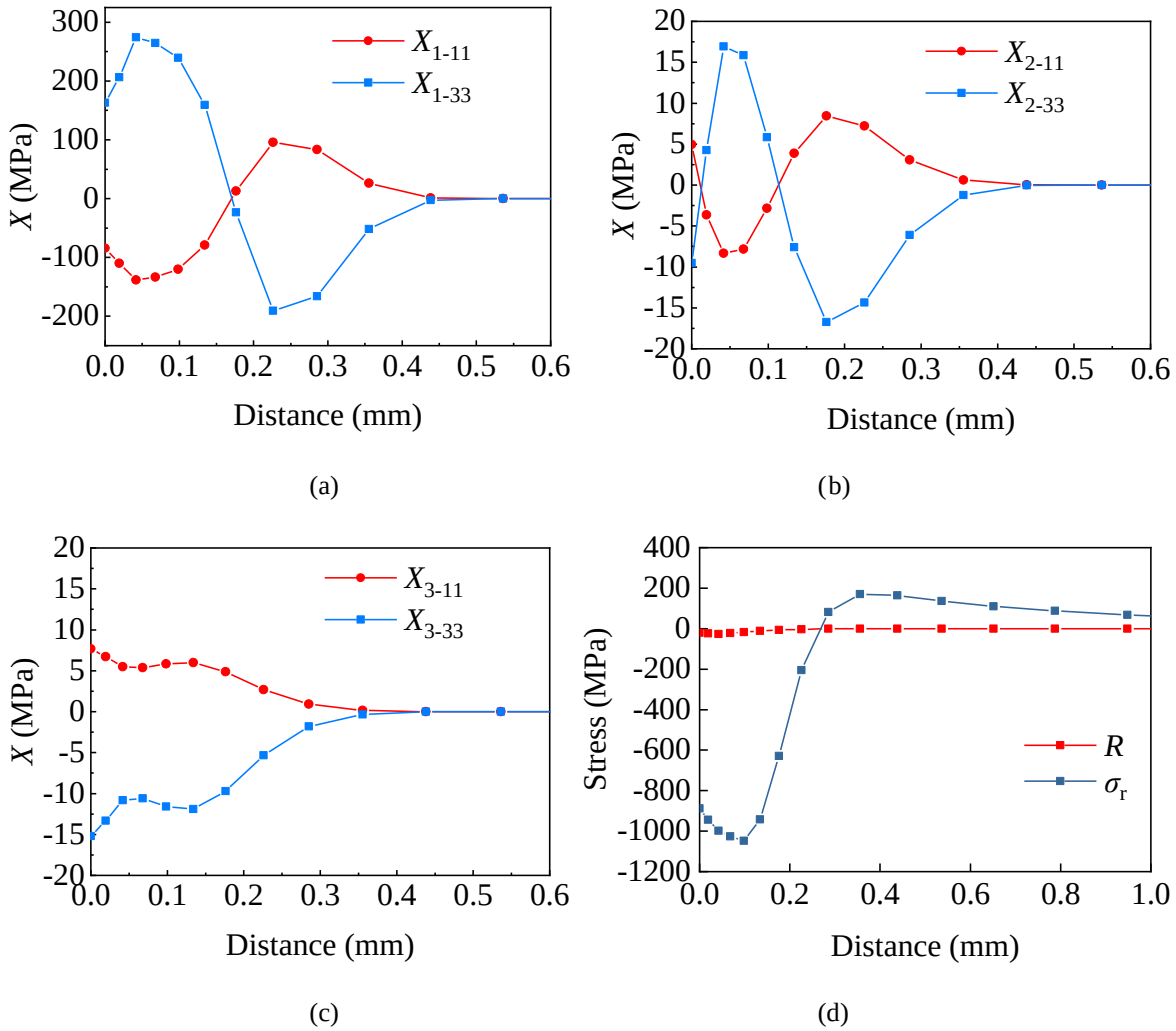

Fig.2-9 The distribution of (a) First backstress component (b) Second backstress component (c) Third backstress component (d) R and residual stress after shot peening.

The surface is located at zero. Only X_{i-11} and X_{i-33} are shown in the figure, X_{i-22} has the same profile as X_{i-11} and the values of other components are close to zero and neglected not shown in the figure.

The residual stress distribution shown in Fig.2-9(d) is similar to the distributions published previously [97][98]. It can be seen from Fig.2-9(a-c) that the backstress has a similar distribution as residual stress. The values of 12, 13 and 23 components of each backstress $\bar{\bar{X}}$ are close to zero. The 11 and 22 components of each backstress $\bar{\bar{X}}$, representing the components along the plane are indiscernible as expected due to the symmetry of the problem. Moreover, as the backstress tensor is deviatoric, $\bar{\bar{X}}$ can be described as:

$$\bar{\bar{X}}_k = \begin{bmatrix} X_{k-11} & 0 & 0 \\ 0 & X_{k-22} = X_{k-11} & 0 \\ 0 & 0 & -2X_{k-11} \end{bmatrix}$$

2.2.3. The equivalent backstress

The **Standard/Implicit* analysis method is used in nanoindentation simulation, with 3D finite element model and no subroutine is used (The preset construction in ABAQUS is able to provide this information in *Implicit analysis). The spherical tip, radius 10 μm, is used in this model and treated as a rigid body. One thing to note is that the kinematic hardening evolution rule is slightly different in ABAQUS scheme than the one described in Section 2.1. In ABAQUS, the backstress tensor is denoted as $\bar{\bar{\alpha}}$, and the evolution rule is [99]:

$$\dot{\bar{\bar{\alpha}}}_k = C_k \frac{1}{\sigma_y}(\bar{\bar{\sigma}} - \bar{\bar{\alpha}})\dot{\varepsilon}_p^{eq} - \gamma_k \bar{\bar{\alpha}}_k \dot{\varepsilon}_p^{eq} \qquad (2-13)$$

Which follows Ziegler's assumption. In this case, the backstress tensor $\bar{\bar{\alpha}}$ is generally not a deviatoric tensor. However, the evolution rule classically used, as shown in Eq.2-3, follows Prager's assumption. In this case, the backstress tensor is then a deviatoric tensor, as shown in Fig.2-9. Despite following distinct expressions ($\bar{\bar{\alpha}}$ or $\bar{\bar{X}}$) and evolution rules, both approaches lead to the same mechanical field. The relationship between them can be summarized as follows:

$$\bar{\bar{\alpha}}' = \bar{\bar{X}} = \bar{\bar{X}}'$$

To investigate indentation with initial backstresses in ABAQUS, a non-deviatoric backstress tensor $\bar{\bar{\alpha}}$ should be introduced in the nanoindentation model. According to the Eq.2-2, it is assumed that only $\bar{\bar{X}}'$, i.e. $\bar{\bar{\alpha}}'$, can affect the indentation responses in this work. To verify this assumption, two simulations with different backstress states are carried out, with the same indentation depth of 2000 nm. The different backstress states case 1 and case 2 are shown below.

Case 1:

$$\bar{\bar{\alpha}}_1 = \begin{bmatrix} -400 & 0 & 0 \\ 0 & -400 & 0 \\ 0 & 0 & 50 \end{bmatrix} \bar{\bar{\alpha}}_2 = \begin{bmatrix} -40 & 0 & 0 \\ 0 & -40 & 0 \\ 0 & 0 & 50 \end{bmatrix} \bar{\bar{\alpha}}_3 = \begin{bmatrix} -120 & 0 & 0 \\ 0 & -120 & 0 \\ 0 & 0 & 120 \end{bmatrix}$$

Case 2:

$$\bar{\bar{\alpha}}_1 = \begin{bmatrix} 0 & 0 & 0 \\ 0 & 0 & 0 \\ 0 & 0 & 450 \end{bmatrix} \bar{\bar{\alpha}}_2 = \begin{bmatrix} 0 & 0 & 0 \\ 0 & 0 & 0 \\ 0 & 0 & 90 \end{bmatrix} \bar{\bar{\alpha}}_3 = \begin{bmatrix} 0 & 0 & 0 \\ 0 & 0 & 0 \\ 0 & 0 & 240 \end{bmatrix}$$

It can be seen that case 1 and case 2 have different tensor shapes and trace values. However, the deviatoric tensors of each kinematic component are the same:

$$\bar{\bar{\alpha}}_1' = \begin{bmatrix} -150 & 0 & 0 \\ 0 & -150 & 0 \\ 0 & 0 & 300 \end{bmatrix} \quad \bar{\bar{\alpha}}_2' = \begin{bmatrix} -30 & 0 & 0 \\ 0 & -30 & 0 \\ 0 & 0 & 60 \end{bmatrix} \quad \bar{\bar{\alpha}}_3' = \begin{bmatrix} -80 & 0 & 0 \\ 0 & -80 & 0 \\ 0 & 0 & 160 \end{bmatrix}$$

The *P*-*h* curves of these two cases are shown in Fig.2-10. Moreover, the nanoindentation response: P_{max} and contact stiffness (S) of each case are shown in Tab.2-3.

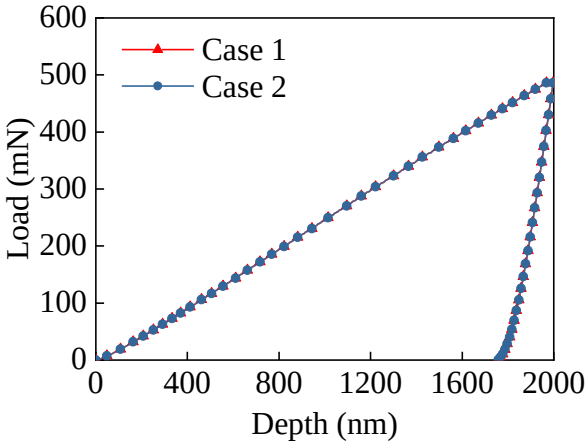

Fig.2-10 *P*-*h* curves with different backstress full tensor

It is obvious that both the *P*-*h* curves of the nanoindentation responses of case 1 and case 2 are perfectly superimposed. This means that, in nanoindentation simulations, if the deviatoric part of a backstress tensor is kept constant, the indentation responses will be the same regardless the values of its components. This property is very useful for a general study of the effect of backstresses on indentation test.

Tab.2-3: P_{max} and contact stiffness (S) of each case

N°	P_{max} (mN)	S (mN/nm)
Case1	493.4	3.09
Case2	493.4	3.09

Based on this observation, if we keep the deviatoric part shown in Section 2.2.2, the backstress tensor can be equivalent to a uniaxial state:

$$\bar{\bar{X}}_k = \begin{bmatrix} X_{k-11} & 0 & 0 \\ 0 & X_{k-11} & 0 \\ 0 & 0 & -2X_{k-11} \end{bmatrix} \rightarrow \bar{\bar{\alpha}}_k^{eq} = \begin{bmatrix} 0 & 0 & 0 \\ 0 & 0 & 0 \\ 0 & 0 & -3X_{k-11} \end{bmatrix} = \begin{bmatrix} 0 & 0 & 0 \\ 0 & 0 & 0 \\ 0 & 0 & \alpha_k^{eq} \end{bmatrix}$$

2.2.4. The effect of shot peening backstress

2.2.4.1. Applying shot peening backstress to nanoindentation simulation

According to Eq.2-8, the saturation value of each backstress component can be known as:

$$\alpha_1^{\text{uni}} = \frac{C_1}{\gamma_1} = \frac{470000}{1000} = 470 \text{ MPa}$$

$$\alpha_2^{\text{uni}} = \frac{C_2}{\gamma_2} = \frac{9000}{100} = 90 \text{ MPa}$$

$$\alpha_3^{\text{uni}} = \frac{C_3}{\gamma_3} = \frac{2400}{10} = 240 \text{ MPa}$$

Firstly, the effect of backstresses on the nanoindentation response is investigated from a purely numerical point of view. A series of nanoindentation simulations is carried out with each equivalent backstress component as the initial state. The values of the introduced equivalent backstress component are from -470 MPa to 470 MPa, from -90 MPa to 90 MPa and from -240 MPa to 240 MPa, respectively. The tip radius is kept equal to 10μm and the indent depth is 2000 nm. The normalized $P_{\max}$ and S under different equivalent backstress levels are shown in Fig.2-11 (comparison of effects with residual stress and cumulative plastic strain is shown in Fig.2-17.). $P_{0\max}$ and S_0 are the responses of the reference material without backstress. In the next chapters, in practice, these responses will be taken as the bulk value, far from the peened surface.

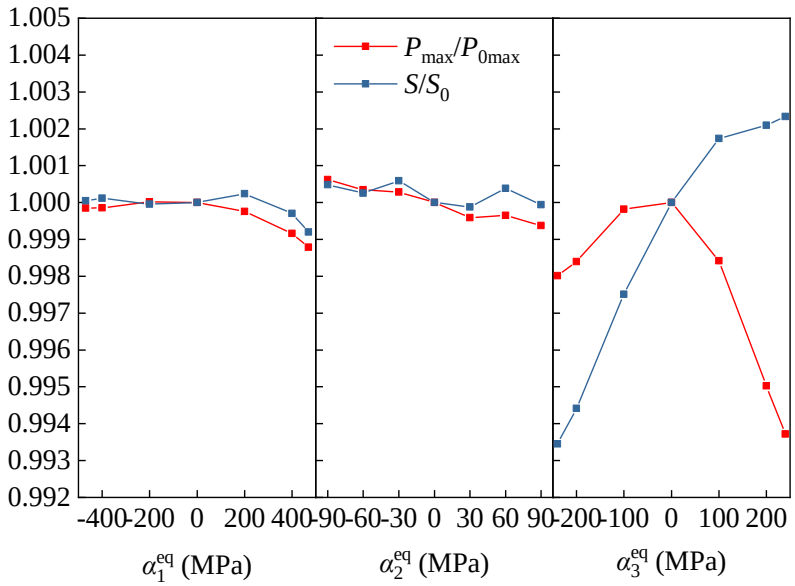

Fig.2-11 Nano indentation response under each equivalent backstress component

From Fig.2-11, it can be observed that neither α_1^{eq} nor α_2^{eq} has a significant effect on the indentation responses. The normalized $P_{\max}$ will decrease in either the negative or positive range as α_3^{eq} changes from 0 MPa to ±240 MPa. The normalized S will increase as the α_3^{eq} changes from -240 MPa to 240 MPa.

The maximum difference in normalized $P_{\max}$ is about 0.6% when α_3^{eq} is equals to 240 MPa; the maximum difference in S is about 0.65% when α_3^{eq} is -240 MPa. However, the effect of α_1^{eq} and α_2^{eq} on the responses is less than 0.1%.

To interpret our result, we can use the concept of indentation representative strain. Tabor [78] proposed the concept of indentation representative strain ε_r, that can be associated with the strain in a uniaxial true stress-true strain curve. For a spherical indenter, the representative strain can be described as:

$$\varepsilon_r = 0.2\frac{a}{R_i} \qquad (2-14)$$

Where a is the contact radius and R_i is the radius of indenter. It should be noted that other definitions of the representative strain are proposed in the literature [100][101]. By employing the representative strain concept considering nanoindentation as a uniaxial stress state, Fig.2-12 shows the evolution of the backstress during the indentation process as calculated by Eq.2-8. This evolution is represented by adding the representative strain to the initial value equivalent backstress, taken equal to 470 MPa, 240 MPa and 90 MPa respectively.

The blue dot at the top left corner indicates that α_1^{eq} has reached saturation, for an initial state of $\alpha_1^{eq} = 470$ MPa. The blue line can represent the final backstress state under this initial state, as the backstress is expected to evolve due to the representative strain ε_r introduced by nanoindentation. Similarly, the purple line represents the final backstress state with an initial state of $\alpha_2^{eq} = 90$ MPa and the orange line represents the final backstress state with an initial state of $\alpha_3^{eq} = 240$ MPa.

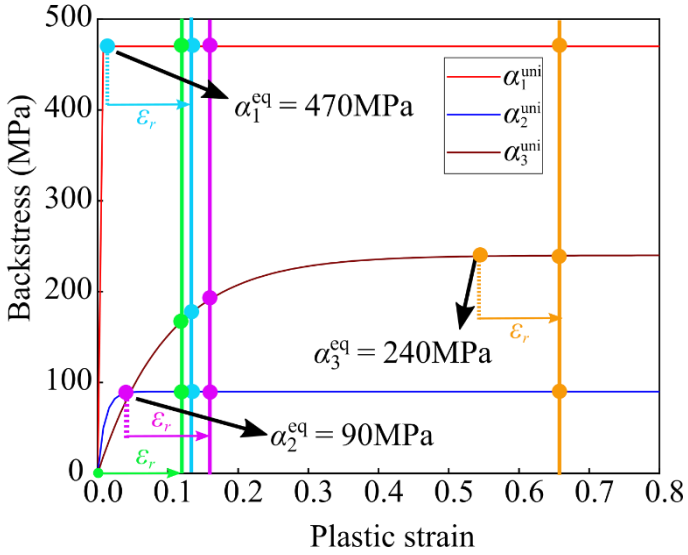

Fig.2-12 The uniaxial backstress stress evolution under different initial conditions

Additionally, the green line represents the final backstress state with no initial backstress. It is clear that $\alpha_1^{eq}$and α_2^{eq} will quickly reach saturation due to the high value of γ. As a result, after nanoindentation, there is no significant difference in the final backstress state with (the green line) or without (the blue and purple line) the initial states of α_1^{eq} or α_2^{eq}. The different final backstress states will cause different indentation responses, providing an explanation that the backstress component marked by the slow evolution rate, such as α_3^{eq} in our work, will have the most significant effect on the responses.

In practice, the backstress evolution in nanoindentation is not entirely uniaxial. However, its evolution trends can still be used as a reference. In summary, compared to α_1^{eq} and α_2^{eq}, the α_3^{eq} backstress has the most significant effect on the indentation responses, thus playing an important role. The results shown above regarding the saturation of the backstress component are observed from a purely numerical point of view. However, it could be interesting to investigate whether the backstress can reach saturation under different shot peening conditions.

2.2.4.2. The backstress evolution under different shot peening parameters

To study this issue, a series of simulations is then carried out under different shot speeds (10 m/s, 30 m/s, 50 m/s, 70 m/s) and coverage rate levels (100%, 300%, 500%).

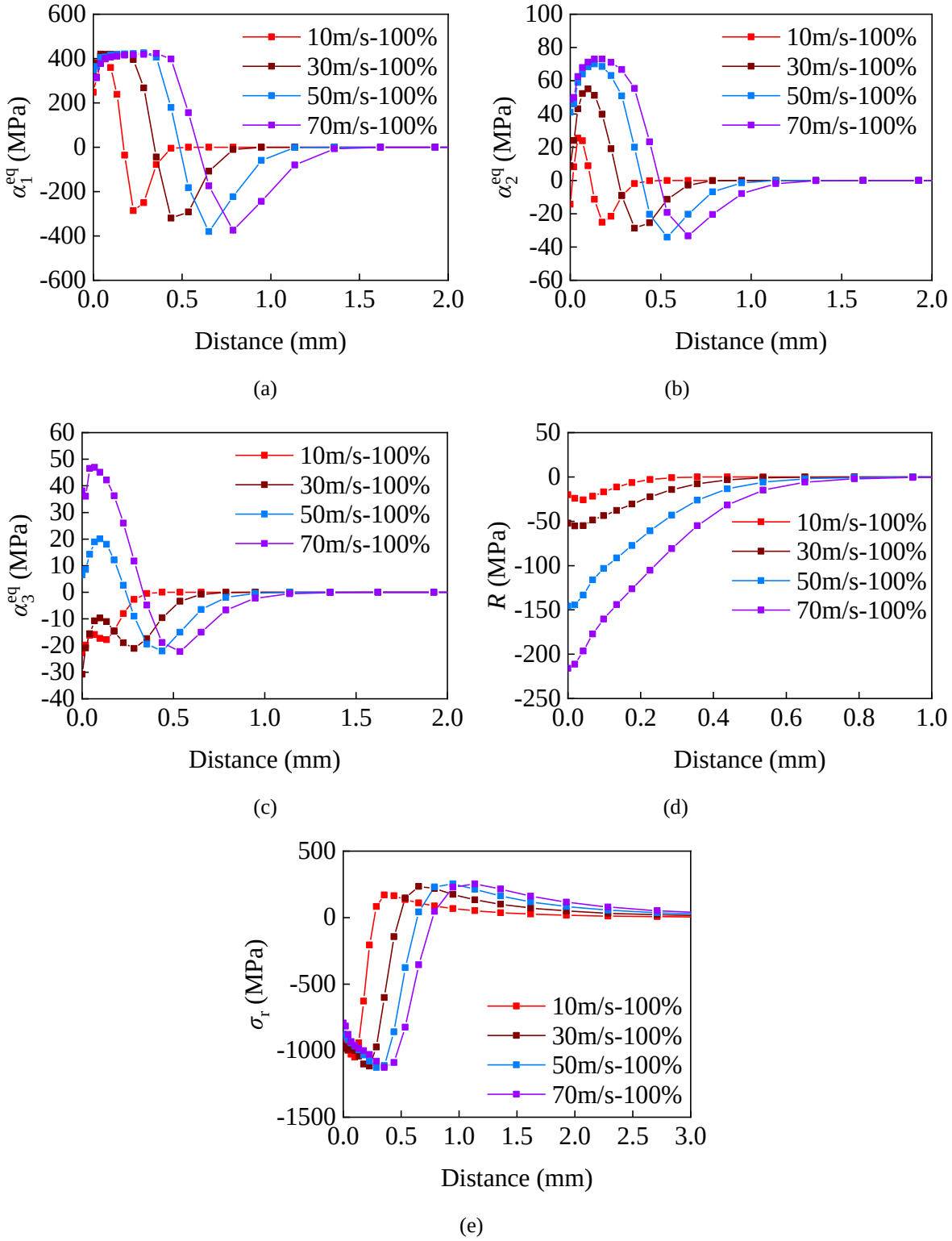

Fig.2-13 The distribution of (a) First equivalent backstress component (b) Second equivalent backstress component (c) Third equivalent backstress component (d) *R* (e) Residual stress under different shot speeds with the coverage rate 100%

Fig.2-13(a), (b) and (c) show that the affected depth, which is the position of the maximum negative α value, increases slightly with shot speed. It can be observed that the value of α_1^{eq} close to the shot peened surface remains relatively constent across different shot speeds. However, the absolute value of α_1^{eq} away from the surface increases slightly with speed. The value of α_2^{eq} presents a similar trend as α_1^{eq}.The value of α_3^{eq} exhibits a slightly different trend, remaining negative near the surface when the speed is 10 m/s and 30 m/s. In addition, Fig.2-13(d) and (e) show the isotropic hardening R and residual stress distributions, which show a similar trend. It could be seen that both the affected depth and the corresponding absolute value increases with increasing speed.

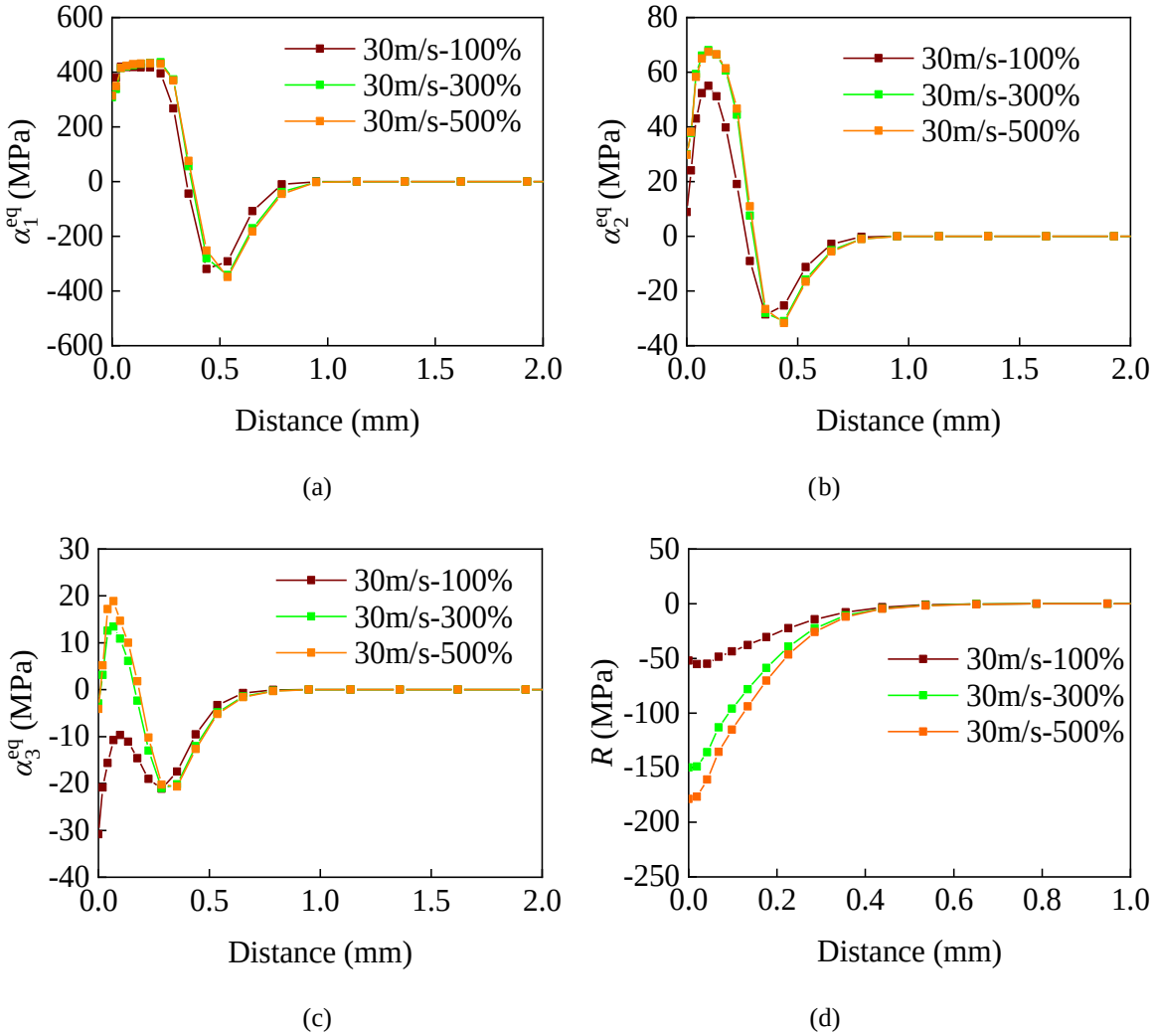

Fig.2-14 The distribution of (a) First equivalent backstress component (b) Second equivalent backstress component (c) Third equivalent backstress component (d) R under different coverage rate with the speed 30m/s

(Continued on the next page)

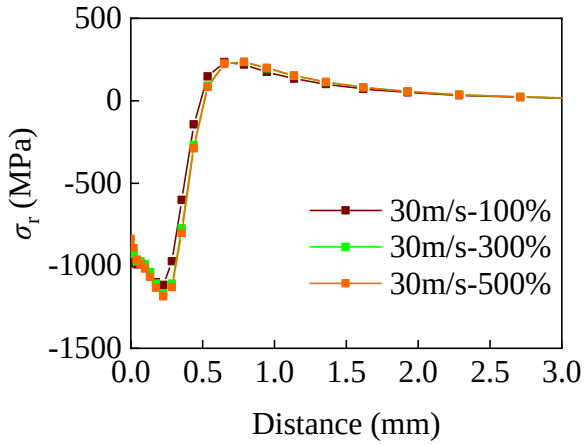

(e)

Fig.2-14 The distribution of (e) Residual stress under different coverage rate with the speed 30m/s (Continued)

Fig.2-14(a), (b) and (c) show that the values of α_1^{eq} and α_2^{eq} do not vary significantly with increasing coverage rate. Similarly, the value of α_3^{eq} has a different trend when the coverage rate is 100%. In this case, the values remain negative close to the surface.

Similarly, Fig.2-14(d) and (e) show the distributions of *R* and the residual stresses. There is no doubt that the absolute value of *R* increases because the increasing coverage rate leads to higher cumulative plastic strain. The residual stress shows a similar trend as the backstress. It is not significantly affected by the coverage rate when shot speed is 30 m/s, which is consistent with previous literature [102].

Some of the phenomena could be explained by the shot peening backstress change rate. Unlike the uniaxial state, for shot peening, the plastic strain tensor $\dot{\bar{\bar{\varepsilon}}}_p^{\,\mathrm{sp}}$ needs to be written as:

$$\begin{bmatrix} \varepsilon_p^{\mathrm{sp}} & 0 & 0 \\ 0 & \varepsilon_p^{\mathrm{sp}} & 0 \\ 0 & 0 & -2\varepsilon_p^{\mathrm{sp}} \end{bmatrix}$$

Following Eq.2-3, the backstress evolution during shot peening could be written as:

$$\dot{\bar{\bar{\alpha}}}_k^{\mathrm{sp}} = \frac{2}{3} C_k \, \dot{\bar{\bar{\varepsilon}}}_p^{\,\mathrm{sp}} - \gamma_k \, \bar{\bar{\alpha}}_k \, \dot{\bar{\bar{\varepsilon}}}_p^{\,\mathrm{sp,eq}} \qquad (2-15)$$

Where the variables have the same meaning as Eq.2-3. The superscript "sp" denotes the equation for the shot peened state. Here, the equivalent shot peening plastic strain can be described as:

$$\dot{\varepsilon}_p^{\mathrm{sp,eq}} = \sqrt{\frac{2}{3} \dot{\bar{\bar{\varepsilon}}}_p^{\,\mathrm{sp}} : \dot{\bar{\bar{\varepsilon}}}_p^{\,\mathrm{sp}}} = 2\left|\dot{\varepsilon}_p^{\mathrm{sp}}\right| = \begin{cases} 2\dot{\varepsilon}_p^{\mathrm{sp}} \left(\dot{\varepsilon}_p^{\mathrm{sp}} > 0\right) \\ -2\dot{\varepsilon}_p^{\mathrm{sp}} \left(\dot{\varepsilon}_p^{\mathrm{sp}} < 0\right) \end{cases} \qquad (2-16)$$

When $\dot{\varepsilon}_p^{\mathrm{sp}} > 0$, if we take the *k*-11 component $\dot{\alpha}_{k-11}^{\mathrm{sp}}$ as an example, Eq.2-15 will be:

$$\dot{\alpha}_{k-11}^{\mathrm{sp}} = \frac{2}{3} C_k \, \dot{\varepsilon}_p^{\mathrm{sp}} - 2\gamma_k \, \alpha_{k-11} \dot{\varepsilon}_p^{\mathrm{sp}} \qquad (2-17)$$

Integrating the Eq.2-17, we get:

$$\alpha_{k-11}^{\mathrm{sp}} = \frac{C_k}{3\gamma_k}\left(1 - e^{-2\gamma_k \varepsilon_p^{\mathrm{sp}}}\right) \quad (\varepsilon_p^{\mathrm{sp}} > 0) \qquad (2-18)$$

Similarly, $\alpha_{k-22}^{\mathrm{sp}}$ will write as Eq.2-18. For $\alpha_{k-33}^{\mathrm{sp}}$, we will have:

$$\alpha_{k-33}^{\mathrm{sp}} = -\frac{2C_k}{3\gamma_k}\left(1 - e^{-2\gamma_k \varepsilon_p^{\mathrm{sp}}}\right) \quad (\varepsilon_p^{\mathrm{sp}} > 0) \qquad (2-19)$$

When $\dot{\varepsilon}_p^{\mathrm{sp}} < 0$, Eq.2-18 and 2-19 will become:

$$\alpha_{k-11}^{\mathrm{sp}} = \frac{C_k}{3\gamma_k}\left(e^{2\gamma_k \varepsilon_p^{\mathrm{sp}}} - 1\right) \quad (\varepsilon_p^{\mathrm{sp}} < 0) \qquad (2-20)$$

$$\alpha_{k-33}^{\mathrm{sp}} = -\frac{2C_k}{3\gamma_k}\left(e^{2\gamma_k \varepsilon_p^{\mathrm{sp}}} - 1\right) \quad (\varepsilon_p^{\mathrm{sp}} < 0) \qquad (2-21)$$

To make it clearer, the equivalent shot peening backstress evolution will be:

$$\alpha_k^{\mathrm{eq}} = -\frac{C_k}{\gamma_k}\left(1 - e^{-2\gamma_k \varepsilon_p^{\mathrm{sp}}}\right) \quad (\varepsilon_p^{\mathrm{sp}} > 0) \qquad (2-22)$$

$$\alpha_k^{\mathrm{eq}} = -\frac{C_k}{\gamma_k}\left(e^{2\gamma_k \varepsilon_p^{\mathrm{sp}}} - 1\right) \quad (\varepsilon_p^{\mathrm{sp}} < 0) \qquad (2-23)$$

In reality, the loading path during shot peening is quite complex. However, there is still valuable information that can be gained from these equations. Eq.2-22 and 2-23 describe the equivalent shot peening backstress evolution. It can be seen that each backstress has a different rate of evolution due to the different γ, however, the rate during shot peening (2γ) is higher than the uniaxial state (γ) shown in Eq.2-8. Thus, α_1^{eq} saturates rapidly, followed by α_2^{eq} which slows down slightly, and finally α_3^{eq} saturates the slowest. Taking one shot as an example (shot speed=30 m/s), Fig.2-15(a) shows the distribution of the resulting plastic strain ε_{p11}. The trend of ε_{p11} indicates that the deformation is not uniaxial even when there is only one shot, consistently with previous literature [75].

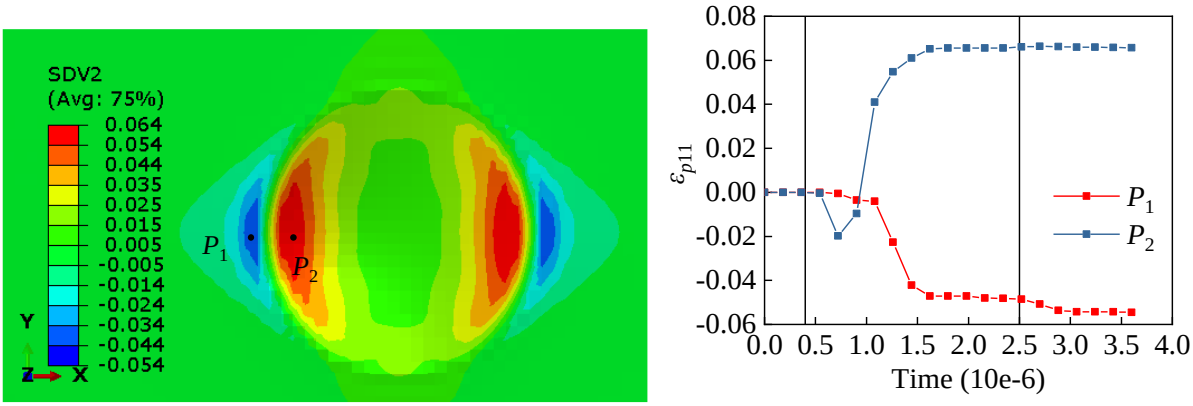

(a) (b)

Fig.2-15 The (a) Contour of plastic strain ε_{p11} (b) Evolution with time of ε_{p11} (c) Evolution of X_{1-11} (d) Evolution of X_{3-11} for two points P_1 and P_2 in a single shot simulation. The location of the two points is shown in (a).

(Continued on the next page)

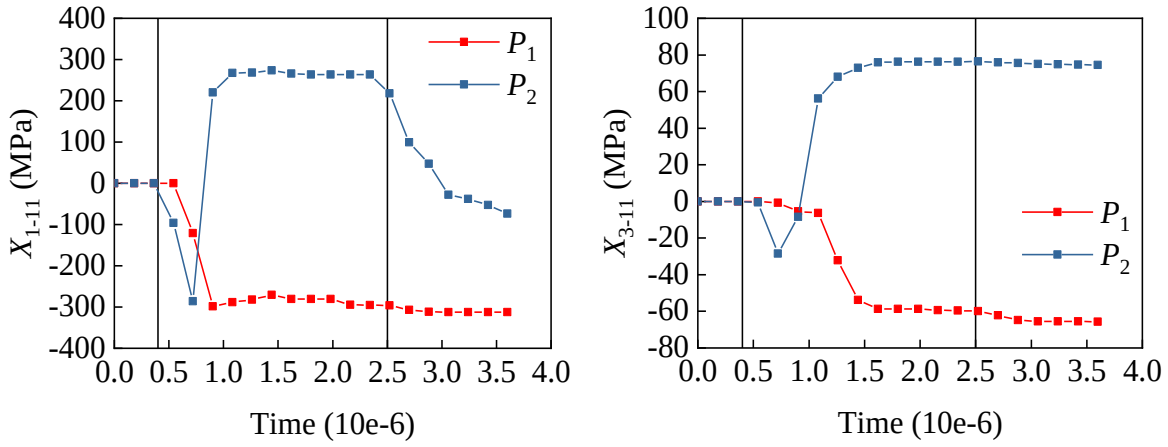

(c) (d)

Fig.2-15 The (c) Evolution of X_{1-11} (d) Evolution of X_{3-11} for two points P_1 and P_2 in a single shot simulation. The location of the two points is shown in (a).
(Continued)

Here two points named P_1 and P_2 are selected to analyze two different load paths during one shot. In Fig.2-15(b), (c) and (d), the left vertical line means the shot is getting into contact with the target surface, the right line means the shot is leaving the target. Along *x* direction, point P_1 always undergoes compression and P_2 undergoes compression first then tension. However, when the shot leaves the surface, it can be seen that point P_1 remains in a compressed state and continues to undergo compression, point P_2 remains in a tensile state but has been compressed slightly. Note that for X_{1-11} at point P_2, with the large 2γ, even the slight compression of ε_{p11} could reverse the sign of X_{1-11}, as shown in Fig.2-15(c). However, for X_{3-11}, the slight compression might be not sufficient, as shown in Fig.2-15(d).

With multiple shots, the load paths are coupled to each other between adjacent craters. As we mentioned in Section 2.2.1, the average value, which is a combination results of different positive and negative backstresses, is extracted from the simulations. At high speeds or coverage rates, the plastic region is larger, and the coupling between adjacent craters is stronger, making the order of arrival of the impacts significant. Conversely, at low speeds or coverage rates, the plastic region is smaller, resulting in less coupling between adjacent craters, thus the order of arrival of the shot has no influence. Consequently, the backstress distribution at a certain depth will be different. Taking X_{3-11} as an example, the distribution in the first layer is shown in Fig.2-16(a) and (b). It can be seen that the distribution of first layer in Fig.2-16(a) is almost periodic while in Fig.2-16(b) is more complex. Different distributions lead to distinct average values (marked in the figure). This could explain why there is a different distribution of $\bar{\bar{X}}_3$ when the speed and coverage rate are low.

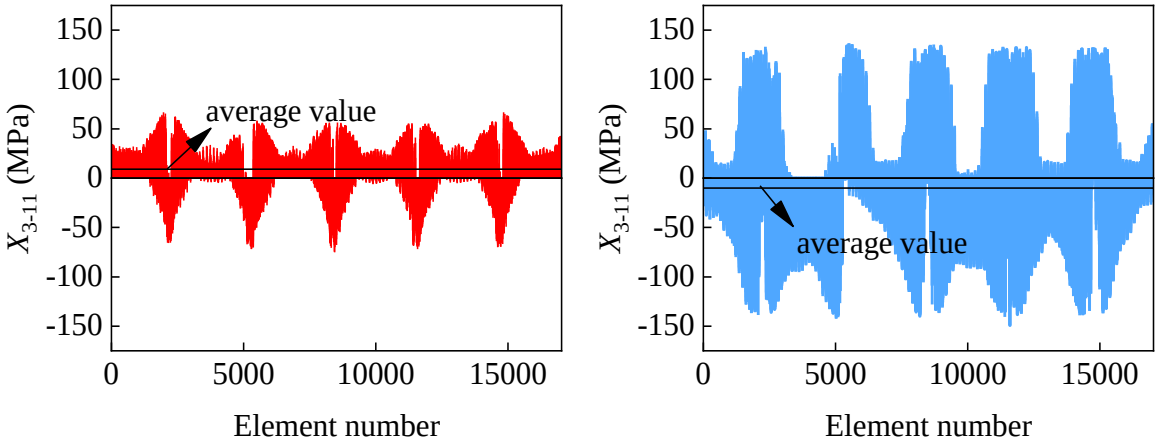

Fig.2-16 The $X_{3\text{-}11}$ distribution at the first layer under coverage = 100% and (a) shot speed = 30 m/s, (b) shot speed = 70 m/s

Therefore, considering the saturating value of each backstress component, it can be seen from Fig.2-13 and Fig.2-14 that α_1^{eq} and α_2^{eq} are easily saturated in shot peening. However, it is more complicated for α_3^{eq}. Even at a speed of 70 m/s, the value of α_3^{eq} is only around 50 MPa, which is far from saturation (The saturated α_3^{eq} equals to 240 MPa).

Fig.2-17 shows the normalized nanoindentation responses under different residual stress, cumulative plastic strain and α_3^{eq} levels. In which $P_{0\max}$ and S_0 mean the responses without any introduced field. The residual stress is up to yield stress, and the cumulative plastic strain is up to 60%, which is a reasonable value after shot peening.

It is observed that the maximum variations of normalized $P_{\max}$ with residual stress, cumulative plastic strain and α_3^{eq} are approximately 3% (at -850 MPa), 10% (at 60%) and 0.6% (at 240 MPa) respectively. The maximum difference of S for residual stress, cumulative plastic strain and α_3^{eq} is approximately 2% (at -850 MPa), 1.2% (at 60%) and 0.65% (at -240 MPa), respectively. Compared to the effect of residual stress or cumulative plastic strain, the effect of backstress is insignificant.

In addition, a line of α_3^{eq} equal to 50 MPa is shown in Fig.2-17, which represents the value that can be reached in shot peening. The difference of $P_{\max}$ and S are 0.1% and 0.05%, respectively, in this situation. Achieving such a value is nearly impossible, as the shot speeds used in practice [103] are lower than what we used in our simulations. In addition, the effect of backstress on $P_{\max}$ and S is in same order of even smaller than the difference in the model simplification shown in Section 2.1. Consequently, the effect will be much smaller and can therefore be neglected.

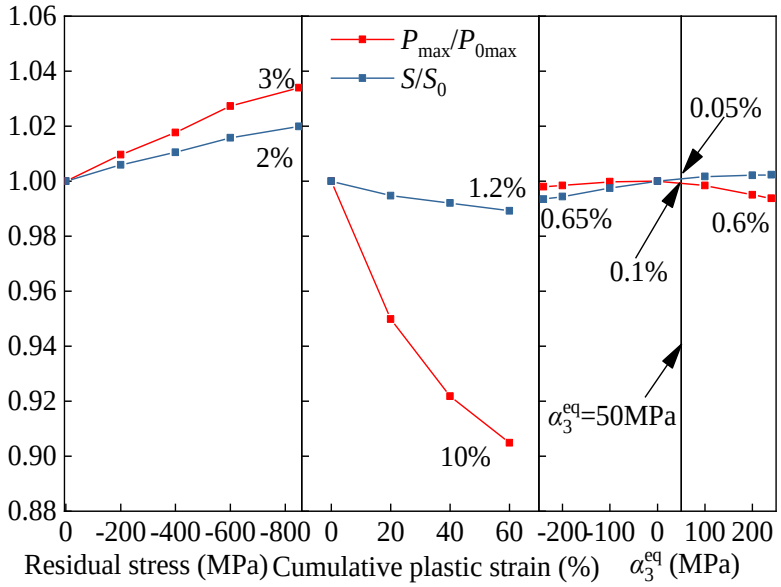

Fig.2-17 Nanoindentation responses under different residual stress, cumulative plastic strain and the third equivalent backstress levels (Please notice that here isotropic hardening parameters Q is negative)

Furthermore, as mentioned in Section 3.1, the simulations in this work do not consider the strain rate effect. However, the temperature or the strain rate will affect the mechanical properties of Inconel 718 [93][104], which could show different results in the investigations on the trend of equivalent backstress under different shot speeds and coverage rates. However, this effect manifests itself when the strain rate varies by several orders of magnitude [105]. In this study, the speed varies from 10 m/s to 70 m/s, without a significant change in order of magnitude. Considering our experiments where ultrasonic shot peening is used, the variation range in shot velocity is even smaller. Therefore, the effect of backstress on nanoindentation remains convincing. The constitutive behavior considering strain rate effect could be investigated in the future work.

According to the analysis presented in this section, it is not possible to use indentation to characterize backstress. However, it is still possible to separate residual stresses and cumulative plastic strain with indentation. The attempt of characterization is shown in next section.

2.3. Characterization of residual stress and cumulative plastic strain

2.3.1. The Response Surface Function method

Three normalized parameters P_{max}/P_{0max}, S/S_0 and H/H_0 can be extracted from indentation curves so that they can be used for the characterization of residual stresses and cumulative plastic strain. Where the subscript 0 indicates the response without any mechanical field introduced. As shown in Chapter1, the reduced modulus E^* is calculated from indentation as:

$$E^* = \frac{1}{\beta}\frac{\sqrt{\pi}}{2}\frac{S}{\sqrt{A_c}} \qquad (2-24)$$

If we assume that shot peening will not change the material elastic properties, then E^* remains constant and the variations of S will be directly related to the variations of A_c. Thus

$$E^* = \frac{1}{\beta}\frac{\sqrt{\pi}}{2}\frac{S_0}{\sqrt{A_{c0}}} \qquad (2-25)$$

Combining these Eq.2-24 and 2-25, it comes:

$$\frac{A_c}{A_{c0}} = \left(\frac{S}{S_0}\right)^2$$

Thus the normalized parameters H/H_0 could be expressed as:

$$\frac{H}{H_0} = \frac{P_{max}}{P_{0max}}\left(\frac{S_0}{S}\right)^2 \qquad (2-26)$$

Though residual stress and cumulative plastic strain can affect these three parameters, the way or the trend affected for them may not be the same, which give us the possibility to separate residual stress and cumulative plastic strain.

It should be noted that we considered Eq.2-26 as more reliable to compute the hardness than the usual equation $H = P_{max}/A_c$ because the projected contact area A_c is influenced by residual stress although the intrinsic hardness of the material is not changed. Furthermore, in equation Eq.2-26, the maximum load and the contact stiffness are extracted directly from the experimental data without assumption.

Simulations are conducted with varying levels of residual stress and cumulative plastic strain. Then, the normalized parameters P_{max}/P_{0max}, S/S_0 and H/H_0 versus these two parameters can be extracted from simulations.

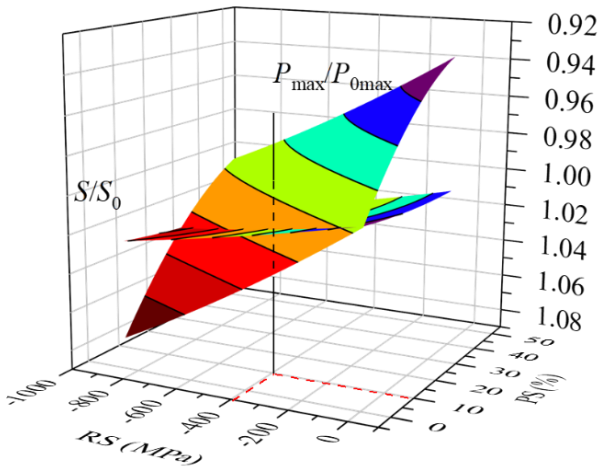

Fig.2-18 Characterization of residual stress and cumulative plastic strain using two response surface functions

Li et.al [106] firstly proposed the method to obtain the residual stress or cumulative plastic strain values through the normalized response contours, with a Berkovich indenter. By plotting the contours in a single figure, the intersection of the contour line represents the obtained values. However, this method requires each solution to be found by plotting the given

contour line, which is complicated. In our case, response surfaces obtained from a spherical indenter can be fitted using polynomials based on these normalized parameters in 3D space. Thus, the polynomials, i.e., functions of normalized parameters versus residual stress and cumulative plastic strain were established. Two unknown parameters (residual stress and cumulative plastic strain) can thus be solved from two of the three functions.

The characterization scheme is shown in Fig.2-18, taking two normalized parameters P_{max} and S as an example. The response surfaces are fitted in 3D space. If the entire procedure is self-consistent, all of the provided normalized parameters should correspond to a unique group of residual stresses and cumulative plastic strain within a certain range.

2.3.2. Application of the method with a pure simulation view

2.3.2.1 Application on Inconel 718

The 2D axisymmetric model was used in the simulations according to the analysis made in Section 2.1.3. A series of nanoindentation simulations on the material shown in Tab.2-2 were carried out, for which the indentation depth is 800 nm. The levels of cumulative plastic strain are 0%, 10%, 20%, 30% and 40% respectively. The levels of residual stress are 0 MPa, -200 MPa, -400 MPa, -600 MPa, -800 MPa and $-\sigma_{yc}$, where σ_{yc} is the yield stress for each imposed cumulative plastic strain level, calculated by Eq.2-9. The other simulation parameters, such as the friction coefficient and the contact options, are kept constant in these simulations in order to avoid their effect. The contour plots of the three normalized parameters are shown in Fig.2-19. In which, RS represents residual stress and PS represents the cumulative plastic strain.

It is reasonable to observe that P_{max} decreases as the cumulative plastic strain increases, due to the negative constitutive behavior parameters Q (-215 MPa) for this material. Additionally, P_{max} is equally influenced by residual stress and cumulative plastic strain. The stiffness increases as the cumulative plastic strain or compressive residual stress increases. Additionally, the stiffness is more easily affected by residual stress, mostly because of a change in contact area (as the Young's modulus is constant). Similar to P_{max}, hardness increases with an increase in compressive residual stress, but decreases with an increase in cumulative plastic strain. However, the hardness is more easily affected by cumulative plastic strain. Besides, P_{max} is the most sensitive parameter because it varies by ±7% between the material with and without the introduced mechanical field. Corresponding variations for the stiffness are about 3%. For hardness, it varies from around -8% to 3%.

It is obvious that the trends of three normalized parameters are quite different, which indicates the potential of our method.

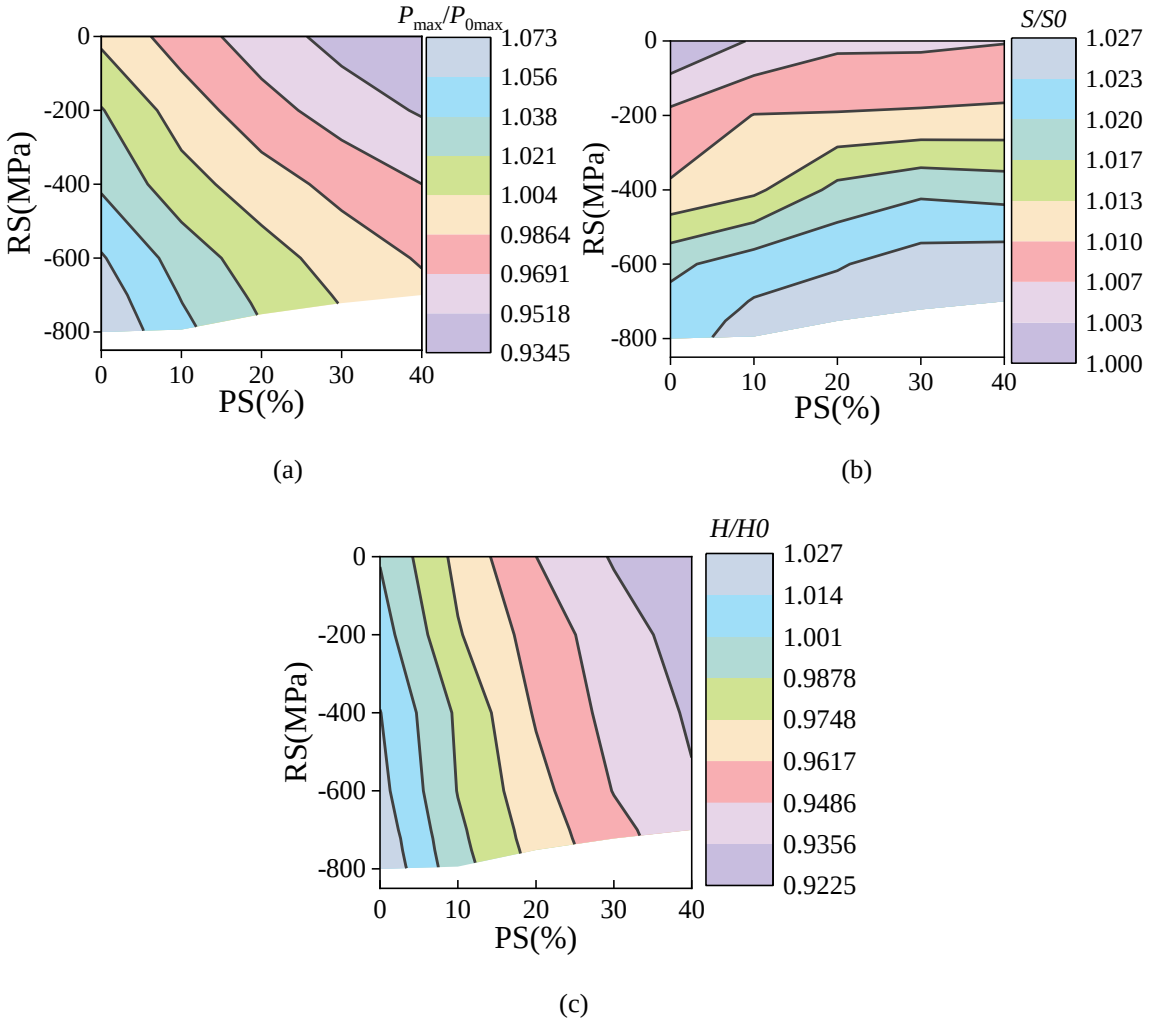

Fig.2-19 The Inconel 718 contour of (a)P_{max}/P_{0max} (b) S/S_0 (c) H/H_0

The response surface of P_{max}/P_{0max}, S/S_0 and H/H_0 are shown in Fig.2-20 respectively. The surface is fitted with a second order polynomial, and the surface functions are listed as follows:

$$\frac{P_{\max}}{P_{0\max}} = 1.00123 - 0.00263x + 0.0000243489x^2 - 0.0000994773y + 2.01648 \times 10^{-7}xy - 1.64448 \times 10^{-8}y^2$$

$$\frac{S}{S_0} = 1.00069 + 0.000285587x - 0.0000039335x^2 - 0.000031925y - 5.63865 \times 10^{-8}xy - 6.13881 \times 10^{-9}y^2$$

$$\frac{H}{H_0} = 0.99977 - 0.00315x + 0.0000316478x^2 - 0.0000353463y + 2.0564 \times 10^{-7}xy - 6.15935 \times 10^{-9}y^2$$

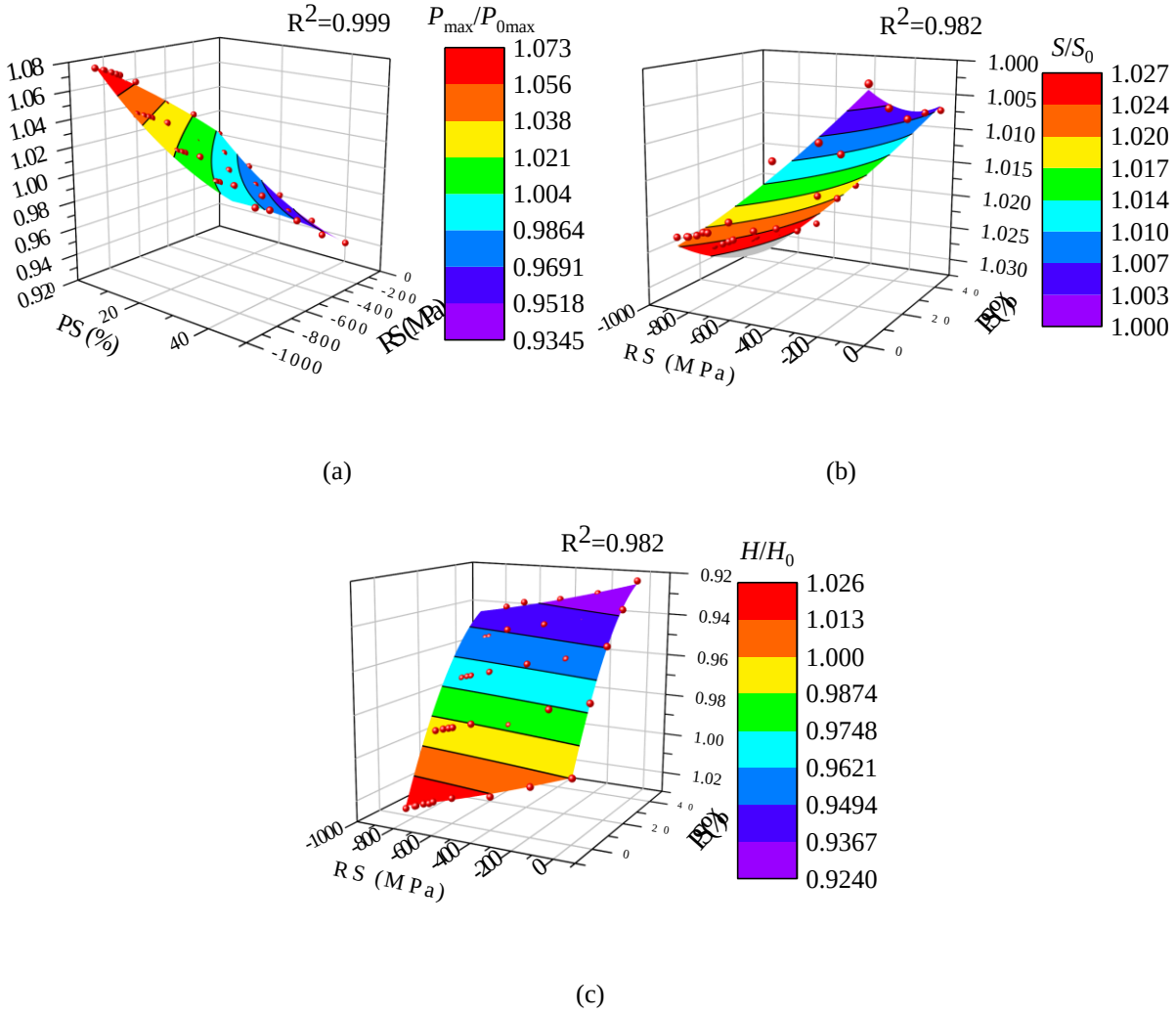

Fig.2-20 The Inconel 718 response surface of (a)P_{max}/P_{0max} (b) S/S_0 (c) H/H_0

Where x means the cumulative plastic strain and y means the residual stress. The residual stress and cumulative plastic strain can be obtained from two of these three equations. Another series of simulations with different residual stress and cumulative plastic strain levels were conducted to validate the method. Moreover, to verify the stability of the method, a random perturbation of the 3 input parameters was introduced. According to the experimental indentation tests (See in Chapter 4), the dispersion (Characterized by a standard deviation) of normalized P_{max}, S and H is around 1%, 0.5% and 1% respectively. The dispersion of indentation responses is due to the inhomogeneity of the material, the sensitivity of the machine, and some other random uncertainties (vibrations, thermal fluctuation, etc.). For the same kind of material, these dispersion levels can be trusted as typical dispersions and then introduced as a perturbation. Thus, for each response, 1000 values following a normal distribution with the prescribed standard deviation were used as input responses. The mean of this normal distribution is the normalized responses obtained from the simulations, and the standard deviation is the dispersion mentioned above.

Tab.2-4 displays the mean output values and relative errors for three combinations of the normalized parameters. The relative error of output mean value is calculated as

$|(\text{output} - \text{input})/\text{input}| \times 100\%$. The relative standard deviation of output mean is calculated as $(\text{standard deviation}/\text{output}) \times 100\%$.

Tab.2-4. Five comparisons of the input (in red) and output parameters using the three possible couples of input parameters (P_{max} and S, P_{max} and H, or S and H). Relative errors are also given under the output values.

Input: Normalized responses under PS=5% RS=-250 MPa,						
	P*max-*S		***P*max-*H***		***S*-*H***	
	Output mean	Standard deviation	Output mean	Standard deviation	Output mean	Standard deviation
PP (%)	7.2	4.9	6.9	4.5	5.5	3.0
Rel (%)	44	68	38	65	10	55
RS (MPa)	-274	118	-304	175	-269	144
Rel (%)	9.6	43	21.6	58	7.6	54
Input: Normalized responses under PS=5% RS=-500 MPa						
	P*max-*S		***P*max-*H***		***S*-*H***	
	Output mean	Standard deviation	Output mean	Standard deviation	Output mean	Standard deviation
PP (%)	7.5	4.8	6.3	3.7	6.2	3.4
Rel (%)	50	64	26	59	24	55
RS (MPa)	-568	127	-537	163	-547	154
Rel (%)	13.6	22	7.4	30	9.4	28
Input: Normalized responses under PS=15% RS=-250 MPa						
	P*max-*S		***P*max-*H***		***S*-*H***	
	Output mean	Standard deviation	Output mean	Standard deviation	Output mean	Standard deviation
PP (%)	16.0	7.1	16.6	5.9	15.4	4.6
Rel (%)	6.3	44	11	36	2.7	30
RS (MPa)	-235	118	-280	175	-254	142
Rel (%)	6.0	50	12	63	1.6	56
Input: Normalized responses under PS=15% RS=-500 MPa						
	P*max-*S		***P*max-*H***		***S*-*H***	
	Output mean	Standard deviation	Output mean	Standard deviation	Output mean	Standard deviation
PP (%)	16.0	6.9	15.6	5.7	16.6	4.6
Rel (%)	11	43	4.0	37	11	28
RS (MPa)	-538	136	-516	185	-534	153
Rel (%)	7.6	25	3.2	36	6.8	29
Input: Normalized responses under PS=35% RS=-250 MPa						
	P*max-*S		***P*max-*H***		***S*-*H***	
	Output mean	Standard deviation	Output mean	Standard deviation	Output mean	Standard deviation
PP (%)	27.8	6.4	30.0	5.3	29.6	5.3
Rel (%)	21	23	14	18	15	18
RS (MPa)	-157	90	-177	113	-200	124
Rel (%)	37	57	29	64	20	62

Input: Normalized responses under PS=35% RS=-500 MPa,						
	P_{max}-S		P_{max}-H		S-H	
	Output mean	Standard deviation	Output mean	Standard deviation	Output mean	Standard deviation
PP (%)	28.9	6.8	30.1	6.1	31.8	4.9
Rel (%)	17	24	14	20	9.1	15
RS (MPa)	-487	126	-437	168	-506	162
Rel (%)	2.6	26	13.4	38	1.2	32

It can be seen that the mean output values corresponds to the input values. For some residual stress and plastic strain values, the relative error is relatively high. For example, the error for the cumulative plastic strain obtained from the combination of normalized parameters P_{max}-S at 5% and -500 MPa is approximately 50%. However, the other two combinations can give a better result.

The standard deviation represents the dispersion of the output values due to the perturbation of the input normalized responses. It is evident there are some dispersions in the output values due to the perturbation. However, no more significant dispersions of the output values were observed for the combinations of P_{max}-H, while the dispersion for normalized P_{max} and H is higher than the normalized S. This indicates that the dispersion of the output values is not affected by the dispersion of the selected combination of input values. In addition, it is clear that dispersion is more significant for the input values near the domain boundary. Here the domain boundary means the boundary of the simulation parameters. For instance, the domain boundary of residual stress is 0 MPa or $-\sigma_y$ MPa while that of cumulative plastic strain is 0% or 40%.

Although the dispersions indicate that the proposed method is easily affected by disturbances, however, the mean output values show the accuracy of the proposed method. The validation with Inconel 718 in pure numerical view indicates that the proposed method can characterize the residual stress and cumulative plastic strain, based on the enough data from nanoindentation tests. It is possible that using all the three input values (P_{max}, H and S) instead of only two of them makes the method more accurate and gives lower dispersion. It is not obvious since they are not independent as shown by Eq.2-26. It can be investigated in further studies.

2.3.2.2 Application on a virtual material

The method was applied to another virtual material to analyze its application on materials with different constitutive behaviors. The virtual material constitutive behavior parameters are shown in Tab.2-5. These parameters are chosen based on the behavior of stainless steel.

Tab.2-5. Virtual material behavior parameters

E = 186000 MPa, ν= 0.3, σ_y = 850 MPa,
Q = 98.624 MPa, b = 12.06
C_1 = 196994 MPa, γ_1 = 1618.12, C_2=33299.1 MPa, γ_2 = 181.17

Similarly, a series of simulations of indentation depth of 600 nm are conducted in order to obtain the contours and functions. The contour plots of the three normalized parameters are shown in Fig.2-21.

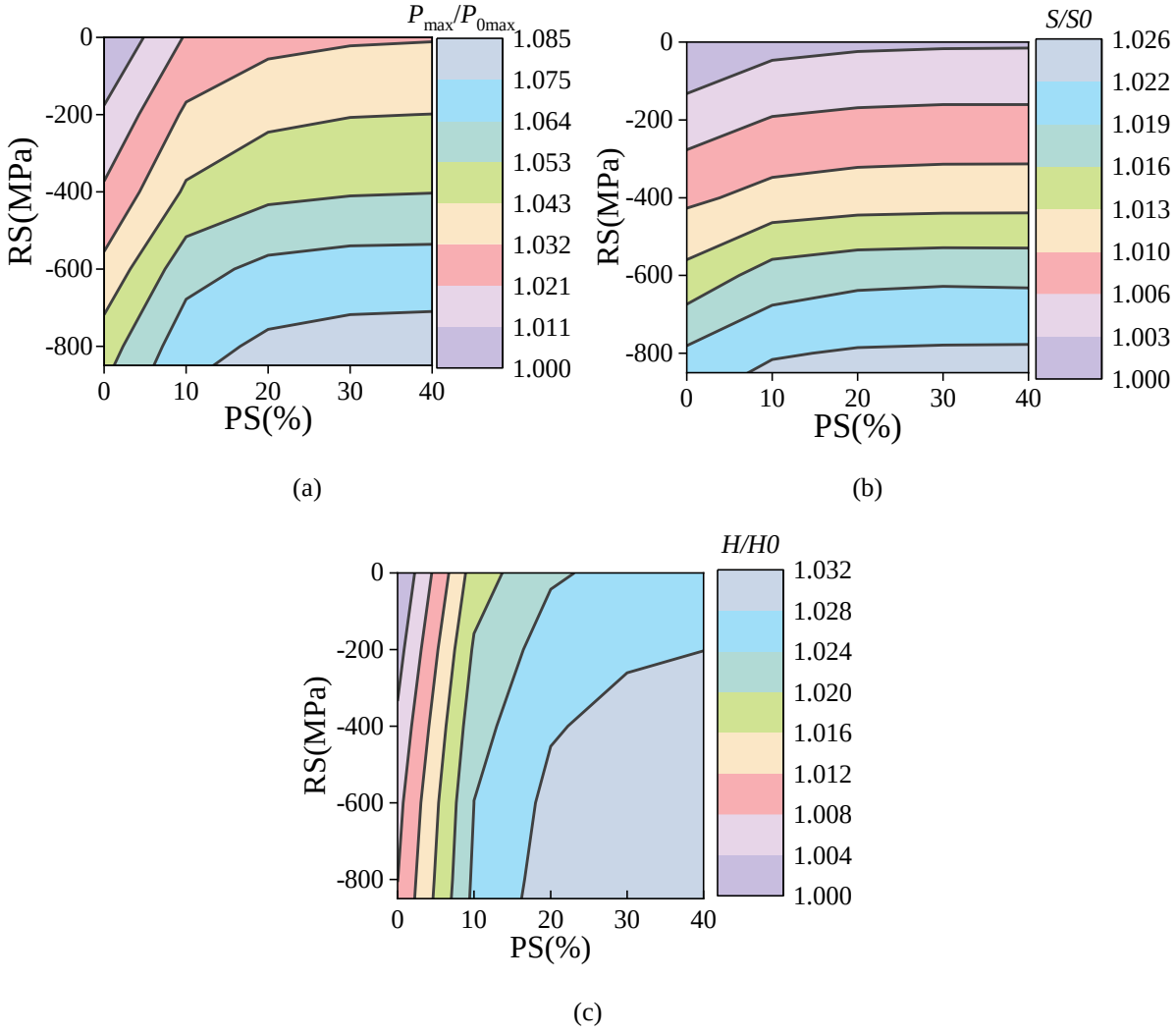

Fig.2-21 The virtual material contour of (a)P_{max}/P_{0max} (b) S/S_0 (c) H/H_0

Unlike with Inconel 718 in the previous section, in Fig.2-21 it could be seen that both P_{max}, S and H increase with the cumulative plastic strain, as the constitutive behavior parameters Q is positive. For this material, the normalized values of P_{max} and S exhibit a significant variation for cumulative plastic strain levels between 0% and 10%, followed by a slower variation. When the strain level is between 30% and 40%, P_{max} and S are almost unaffected by cumulative plastic strain but vary with residual stresses. Hardness is more easily affected by cumulative plastic strain when the strain level is between 0 and 10%. The hardness is almost saturated when strain level is more than 20%. Additionally, P_{max} is still the most sensitive parameter because it varies by around 8% when mechanical fields are introduced. Corresponding variations for the stiffness and hardness are about 3%.

The monotonic true stress-strain curve for Inconel 718 and virtual material are shown in Fig.2-22(a). The difference in elastic range is due to the difference in elastic modulus.

Although some softening comes from the isotropic component of hardening (Q=-215 MPa), Inconel 718 reaches a higher stress level due to the high values of backstress components.

The differences in the contour plots between these two materials can be explained by the isotropic hardening constitutive behavior parameter b, as shown in Fig.2-22(b). The yield stress of the simulated material (b=12.06) increases rapidly at the beginning and reaches saturation at a strain level of approximately 40%. The yield stress of Inconel (b=3) increases gradually as the cumulative plastic strain increases. Therefore, Fig.2-21 shows a saturation trend at high cumulative plastic strain level but no obvious saturation can be observed in Fig.2-19.

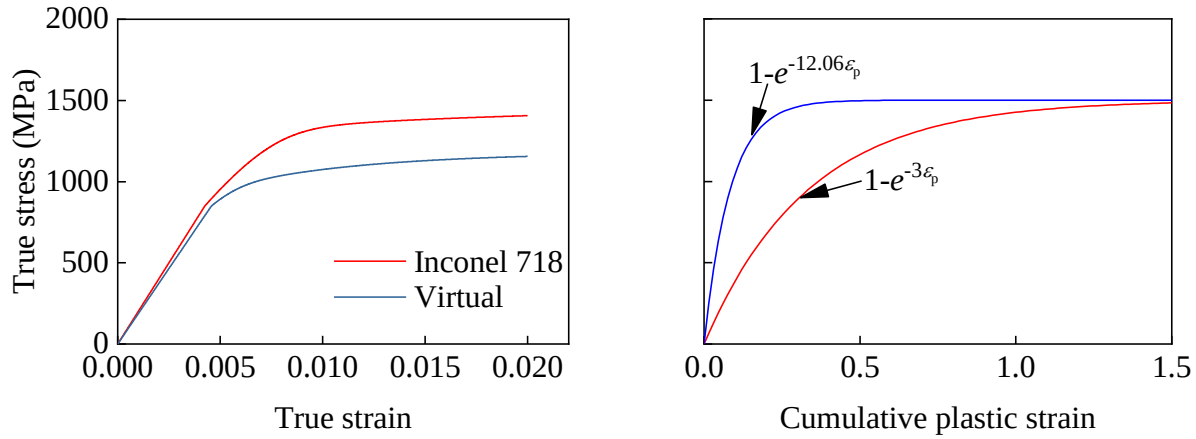

(a) (b)

Fig.2-22 Material behaviors of the virtual material and Inconel 718 (a) The monotonic true stress-strain curve (b) The rate at which the two materials reach the asymptote.

The response surface of P_{max}/P_{0max}, S/S_0 and H/H_0 are shown in Fig.2-23 respectively. A third order polynomial is taken to fit the surfaces.

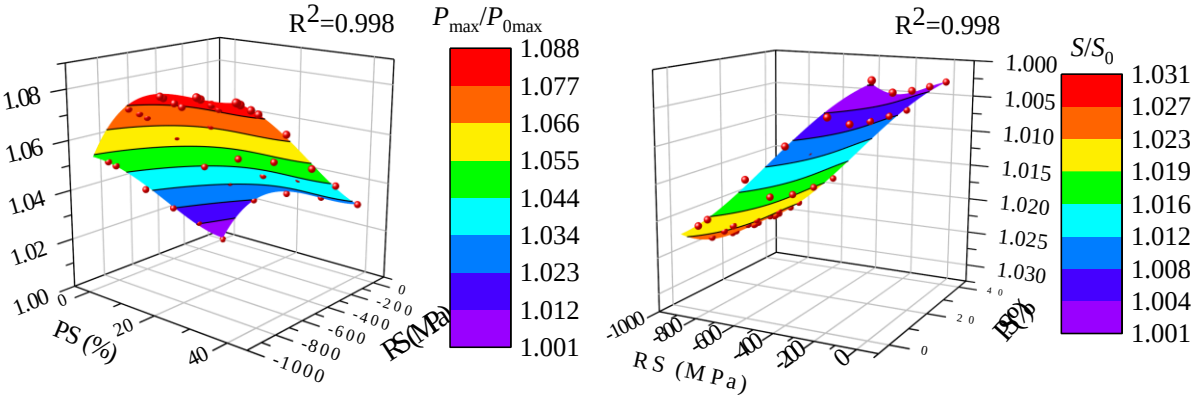

(a) (b)

Fig.2-23 The virtual material response surface of (a)P_{max}/P_{0max} (b) S/S_0

(Continued on the next page)

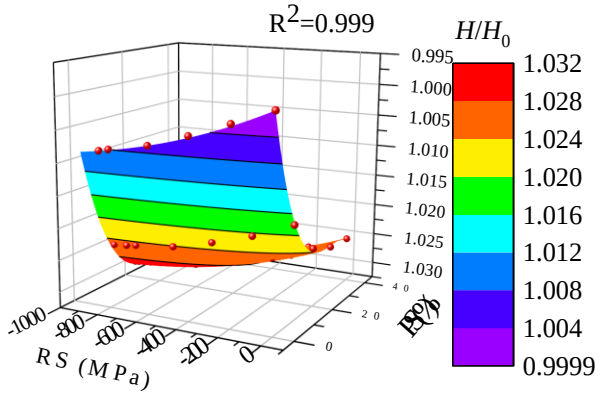

(c)

Fig.2-23 The virtual material response surface of (c) H/H_0 (Continued)

The surface functions for the virtual material are listed as follows:

$$\frac{P_{\max}}{P_{0\max}} = 1.00064 + 0.00309x - 0.000105332x^2 + 0.00000118449x^3 - 0.0000401694y - 1.02706 \times 10^{-7}xy + 2.02587 \times 10^{-10}x^2y + 5.85709 \times 10^{-8}y^2 - 9.48898 \times 10^{-11}xy^2 + 4.36277 \times 10^{-11}y^3$$

$$\frac{S}{S_0} = 1.00033 + 0.000290826x - 0.0000107526x^2 + 1.26744 \times 10^{-7}x^3 - 0.0000128856y - 8.70504 \times 10^{-8}xy + 7.14897 \times 10^{-10}x^2y + 3.093679999999999 \times 10^{-8}y^2 - 4.23077 \times 10^{-11}xy^2 + 2.11835 \times 10^{-11}y^3$$

$$\frac{H}{H_0} = 0.99999 + 0.00247x - 0.00008179x^2 + 8.9961 \times 10^{-7}x^3 - 0.0000151847y + 1.65017 \times 10^{-7}xy - 2.66956 \times 10^{-9}x^2y - 7.22031 \times 10^{-9}y^2 - 5.55646 \times 10^{-12}xy^2 - 9.35643 \times 10^{-13}y^3$$

Tab.2-6 displays the mean output values of the three normalized parameter combinations for the virtual material. Similarly to the Inconel 718, the perturbations of input normalized responses were introduced.

Tab.2-6. For virtual material: Three comparisons of the input (in red) and output parameters using the three possible couples of input parameters ($P_{\max}$ and S, $P_{\max}$ and H, or S and H). Relative errors are also given under the output values

Input: Normalized responses under PS=3% RS=-150 MPa						
	P*max-*S		***P*max-*H***		***S*-*H***	
	Output mean	Standard deviation	Output mean	Standard deviation	Output mean	Standard deviation
PP (%)	5.3	5.5	3.9	3.7	5.5	5.3
Rel (%)	77	103	30	95	83	96
RS (MPa)	-195	118	-238	135	-250	141
Rel (%)	30	61	59	57	67	56

Input: Normalized responses under PS=9% RS=-600 MPa						
	P_{max}-S		P_{max}-H		S-H	
	Output mean	Standard deviation	Output mean	Standard deviation	Output mean	Standard deviation
PP (%)	9.2	7.6	10.7	8.1	10.2	8.2
Rel (%)	2.2	83	19	76	13	80
RS (MPa)	-636	137	-613	159	-581	-159
Rel (%)	6	22	2.1	26	3.2	27
Input: Normalized responses under PS=35% RS=-900 MPa						
	P_{max}-S		P_{max}-H		S-H	
	Output mean	Standard deviation	Output mean	Standard deviation	Output mean	Standard deviation
PP (%)	15.7	9.1	17.2	8.9	12.2	7.7
Rel (%)	55	58	51	52	65	63
RS (MPa)	-783	91	-795	97	-772	120
Rel (%)	13	12	12	12	14	16

For the virtual material, it can be seen that the output mean value corresponds relatively well to the input value for the medium cumulative plastic strain. That is, for the case of PS=9%/ RS=-600 MPa. However, the performance of the method on the cases of PS=3%/RS=-150 MPa and PS=35%/RS=-900 MPa is not as good. For the former, the poor performance is due to the domain boundary. This also occurs for the Inconel 718 shown in Tab.2-4. When the input value is near the domain boundary, the dispersion of output values is strong. Especially for this material, the standard deviation is even more significant, as shown in Tab.2-6. For the latter, the bad performance indicates that the method is not optimal within this range. The reason for this is that the three normalization parameters approach saturation in this range so a small perturbation can lead to a large error.

Above all, it can be seen that there are some limitations in our proposed method. First, the method is easily affected by disturbances, which requires a high quality of the experiment indentation tests data. Then, the performance for the input values near the domain boundary is not good, which requires a large residual stress and cumulative plastic strain domain range in the simulations. Finally, the method is not suitable for the range where there is no significant gradient in the indentation responses versus input variables. However, in the suitable range, it can be seen that the proposed method can characterize correctly the residual stress and work hardening simultaneously.

2.3.2.3 Things to consider when applying the method

These two examples demonstrate that the application of the method requires a calibration with FEM and thus to have a good knowledge of the constitutive behavior (including the kinematic hardening) which is not always the case. For XRD or the hole drilling method, the only required information are the elasticity constants or the diffraction elasticity constants, which are well known for common materials.

Moreover, it is necessary to have a reference material that is free from residual stress or cumulative plastic strain. In practice, the part of material far from the shot peened surface can be used as reference. However, the mechanical state of this part can also be affected by the

sample preparation process. This requires careful sample preparation to avoid any hardening or stress during the process. As demonstrated by the results shown above, the perturbation of input values significantly affects the output results. Therefore, high-quality sample preparation and material microstructure are necessary.

Altogether, this method provides a way to characterize residual stresses and cumulative plastic strains simultaneously with instrumented indentation technique. The application of this method in practice is demonstrated in Chapter 3.

2.4. The relaxation of residual stress during cutting process

As stated in Section 2.1.2, the nanoindentation tests are performed on the cross section of the shot peened sample (see Fig.2-1). At first glance, it could be considered that only the σ_{yy} component is set to zero as the cross-section becomes a free surface. However, the coupling between the directions due to Hooke's law could also affect the σ_{xx} and σ_{zz} components. Therefore, it is necessary to investigate the relaxation of residual stress on the cross section. In this section, the residual stress relaxation is analyzed through finite elements simulations. This analysis assumes that the residual stress perpendicular to the cross section is supposed to be completely released and that the final equilibrium state is reached purely elastically (it may not be true in practice).

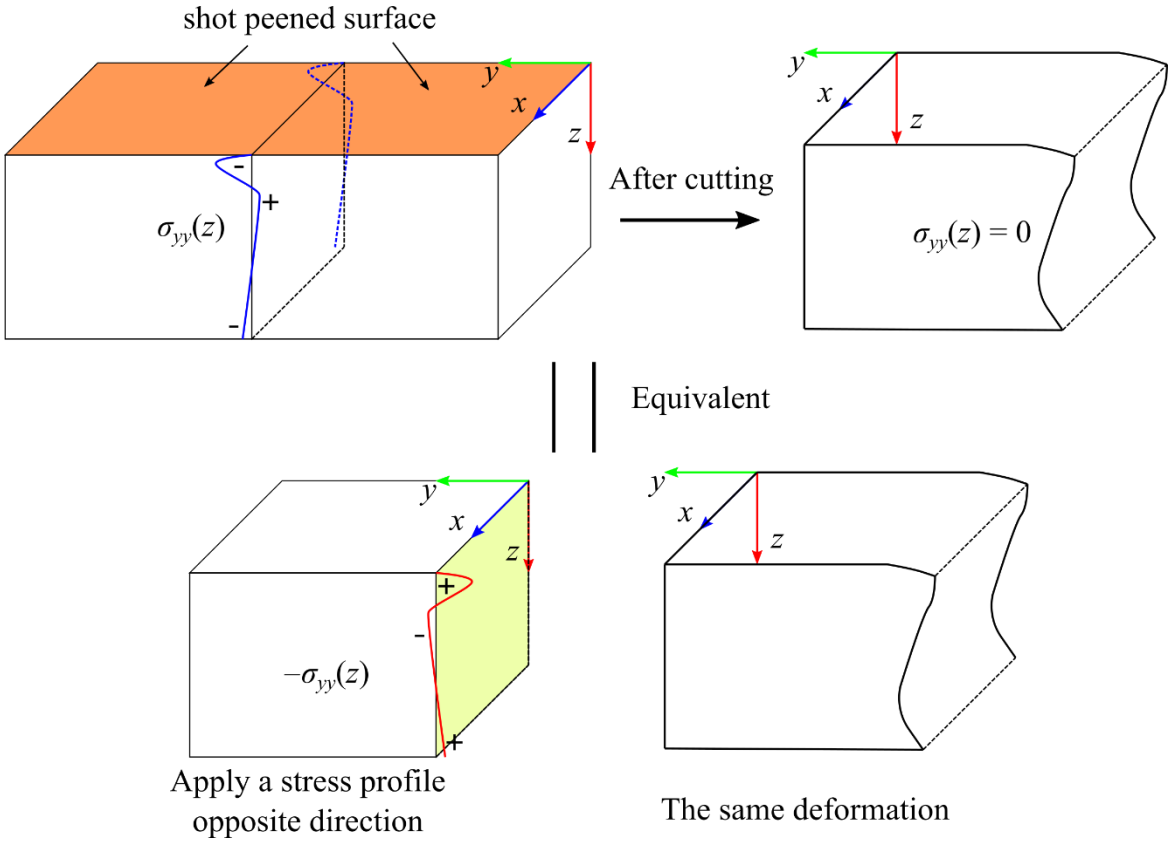

Fig.2-24 Applying a stress distribution in the opposite direction of its original orientation

The typical residual stress profile σ_{yy} of a shot peened material is shown in Fig.2-24 using the blue line. The sign + and − represent the direction of the residual stress profile, which

means tensile and compressive residual stress respectively. After cutting, σ_{yy} is relaxed and the deformation occurs. The aim in this section is to analyze the relaxation of the residual stress σ_{xx} due to the deformation, which affects the nanoindentation responses, as illustrated in Fig.2-4.

A stress profile shown by the red line ($-\sigma_{yy}$), which is opposite to the original distribution, can result in the same deformation as that caused by residual stress relaxation due to cutting. Therefore, the simulations shown below use this equivalence by applying the stress profile in opposition to the original orientation on the cross section.

2.4.1. Define a residual stress profile

The stress distribution must satisfy the equilibrium conditions to ensure that all external surfaces, except for the cross-section, are stress-free and have free displacement. The geometry of the sample is shown in Fig.2-25. The (x, y, z) directions are assumed to be the principal directions so that the stress and strain tensors are purely diagonal.

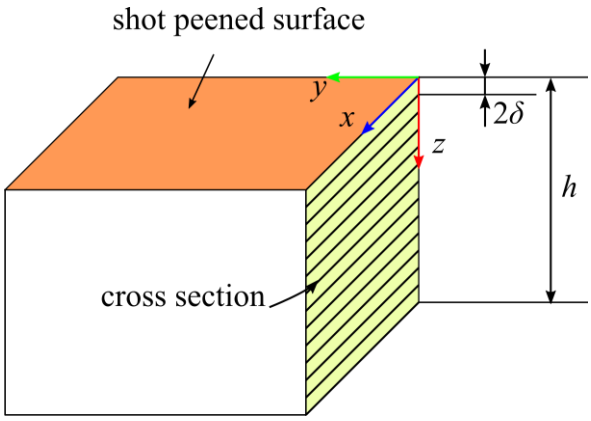

Fig.2-25 The geometry parameters of the sample when define the resiual stress profile

The size of the cell along z direction is noted as 2δ, the height of the sample is h, the number of elements along z direction is N, thus $h = 2\,\delta\,N$.

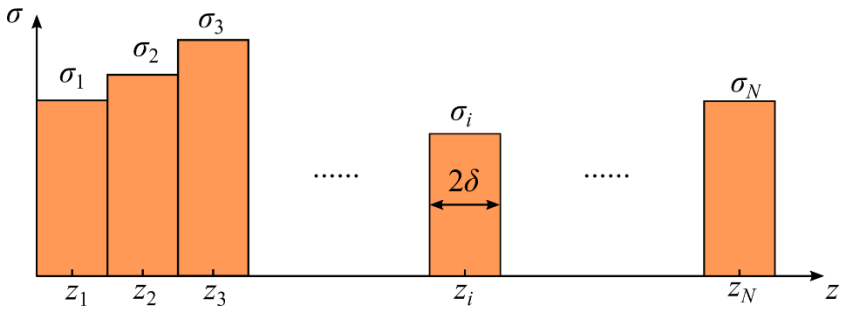

Fig.2-26 Discretization of the stress distribution

The position of the cell along z direction is denoted by z_i and the corresponding stress is σ_i. The coordinate z_i can be expressed with the index i:

$$z_i = (2\,i - 1)\,\delta$$

According to the equilibrium conditions, we can write

$$\iint_S \sigma_{yy}\, dxdz = 0$$
$$\iint_S z\sigma_{yy}\, dxdz = 0$$
$$\iint_S x\sigma_{yy}\, dxdz = 0 \qquad (2-27)$$

As the stress field only depends on *z*, integration of Eq.2-27 along x direction gives:

$$\int_{z=0}^{h} \sigma_{yy}\, dz = 0$$
$$\int_{z=0}^{h} z\sigma_{yy}\, dz = 0 \qquad (2-28)$$

The third condition is automatically fulfilled as the stress distribution is constant along x. With a constant cell width, the conditions become, without approximation:

$$\sum_{i=1}^{N} 2\,\delta\,\sigma_i = 0$$
$$\sum_{i=1}^{N} 2\,\delta\,z_i\,\sigma_i = 0 \qquad (2-29)$$

As δ is constant, it can be factored and cancelled out, thus the two conditions become:

$$\sum_{i=1}^{N} \sigma_i = 0$$
$$\sum_{i=1}^{N} (2\,i-1)\sigma_i = 0 \qquad (2-30)$$

A residual stress profile resulting from shot peening along the *z*-axis can be described by a second order polynomial:

$$\sigma(z) = a_0 + a_1\,z + a_2\,z^2 \qquad (2-31)$$

To determine the coefficients of the polynomial, three conditions must be met:

(1) The stress on the free surface, at $z = 0$, is equal to σ_0;

(2) The maximum compressive residual stress is equal to σ_m at a depth $z = z_m$;

(3) The stress is zero at a depth $z = z_p$.

In which σ_0, σ_m, z_m and z_p can be selected freely according to the specific requirements.

For the stress at the location $z > z_p$, according to the eigenstrain theory for an infinite plate, the stress distribution in the layers where no plasticity occurred during the shot peening treatment is linear. The stress and cell location are described as:

$$\sigma_i = b_0 + b_1$$
$$z_i = b_0 + b_1\,(2\,i-1)\,\delta \qquad (2-32)$$

The coefficients b_0 and b_1 can be determined from the two equilibrium conditions shown in Eq.2-30. The stress profile is defined according to the rules outlined above and generated using a Mathematica® script authored by Manuel François.

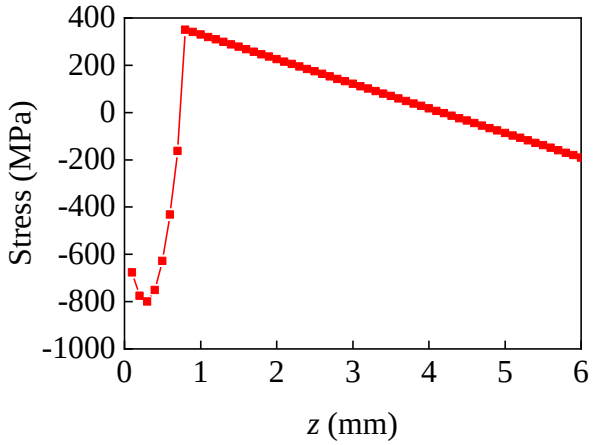

Fig.2-27 The defined stress profile

As an example, the stress on the free surface σ_0 is considered to be -600 MPa, the maximum compressive residual stress σ_m is -800 MPa at $z = 0.25$ mm; zero stress is at $z = 0.7$ mm. The cell size 2δ is 0.1 mm. The profile is shown in Fig.2-27.

2.4.2. Finite element simulation of the residual stress relaxation

A finite element model with a cube shape, identical to the model geometry used to define the stress distribution, was created in ABAQUS. The model size was 6 mm×6 mm×6 mm. The defined stress profile was input as a pressure load in ABAQUS CAE, as shown in Fig.2-28(a). The mesh type is C3D8R, with a size of 0.1 mm along the *z* and *y* directions, and 0.2 mm along the *x* direction. The boundary condition fixed the surface opposite to the cross section. The analysis was conducted using ABAQUS/Standard. The material constitutive behavior parameters presented in Tab.2-2 were utilized in this model.

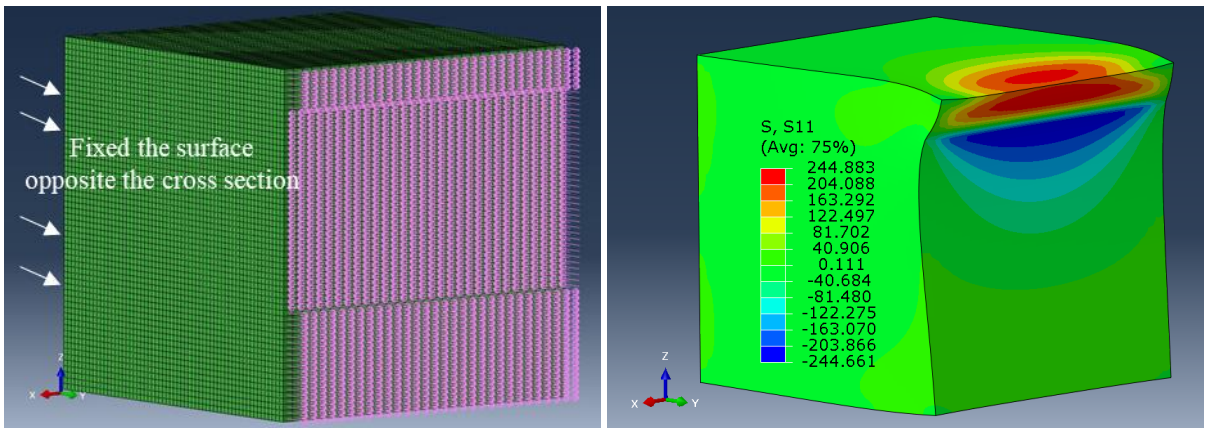

(a) (b)

Fig.2-28 The finite element model of residual stress relaxation (a) Mesh and load (b) The contours of S11, the deformation is magnified 50 times.

The contour map of S11, i.e. $\Delta\sigma_{xx}$, which occurs with the deformation is shown in Fig.2-28(b), in which the deformation is magnified 50 times. This deformation is caused by the relaxation of residual stress perpendicular to the cross section. Fig.2-29(a) shows the final stress profile of one path along the z direction. It can be seen that the deformation results in a significant stress modification for $\Delta\sigma_{xx}$ and $\Delta\sigma_{zz}$ components.

It was observed that the obtained $\Delta\sigma_{xx}$ follows the same trend as the input σ_{yy}, which has the opposite direction of the defined residual stress profile. Therefore, if the material has an initial $\sigma_{xx-\text{initial}}$ that is the same as the defined stress profile, the final state $\sigma_{xx-\text{final}}$ can be obtained by adding it to the obtained $\Delta\sigma_{xx}$. The result is shown in Fig.2-29(b). Obviously, the stress σ_{xx} is released (around 25%).

The maximum compressive residual stress in the defined profile shown here, i.e. the introduced initital stress state, is lower than the material yield stress which indicates that, in this case, plasticity is unlikely to occur due to cutting. Additionally, the mechanical field is more complex in practice, as it includes the cumulative plastic strain, residual stress, and backstress simultaneously. These factors were not considered in the model. Nevertheless, the finite element analysis here still provides valuable information on the relaxation of residual stress.

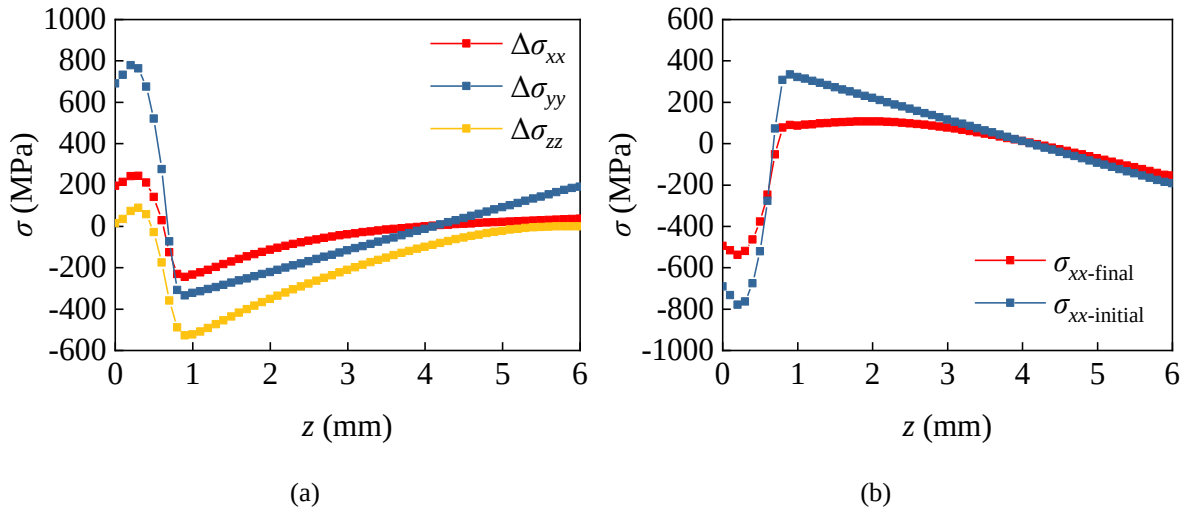

Fig.2-29 The residual stress profiles (a) Stresses in three directions (b) σ_{xx} profile before and after relaxation

2.5. Conclusion

In this chapter, a series of simulations was performed in order to propose a method to characterized residual stress and work hardening with the instrumented indentation technique.

Three different residual stress state with the same hydrostatic stress, which are uniaxial stress state, equibiaxial stress state and a more general stress state respectively, were introduced into the 3D finite element model. Results show that their curves are not identical. However, the differences in indentation responses between the uniaxial stress state and equibiaxial stress state are 0.4% for $P_{\max}$ and 0.01% for stiffness. These small differences are considered insignificant, which means that the 2D axisymmetric finite element model can be used for simulations as long as only residual stress and cumulative plastic strain are introduced.

The shot peening backstress profile was obtained from shot peening simulations. Results show that the shot peening backstress has a similar distribution as residual stress. In addition, for each $\bar{\bar{X}}$, their values of the components on the plane are similar.

Then the shot peening backstress was introduced in the indentation simulation model. With ABAQUS standard analysis, it was found that only $\bar{\bar{\alpha}}'$ affects the indentation responses, thus an equivalent backstress is proposed to study its effects. In addition, the results indicate that α_3^{eq}, characterized by a slow evolution rate, has the most significant influence on indentation responses (0.6% difference on P_{max} and 0.65% difference on S). When compared to the effect of residual stress or cumulative plastic strain, the influence of backstress is relatively insignificant.

The evolution of backstress with different shot peening parameters were also studied. Results show that, when the coverage rate is 100%, the value of each equivalent backstress and the affected depth will increase slightly with increasing shot speed. For a given shot speed, here 30 m/s, the equivalent backstress will not change significantly with the coverage rate. Furthermore, during shot peening, α_1^{eq} and α_2^{eq}exhibit a tendency to saturate relatively easily. In contrast, achieving saturation for α_3^{eq} proves unlikely. Even at a shot speed of 70 m/s, significantly higher than typical practical speeds (for ultrasonic shot peening technique), and without considering the strain rate effect, α_3^{eq} remains at approximately 50 MPa, which is far from saturation. The difference of P_{max} and S is 0.1% and 0.05%, respectively, when α_3^{eq} is equal to 50 MPa. Compared to the effect of residual stress and cumulative plastic strain, the effect of backstress is even smaller and can be neglected.

Then, a Response Surface Function method was proposed to characterize residual stress and cumulative plastic strain simultaneously. The method was verified numerically using two different materials with combined hardening behavior. The results indicate that the response surfaces are influenced by the material hardening rules. However, the solved values accurately represent the input values. The sensitivity of the combinations of the normalized response varies depending on the input value ranges. Therefore, it is important to select the best combination when applying the method in practice.

Finally, the stress relaxation during the cutting process was simulated. Results show that the residual stress component along the surface is also released (around 25%) during the cutting process. This would need to be taken into account in practical applications.

Chapter 3
Experimental characterization of work hardening and residual stress

In the previous chapter, we proposed the Response surface function method to characterize residual stress and cumulative plastic strain simultaneously using the instrumented indentation technique. The method demonstrates good feasibility and quality from a purely numerical perspective. However, its practical application needs to be verified. In this chapter, we attempt to apply the Response surface function method to a real shot peened Inconel 625 alloy. The possibility and feasibility of this method in practice will be analyzed by comparing the characterized result with the measured results using X-ray diffraction.

3.1. Material and sample condition

3.1.1. Received material

The received material was a cylindrical bar (Diameter equals to 16 mm) of Nickel based alloy 625 (Inconel 625), provided by the commercial company NeoNickel France. Ultrasonic inspection indicates no defects in the material. The chemical composition is detailed in Tab.3-1.

Tab.3-1 Chemical composition (wt. %) of the received Inconel 625 (from the provider)

C	Mn	Si	P	S	Co	Al	Ti	Cb+Ta	Fe	Ni	Mo	Cr
0.04	0.08	0.12	0.005	0.001	0.07	0.21	0.27	3.55	3.78	60.61	8.79	22.32

3.1.2. Samples for mechanical tests

The dimension of samples for mechanical tests was designed according to the standard ASTM E606/E606M-21 [107], as illustrated in Fig.3-1. The final machining parameters were set as follows: cutting speed (V_c) = 40 m/min, feed rate (f_c) = 0.1 mm and cutting depth (a_p) = 0.1 mm; in order to minimize the work hardening caused by the turning.

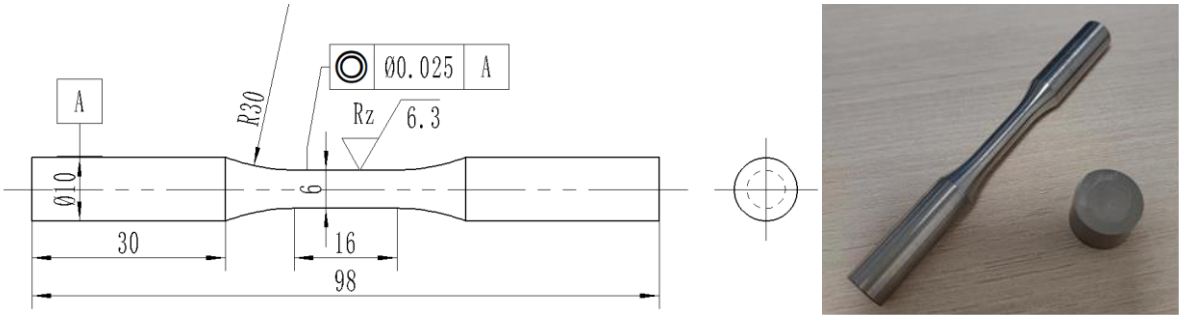

Fig.3-1 Machined specimen

The roughness of the gauge section was measured using a non-contact optical profiler, Altisurf 500 (Altimet, FR). The measurement length was 10mm. The roughness profile and results are shown in Tab.3-2 and Fig.3-2. There is no polishing process after machining, thus resulting in a high roughness value.

Tab.3-2 Roughness of received material

	Ra (μm)	Rt (μm)
Mean value	0.414	7.767
Standard deviation	0.156	2.293

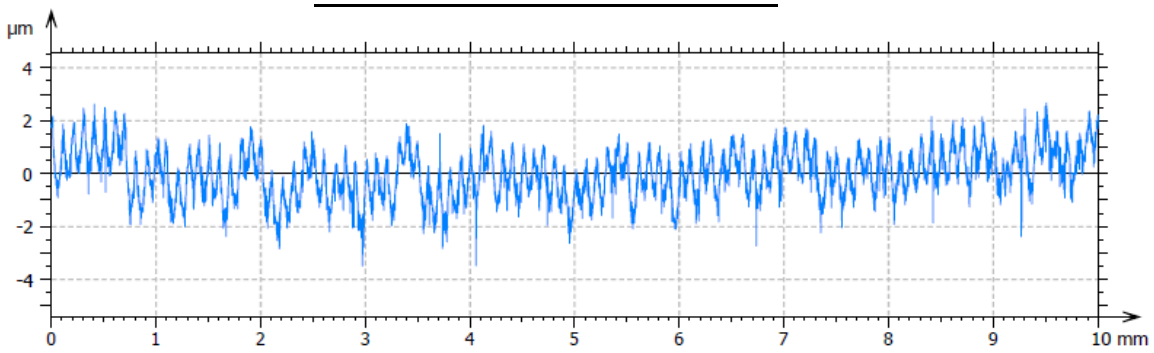

Paramètres	Valeur	Unité
Longueur	10.00	mm

ISO 4287

Paramètres d'amplitude - Profil de rugosité

Ra	0.2340	μm	*Filtre gaussien, 0.08 mm*	*Écart moyen arithmétique du profil de rugosité.*
Rt	3.764	μm	*Filtre gaussien, 0.08 mm*	*Hauteur totale du profil de rugosité.*

Fig.3-2 The roughness profile and results

3.2. shot peening

Two short cylindrical samples, each approximately 12 mm in thickness, were cut from the received material. Subsequently, the surface of each sample was mechanically polished using MetaServ® 250 single & twin grinder-polishers (BUEHLER, USA) using abrasive discs of 800 and 1200 grit. The polishing process aimed to eliminate the layer affected by the cutting process and achieve optimal flatness.

Tab.3-3 Shot peening parameters

Parameters	Values
Diameter of shot (mm)	2
Mass of shot (g)	5
Material of shot	100Cr6 steel
Distance between sample and sonotrode (mm)	15
Power (%)	50
Durations (s)	35

The two samples were subsequently fixed in a plastic holder, which was then placed in the treatment chamber of the ultrasonic shot peening system. A specified mass of shot (5 g) was introduced into the chamber. The sonotrode converts electrical energy into mechanical vibrations through an ultrasonic transducer. The shot rapidly bounce and shock the sample surface as the sonotrode vibrates at 20 kHz. The shot peening parameters are listed in Tab.3-3,

and the shot peening process schematic diagram is shown in Fig.3-3. One of the samples will be characterized with X-ray diffraction and another one with nanoindentation.

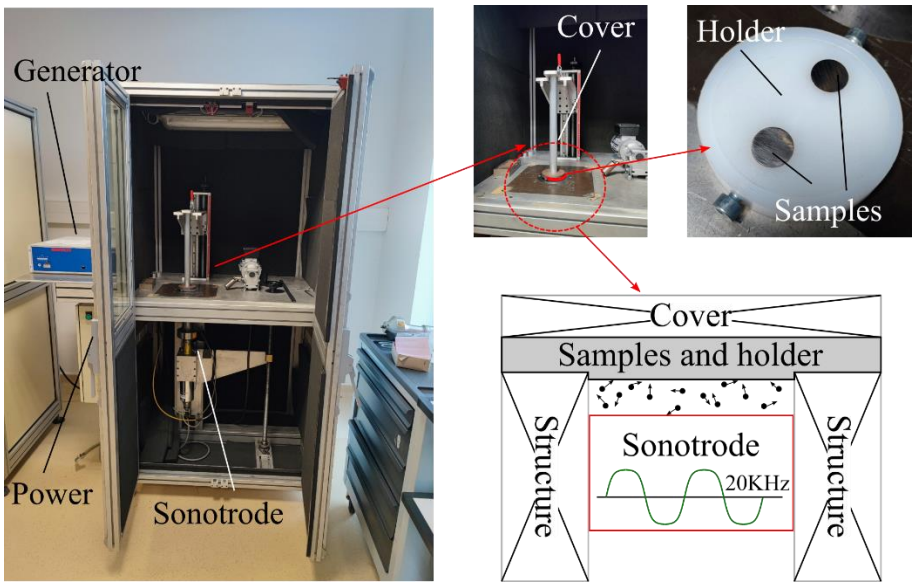

Fig.3-3 Ultrasonic shot peening process

3.3. X-ray diffraction measurement

X-ray diffraction (XRD) tests were conducted using a D8 DISCOVER X-ray diffractometer (Bruker, USA), which was equipped with a chromium anode tube operating at 40 kV and 30 mA. The {220} planes of the nickel alloy, with the peak position at $2\theta = 128°$, were chosen for measurements, as diffraction peaks at higher angles are more sensitive to residual stress and lattice distortion. The collimator diameter is 1mm. The 2D detector (Dectris PILATUS 100K) collected the diffraction signal in the range of $2\theta = 123°{\sim}133°$. Each image acquisition by the detector lasted 40 seconds. The diffraction system is shown in Fig.3-4.

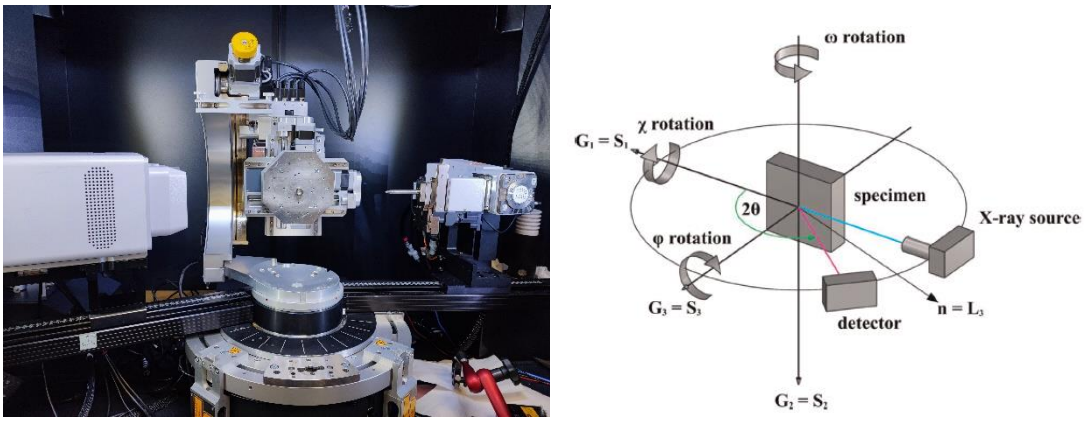

(a) (b)

Fig.3-4 X-ray diffraction system (a) The photo of the D8 DISCOVER X-ray diffractometer (b) Reference position for goniometric angles $\omega = \varphi = \chi = 0$, in which θ is Bragg angle, S_1, S_2 and S_3 are sample coordinate systems and G_1, G_2 and G_3 are the goniometer reference system [108].

The $\sin^2\psi$ method was employed for the measurement, necessitating a series of diffractions at various ψ angles. Eleven ψ angles (0°, 6°, 12°, 18°, 24°, 30°, 36°, 42°, 48°, 54°

and 60°) were used. Additionally, four ϕ angles (0°, 90°, 180° and 270°) were employed to obtain the biaxial stress tensor.

X-ray diffraction can only provide physical quantities, such as stress and work hardening, averaged between 0 and infinity. Because of exponential attenuation (Beer-Lambert's law) these average quantities correspond to their value at the average penetration depth which is 3.5 µm in the chosen conditions. Similar concepts were illustrated in Chapter 2. To obtain the profile of the physical field introduced by shot peening, material removal must be carried out gradually. Electrolytic polishing was chosen for material removal, as it introduces no additional stress or hardening. The electrolytic polishing process was conducted using the LectroPol-5 electrolytic polishing unit (Struers, DK) with D11 solution (70% ethanol, 20% perchloric acid and 10% ethylene glycol monobutyl ether). Each polishing step was performed in the same area while the adjacent region was protected by tape, as shown in Fig.3-5. The polishing area was polished with a voltage of 25 V for 30 seconds each time, followed by cleaning with cold running water. The thickness of the layer removed during the electrolytic polishing process was monitored using a Coordinate Measuring Machine.

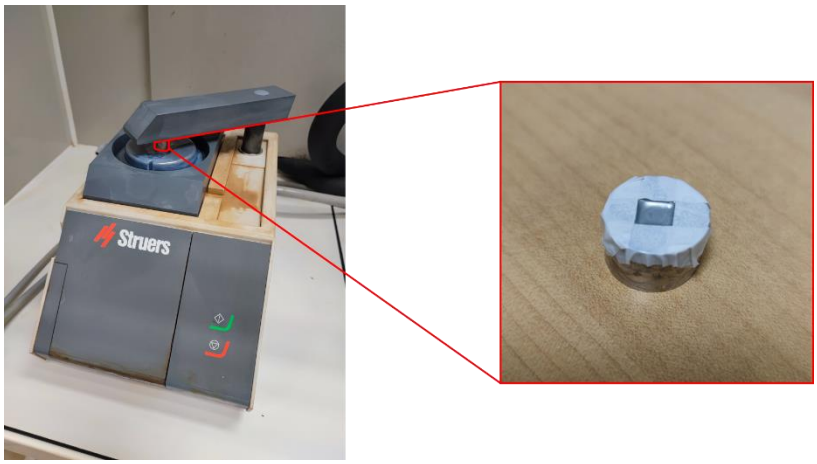

Fig.3-5 Electrolytic polishing system

A Wolfram Mathematica® script written by Manuel François (LASMIS/UTT) was used for extracting the residual stress and peak width information from the X-ray diffraction data. The diffraction peak was fitted with a Pseudo-Voigt function, which is a linear combination of a Gaussian function $G(2\theta)$ and a Lorentzian function $L(2\theta)$:

$$L(2\theta) = \frac{H}{\left(1 + \pi^2 \left(\frac{2\theta - p}{B}\right)^2\right)} \qquad (3-1)$$

$$G(2\theta) = He^{\left(-\pi\left(\frac{2\theta-p}{B}\right)^2\right)} \qquad (3-2)$$

$$Pv(2\theta) = \eta G(2\theta) + (1-\eta)L(2\theta) \qquad (3-3)$$

Where H is the peak height, B is the integral peak width, p is the peak position, η and $(1-\eta)$ defines the proportions of Gaussian function and Lorentzian function respectively. The diffraction background was characterized by a straight line obtained through least squares fitting using a specified number of points (about 30) at the start and end of the acquisition range. The standard uncertainty is calculated from the residuals of the least square regression resulting

from the non-linear fitting of the peak. The widths ($K_{\alpha 1}$ component) are calculated as the average among the peaks with different ψ and ϕ.

The residual stress and peak integral width profiles along the depth are shown in Fig.3-6. As the sample is quite thick, no layer removal correction is performed on the stress profile.

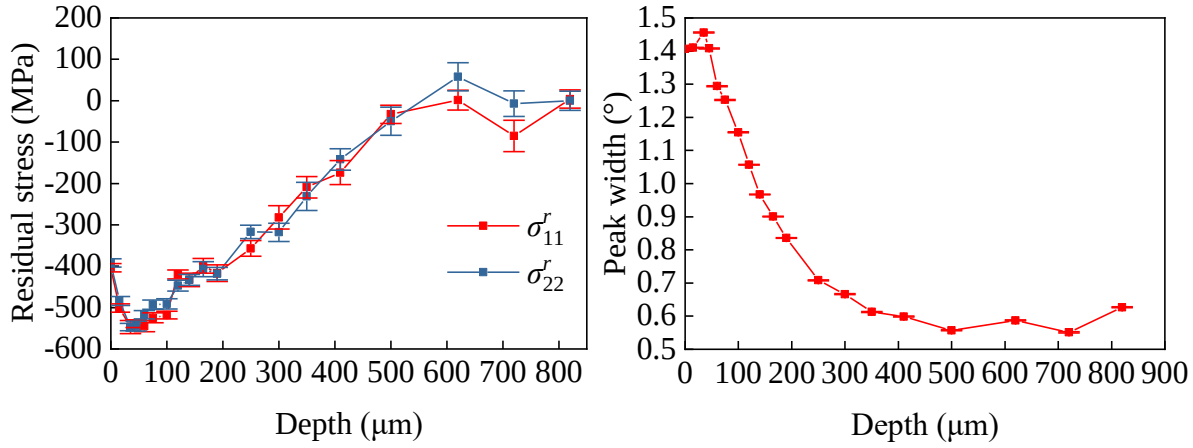

Fig.3-6 The profiles of (a) residual stress (b) integral peak width along depth

σ_{11}^r and σ_{22}^r are the residual stresses in two directions on the stress plane. It is clear that the σ_{11}^r and σ_{22}^r profiles are overlapping, indicating an equibiaxial state, which is characteristic of a shot peened bulk material. For the remainder of this chapter, only σ_{11}^r will be shown to denote the residual stress in the specimen.

A significant compressive residual stress, close to -400 MPa, is observed at the top surface layer. The maximum compressive residual stress, approximately -600 MPa, is obtained at a depth of 50 μm. Subsequently, the compressive residual stress gradually decreases, approaching nearly 0 MPa at depths beyond 500 μm. Similarly, a peak width of 1.4° is observed at the top surface layer. The maximum peak width, around 1.5°, is noted at a depth of 50 μm. The peak width then diminishes, reaching 0.6° at depth exceeding 400 μm. As the optical set-up used in the experiment is constant, the peak width is not corrected for instrumental broadening.

3.4. Calibration of peak width and cumulative plastic strain

In the literature, a method was proposed to quantify the level of work hardening by correlating the peak width with specific plastic strain levels [50]. To implement this calibration, several uniaxial tensile tests at predetermined plastic strain levels and X-ray diffraction tests need to be conducted.

It can be seen in Fig.3-6(b) that, despite the last machining step being performed slowly and carefully, a hardened layer persists on the surface of the specimen. Thus, the hardened layer should be removed as much as possible to ensure a more accurate characterization firstly. The electrolytic polishing process is employed to eliminate the hardening induced by machining. The solution is also D11, and the voltage is 20 V. As depicted in Fig.3-6, the stable peak width

of the raw material is approximately 0.6°. Following each polishing session, the sample undergoes X-ray diffraction measurements to verify if the peak width approaches 0.6°.

The tensile tests were conducted using the Denison Mayes Group 100 kN hydraulic fatigue frame (Denison Mayes Group Ltd., Beeston, UK). Extensometer control was used with a strain rate of 1×10^{-3}/s to achieve the specified strain level. An electronic extensometer was attached on the gauge part of the sample to monitor elongation in the calibrated section, with a gauge length of 12.5 mm.

For each strain level, the peak width was measured by X-ray diffraction and then the specimen was stretched again. The peak widths are shown in Fig.3-7(a). Power law was used to fit the data.

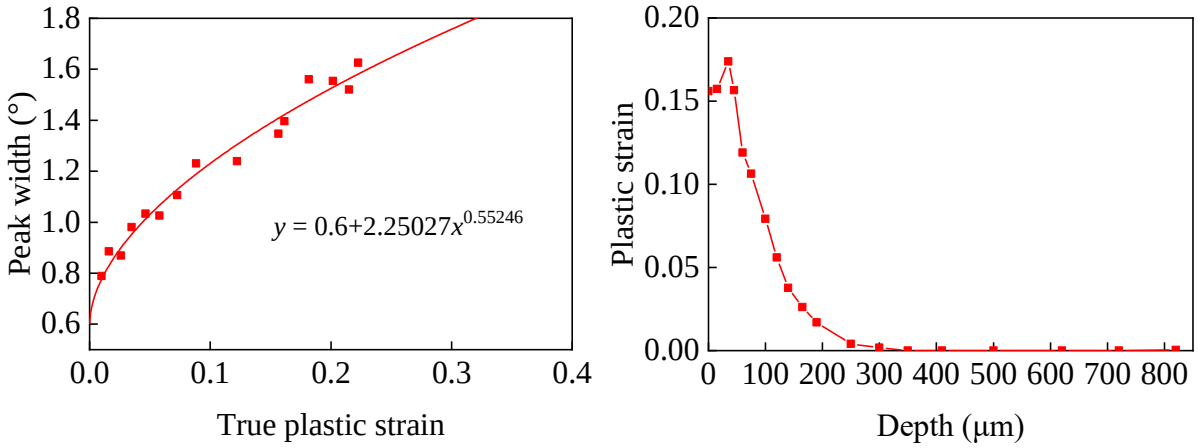

(a) (b)

Fig.3-7 Calibration of peak width and cumulative plastic strain (a) experiment data and power law fitting curve (b) resulting profile of the cumulative plastic strain

With the fitting function and the peak width profile shown in Fig.3-6(b), the profile of the cumulative plastic strain can be estimated, which is shown in Fig.3-7(b). A 15% level of cumulative plastic strain is observed near the shot peened surface. This may be due to the short shot peening time. The maximum strain level, around 17%, is located in the subsurface. Then it decreases rapidly and tends towards zero beyond 300 μm.

3.5. Instrumented indentation tests

3.5.1. Sample preparation

Another shot peened sample shown in Fig.3-3 was used to perform nanoindentation tests. The sample was cut into small pieces using a metallographic cut-off saw, Secotem-15 (Struers, DK) with a feed speed of 0.01 mm/s to minimize the influence of cutting process. Then the pieces were hot mounted with resin using the LaboPress-3 hot mounting machine (Struers, DK). The procedure is shown in Fig.3-8.

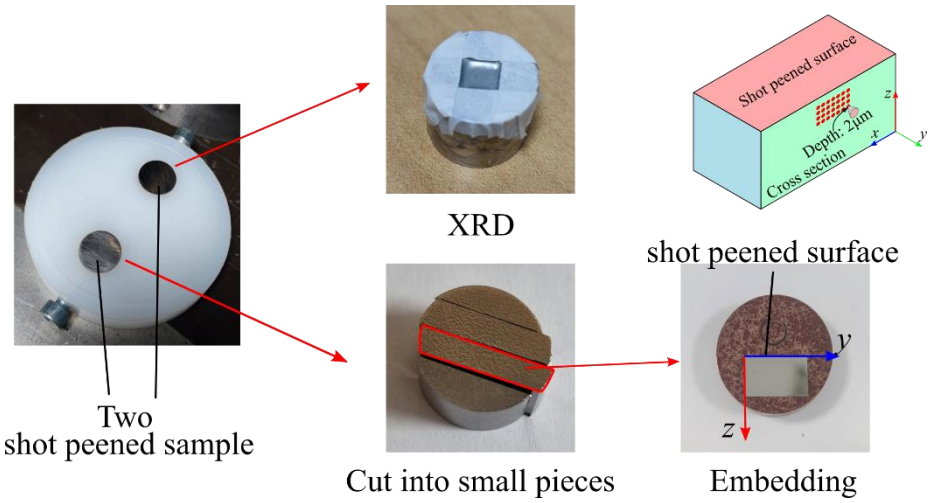

Fig.3-8 Shot peened sample for XRD and nanoindentation test

The samples were polished in order to obtain a mirror flat surface. During this procedure, extra strain hardening should not be introduced. Thus, the polishing procedures are as following:

1) 800 grit abrasive disc, 3 mins;
2) 1200 grit abrasive discs; 5 mins;
3) 6 μm diamond paste; 10 mins;
4) 3 μm diamond paste; 20 mins;
5) 1 μm diamond paste; 40 mins;
6) 0.25 μm diamond paste; 80 mins;

Finally, the samples were vibration polished with A3 alumina suspension (0.25 - 0.3 μm) for 15 hours to remove the surface hardening as much as possible.

The peak width of the polished sample was compared with the raw material got from electrolytic polishing. The peak profiles at $\psi = 0°$ with the background subtracted are shown in Fig.3-9. It could be observed the peak width of the polished sample is still broader than for the raw material.

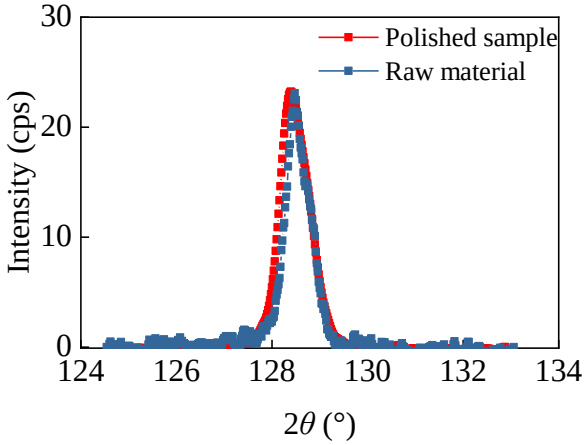

Fig.3-9 The profiles of diffraction peak for polished sample and raw material ($\psi = 0°$)

The average peak width of the polished sample is 0.77°, while the raw material is 0.6°. Even with careful polishing, some hardening is still introduced to the material.

3.5.2. Spherical indentation tests

Series of indentation tests were performed on Nano indenter®XP (MTS, USA), as shown in Fig.3-10, with a spherical tip of radius 10 μm. For all tests, the indenter was controlled until the maximum indentation depth was reached. Then, it was unloaded until 10% of the maximum load and held for 50 seconds to observe thermal drifting.



Fig.3-10 Nano indenter®XP instrumented indentation machine

As previously stated, despite careful polishing, some hardening was still introduced to the material. To obtain information on the mechanical state introduced by shot peening, indentation tests were conducted perpendicular to the shot peened surface (indentation axis along y), with depths of 800 nm and 2000 nm. At each distance from the shot peened surface, 20 tests were conducted with a 50 μm distance between each indent position. The indentation responses, including maximum load P_{max}, contact stiffness S, and indentation hardness H are shown in Fig.3-11. The stiffness and hardness are calculated with Eq.1-11 to Eq.1-15.

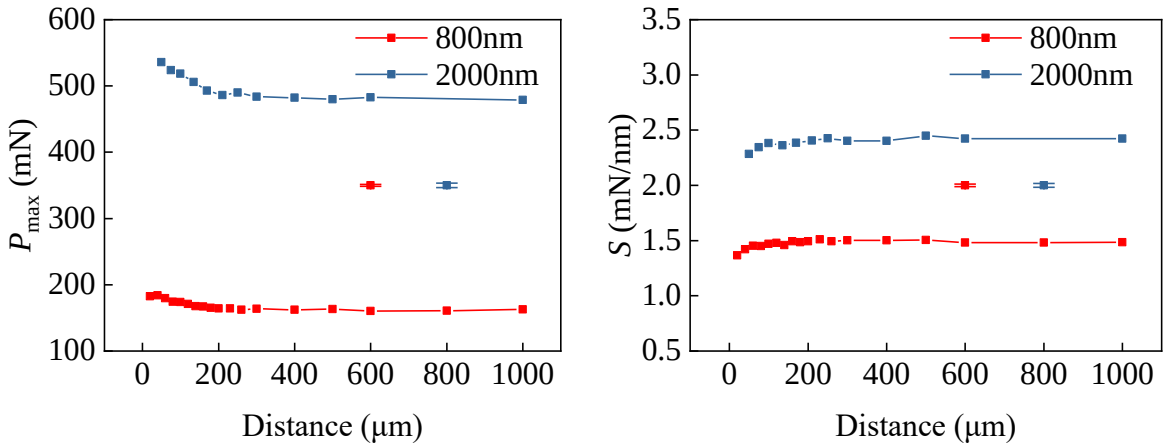

Fig.3-11 Indentation responses along with distance from shot peening surface (a) P_{max} (b) S
Two points besides the curves are represented to show the average error bar of each set.
(Continued on the next page)

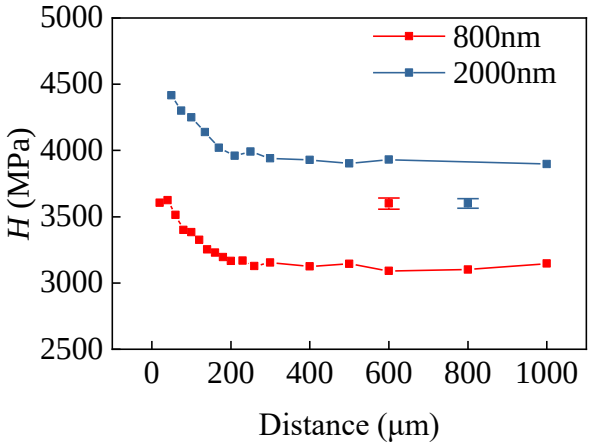

(c)

Fig.3-11 Indentation responses along with distance from shot peening surface (c) H
Two points besides the curves are represented to show the average error bar of each set.
(Continued)

The results at each specific distance represent the average of 20 tests. The error bars shown on the figures are the average standard deviations of the indentation tests at all the distance. It can be seen that P_{max} and H increase due to the combined effect of strain hardening and compressive residual stress introduced by shot peening. This phenomenon is similar to what was found in [109]. However, S show a different trend which is a decrease due to shot peening. Furthermore, the indentation responses remain stable beyond 500 μm from the shot peened surface, indicating that this part is not influenced by shot peening.

The indentation responses at a distance of 1000μm away from the shot peened surface, which are presumed to be unaffected by shot peening, were noted as P_{0max}, S_0, and H_0 and taken as the reference values representing the 'Raw Material State'. Therefore, the normalized indentation responses P_{max}/P_{0max}, S/S_0 and H/H_0 are shown in Fig.3-12.

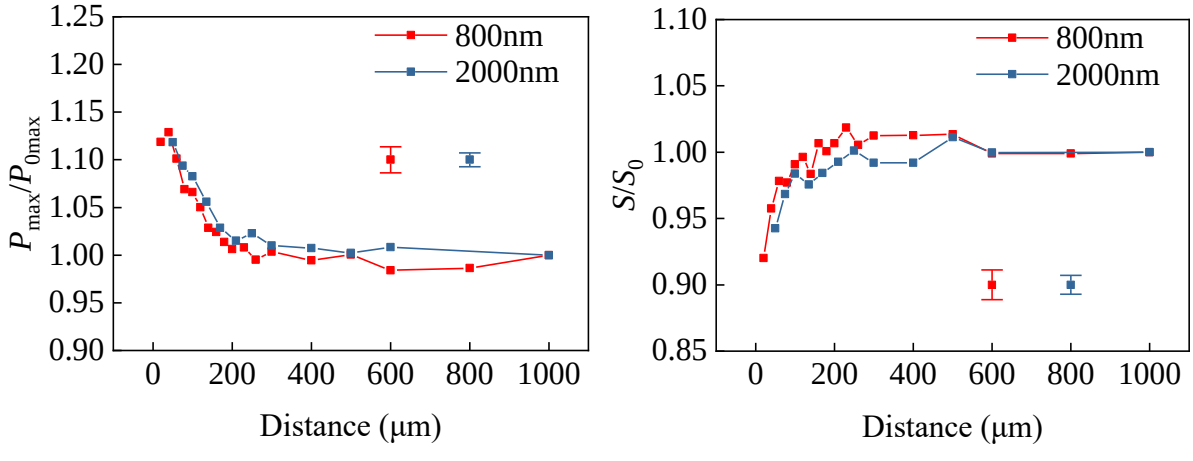

(a) (b)

Fig.3-12 Normalized indentation responses along with distance from shot peening surface (a) P_{max}/P_{max0} (b) S/S_0
Two points besides the curves are represented to show the average error bar of each set.
(Continued on the next page)

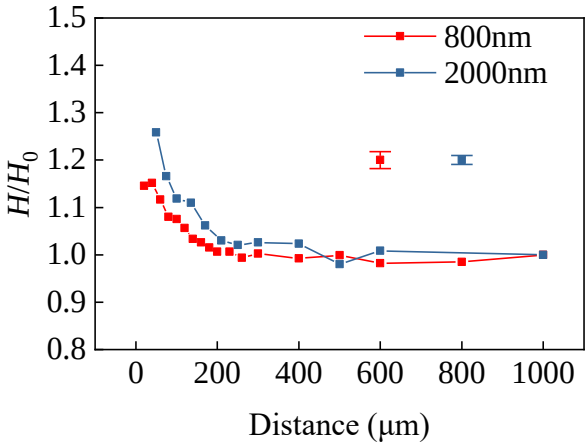

(c)

Fig.3-12 Normalized indentation responses along with distance from shot peening surface (c) H/H_0
Two points besides the curves are represented to show the average error bar of each set.
(Continued)

The normalized P_{max} and H show a similar trend, which gives a clear gradient along with the distance. The normalized S shows an opposite trend, i.e. a decrease when approaching the shot-peened surface. Besides, the trends in normalized indentation responses at depths of 800 nm and 2000 nm are consistent, which means both of them are able to characterize the mechanical state introduced by shot peening.

3.5.3. The correction of edge effect

The sample edge effect, which is the effect caused by the insufficient distance between indentation and the edge of the sample, is an issue in the indentation tests. It is more critical for stiffness than hardness since the volume influenced by elastic strains under the indenter is much larger than the plastically deformed volume. Though our sample was embedded in resin, the indentation responses from resin is quite different from the sample, which indicates the edge effect should be corrected.

Jakes et al. [110] analyzed the edge effect and proposed an estimate of structural compliance C_{str} caused by a free edge as:

$$C_{\mathrm{str}} = \frac{0.2 + 0.11\,\nu}{E\,d} \qquad (3-6)$$

Where E and ν are elastic modulus and Poisson's ratio of the target material, and d is the distance from the indent position to the sample edge. In order to characterize the mechanical field near shot peened surface, the structural compliance C_{str} must be considered. The composite compliance C obtained from indentation test should be:

$$C = \frac{\mathrm{d}h}{\mathrm{d}P} = C_f + C_s + C_{\mathrm{str}} \qquad (3-7)$$

Where C_f is the frame compliance of the indentation machine and C_s is the sample compliance. Thus, the stiffness S without considering the free edge can be corrected. The corrected normalized S of the indentation test with the depth of 800 nm is shown in Fig.3-13.

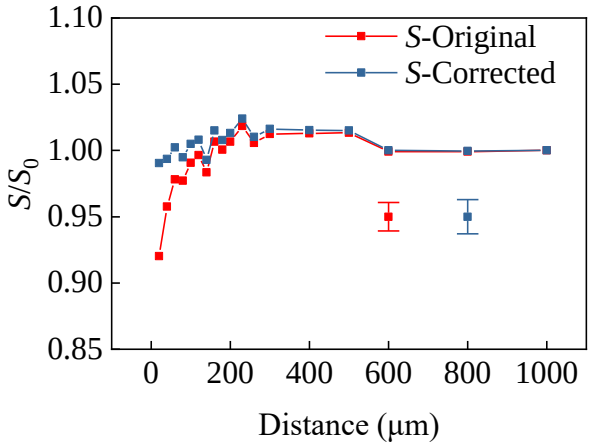

Fig.3-13 The corrected and original stiffness *S*

Two points besides the curves are represented to show the average error bar of each set.

3.6. Material behavior parameters identification

3.6.1. Isotropic hardening parameters identification

The entire tensile test was carried on Instron 8950 250kN universal testing machine (Instron, UK) using an extensometer of gauge length 10 mm. The true stress- true strain curve is shown in Fig.3-14. Necking occurs at a strain around 40%. The elastic modulus is linearly fitted in the elastic range, which is 198 000 MPa, and the hardening behavior can be fitted by a Voce rule as shown in Fig.3-14(b). Only the data between the plastic strain of 0.2% and necking were utilized.

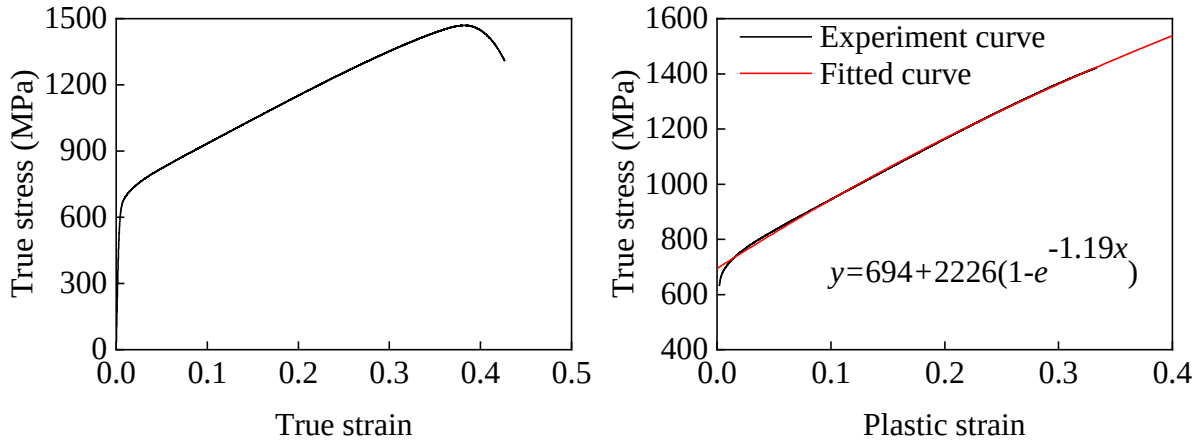

Fig.3-14 Monotonic tensile test (a) True stress- true strain curve (b) True stress-plastic strain curve

3.6.2. Combined hardening parameters identification

A cyclic test of 100 cycles was carried on Instron 8950 universal testing machine. The strain range was imposed at ±0.8%, as shown in Fig.3-15. The cyclic test was conducted by extensometer control, with a triangle waveform.

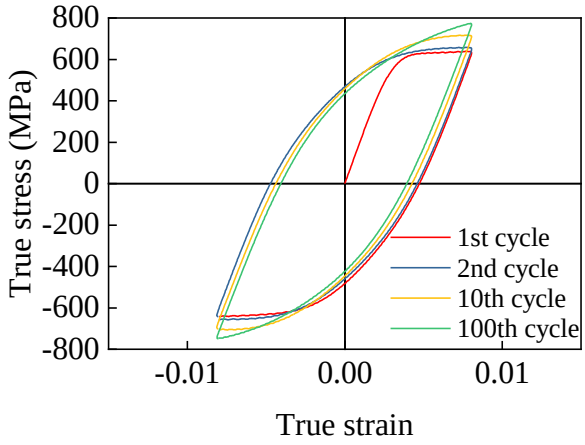

Fig.3-15 True stress-true strain curve within strain range of ±0.8%

The elastic modulus was fitted from the elastic range in the tensile part of the 1st cycle. The isotropic hardening component was fitted from the change of elastic range in the hysteresis loop during the 100 cycles. The elastic range in the hysteresis loop and the fitted isotropic hardening parameters are shown in Fig.3-16.

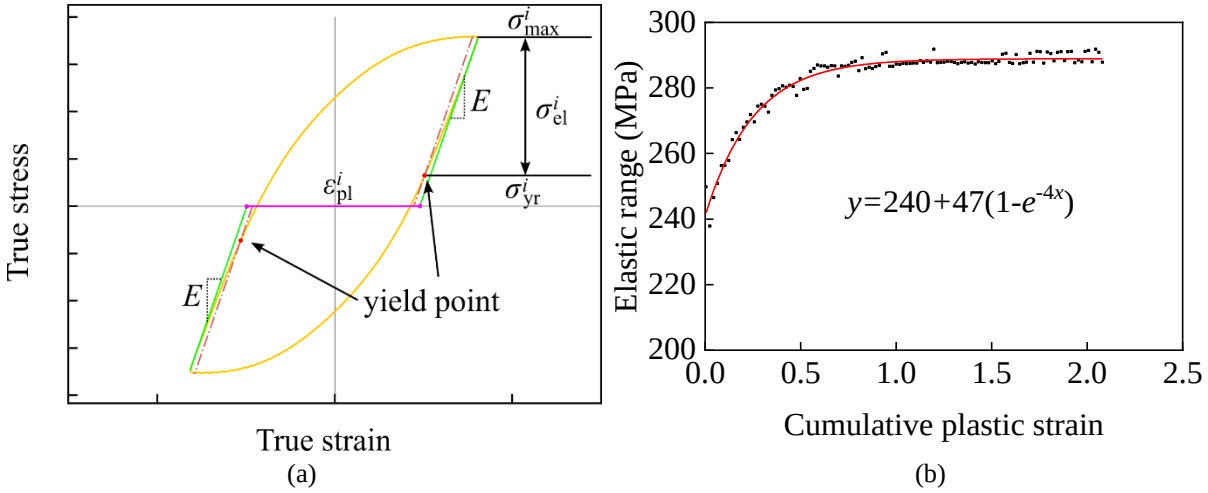

Fig.3-16 (a) Elastic range in hysteresis loop (b) Parameters fitting

In Fig.3-16(a), the superscript i indicates the i-th cycle, σ_{max} is the maximum; σ_{el} is the elastic range; σ_{yr} is the yield stress in the compressed section and ε_{pl} is the plastic strain range. The isotropic hardening parameters Q and b can be fitted as:

$$\frac{\sigma^i_{el}}{2} = \sigma_y + Q\left(1 - e^{-b\,\varepsilon^i_{cp}}\right) \qquad (3-4)$$

In which σ_y is the fitted yield stress of the material and ε^i_{cp} is the cumulative plastic strain in the i-th cyclic test. As only 100 cycles are considered in this work, thus it can be described as:

$$\varepsilon^i_{cp} = \begin{cases} \dfrac{\varepsilon^i_{pl}}{2} & i = 1 \\ \varepsilon^{i-1}_{cp} + \varepsilon^{i-1}_{pl} + \varepsilon^i_{pl} & i > 1 \end{cases} \qquad (3-5)$$

The experiment data and fitting result are shown in Fig.3-16(b). In this case, $\sigma_y = 240$ MPa, $Q = 47$ MPa and $b = 4$.

Once isotropic hardening parameters are known, the kinematic hardening parameters can be fitted with uniaxial tensile stress-plastic strain data using the following model:

$$\sigma = \sigma_{\mathrm{y}} + \sum_{i=1}^{n} \frac{C_i}{\gamma_i}(1 - e^{-\gamma_i \varepsilon_p}) + Q\left(1 - e^{-b\varepsilon_p}\right) \qquad (3-6)$$

The parameters in Eq.3-6 have the same meaning as the formulae in Chapter 2. In this case, the number of kinematic hardening components is $n = 3$.

The constrained nonlinear minimum function Fmincon in Matlab® was used to fit the parameters. Six parameters C_1, C_2, C_3, γ_1, γ_2 and γ_3 need to be identified. The upper limit for C_1, C_2, C_3 is 10e6 and for γ_1, γ_2, γ_3 is 10e4. The lower limit for all parameters are 0. The objective function is:

$$\mathrm{fun} = \min \sum (\sigma_{\mathrm{fit}} - \sigma)^2$$

Previous literature [111-112] showed that the material properties are different in monotonic and cyclic loading. Besides, the material behavior in tensile section of the first cycle and the subsequent cycles is also different. Here two groups of kinematic hardening parameters were found, which could describe the tensile section of the 1st cycle and the subsequent cycles, respectively, are shown in Tab.3-4. The 1st cycle parameters are fitted with the tensile section of the first cycle, and the subsequent cycles parameters are fitted with the tensile section of the second cycle.

Tab.3-4 Two groups of kinematic hardening parameters

Group 1: 1st cycle	Group 2: Subsequent cycles
$C_1 = 4638532$ MPa	$C_1 = 265974$ MPa
$\gamma_1 = 21999$	$\gamma_1 = 693$
$C_2 = 269797$ MPa	$C_2 = 7760$ MPa
$\gamma_1 = 1515$	$\gamma_1 = 99$
$C_3 = 2694$ MPa	$C_3 = 2381$ MPa
$\gamma_1 = 1.3$	$\gamma_1 = 0.77$

The fitting method shown here is obviously not suitable for the material behavior under a large number of cycles. However, it is worth noting that the aim of the fitted parameters is for the simulation of shot peening or indentation, during which the material undergoes only a few cycles. As a result, the fitted parameters can still be used to study the application of combined hardening parameters in indentation simulation. As mentioned above, the comparison of simulated and experimental curves does not include the 5th and subsequent cycles.

Fig.3-17 shows the cyclic stress strain curve of finite element simulation with parameters group 1 and group 2. It could be observed that the parameters of group 1 accurately describe the tensile section of the 1st cycle, but are less effective for subsequent cycles. Conversely, the parameters of group 2 effectively describe the 2nd, 3rd, and 4th cycles, but are less effective for the tensile section of the first cycle.

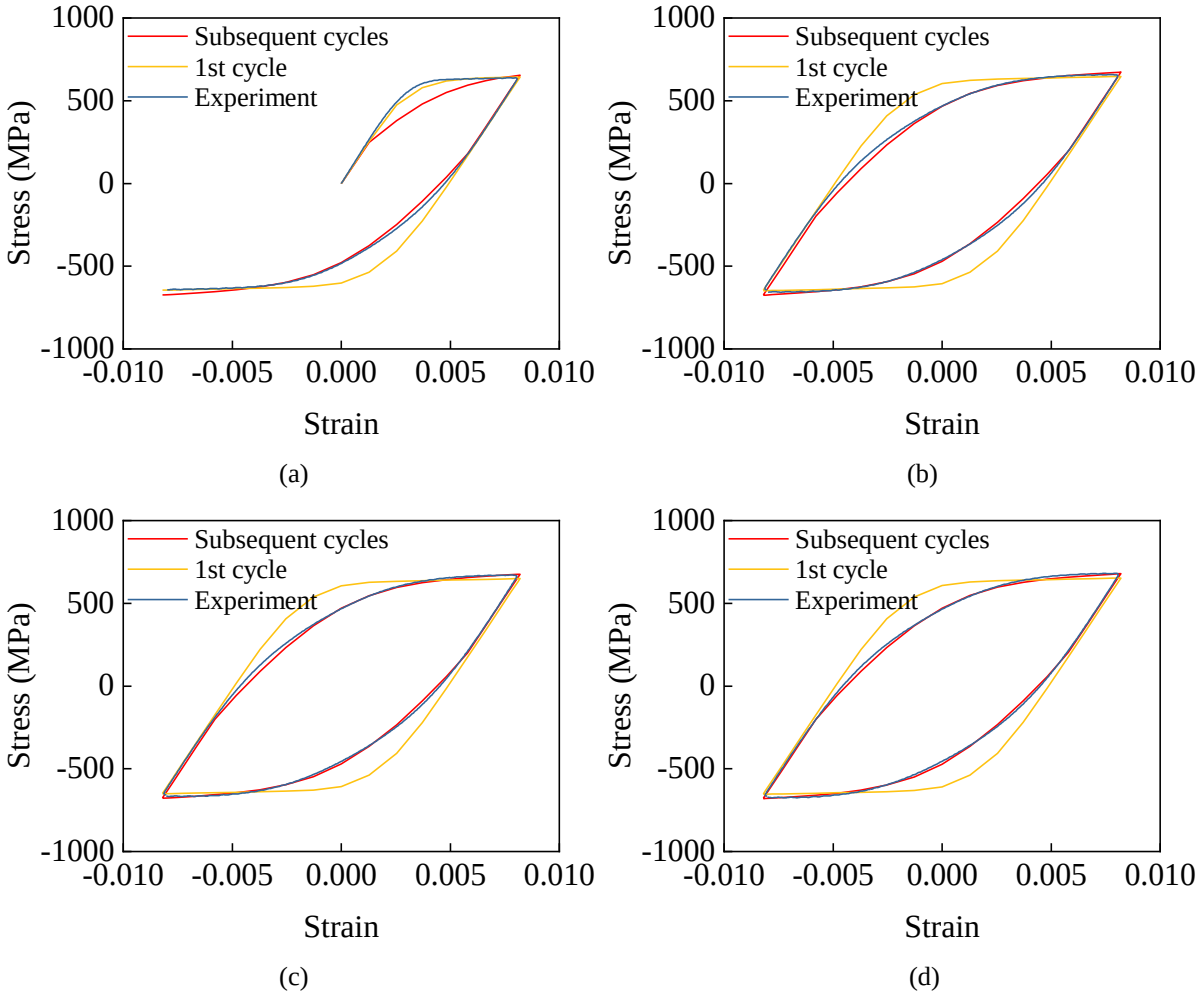

Fig.3-17 Cyclic stress strain curves of finite element simulation and experiment (a) 1st cycle, (b) 2nd cycle, (c) 3rd cycle, (d) 4th cycle (Yellow (1st cycle) corresponds to simulations with Group 1 parameters and red (subsequent cycles) to simulations with Group 2 parameters).

3.6.3. Indentation simulation with identified behavior parameters

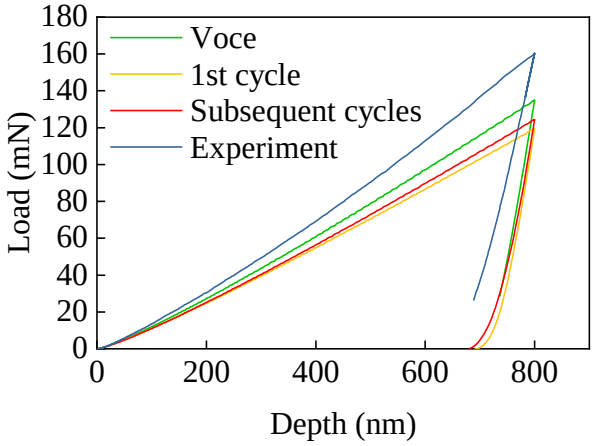

Fig.3-18 The experimental and simulated *P-h* curves. Voce is taken from the monotonic curve.

Nanoindentation simulations were performed using the identified material constitutive behavior parameters, which are Voce parameters shown in Section 3.6.1 and two groups of the combined hardening parameters (called 1st cycle and Subsequent cycles) shown in Section

3.6.2. The indentation depth was 800 nm, and the spherical indenter radius was 10 μm. The *P-h* curves are shown in Fig.3-18. The experimental curve is the average of the data obtained at the distance of 1000 μm from the shot-peened surface.

The parameters of the following cycles have a higher P_{max} value than the parameters of the 1st cycle. Besides, the Voce parameters have the maximum P_{max} value. However, regardless of which constitutive models is used, the Voce parameters or the combined hardening parameters, their *P-h* curves show a significant difference with the experiment. The indentation responses of simulation and experiment are shown in Tab.3-5.

Tab.3-5 Indentation responses with different constitutive behavior parameters

Response	1st cycle	Subsequent cycles	Voce	Experiment
P_{max} (mN)	119.3	124.5	135.0	160.3±7.8
S (mN/nm)	1.83	1.80	1.82	1.62±0.08

3.7. Optimizing the simulation parameters

3.7.1. The possible reasons for the difference between simulation and experiment

Noticing a significant difference in the *P-h* curves between the simulation and experiment, it is evident that some factors were not properly considered. The possible reasons for this discrepancy are listed below.

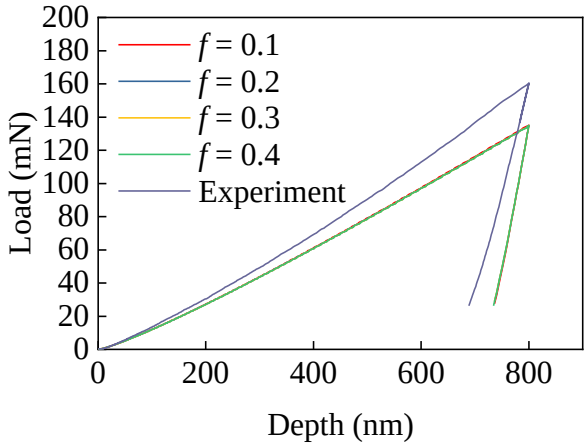

Fig.3-19 The *P-h* curves with different friction coefficients (the radius of the indenter is 10 μm)

The first possible reason is the friction coefficient *f*. The friction coefficient used in our study was chosen as the reference friction value between the diamond and the metallic materials taken from the literature, which are usually obtained with the conventional sliding friction experiments. The friction coefficient in practical indentation process may be different from the reference value. It has been presented in the literature that the friction coefficient affects the hardness [113] or the maximum load [114], and cannot be neglected. However, according to other studies [115-117], the friction coefficient affects the pile-up, which refers to the profile of the crater, but has only a slight effect on the maximum load and the *P-h* curve. The literature presents varying results, indicating that the effect may be dependent on the constitutive behaviors of the material and the surface preparation or microroughness. The *P-h* curves of the

simulations using identified Voce parameter are shown in Fig.3-19. The effect of *f* is quite small and cannot explain the significant difference between the simulated and experimental curves.

The second possible reason is the material parameters that were identified from the monotonic tensile test and the cyclic test may not be able to represent the behavior in indentation test. During indentation process, the indenter was controlled to compress and penetrate the target surface, which makes the material beneath the indenter undergo a multiaxial path. The Voce parameters, identified on a uniaxial tensile test, may not accurately describe the non-proportional loading that occurs during the indentation process. In addition, the identified combined hardening parameters may be overly focused on changes in the yield surface during cyclic loading. However, the material undergoes very few cycles during nanoindentation, for some region even less than 1 full cycle. Moreover, the representative strain, for indentation test of depth 800 nm, as calculated using Eq.2-14, is around 0.12. The Voce parameters from the monotonic curve were identified on a large plastic strain range, which is 0-0.3. Conversely, the kinematic components of the combined hardening parameters from cyclic curves were identified on a relatively small plastic range, which are around 0-0.005 for group 1 and 0.015-0.025 for group 2 respectively. The experimental representative strain was not included in the fitting range.

The third possible reason is the scale effect. Previous literature indicated that the material behavior under non-uniform plastic deformation on order of micrometers differs from the behavior under macroscopic scale deformation [118][119]. This can also be observed in nanoindentation tests while the material hardness increases when the indentation depth is in order of submicrometers [120][121]. This phenomenon is considered to be influenced by GNDs, which is related to the gradients of plastic shear in a material. However, this phenomenon is not the field to be focused on in this thesis. For the deeper investigation on the difference between simulation and experimental curve caused by this phenomenon could be performed in the future.

As mentioned above, neither the Voce parameters nor the combined hardening parameters (group 1 and group 2) cannot reproduce the experimental *P-h* curve. In addition, the effect of friction coefficient *f* on indentation responses can be neglected. Therefore, the material constitutive behavior parameters can be the main factor in optimizing simulation responses. In our study, the inverse analysis was applied to optimize the material parameters.

3.7.2. The constitutive behavior model selection strategy

To optimize material parameters, it is necessary to select the correct constitutive behavior model that describes as accurately as possible our indentation tests. As discussed in Chapter 2, our study used the combined hardening behavior. However, the choice of this constitutive model requires consideration of several factors, including the amount of kinematic components and the limitation of parameters for each kinematic component. Typically, 2 or 3 kinematic components are used to describe fatigue test behaviors, but it is unclear how many are needed for indentation. Additionally, determining the limitations of C and γ for each

kinematic component is not easy, making optimization more complex to find the feasible solutions and avoid multiple solutions.

Previous research [122] proposed a computation method and hypothesis to obtain the combined hardening rule with 1 kinematic hardening component by supposing that $b = \gamma$. Following this assumption, the uniaxial stress-strain relation could be described as:

$$\sigma = \sigma_y + Q\left(1 - e^{-b\varepsilon_p}\right) + \frac{C}{b}\left(1 - e^{-b\varepsilon_p}\right)$$
$$= \sigma_y + \left(Q + \frac{C}{b}\right)\left(1 - e^{-b\varepsilon_p}\right)$$

Thus, the stress calculated using the combined hardening equation is equivalent to the stress calculated using Voce parameters. This provides a possible range of parameters to be selected in optimization. In summary, 5 material parameters were selected to optimize: E, σ_y, Q, C and b.

3.7.3. Inverse analysis technique

The inverse analysis technique is a mature method for identifying model parameters. The model parameters are optimized by minimizing the objective functions using numerical optimization algorithms. The inverse analysis technique is widely used for identifying material constitutive behavior parameters during indentation process [122-123].

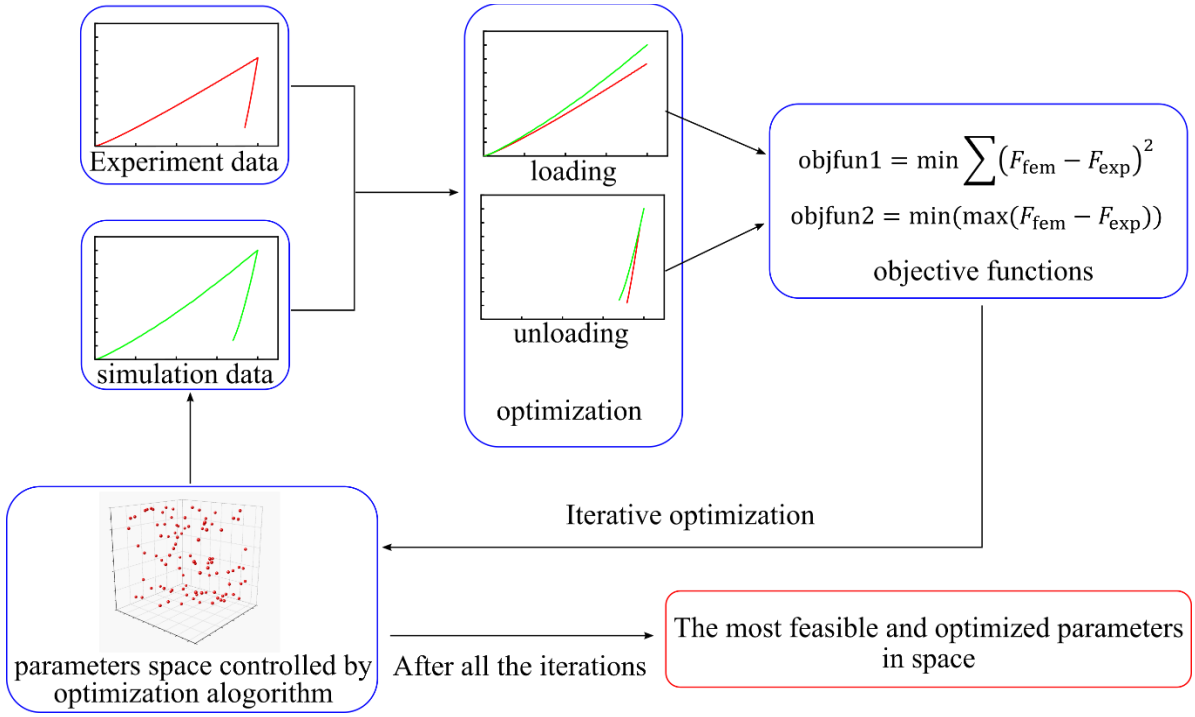

Fig.3-20 The scheme of the inverse optimization process

In this study, the inverse analysis technique is performed with the optimization software Isight®. Isight can easily read and revise the ABAQUS input files or result files thanks to its powerful data interface. The scheme of the inverse optimization process performed in the present study is shown in Fig.3-20. The optimization focused on the loading and unloading processes separately. The aim was to minimize the sum of squares of the differences and the

maximum difference between experiment curve and simulation curve for each process. Therefore, 4 objective functions were applied in total.

The optimized parameters and their possible ranges are shown in Tab.3-6. Non-dominated Sorting Genetic Algorithm (NSGA-II) was used for optimization to find the most feasible and optimal parameter. NSGA-II is a multi-objective optimization algorithm that is well-suited for highly non-linear design spaces. A population size of 12 and runs for 20 generations with a crossover probability of 0.9 was applied in optimization.

Tab.3-6 The range of the optimized parameters

Optimized parameters	Range
E (MPa)	180000-210000
σ_y (MPa)	600-900
Q (MPa)	0-2000
C (MPa)	0-15000
b	0-5

Fig.3-21 show the correlation chart of the optimized parameters and the 4 objective functions.

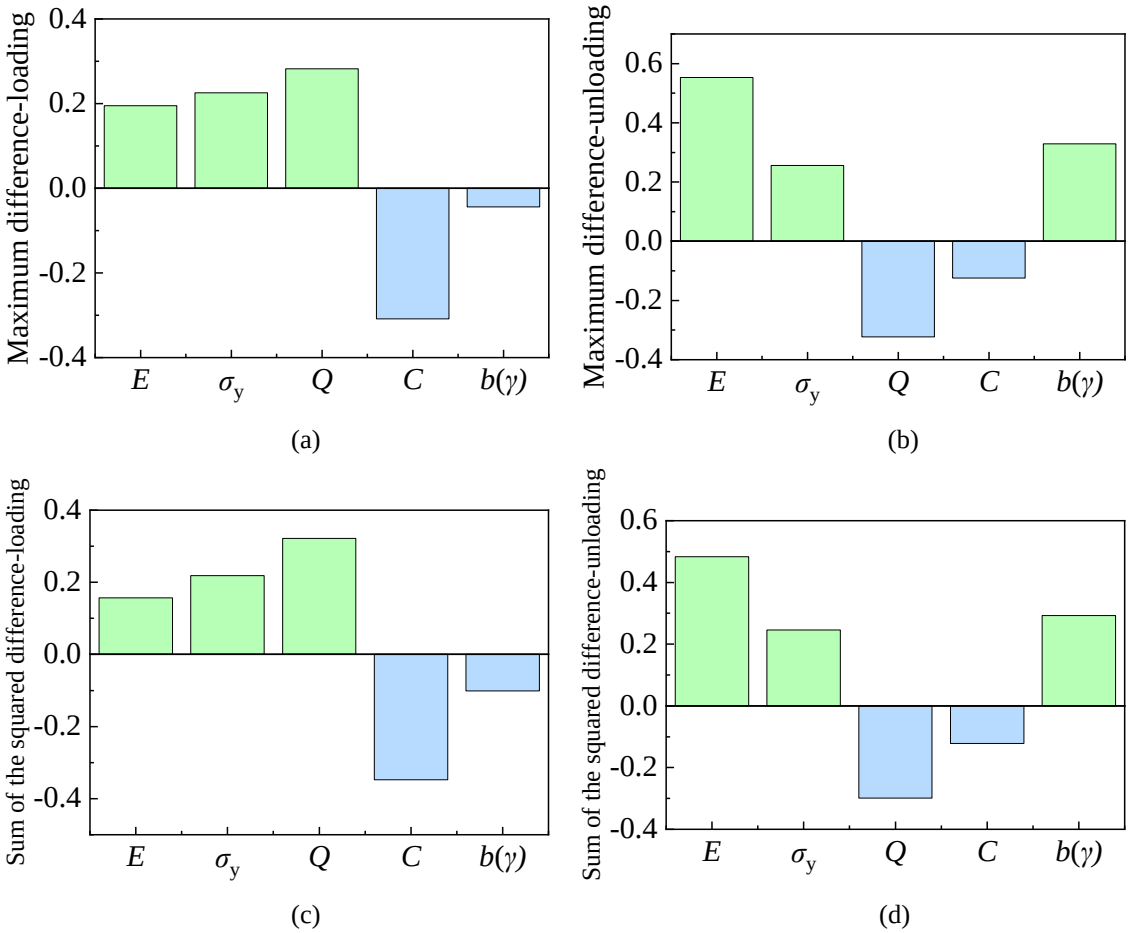

Fig.3-21 The correlation chart of the optimized parameters and (a) The maximum difference-loading (b) The maximum difference-unloading (c) The sum of squared difference-loading (d) The sum of squared difference-unloading

In the loading process, there is a positive correlation between E, σ_y and Q and the objective functions, and there is a negative correlation between C and b and the objective function. However, in unloading process, E, σ_y, and b have a positive correlation with the objective functions, while Q and C have a negative correlation with the objective functions.

The optimization history is shown in Fig.3-22. The #211 optimization provides the most feasible and optimal parameters.

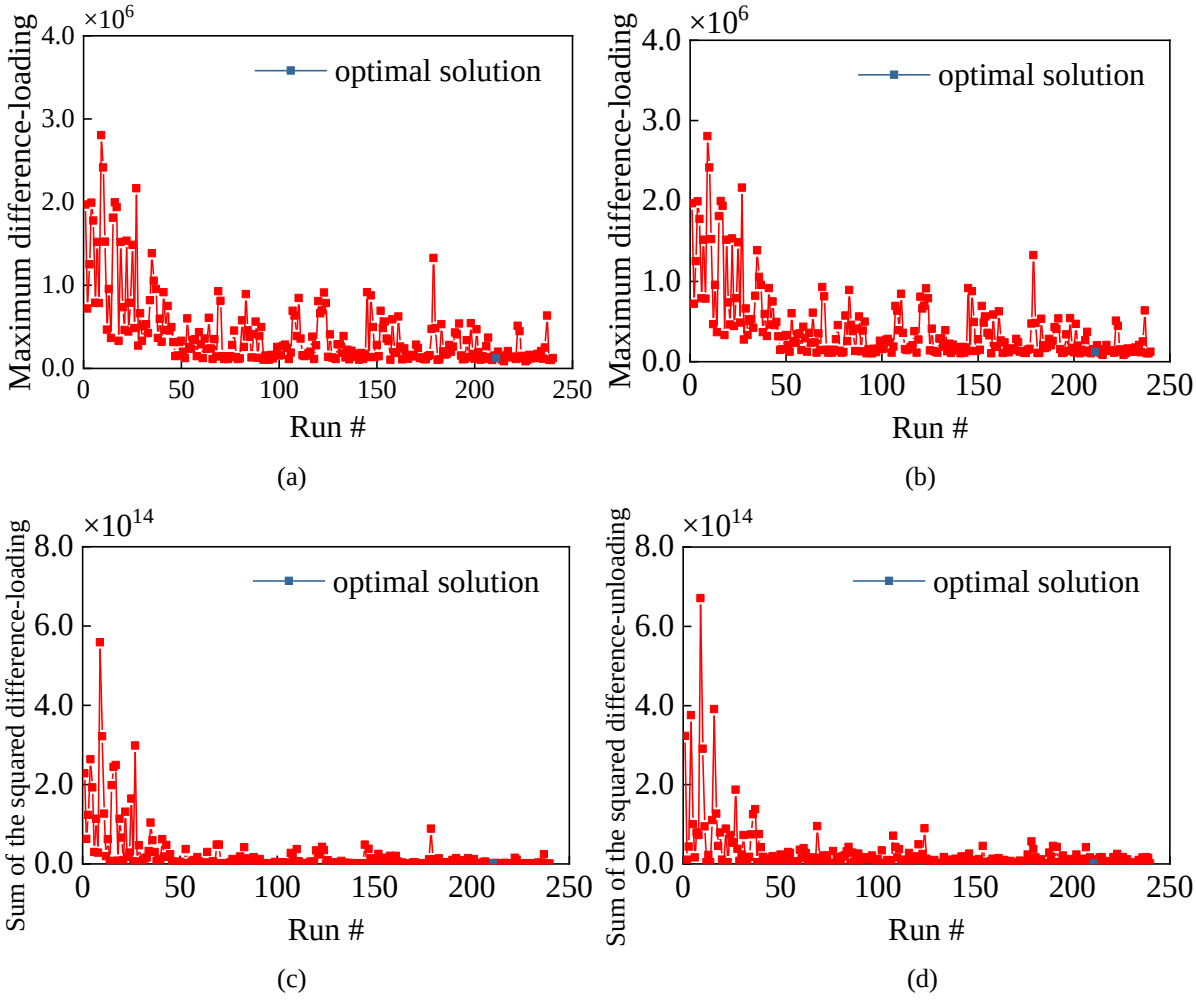

Fig.3-22 The optimization history of (a) The maximum difference-loading (b) The maximum difference-unloading (c) The sum of squared difference-loading (d) The sum of squared difference-unloading

The optimized parameters are shown in Tab.3-7.

Tab.3-7 The optimized parameters

Optimized parameters	The optimized result
E (MPa)	181942
σ_y (MPa)	673
Q (MPa)	818
C (MPa)	11299
b	2.64

The *P-h* curves with the initial Voce parameter, the optimized parameters and experiment are shown in Fig.3-23. It can be seen that the *P-h* curve with the optimized

parameters is close to the experiment curve and the indentation responses are shown in Tab.3-8.

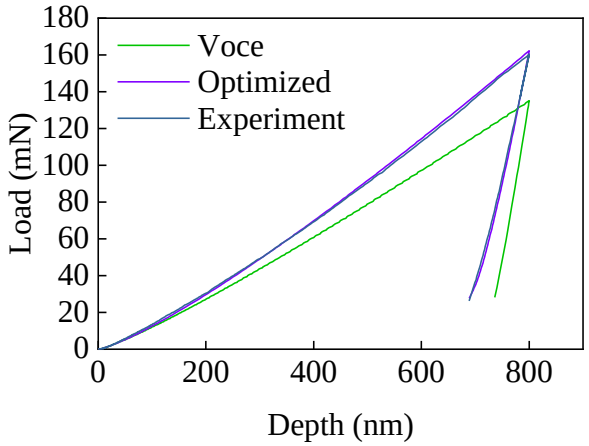

Fig.3-23 The *P-h* curves with the initial Voce parameter, the optimized parameters and experiment

After optimization, P_{max} fits the experiment well. However, *S* is still outside the range of the experimental values. It has been shown that the key parameters we used to build the function of the method presented in Chapter 2 are the normalized responses, which means that the evolution with depth of the responses is more important than the value itself. Thus, the difference on *S* value could be accepted in practice.

Tab.3-8 Indentation responses with optimized parameters

Response	1st cycle	Subsequent cycles	Voce	Optimized	Experiment
P_{max} (mN)	119.3	124.5	135.0	162.2	160.3±7.8
S (mN/nm)	1.83	1.80	1.82	1.73	1.62±0.08

3.7.4. The examination and analysis on rationality of the optimal parameters

Fig.3-24 shows the true stress-true strain curve for the monotonic simulation with the optimized parameters and the experimental monotonic tensile true stress-true strain curve obtained from the tensile test. It can be seen that there is no significant difference between the curves in the elastic range, but an important gap is observed in the plastic range.

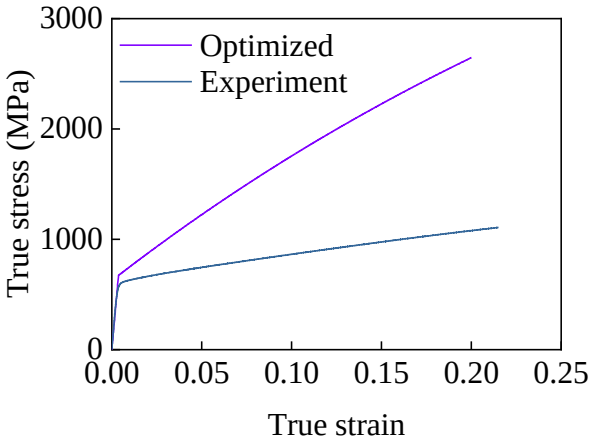

Fig.3-24 The experiment and simulated monotonic true stress-true strain curve

The possible reasons and explanations are listed below. The first possible reason comes from the indenter. In our simulation, an ideally shaped spherical indenter was applied. However,

in practice, the surface of the indenter may be more like parabolic or elliptical than perfectly spherical, and the actual diameter may differ from the nominal diameter. A report from Zhu Yingying (internship report in LASMIS, 2019) shows that the measured radius of the indenter with scanning electron microscope (SEM) is around 9.8-11.15 μm (nominal diameter 10 μm). The simulated *P-h* curves with the radius of 9.8 μm and 11.2 μm are shown in Fig.3-25.

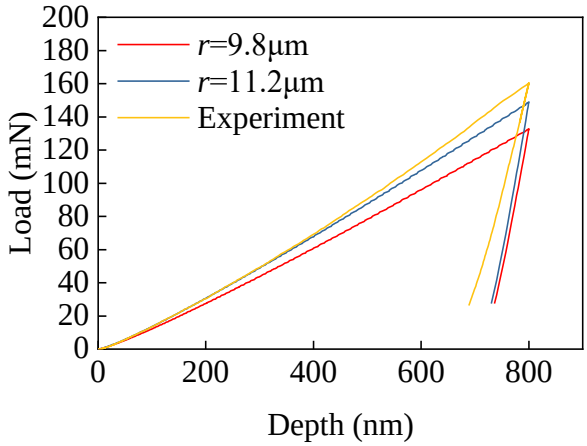

Fig.3-25 The simulated *P-h* curves with different indenter radius, using Voce parameters shown in Section 3.6.1

It could be seen that a higher radius results in a higher P_{max}. The simulated P_{max} considering the variation of indenter radius falls within the range of 132 mN to 149 mN (For the nominal diameter indenter used now, P_{max} equals to 135 mN). The simulated *P-h* curve closely matches the experimental results with a high radius indenter. However, there is still a 7% discrepancy with the experimental value of 160 mN, indicating that the material parameters should also be optimized, suggesting that the material parameters need further optimization. It is possible that the optimal material parameters in this case are closer to the initial parameters, resulting in a smaller difference on the monotonic true stress-true strain curve.

The second possible reason could be the material properties. Tension-compression asymmetry has been widely observed on the nickel-based alloys, especially on single crystal alloys [124-127]. For nickel-based alloys, which have face-centered cubic structure, the deformation mechanism is slip. Two phases are generally present in nickel-based alloys: the γ phase and the γ' phase. The incompatibilities between two phases are constructed during the initial loading process and subsequently influence the yield when the loading is reversed, which is a possible reason for the tension-compression asymmetry [127]. For the polycrystalline nickel-based alloys (i.e. the material in our study), the deformation mechanisms are often more complex and can vary depending on the factors such as temperature and grain boundaries. No matter for the aged nickel-based alloy [128] or the additive manufactured nickel-based alloy [129], the asymmetry of tension-compression stress was observed. The difference of the yield strength varies from 3.5% to 5% at the room temperature and to 11% at high temperature (A positive values means that the compression yield stress is higher than the tensile yield stress). Up to now, the research on the tensile-compressive asymmetry of polycrystalline nickel-based alloys is still limited. Thoroughly understanding the asymmetry is a significant challenge, which is far out of the range of our study. Although the difference presented in the literature is smaller

than in our case (19%), and the reasons for the differences in the plastic regime after yield are not clear, the asymmetry still indicates a direction to explain the difference.

The third possible reason could be the strategy of the selection of the constitutive behavior model. It was assumed that $b = \gamma$ in this case, indicating that the evolution of kinematic hardening is the same as that of isotropic hardening with cumulative plastic strain. However, the equivalent plastic deformation of a material with combined hardening behavior has not yet been proposed in the literature due to the complex stress field under the indenter during the test. Thus, the assumption that b equals γ is not physically supported [75], it is a convenient phenomenological way to reduce the size of the solution space. However, as mentioned above, the possible range and amount of each C and γ for the kinematic components are unclear. Therefore, this is the best way to apply parameter optimization to the combined hardening rule in indentation simulation. In practice, the evolution of kinematic hardening and isotropic hardening may differ from each other. Therefore, the assumption of $b = \gamma$ may explain the difference on monotonic true stress-true strain curves.

Overall, it is difficult to fully explain the discrepancy between the experiment monotonic true stress-true strain curve and the curve simulated using the optimized parameters. However, we have listed here the possible reasons that could explain these results.

Despite the unresolved questions, we have decided to proceed with our demonstration of the use of the indentation technique to determine the residual stresses and work hardening in the material after shot peening. The optimized parameters will then be employed in the subsequent sections.

3.8. Application of the Response surface function method in practice

3.8.1. The indentation simulations with the optimized parameters

Similar to the process presented in Chapter 2, in order to apply the Response surface function method, a series of nanoindentation simulations with the optimized material constitutive behavior parameters were performed with the indentation depth of 800 nm. The levels of cumulative plastic strain introduced in the model are 0%, 10%, 20% and 30% respectively. The levels of residual stress are 0 MPa, -200 MPa, -400 MPa, -600 MPa and $-\sigma_{yc}$. Similarly, σ_{yc} represents the yield stress for each imposed cumulative plastic strain level, calculated using Eq.2-9. The contours of normalized parameters are shown in Fig.3-26. In which the normalized hardness is still calculated with normalized P_{max} and S, as shown in Eq.2-26.

It is evident in Fig.3-26 that, unlike Fig.2-19 of chapter 2, the normalized P_{max} increases as the cumulative plastic strain increases due to the positive Q in our optimized parameters. Normalized P_{max} appears more influenced by cumulative plastic strain than residual stress. The normalized S increases with increasing compressive residual stress but decreases with increasing cumulative plastic strain. Additionally, the normalized S is equally influenced by residual stress and cumulative plastic strain. As the normalized H is calculated with Eq.2-26, it

is strongly affected by cumulative plastic strain and very little by residual stress. Moreover, the material with an introduced mechanical field exhibits a variation of approximately 36% in normalized P_{max} and 43% in normalized H, compared to the material without an initial mechanical state (raw material). However, the normalized S is not sensitive to the mechanical fields, as it only varies between -7% and 4%. Also, that the trends of three normalized parameters are different, which means that it can be used for the characterization of the mechanical state after shot peening.

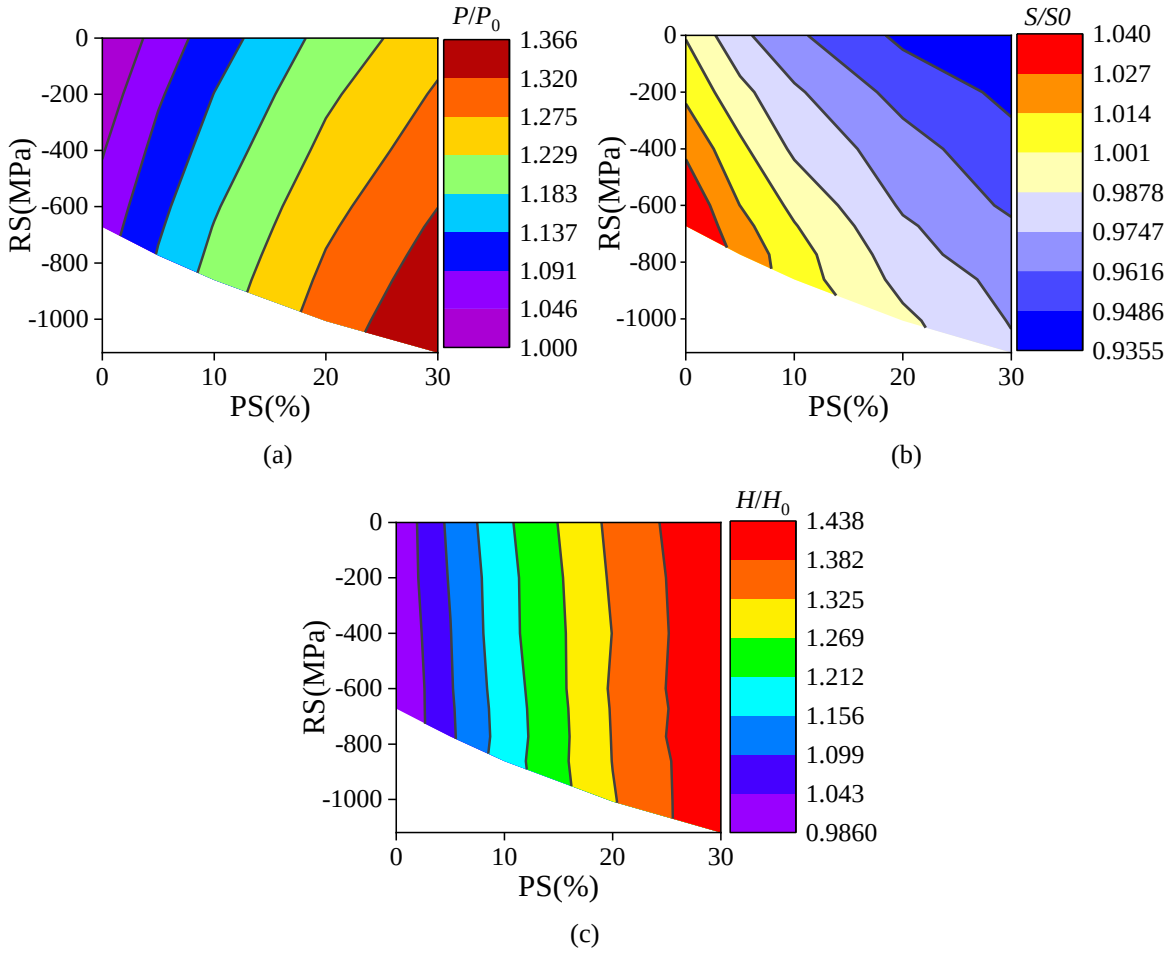

Fig.3-26 The contour of (a) P_{max}/P_{0max} (b) S/S_0 (c) H/H_0

The response surfaces of P_{max}/P_{0max}, S/S_0 and H/H_0 are shown in Fig.3-27 respectively. The second order polynomial was used to fit the response surface functions.

The surface functions are listed as follows:

$$\frac{P_{\max}}{P_{0\max}} = 1.00171 + 0.01267x - 0.000138564x^2 - 0.000112724y$$
$$-7.52444 \times 10^{-8}xy - 1.63435 \times 10^{-8}y^2$$

$$\frac{S}{S_0} = 0.99828 - 0.00394x + 0.0000626353x^2 - 0.000066448y$$
$$+6.91076 \times 10^{-7}xy - 8.45015 \times 10^{-9}y^2$$

$$\frac{H}{H_0} = 1.00652 + 0.02133x - 0.000233927x^2 + 0.00003031y$$
$$-7.07545 \times 10^{-7}xy + 3.12329 \times 10^{-9}y^2$$

The surface functions represent the normalized responses under different residual stress and cumulative plastic strain state. In these functions, the independent variables x and y, respectively represent cumulative plastic strain and residual stress.

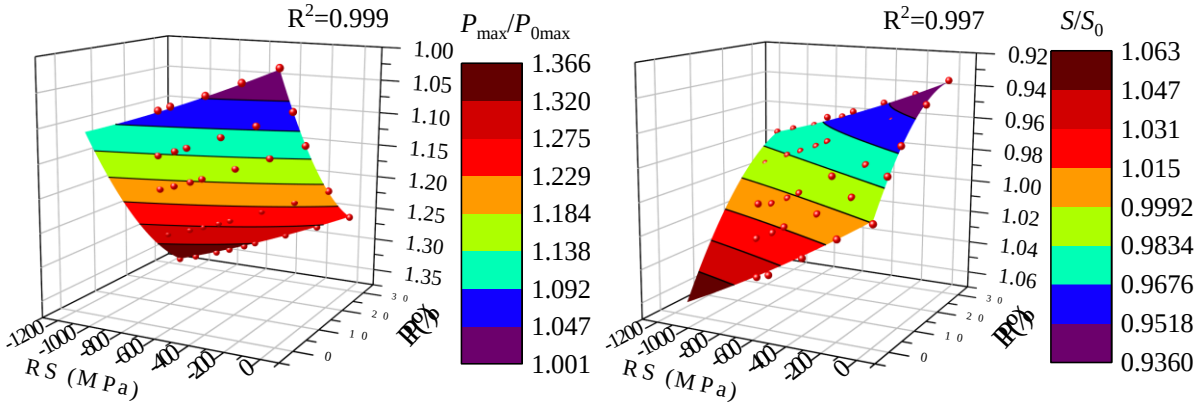

(a)

(b)

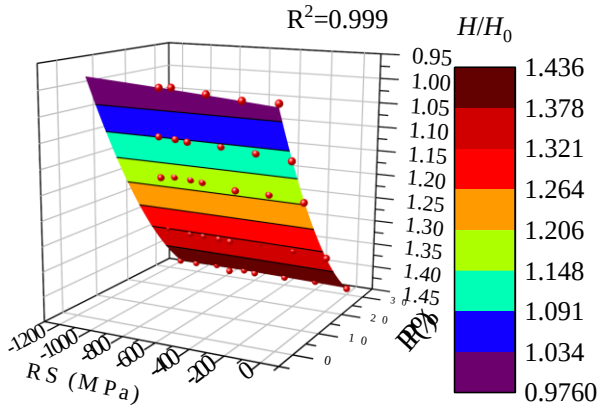

(c)

Fig.3-27 The response surface of (a) P_{max}/P_{0max} (b) S/S_0 (c) H/H_0

3.8.2. Application of Response surface function method

Once the response surface functions are obtained, the experiment residual stress and cumulative plastic strain profile can be solved with two of these three functions using the experimental indentation normalized responses shown in Fig.3-12. The determined residual stress profile and cumulative plastic strain profile are shown in Fig.3-28. When solving the equations, the solution range was limited to the following parameters: residual stress ranging from -1119 MPa to 0 MPa, and cumulative plastic strain ranging from 0% to 30%. When the solution for cumulative strain tends to be negative, x is replaced by 0 in the equations, which means no cumulative plastic strain exists at this position. This allows the residual stress profile beyond 160 μm to be solved.

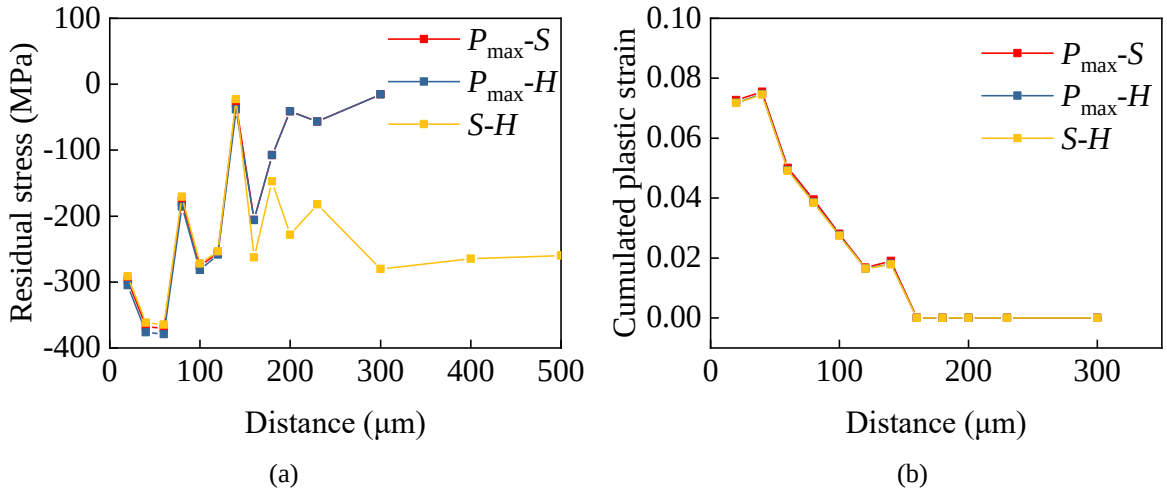

(a) (b)

Fig.3-28 The solved profiles of (a) Residual stress (b) Cumulative plastic strain with different combinations of equations

It can be seen that the solved profiles are reasonable for a shot peened sample. All the three combinations lead to a similar profile, except for the residual stress profile beyond 200 μm.

When the distance exceeds 200 μm, the cumulative plastic strain is zero, indicating that the residual stress profile is obtained by a single equation. The combination of S-H uses $f(S/S_0)$ to calculate residual stress, while the other two combinations use $f(P_{max}/P_{0max})$. It is clear that the profile obtained with $f(P_{max}/P_{0max})$ is more reasonable because P_{max} is a direct variable from the experiment, whereas H are indirect variable. In the following, only the profile solved from the combination P_{max}-S is used.

The residual stress profiles between 100 μm and 200 μm exhibit an oscillatory pattern. This also reflects the fact that nanoindentation is an extremely localized testing technique that is quite easy to be affected by localized material properties or mechanical state, even though it is an average of 20 tests.

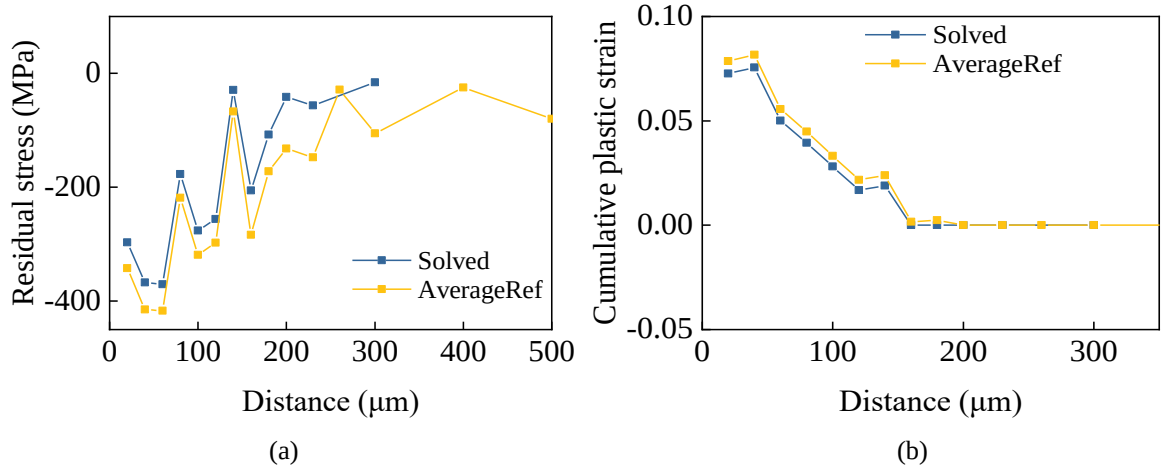

(a) (b)

Fig.3-29 The profiles solved with reference values taken at 1000 μm depth (blue) and with reference values averaged at several depth (yellow) for (a) Residual stress (b) Cumulative plastic strain

The reference state, e.g. the reference P_{0max}, S_0, and H_0 are not known a priori. In the previous attempt, the values at a depth of 1000 μm were chosen. However, as the values above

500 µm are quite stable, the average of the values at 600 µm, 800 µm, and 1000 µm can also be used as reference values. The result can be seen in Fig.3-29.

However, it appears that the revised profile has not changed significantly. It can also be seen that the solved profiles exhibit strong oscillations, especially for residual stresses. To reduce these oscillations it is possible to smooth the experimental responses (P_{max} and S). The original and smoothed P_{max} and S along the depth are shown in Fig.3-30. To prevent distortion, the first value closest to the shot peened surface was not smoothed. The data was smoothed using the 'Lowess' (locally weighted scatterplot smoothing) method [130].

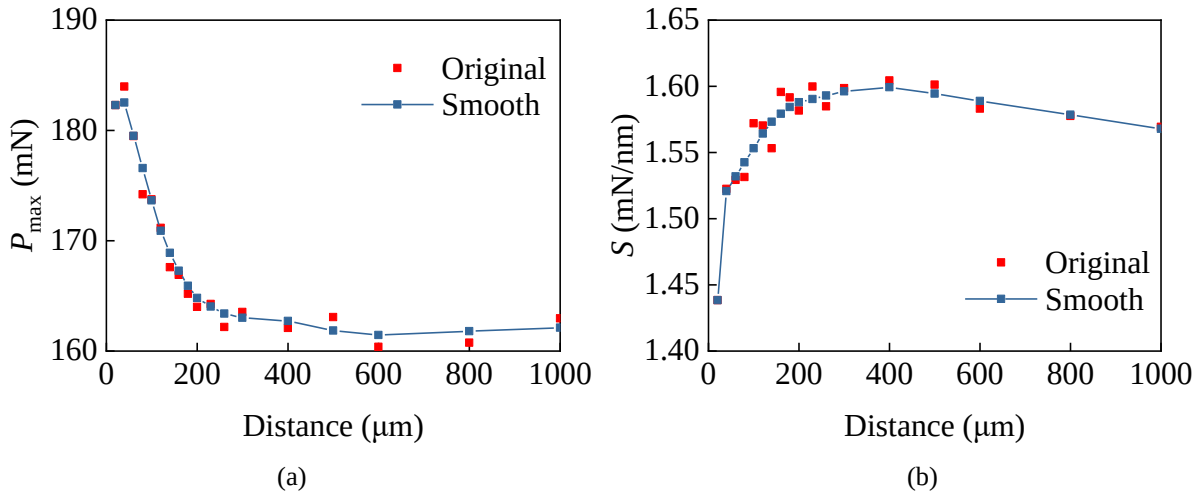

Fig.3-30 Smoothed data of (a) P_{max} (b) S

Based on the smoothed normalized responses, the revised solved profiles are shown in Fig.3-31. It can be seen that, after data smoothing, there is not longer significant oscillation in the solved profile.

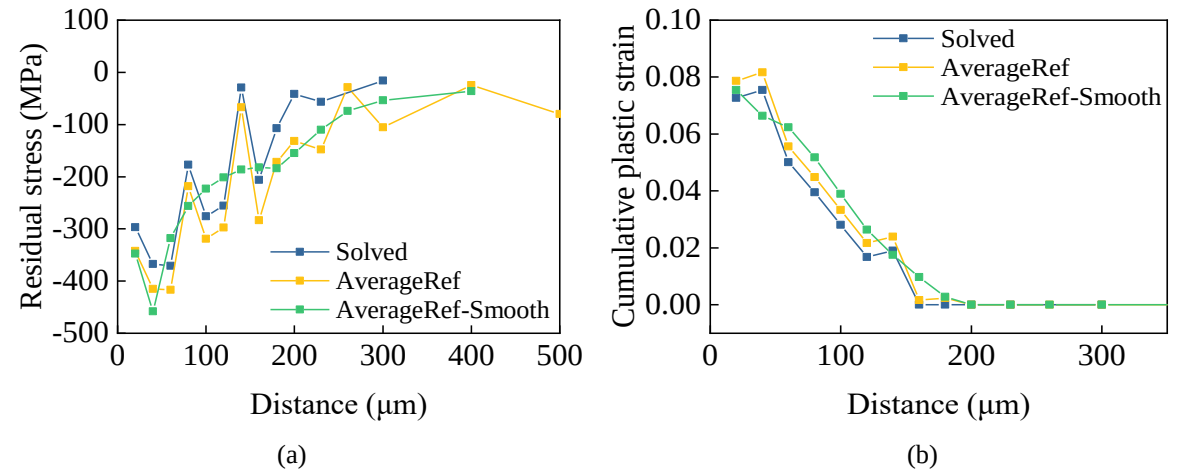

Fig.3-31 The revised solved profiles of (a) Residual stress (b) Cumulative plastic strain after smooth

The comparison of solved profiles and experimental profiles obtained from XRD are shown in Fig.3-32. The solved profile based on the smoothed normalized responses is called profile from nanoindentation technique in the following. The indentation profiles have the same trend as the diffraction profiles. However, there is a significant difference on values.

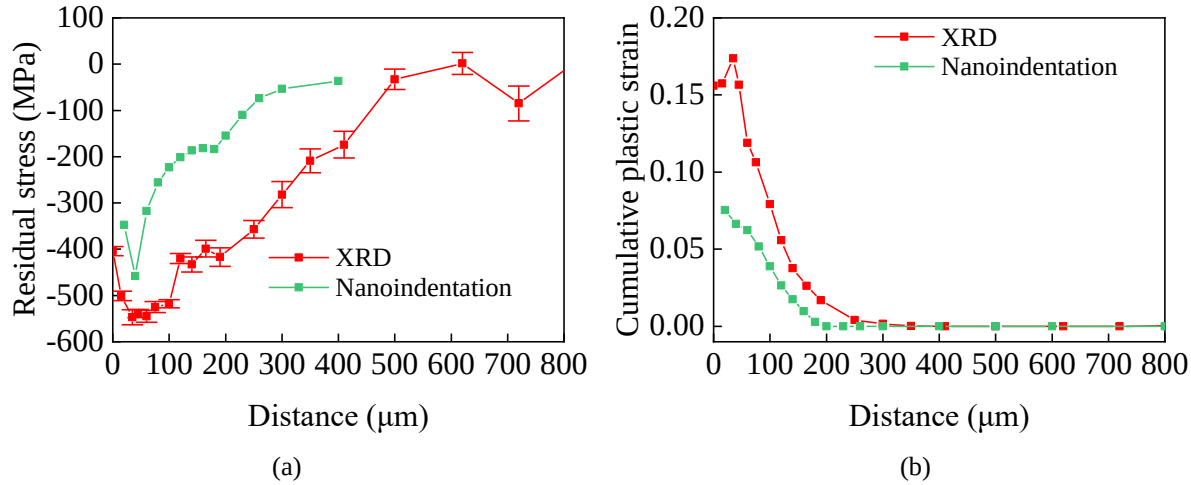

Fig.3-32 The comparison of solved and XRD profiles (a) Residual stress (b) Cumulative plastic strain

As presented in Chapter 2, the Response surface function method is easily affected by perturbations of the input normalized responses. Therefore, the difference in the figure may be due to the dispersions. Consequently, we take the values of residual stress and cumulative plastic strain measured by X-ray diffraction as the known variables and put them in the response surface functions to calculate the normalized responses, which we call inverse simulation responses here.

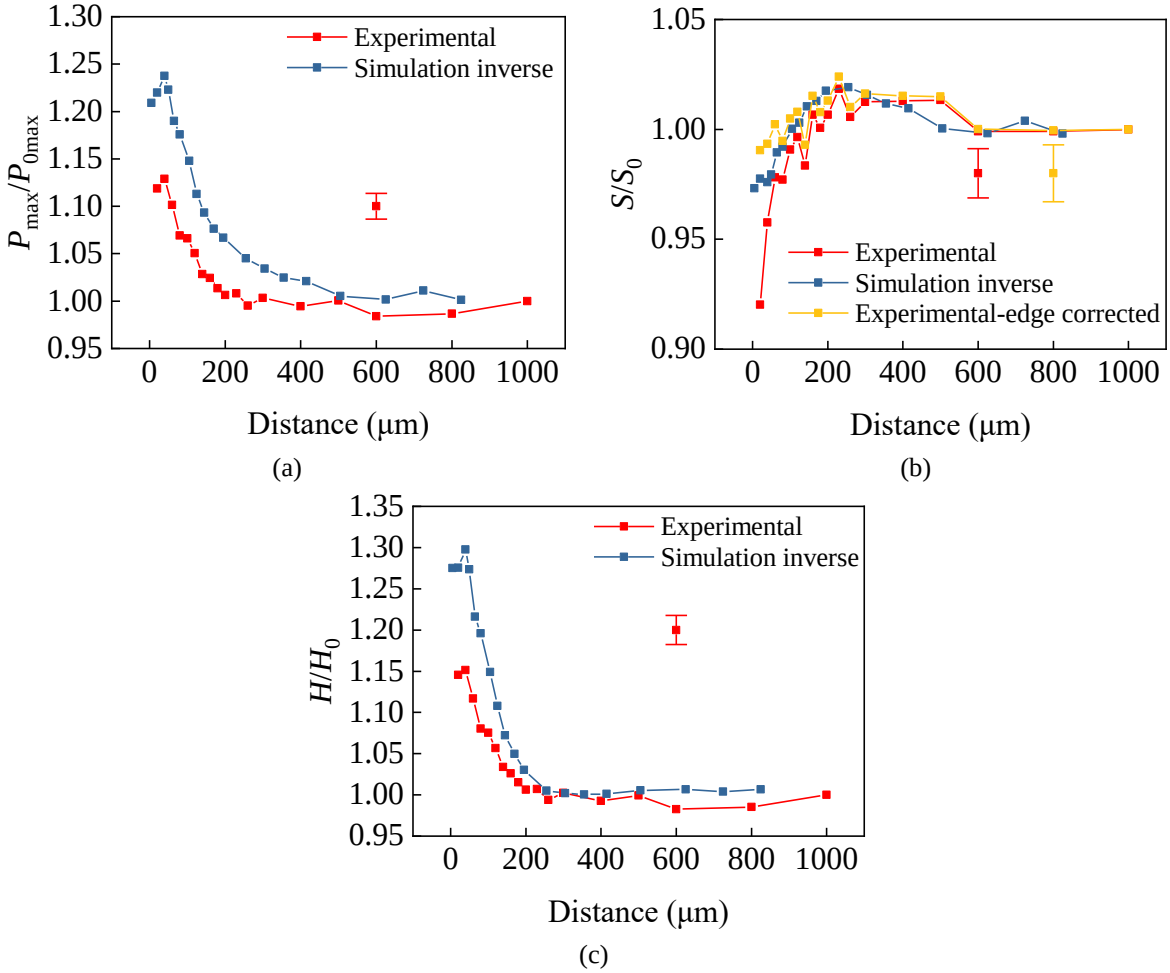

Fig.3-33 The comparison of experimental and inverse simulation normalized responses (a) P_{max}/P_{0max} (b) S/S_0 (c) H/H_0

The comparison between the simulation inverse curves and the experimental curves are shown in Fig.3-33. The differences shown in Fig.3-33 are out of the range of dispersion, which indicates the difference shown in Fig.3-32 is caused by other reason. The possible reasons are listed below.

The first possible reason for the difference between the two methods could be the effect of layer removal. The residual stress profile measured by XRD, as shown in the figure, does not account for the layer removal effect. However, due to the material removal, the residual stress state is re-equilibrated each time. Fig.3-33 below shows the comparison of the solved profile with the corrected experiment residual profile considering layer removal. The correction for layer removal is based on the eigenstrain theory, which assumes that the eigenstrain was not affected by the removal of the layer. The eigenstrain profile is described by a Gaussian function up to a depth of 625 μm and is equal to 0 beyond the distance. Fig.3-34 shows the fitted residual stress curve that obeys the equilibrium conditions. The corrected residual stress, taking into account the electrolytic polishing, is represented by the yellow line. The correction was made under the assumption that the entire surface layer had been removed. However, the removal was limited to a specific area, as shown in Fig.3-5. Therefore, the actual effects of the removal are smaller than what is depicted in Fig.3-34. However, there is still a significant difference between residual stress profile obtained from the XRD corrected result and nanoindentation.

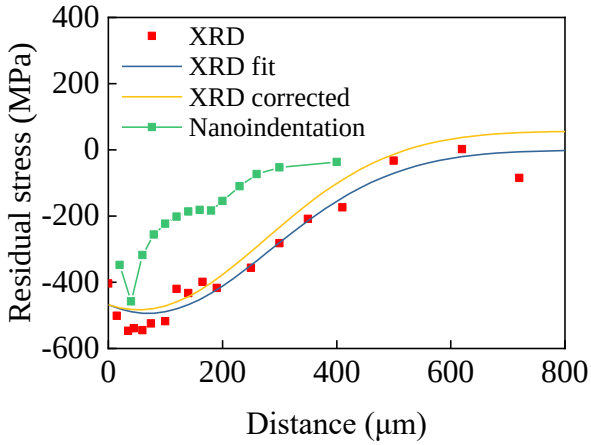

Fig.3-34 The comparison of solved and corrected experiment residual stress profile

The second possible reason for the difference between the nanoindentation and XRD residual stress profiles could be the stress relaxation discussed in Section 2.4. The cutting process not only releases residual stress perpendicular to the cross section, but also releases some of the σ_{xx} component that we try to obtain (about 25% for the maximum compressive residual stress, simulated with the given stress profile shown in Section 2.4). Although the stress profile is not identical to that observed in the experiment, this provides a reasonable explanation for the observed difference. In addition, it also can be seen in Section 2.4 that after cutting process, a $\Delta\sigma_{zz}$ component appears. The trace of the stress tensor after cutting is not simply σ_{xx}; rather, it is the sum of $\Delta\sigma_{zz}$ and the relaxed σ_{xx} i.e. $\sigma_{xx} + \Delta\sigma_{xx}$, which results in a different hydrostatic stress state. The further influence of the different hydrostatic stress state after cutting

process can be investigated in a future study.

Regarding the cumulative plastic strain profile, the difference could be due to sample preparation. As stated in Section 3.5.1, despite careful and precise polishing, the peak width is still 0.77°, which is wider than the peak width for the raw material, which is 0.6°. This indicates that some strain hardening may have been introduced to the sample. Seeing the calibration shown in Fig.3-6 and 3-7, the peak width 0.77° corresponds to a cumulative strain around 2%. If we shift the values by 2%, we obtain the corrected cumulative plastic strain profile shown in Fig.3-35.

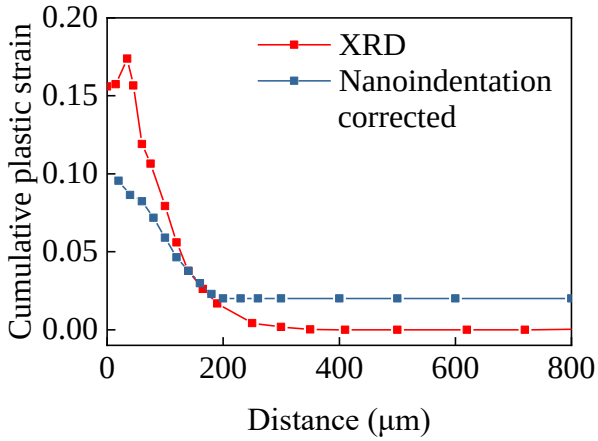

Fig.3-35 The comparison of solved and corrected experiment cumulative plastic strain profile

The corrected profile corresponds better with the experimental curve at a distance of around 150-200 μm. However, a significant difference still exists in the layers near the shot peened surface.

Another possible reason could be the deformation mechanism. The experimental cumulative plastic strain profile is simply a correlation between peak width and monotonic tensile plastic deformation. However, the plastic deformation in the shot peening process is more complex, involving mostly compressive and cyclic loading paths which are non proportional. The deformation state is illustrated in Fig.2-15. Therefore, the cumulative plastic strain profile calibrated from the monotonic uniaxial tensile test may not accurately reflect the conditions in the shot peening process.

As the analysis shown in Section 3.7.4, the selected constitutive behavior may lead to a difference between the monotonic true stress-true strain curves of optimized parameters and experimental. In addition, the choice of constitutive behavior may also be a potential explanation for the observed differences in residual stress profile or cumulative plastic strain.

Considering the analysis in this chapter, it can be concluded that the constitutive behavior plays an important role in the Response surface function method. Both the link between the isotropic and kinematic components ($b = \gamma$) and the saturation behavior for the chosen parameters can influence the solved results. A further investigation can be conducted in the future research. As the spherical indenter is not a self-similar shape, the responses under the indentation tests with different indentation depth or different indenter radius correspond to different representative strain level. Thus, the inverse method can be applied using two more

experimental indentation curves, with different representative strain, as the reference. This may lead to a better optimization on the material constitutive behavior parameters.

3.9. Conclusion

In this chapter, we applied the Response surface function method to a real shot peened Inconel 625 alloy, and its quality and feasibility was verified.

Two pieces of Inconel 625 were shot peened, with one being measured by X-ray diffraction (XRD). The residual stresses were obtained from the diffraction peak displacement, while the cumulative plastic strain was obtained through calibration of the peak widths and a uniaxial tensile test. The results indicate that the maximum compressive residual stress is approximately -600 MPa, and the compressive residual stress can extend to a depth of 500 μm. Furthermore, the surface cumulative plastic strain is approximately 17%, and the influence depth can extend to around 300 μm.

Another shot peened sample was cut into four pieces and one of them was used to perform nanoindentation test on the cross section. Results show that P_{max} and H increase due to the combined effect of strain hardening and compressive residual stress. However, S shows a different trend. Then the stiffness is corrected by the edge effect and after correction, S tend to remain stable and is not significantly affected by shot peening. Furthermore, the indentation responses remain stable beyond 500 μm from the shot peened surface, which corresponds to the residual stress profile observed by XRD.

Voce hardening model and Combined hardening model were applied on indentation simulation. Two sets of material parameters were employed due to variations in material behavior between the subsequent cycles and the tensile section of the first cycle. Despite the use of the Voce hardening model and the two sets of material parameters, there was a notable difference between the simulation and experimental results. Thus, an inverse analysis technique was used to optimize the material parameters. The optimized parameters include only one kinematic hardening component. The optimized parameters exhibit a good fit on the experimental and simulated *P-h* curve. However, their behaviors on the monotonic tensile test differ significantly. The difference may be due to the indenter radius, asymmetry in tension and compression properties, or the selection strategy of the hardening model. However, considering all the possible reasons, we have decided to use the optimized parameters for the following research.

With the optimized material parameters, the Response surface function method was applied. The results indicate that the three combinations of normalized responses lead to a similar profile. The solved profile shows a clear gradient along the shot peening direction. However, there is a difference between the values solved with nanoindentation and the values measured by XRD and on the affected depth as well. This difference of residual stress could be due to stress relaxation during cutting and layer removal during electrolytic polishing. The difference of cumulative plastic strain may be attributed to surface hardening caused by polishing, as well as the different loading paths between the monotonic tensile test and shot

peening. Although the difference between the profile obtained by nanoindentation and X-ray diffraction still need to be investigated, our method still achieved a progress on characterization, and the method has demonstrated its feasibility, indicating its potential for practical applications.

To take a further view, there are some points to be noticed that could improve the accuracy of the data obtained by nanoindentation in future research. The first consideration is the material parameters. The constitutive behavior parameters will affect the simulation *P-h* curve directly, then they affect the determination of the kinematic hardening and the optimization. As demonstrated above, the loading paths during the indentation process resemble compression more than tension. Therefore, compression constitutive behavior parameters may be used for indentation simulation. The second aspect concerns the smoothing of the experimental indentation data. Smoothing can effectively reduce oscillations caused by localized properties fluctuations, but it can also lead to distortion. Therefore, the best smoothing method should be selected. In this research, the 'Lowess' method was used for smoothing, while in the future, other functions such as the Gaussian or exponential function could be considered. The third issue to be considered is the stress state after the cutting process. It can be observed that the residual stress component along the *x*-direction is relaxed, while the residual stress component along the *z*-direction appears. This leads to a quite different residual stress state in the area where performed the indentation tests. The actual stress state considering the relaxation and appearance should be investigated in the future.

Chapter 4

Mechanical properties characterization under cyclic and monotonic tensile test

Residual stresses and work hardening will undergo continuous changes throughout the entirety of the fatigue process. In particular, low cycle fatigue (LCF) will result in cyclic deformation reaching the plastic range at all times. Consequently, the investigation of the evolution of residual stresses and work hardening during the low cycle fatigue process becomes highly significant in the study of the application of shot peening for the improvement of fatigue resistance performance in materials.

Inconel 625 is a nickel-based alloy with good strength, ductility, corrosion resistance and high temperature performances. In addition, the additive manufacturing of Inconel 625 has been popular in material engineering field in the recent years. The additive manufacturing process, called Atomic Diffusion Additive Manufacturing (ADAM), proposed by Markforged®, is a new metal printing technique. It is therefore interesting to investigate the material properties of Inconel 625 printed by this process.

In this chapter, a series of monotonic tensile tests and strain controlled cyclic tests will be conducted on printed and commercial cold rolled Inconel 625 treated by two different shot peening times. The characterization of residual stresses and work hardening in the samples will be conducted by electron backscatter diffraction (EBSD), instrumented indentation, and X-ray diffraction techniques. These techniques can provide information on their evolution during the tests.

4.1. Material and sample condition

Our work investigates two types of Inconel 625: the cold rolled commercial alloy and the additively manufactured alloy. The state of the received commercial (Cold rolled, CR) alloy has been illustrated in Section 3.1. The state of the additively manufactured alloy (Printed by ADAM Process, MF) will be shown in the following.

4.1.1. The printed material

The additively manufactured Inconel 625 alloy was printed by Metal X™ System (Markforged, USA). The chemical composition is shown in Tab.4-1.

Tab.4-1 Chemical composition (wt. %) of the printed Inconel 625

C	Mn	Si	P	S	Co	Al	Ti	Fe	Ni	Mo	Cr	C
<0.1	<0.5	<0.5	<0.015	<0.015	<1	<0.4	<0.4	<5	Balance	8~10	20~23	<0.1

A round bar, which dimension is ϕ18 mm ×110 mm, was designed and the *.*stl* file was introduced in the Eiger® printing platform for slicing [131]. Two walls and *Solid Fill* were selected for the printing, without raft. The Post-Sintered Layer Height was 0.125 mm. In this case, the printing time for each sample is 4 h 41 mins. The samples were printed horizontally in order to optimize the strength in the loading direction.

The printing system is shown in Fig.4-1.

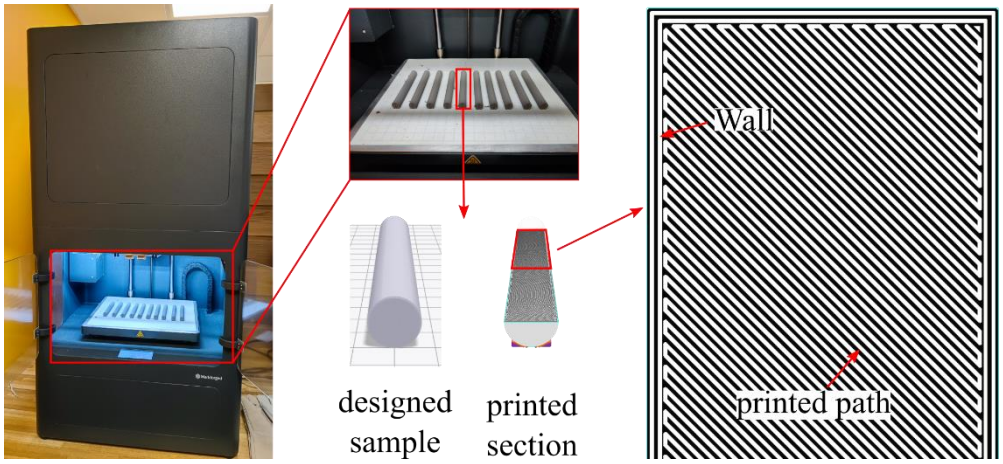

Fig.4-1 The printing system of Metal X™

The printed samples were then put into the heated debinding system Wash-1 for 15 hours using the solution Opteon SF 79 in order to remove the polymer and most of the binder material. After drying for 4 hours, the samples were finally put into a furnace for sintering to transform the part from lightly bound metal powder to a full metal part [131]. The sintering lasted for 28 hours. Then the samples were machined to the shape as Fig.3-1 shown with the same machining parameters.

Tab.4-2 Roughness of printed material

	Ra (μm)	Rt (μm)
Mean value	0.396	6.062
Standard deviation	0.072	3.964

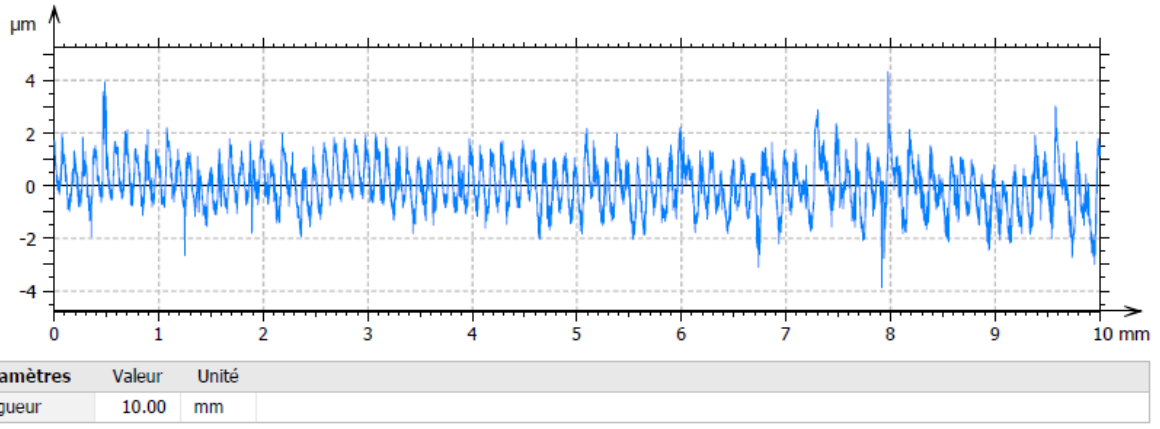

Paramètres	Valeur	Unité
Longueur	10.00	mm

ISO 4287

Paramètres d'amplitude - Profil de rugosité

Ra	0.2871	μm	*Filtre gaussien, 0.08 mm*	*Écart moyen arithmétique du profil de rugosité.*
Rt	5.901	μm	*Filtre gaussien, 0.08 mm*	*Hauteur totale du profil de rugosité.*

Fig.4-2 The roughness profile of the printed material

The roughness profile and results of the machined surface along the longitudinal direction were shown in Fig.4-2 and Tab.4-2. Similarly to the cold rolled specimens, no polishing process is then conducted.

4.1.2. Tensile properties comparison

A tensile test was performed in order to compare the tensile properties of the cold rolled and the printed materials. The comparison results are shown in Fig.4-3.

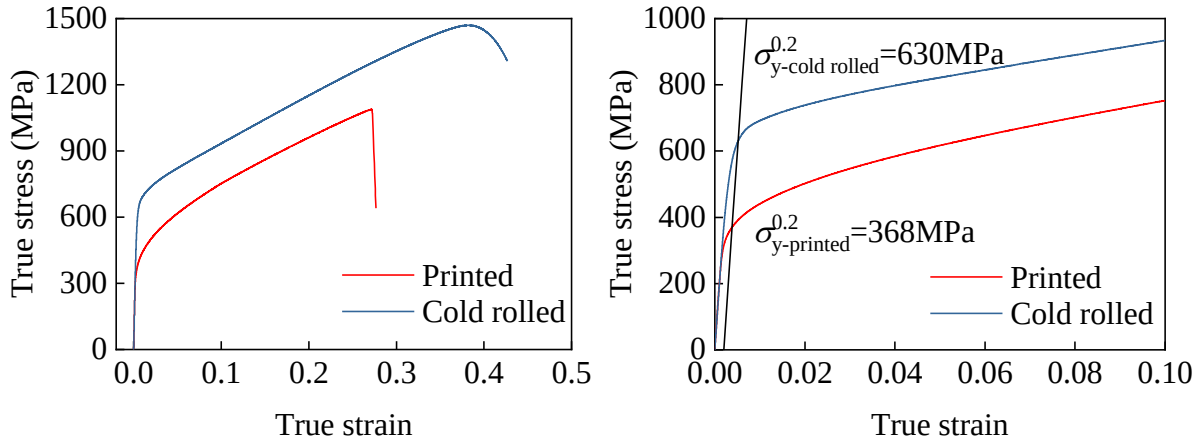

Fig.4-3 Tensile properties comparison of cold rolled and printed material (s) True stress-true strain curves (b) yield stresses at 0.2% plastic strain

There is clearly no difference in the elastic modulus between the printed and the cold rolled materials, as the two true stress-true strain curves in the elastic range coincide. However, the behavior in the plastic range differs. The cold rolled material has an ultimate tensile true stress (UTS) of 1469 MPa, while the printed material has a UTS of 1077 MPa. The cold rolled material exhibited significant necking during the tensile test, with a strain at fracture reaching up to 42%. In contrast, the printed material did not show any significant necking, with fracture occurring almost instantly and a strain at fracture reaching only 27%. Furthermore, Fig.4-3(b) illustrates a notable difference in the yield stress at 0.2% plastic strain between the cold rolled material (630 MPa) and the printed material (368 MPa). From the results, the cold rolled material has a better toughness and strength than the printed material.

4.2. Shot peening treatment

The set-up of ultrasonic shot peening for cylindrical sample is shown in Fig.4-4. One end of the sample is fixed on the side of Hooke's joint with a screw. The Hooke's joint is fixed on a motor. The motor rotates during shot peening in order to have a homogenously treated surface. The steel shots, with a diameter of 2 mm and a total mass of 5 g, were introduced into the chamber. The distance between the sample and the sonotrode was 15 mm and the power was 50%. Two treatment times were selected, which are 120 seconds (120s) and 360 seconds (360s) respectively.

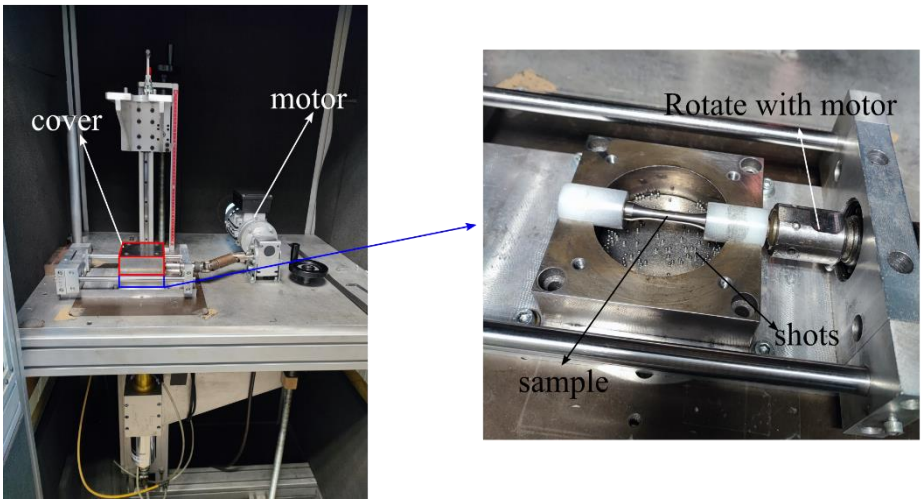

Fig.4-4 The set-up of shot peening for cylindrical sample

The roughness of the shot peened samples were examined. The roughness profile and results of the surface after shot peening along longitudinal direction are shown in Fig.4-5 and Tab.4-3.

Significant craters can be seen in Fig.4-5(b), which remove partly the machining grooves. From Tab.4-3 it can be found that there is no difference on roughness of these two material after shot peening. Comparing the roughness value in Tab.4-3 (after shot peening) with the values in Tab.3-2 and Tab.4-2 (before shot peening), results show that, with the present conditions, shot peening improves the surface roughness.

Tab.4-3 Roughness of shot peened material

	Cold rolled 120s		Cold rolled 360s		Printed 120s		Printed 360s	
	Ra (μm)	Rt (μm)	Ra (μm)	Rt (μm)	Ra (μm)	Rt (μm)	Ra (μm)	Rt (μm)
Mean value	0.203	3.544	0.163	3.140	0.208	4.107	0.164	2.508
Standard deviation	0.019	1.080	0.032	2.448	0.081	3.027	0.013	0.930

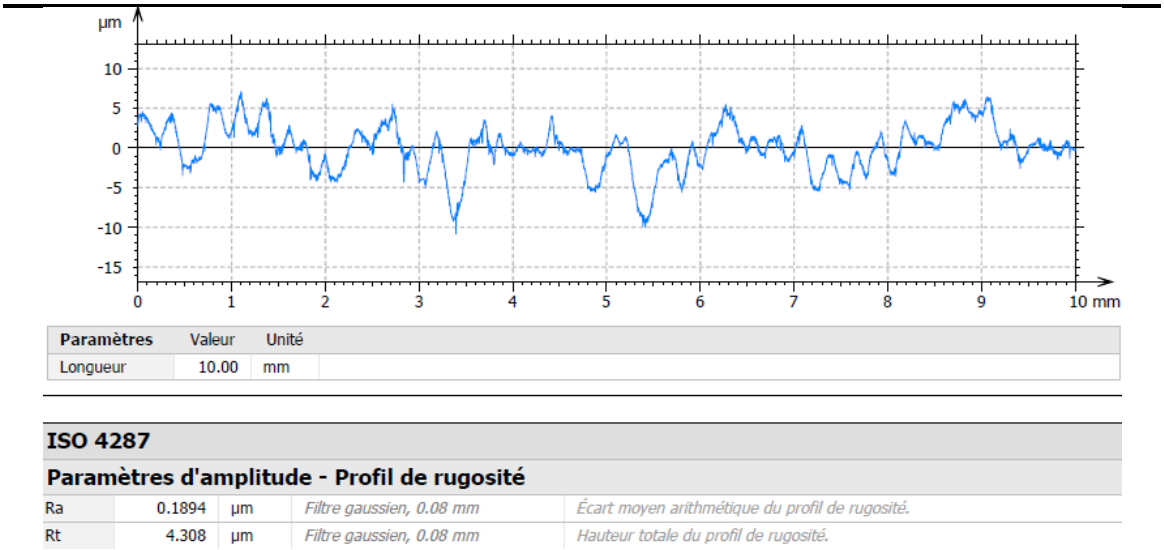

(a)

Fig.4-5 The roughness measurement for cold rolled material shot peened 120s (a) 3D surface topography

(Continued on the next page)

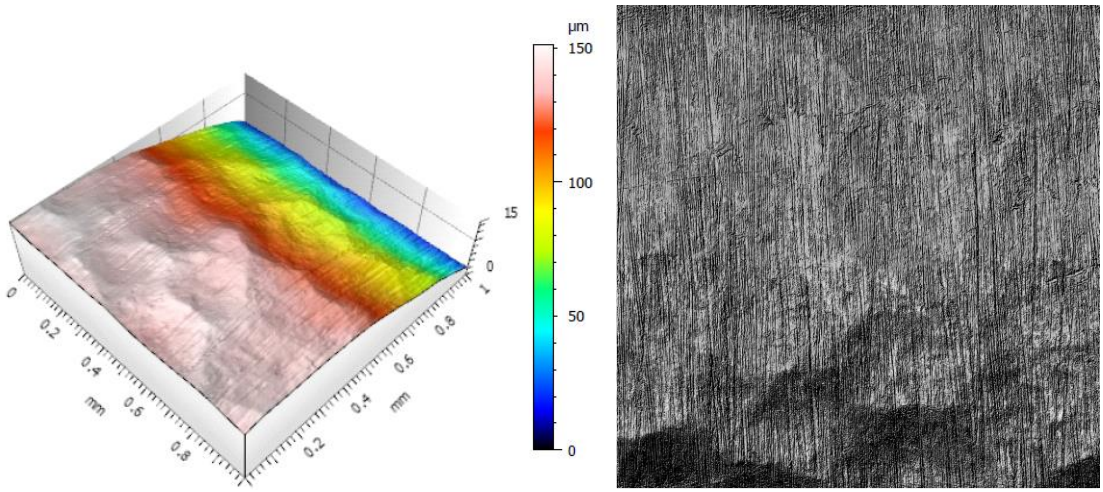

(b)

Fig.4-5 The roughness measurement for cold rolled material shot peened 120s (b) The surface image with optical microscope

(Continued)

Previous literature shows that the surface roughness will increase because of the craters caused by shots impact, no matter if it is conventional shot peening [132-134] or ultrasonic shot peening [135]. Compared with the conventional shot peening, the ultrasonic shot peening has a larger shot diameter and a slower shot speed. Due to the differences of initial surface quality, sonotrode vibration amplitude and shot material, the roughness induced by ultrasonic shot peening will be different [136]. Some similar results can be found in the previous literature [137-139] on the reduction of roughness after ultrasonic shot peening.

4.3. Monotonic tensile test

4.3.1. Selection of the strain level

Two tensile strain levels were selected for each material: a higher level of 24% for the cold rolled material and 15% for the printed material, and a lower level of 8% for the cold rolled material and 5% for the printed material. It is expected that high strain level will result in the complete relaxation of residual stresses, whereas low strain level are expected to lead to the partial relaxation of residual stresses. These levels were chosen based on the difference in tensile properties between the two materials, with the higher level being approximately half of the ultimate strain level for each material. The lower strain levels were determined at approximately one third of the highest level. Meanwhile, all the tests are performed on different samples.

4.3.2. The tensile stress-strain curves

The two materials tensile true stress-strain curves under different strain levels and different shot peening states are shown in Fig.4-6. Here ‘Raw’ means the material as received or as printed, 120s means the sample has been shot peened for 120 seconds, 360s means the sample has been shot peened for 360 seconds.

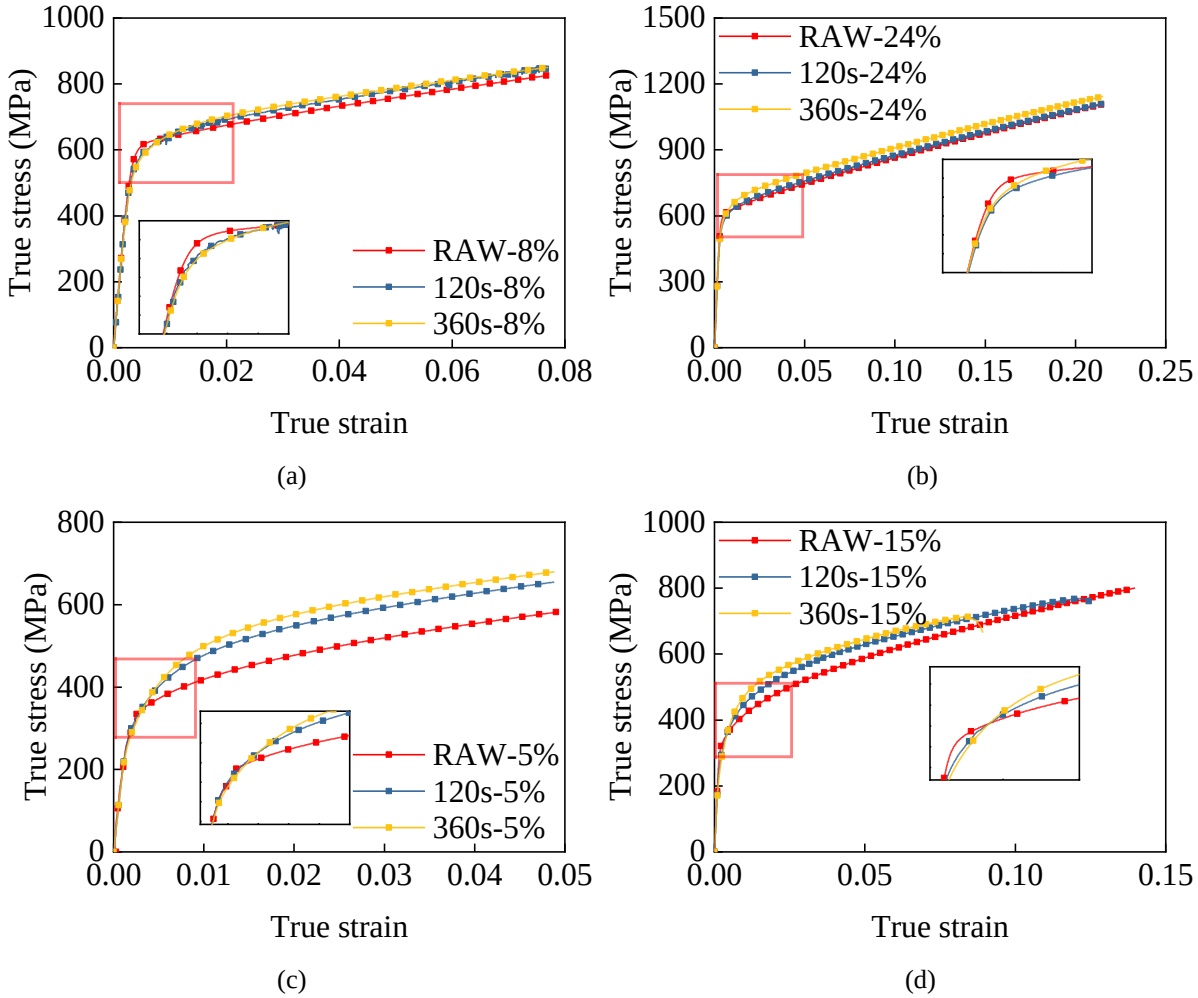

Fig.4-6 True stress-strain curves of cold rolled material (a) low strain level 8% (b) high strain level 24% and printed material (c) low strain level 5% (d) high strain level 15%

Fig.4-6(a), (b) and (c), (d) show the stress-strain curves of the cold rolled material and the printed material respectively. It is clear that shot peening does not affect material properties in the purely elastic region. However, shot peening affects material properties during the elastic-plastic transition, which can be seen from the zoom in each figure. The yield stress at 0.2% plastic deformation of the four cases are shown in Tab.4-4.

Tab.4-4 Yield stress of the tensile test samples

0.2% Yield stress	Cold rolled-8% (MPa)	Cold rolled-24% (MPa)	Printed-5% (MPa)	Printed-15% (MPa)
Raw	615	605	356	353
120s	582	584	372	347
360s	576	574	369	342

Shot peening decreases the yield stress of cold rolled material, as shown in the figure. The minimum yield stress is observed in samples shot peened for 360s. Although the effect is limited, it could be due to the yielding of the core of the specimens where tensile residual stresses can be found. These tensile stresses are here to balance the compressive stresses in the surface layers due to shot peening. Then, once the surface layer starts to yield, its compressive stresses and its work hardening can harden the whole specimen. The yield stress of printed

material follows globally the same trend, but it is not consistent between 5% and 15%. The shot peened samples exhibit higher yield stress for the 5% strain test, but lower yield stress for the 15% strain test. This could be due to the heterogeneity of the printed samples, in particular the presence of pores. The stress-strain curves for 5% and 15% strain levels are plotted in the same figure, as shown in Fig.4-7. The curve for the raw material (not shot peened) shows good coincidence. However, the curve for the shot-peened material at 5% and 15% strain levels shows a difference that could be due to the interaction of the residual stress distribution and the porosities (possibly tensile residual stresses enhanced by stress concentration around pores). Overall, shot peening obviously affects the material properties during the elastic-plastic transition phase.

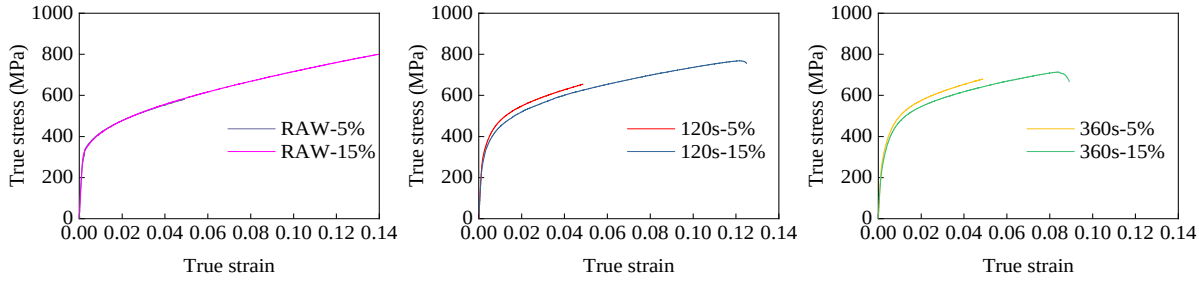

Fig.4-7 True stress-strain curves of printed material (a) Raw (b) shot peened 120s (c) shot peened 360s

In the fully plastic phase, shot peening slightly increases tensile stresses for the cold rolled material. However, for the printed material, shot peening causes a more significant increase in tensile stress. Additionally, the printed material that underwent shot peening for 120s fractured at a strain level of approximately 13%, while the printed material that underwent shot peening for 360s fractured at a strain level of approximately 9%. Again, this could be linked to tensile stresses balancing the compressive stresses in the surface layers.

4.3.3. Analysis of the surface properties by X-Ray diffraction

For better understanding the influence of tensile test on sample surface properties, X-ray diffraction tests were conducted as well. With CrKα radiation, the {220} planes of the nickel alloy, with the peak position at $2\theta = 128°$, were chosen for measurement, using the $\sin^2\psi$ method. Eleven ψ angles (0°, 6°, 12°, 18°, 24°, 30°, 36°, 42°, 48°, 54°, and 60°) and two ϕ angles (0°, 90°) were utilized due to the equibiaxial stress state of shot peened sample. The images were obtained by a 2D detector PILATUS, 100 seconds per image.

The tensile test is known to release the compressive residual stresses due to the induced plastic flow caused by stretching, which will redistribute the residual stresses [140]. Zhu et al. [141] discovered that 90% of the residual stress caused by manufacturing is released for GH4169 alloy when the tensile deformation is 3%. Thus, considering the properties of Inconel, from a pure structural point of view, the residual stress relaxation could be described as Fig.4-8.

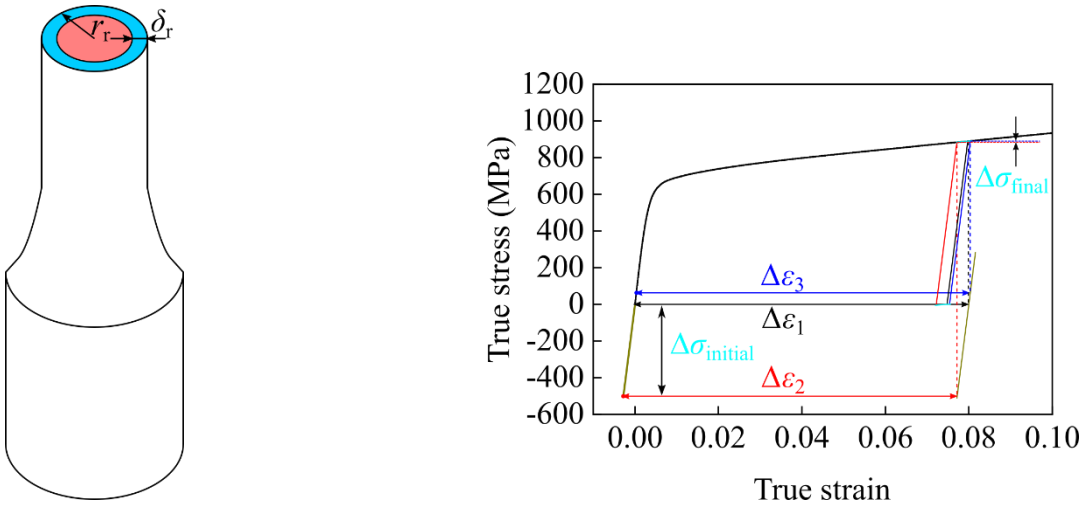

(a) (b)

Fig.4-8 The residual stress relaxation from a pure structural point of view (a) Schema of the simplification of the residual stress profiles in the shot-peened cylindrical fatigue samples (b) The mechanical state at strain level of 8% for cold rolled material

A didactic schema of the relaxation of the residual stress profiles is shown in Fig.4-8(a). It is assumed that shot peening will induce a uniform compressive residual stress and a uniform tensile residual stress, which are balanced over the cross section. δ_r is the layer which has the compressive residual stress, r_r is the radius of the cross section. As an example, the compressive residual stress value can be assumed to be -500 MPa on a thickness of 200 μm in the surface layer. The uniform tensile residual stress value of 74 MPa can be calculated by considering the stress equilibrium inside the calibrated part of the fatigue specimen, described as:

$$\sigma_{\text{tensile}}\pi(r_r - \delta_r)^2 + \sigma_{\text{compressive}}\pi(r_r^2 - (r_r - \delta_r)^2) = 0$$

Assuming that plane cross sections remain plane during the tensile test (which actually can be derived from the compatibility equations), the unloading stress state could be extracted from the monotonic tensile test from a pure structural point of view. Taking the cold rolled sample at 8% strain level as an example, Fig.4-8(b) shows the mechanical state after loading. When the specimen undergoes the tensile stage, if the cross sections remain plane, the deformation is uniform. This implies that all the points on the radial cross section of the calibration part have the same strain value. If we set the strain at the surface (with compressive residual stress) as $\Delta\varepsilon_2$, the strain in the core region (with tensile residual stress) as $\Delta\varepsilon_3$, and the averaged strain on the whole cross section as $\Delta\varepsilon_1$, then we should have $\Delta\varepsilon_1 = \Delta\varepsilon_2 = \Delta\varepsilon_3$. $\Delta\sigma$ is the stress difference between the surface and the core at the maximum tensile strain, in which $\Delta\sigma_{\text{initial}}$ and $\Delta\sigma_{\text{final}}$ respectively represents the stress difference before and after loading. It can be seen from Fig.4-8(b) that after unloading, the residual stress is almost released due to the plastification during loading process.

The diffraction data were analyzed with a Wolfram Mathematica script written by M. François (LASMIS/UTT) in order to obtain the residual stresses and peak widths. Three measurements were taken in each sample. The measurement positions are shown in Fig.4-9. For the two fractured samples, the measurement positions were taken on the gauge part away from the fracture section, as shown in Fig.4-9(b).

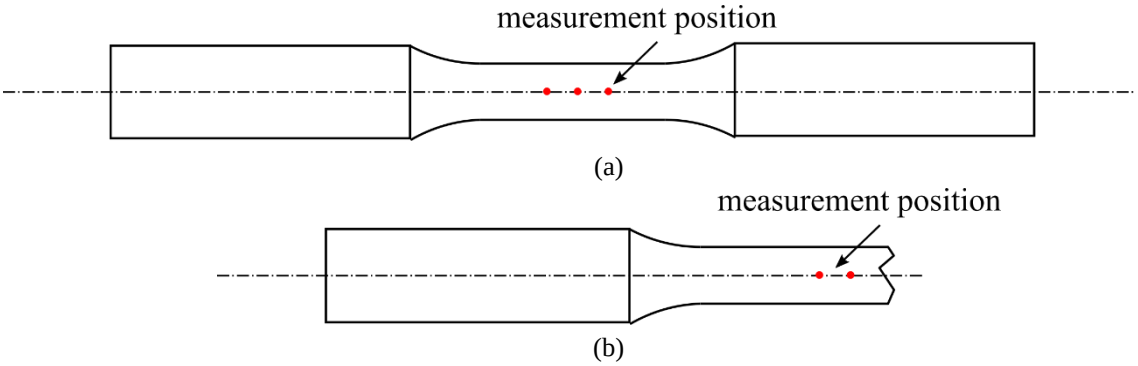

Fig.4-9 Schematic diagram of the measurement positions (a) Three positions (b) Two positions on the fractured sample

The surface axial and hoop residual stress of cold rolled sample before and after tensile test are shown in Fig.4-10. It should be noted that the figure depicts two specimens, the first of which was stretched to 8% and the second to 24%. The same is true for the following figures. Results show that the raw material has significant compressive stresses. Axial and hoop residual stresses around respectively -800 MPa and -400 MPa, which may be introduced by machining, are present at the surface layer of the material. The two shot peening times introduced a similar surface axial residual stress, with values of approximately -600 MPa, in the sample. Additionally, the hoop stress values are nearly identical to the axial residual stress values. This is the difference between the residual stress introduced by shot peening and machining.

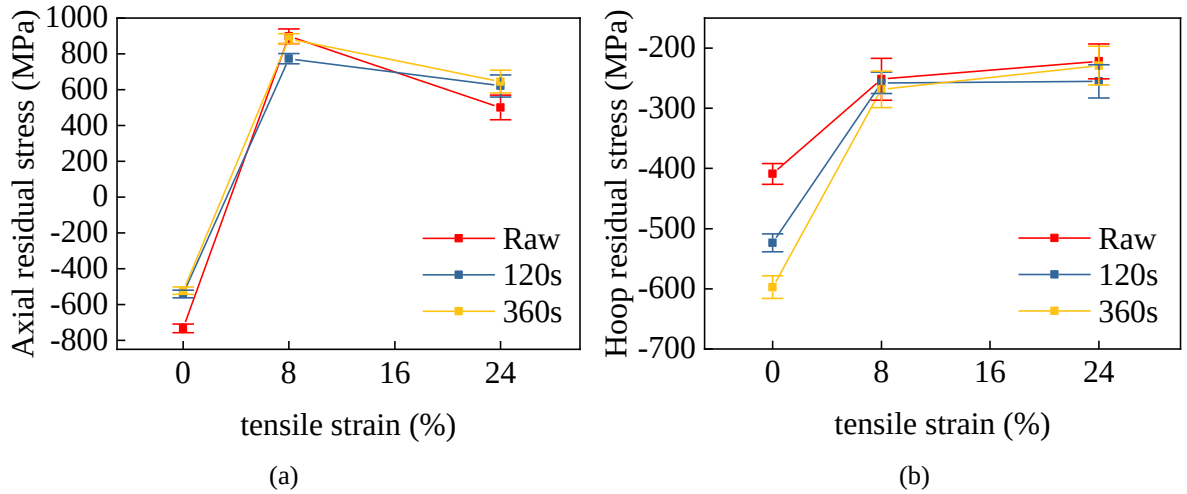

Fig.4-10 Surface residual stress of cold rolled sample before and after tensile test (a) Axial residual stress (b) Hoop residual stress

(For the residual stress values at no tensile strain state, take the average value of each two samples)

However, after tensile test, the relaxation of surface axial residual stress does not occur as expected. At a tensile strain of 8%, the residual stresses shift from a compressive value to a significantly high positive value. Subsequently, at a strain of 24%, the positive residual stress is partially released but is still significant. A longer shot peening time results in a higher compressive residual stress for the hoop direction. The relaxation of hoop residual stress occurs at the strain level of 8% and there are no significant changes observed when the strain level is increased to 24%.

The results of surface axial and hoop residual stress of printed sample before and after tensile test are shown in Fig.4-11.

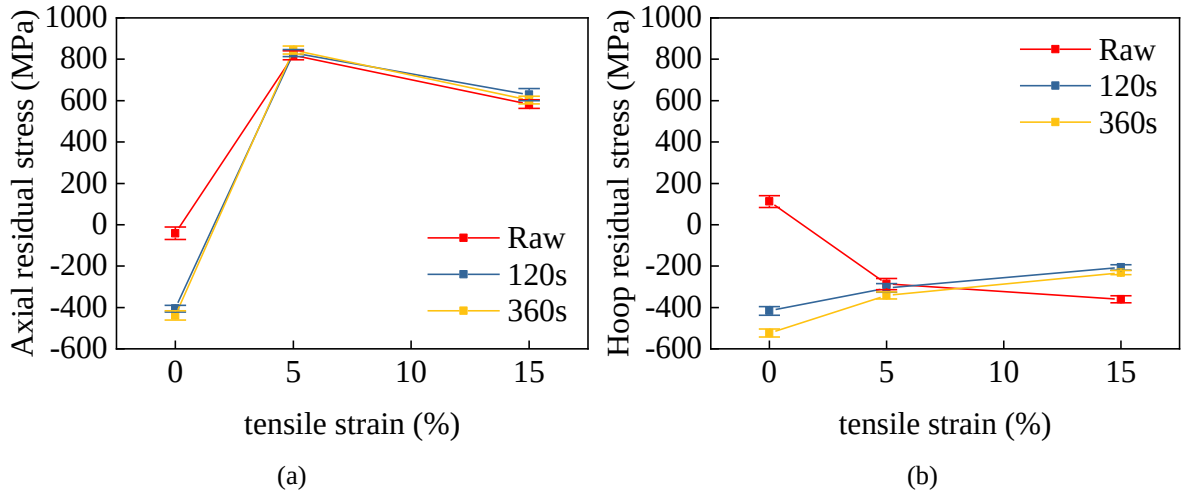

Fig.4-11 Surface residual stress of printed sample before and after tensile test (a) Axial residual stress (b) Hoop residual stress

(For the residual stress values at no tensile strain state, take the average value of each two samples)

The raw printed material has a different initial state (low axial and hoop residual stress) compared to the cold rolled material. Similarly, the residual stresses exhibit a transition from a compressive state to a notably high positive state after plastic straining. Subsequently, upon reaching a strain of 15%, a partial release of the positive residual stress occurs. For the hoop residual stress, the relaxation occurs on the strain level of 5% for the shot peened samples. Besides, compressive residual stress also occurs on the raw material and no significant changes occurs when the strain level increases to 15%.

The role of axial residual stress in the tensile or fatigue performances is significant, which is the main term to be observed in our work. However, we found that the schematic point of view in Fig.4-8 is not suitable for our case due to the unexpected changes in axial residual stress. Using the same analysis approach in Fig.4-8, we have proposed an entire analysis about the surface residual stress state after tensile test in the following section. Several assumptions or simplifications are employed in this analysis:

(1) The shot peened zone (surface), untreated zone (core part) are considered homogeneous;
(2) The work hardening is simplified to linear or perfectly plastic;
(3) The cross section is assumed to remain plane during the tensile process;
(4) The residual stress does not change the yield stress of the shot peened zone but only the initial position within the yield locus;

Taking the two cases shown in Fig.4-12 as a schematic example to explain the possibility of surface residual stress after tensile test.

Fig.4-12(a) illustrates the case where there is no residual stress, but work hardening still exists. Moreover, both the bulk and shot peened zone are linearly hardened. The initial state of the sample is represented by point *A*. When the sample is deformed in tension to strain ε_1, the material on the entire cross-section moves to point *B*. Meanwhile, the surface material moves

to point B_1. Due to the exist of work hardening, the surface material at point B_1 has a high stress value. Upon unloading the sample at strain ε_1, the elastic deformation of the entire section recovers, resulting in a movement to point B' and a movement of the surface material to point B_1'. Thus, a positive residual stress $\Delta\sigma_1$ occurs after test. When the sample is deformed in tension to a higher strain level, at ε_2, the material on the entire cross-section moves to point C and the surface material moves to point C_1. After unloading, they move to point C' and a movement of the surface material to point C_1', respectively. In this case, a positive residual stress occurs in the material after tensile test without any initial residual stress. Because of the same slope (hardening rate, $\Delta\sigma/\Delta\varepsilon$) of linear hardening, the stress differences between the surface and core part (which is positive residual stress here) at two strain levels $\Delta\sigma_1$ and $\Delta\sigma_2$ are the same.

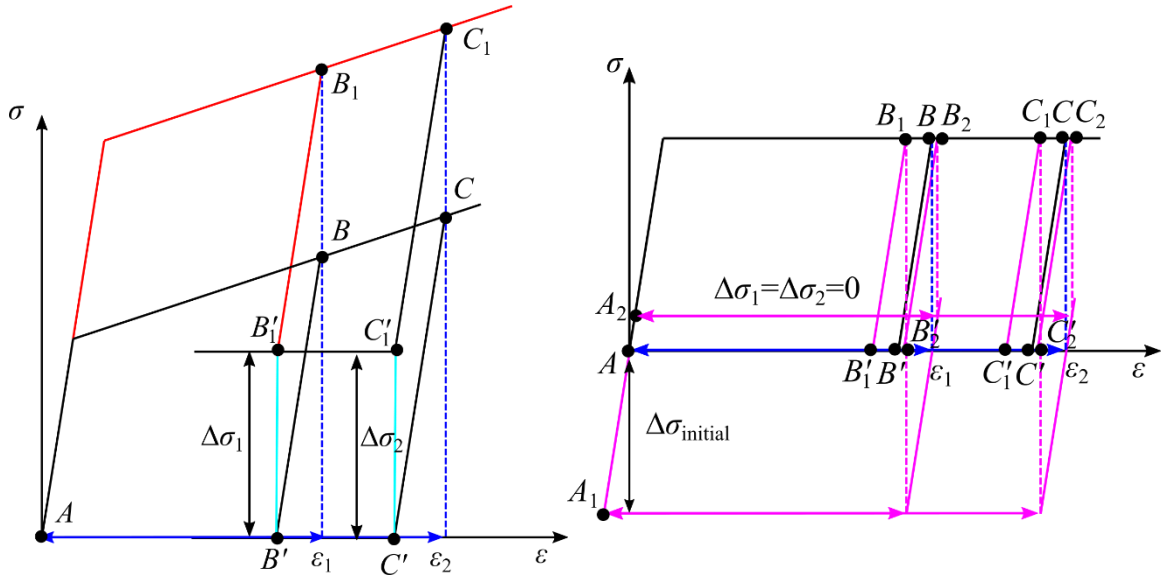

Fig.4-12 Two cases of the surface residual stress state after tensile test

Fig.4-12(b) illustrates the case where there is no work hardening in the shot peened layer and where the bulk material is perfectly plastic. The initial state of the shot peened zone and core part is represented by point A_1 and A_2 respectively. The initial state of the entire section is represented by point A. When the sample is tensioned to strain ε_1, the average strain on the entire section is also ε_1, thus point A moves to point B. Based on the assumption, shot peened zone material moves to point B_1 and the core-part material moves to point B_2. After unloading, the recovery of elastic deformation on the section results in the movement of point B to B'. Moreover, the shot peened material and core part material moves to point B_1' and B_2', respectively. The residual stress $\Delta\sigma_1$ after tensile test is relaxed completely. The situation of tensile strain at a higher level ε_2 is totally the same. In this case, the material has an initial residual stress of $\Delta\sigma_{\text{initial}}$, however, the residual stresses $\Delta\sigma_1$ and $\Delta\sigma_2$ after tensile test are totally released.

The other 6 cases are listed in Fig.4-13(a)-(f). Similarly to the two cases above, ε_1 and ε_2 are two different strain levels, $\Delta\sigma_1$ and $\Delta\sigma_2$ are the stress differences between the surface

and core part under two strain levels respectively, which could represent the residual stress after tensile test.

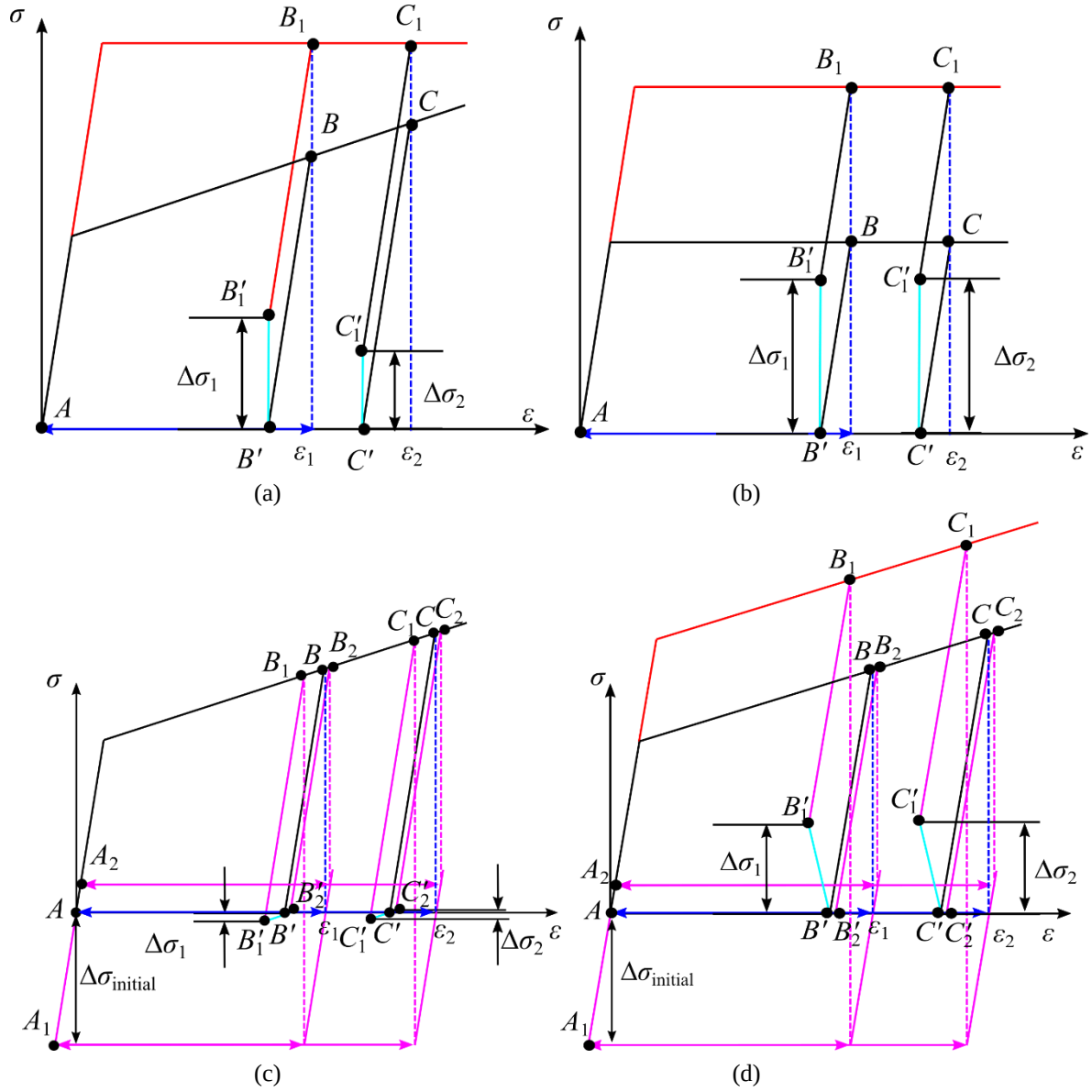

Fig.4-13 Analysis of surface residual stress state after tensile test

(a) Linear strain hardening material, surface perfectly plastic, without residual stress

(b) Perfectly plastic material, surface perfectly plastic, without residual stress

(c) Linear strain hardening material, with residual stress, without surface strain hardening

(d) Linear strain hardening material, surface linear strain hardening, with residual stress

(Continued on the next page)

Fig.4-13(a) and (b) show the cases without residual stress on the surface. The red line means the work hardened stress evolution of the surface material. It could be seen that, in these cases, a positive residual stress occurs after unloading. In case (a), the residual stress under a higher strain level is smaller than the stress under a lower strain level. In case (b), the residual stress stays constant.

Fig.4-13(c) shows the case without surface work hardening but with residual stress. This case is quite the same as the case shown in Fig.4-8, compressive residual stress exists on the

surface and positive residual stress exists in the core part. $\Delta\sigma_1$ and $\Delta\sigma_2$ are almost completely relaxed after tensile test, which means that the residual stress is released in this case. In addition, the degree of the relaxation under two different strain levels is identical.

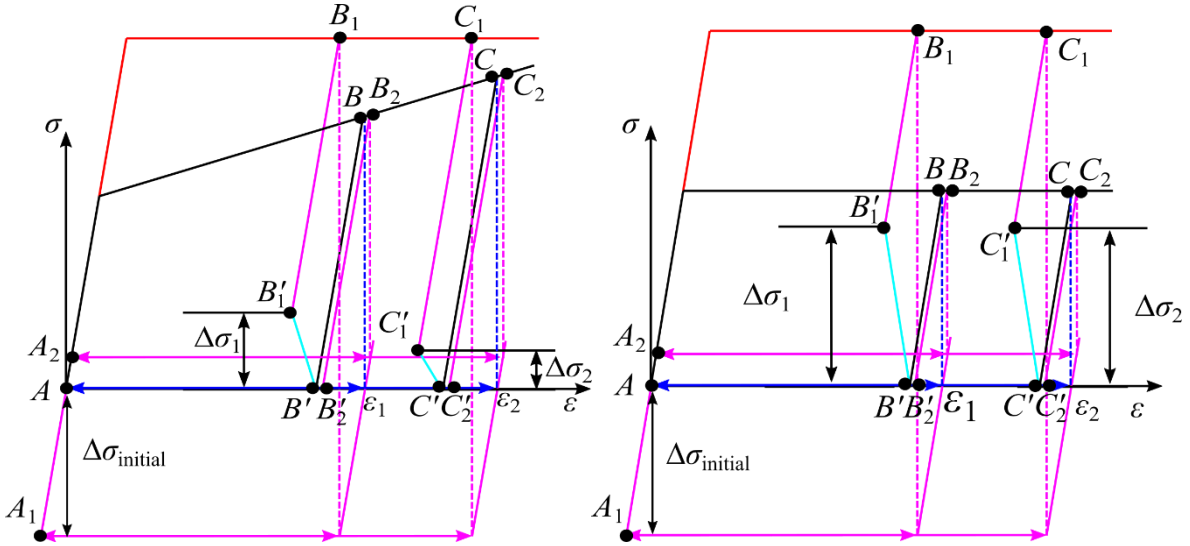

Fig.4-13 Analysis of surface residual stress state after tensile test
(e) Linear strain hardening material, surface perfectly plastic, with residual stress
(f) Perfectly plastic material, surface perfectly plastic, with residual stress
(Continued)

In practice, both work hardening and residual stress exist on the surface, especially for the shot peened samples. Fig.4-13(d-f) represents these cases. In these cases, positive residual stress occurs after unloading. In case (d) and case (f), the residual stress stays constant under different tensile strain levels. However, in case (e), similar to case (a), the residual stress tends to be smaller after a higher strain level.

A comprehensive examination of the 8 cases presented in Fig.4-12 and Fig.4-13 reveals that residual stress relaxation occurs in the absence of work hardening in shot peened surface or the shot peened surface is fully work-hardened. Conversely, if unsaturated work hardening is present on the surface, positive residual stress will be observed after the tensile test, regardless of the initial residual stress. Nevertheless, the positive residual stress can be relaxed if the material is linear plastic, while the surface is perfectly plastic, as the case shown in Fig.4-13(a) and (e).

As shown in Fig.4-10(a) and Fig.4-11(a), the residual stress state of Inconel 625 after the tensile test seems to correspond to case (e), whether it is cold rolled or printed. The surface hardening in case (e) is simplified to a perfectly plastic behavior, which can explain the stress relaxation that occurs as the strain level increases. In practical, the surface hardening may not behave like a perfectly plastic response, but it can be assumed that the strain hardening is closer to saturation, for which the slope of the stress-curve is lower than the not hardened part.

The surface peak widths of cold rolled samples and printed samples are shown in Fig.4-14. In overall consideration, the peak width of the cold rolled samples increases with the tensile strain, which means the surface is work-hardened during the tensile test. For the printed material,

it could be seen that the peak widths remain basically the same or even decrease a little, i.e. the material softens a little. A possible reason for this phenomenon could be the effect of machining. The printed materials are significantly affected by machining (See in Fig.4-22), with the hardened surface caused by machining playing a major role in the change of peak width. Therefore, the effect of tensile strain is not significant in comparison.

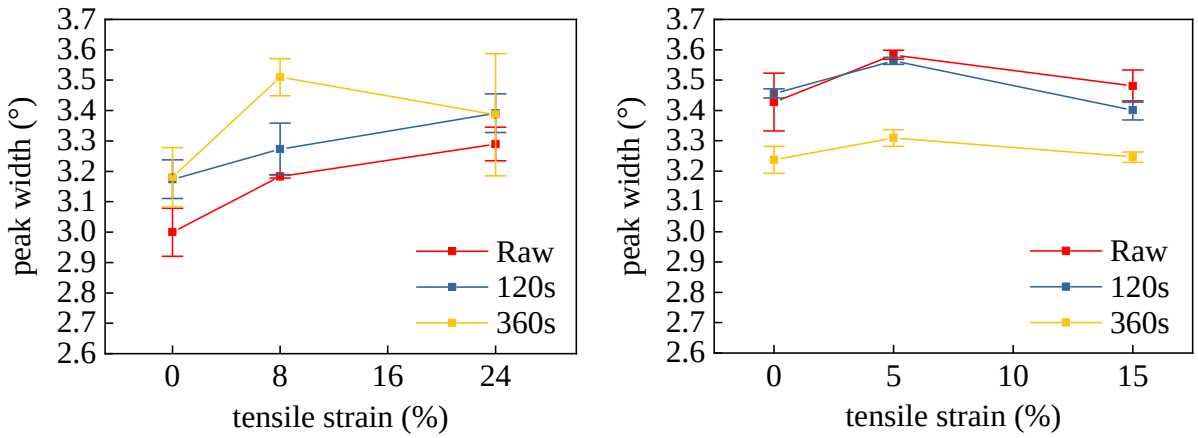

Fig.4-14 Surface peak width of (a) cold rolled sample (b) printed sample before and after tensile test (Only the peak widths in axial direction, for the peak values at no tensile strain state, take the average value of each two samples)

4.3.4. Analysis of EBSD results at longitudinal section

4.3.4.1 Microstructure of two types of Inconel 625

The samples were first cut along the cross section, and then along the longitudinal section. Nanoindentation tests and EBSD measurements were performed on the longitudinal section, as shown in Fig.4-15.

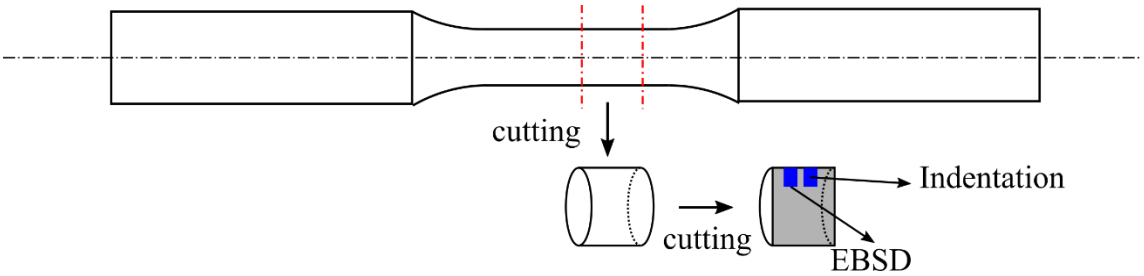

Fig.4-15. Indentation and EBSD on the longitudinal section

EBSD measurements were performed with the EDAX Velocity EBSD Camera (AMETEK, Inc., USA) in a TESCAN MIRA SEM system (TESCAN, Czech Republic). The measurement range is 200 μm ×150 μm, with a step of 0.15 μm. The microstructure of cold rolled sample and printed sample is shown in Fig.4-16. No obvious texture could be found through the IPF. Some refined grains were observed in the cold rolled samples, aligned in a line, as can be seen just above the scale bar in Fig.4-16(a). It is possible that these grains are formed because of the recrystallization, which may occurred because of segregation during the cold rolling and annealing process [142][143]. The printed material displays a notable degree of porosity. The large pores (the size is around 20 μm), with a roughly triangular shape, are related to the unfilled spaces that result from the insufficient melting between adjacent filaments in

each layer [144]. As a result, they typically display as a regular interval pattern. In addition, some tiny round pores (the size is generally a few microns) are found in the printed material. When the polymer or binder materials are removed in the washing process, some air (or gas coming from the decomposition of the polymer) could get into the material and result in the tiny pores [145]. In addition, the intra-bead pores in the filament could be another possible reason for the tiny pores [146]. Finally, the grain size of the printed material is larger than for the cold rolled material.

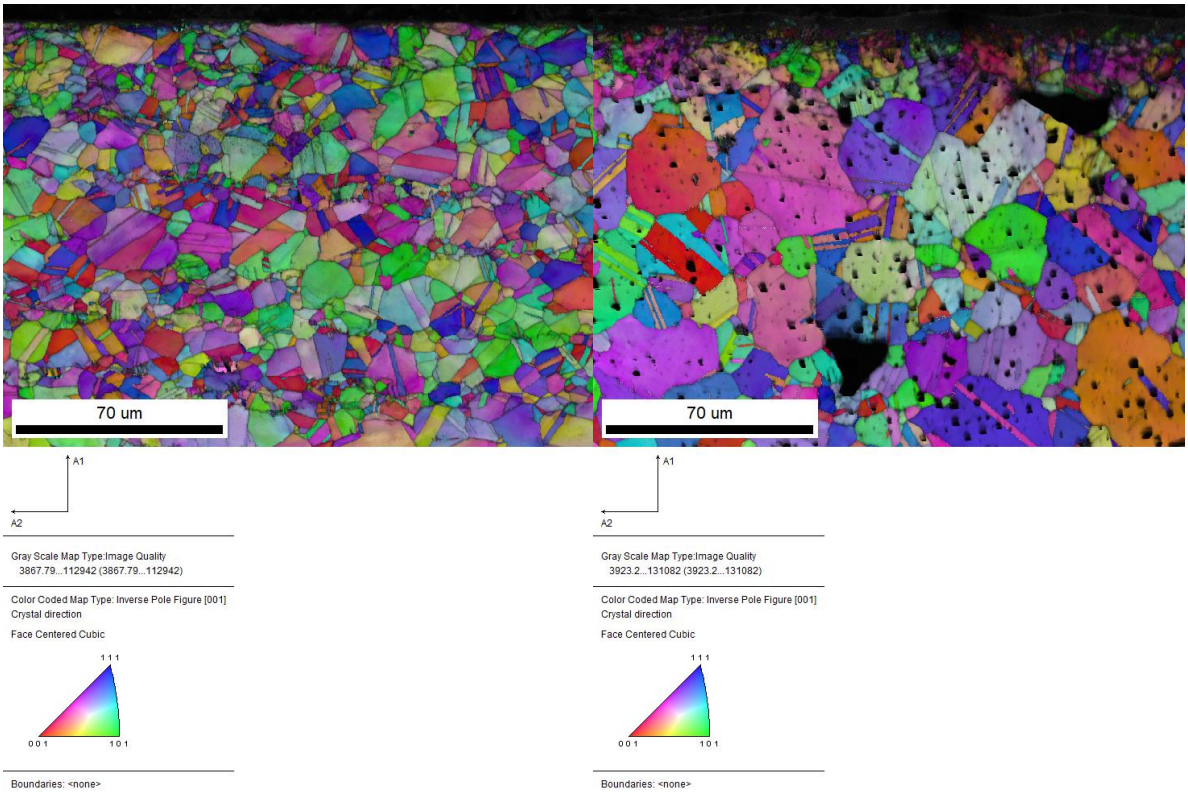

(a) (b)

Fig.4-16 The IPF (Inverse Pole Figure) of (a) Cold rolled sample, Raw-8% strain (b) Printed sample, Raw-5% strain

4.3.4.2 Analysis of dislocations evolution

The KAM maps of cold rolled tensile test samples are shown in Fig.4-17. It can be seen that the shot peening introduces a significant degree of plastic deformation in the material. As shown in Fig.4-17(a-c), the local misorientation at the surface is greater than that in the material far from the shot peened surface, which clearly demonstrates the effect of shot peening. In addition, the thickness of the affected layer increases with the shot peening time. Furthermore, a layer with a higher local misorientation level is observed in Fig.4-17(a), corresponding to the non-shot peened sample, which proves that a layer was affected due to machining. This also illustrates the possible reason for the observation of a high level of compressive residual stress in the non-shot peened sample, as shown in Fig.4-10. This can be due to the machining.

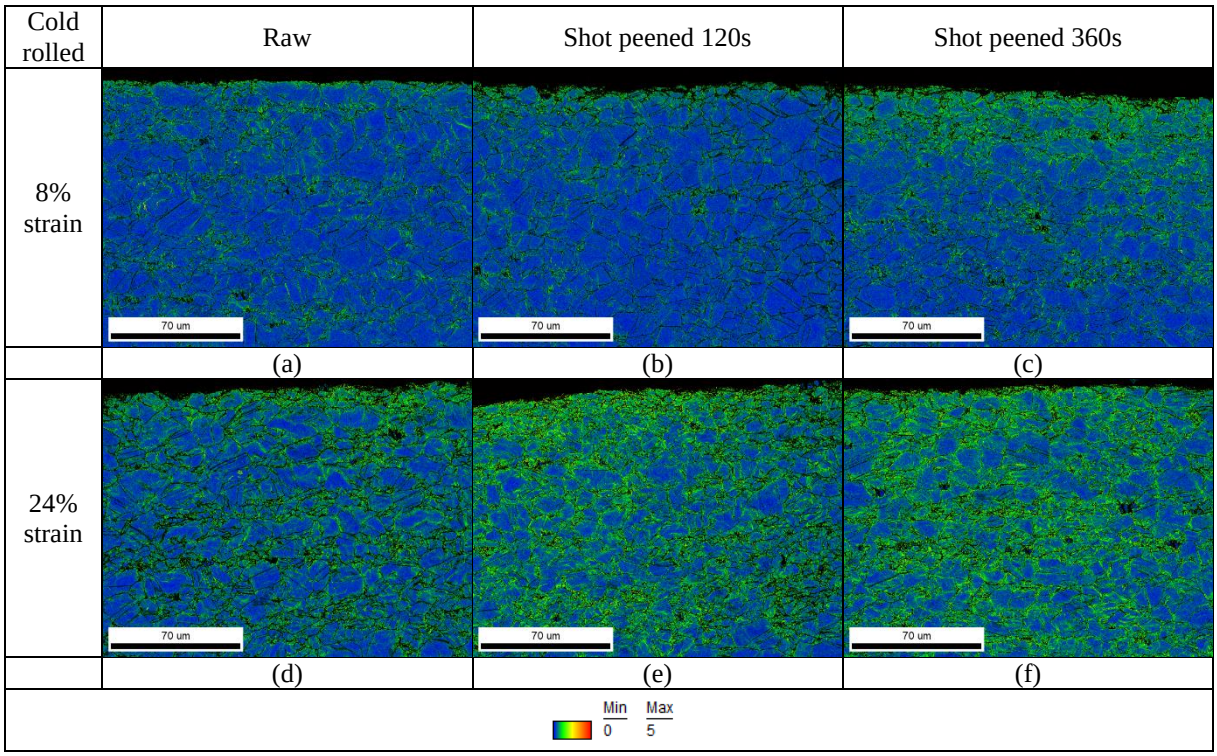

Fig.4-17 KAM map with Confidence index grey scale of cold rolled samples (a) CR-Raw-8% strain (b) CR-120s-8% strain (c) CR-360s-8% strain (d) CR-Raw-24% strain (e) CR-120s-24% strain and (f) CR-360s-24% strain

As shown in Fig.4-17(e) and (f), the difference in shot peened affected layers between two peening states is no longer distinguishable when the specimens are tensioned to 24%. In addition, the misorientation that occurs during tension is mainly distributed around the twins and the refined grains. This is mainly due to the fact that the twins can promote or hinder the slip in the grains [147][148].

The KAM data were subjected to a statistical analysis in order to observe the gradient in the shot peening affected layers. Taking the CR-360s-8% strain sample as an example, the KAM data is shown in Fig.4-18(a). The average line (in red color) is used to represent the KAM gradient more clearly. No KAM data is observed in the region close to the resin. Besides, it should be noted that the average KAM data near surface (around 3-5 μm) are not included in in Fig.4-18(a). As shown in Fig.4-18(b), the image quality grayscale shows the index quality of the results. It is obvious that, due to the high plastic deformation near the surface, many pixels are not well indexed. Consequently, the average KAM data near the shot peened surface is subjected to oscillations and not representative. Meanwhile, the layer depth affected by shot peening is within the range of tens or hundreds of micrometers, which is a considerably deeper level than that of the not well indexed layer depth. Therefore, the not well indexed KAM data are removed in order to facilitate the visualization of the gradient. Subsequent data are treated in the same way.

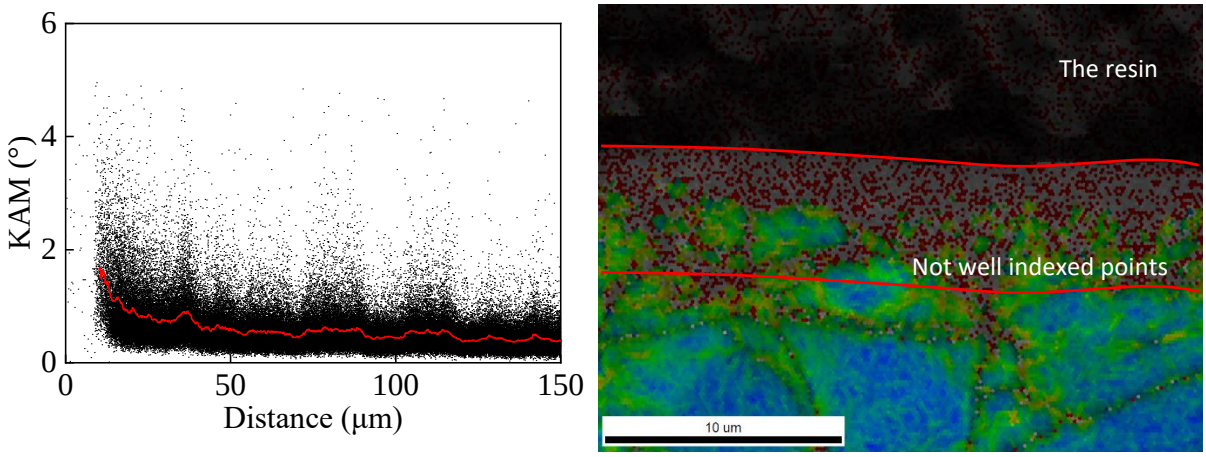

(a) (b)

Fig.4-18 The (a) average KAM plot (b) KAM localized enlargement map near shot peened surface with image quality of CR-360s-8% strain sample

It is important to note that the gradient of the shot peened layers should be along the radius direction. However, it is difficult to achieve precise control to cut through the center of the longitudinal section. As shown in Fig.4-19, if *AB* represents the cutting plane, which does not pass through the section centered in *O*, the measured data along the depth cannot accurately represent the gradient. Therefore, a correction must be applied to transform the depth along the cutting plane to that along the radius. The correction can be expressed as:

$$d = x\frac{R}{D}$$

In which d is the real distance from the shot peened surface, x is the depth along the cutting plane, R is the radius of the sample gauge part, $2D$ is the width of the cutting plane. Taking the CR-120s-8% strain sample as an example, for x = 100 μm, the d value is 119 μm. The distance correction is applied to all the following data.

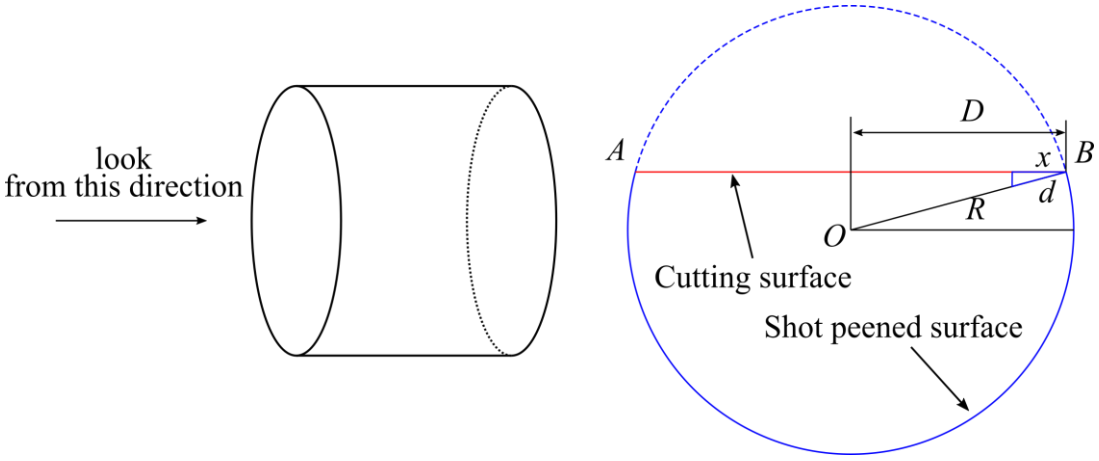

Fig.4-19 The correction of the affected depth

The statistical KAM data for cold rolled samples is shown in Fig.4-20. All the zero points of the KAM data set have been shifted in order to remove the data of resin, as well as the regions that are not well indexed. This method allows for the clear visualization of the depth of the shot peening process. Although those layers not well indexed are also affected by shot

peening, their depth is approximately 3-5 μm. Therefore, the effect of removing them on the observation of shot peening-affected depth can be considered negligible.

In this chapter, the experimental curves (EBSD and nanoindentation) can be fitted by an exponential decay function in order to observe their trends. The function is expressed as:

$$y = Ae^{-x/t} + y_0$$

In which x represents the variable of distance from the shot peened surface, y represents the average responses. The fitted parameters A, t and y_0 represent the amplitude of the effect, the decreasing rate and the response on the bulk material respectively. When x equals $3t$, the amplitude decreases to $0.05A$, indicating that $3t$ may be used to represent the affected depth.

The KAM fitting parameters of cold rolled samples are shown in Tab.4-5. It can be seen in Fig.4-20 that the effect of shot peening remains apparent when the samples were stretched to a strain of 8%. A shot peening process with a longer time could result in a deeper affected layer and a higher misorientation angle. The depth of the affected layer for shot peening 120s and 360s is around 25 μm and 60 μm, respectively. In addition, the depth of the layer affected by the machining for the raw material is around 8 μm. Compared to the depths affected by shot peening, it is much shallower. When the samples are stretched to a strain of 24%, the difference in the depths affected by two shot peening times can no longer be clearly observed. The misorientation caused by the slip between different grains due to large plastic deformation tends to be the major misorientation in the material. It can be observed that the average misorientation angle of the bulk material with a 24% tension strain (around 0.74°) is greater than that of the bulk material with an 8% tension strain (around 0.45°).

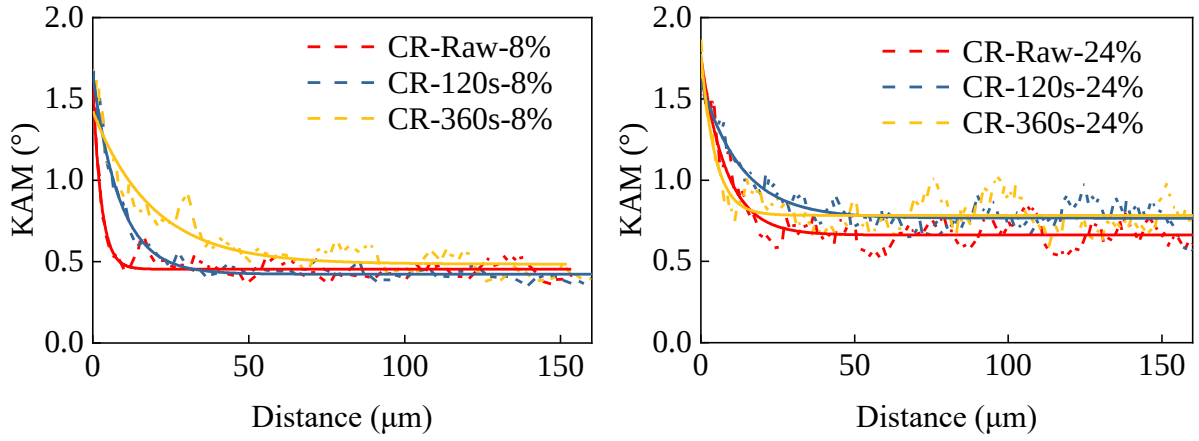

Fig.4-20 The statistical KAM data of cold rolled samples under tension strain of (a) 8% (b) 24%

Tab.4-5 KAM fitting parameters of cold rolled samples after tensile straining for different shot peening states

CR-8% strain						
	A (mN)	$u(A)$ (mN)	t (μm)	$u(t)$ (μm)	y_0 (mN)	$u(y_0)$ (mN)
Raw	1.156	0.022	2.676	0.077	0.4536	0.0016
120s	1.2264	0.0091	8.778	0.099	0.4230	0.0012
360s	0.910	0.013	19.15	0.47	0.4848	0.0034

CR-24% strain						
	A (mN)	$u(A)$ (mN)	t (μm)	$u(t)$ (μm)	y_0 (mN)	$u(y_0)$ (mN)
Raw	1.096	0.019	8.22	0.23	0.6620	0.0025
120s	0.847	0.015	13.18	0.36	0.7661	0.0026
360s	0.995	0.031	4.69	0.22	0.7833	0.0029

Tab.4-6 KAM fitting parameters of printed samples after tensile straining for different shot peening states

MF-5% strain						
	A (mN)	$u(A)$ (mN)	t (μm)	$u(t)$ (μm)	y_0 (mN)	$u(y_0)$ (mN)
Raw	1.4826	0.0058	13.518	0.086	0.3100	0.0011
120s	1.320	0.011	12.81	0.169	0.3890	0.0020
360s	1.010	0.011	29.88	0.74	0.4371	0.0051
MF-15% strain						
	A (mN)	$u(A)$ (mN)	t (μm)	$u(t)$ (μm)	y_0 (mN)	$u(y_0)$ (mN)
Raw	1.0010	0.0070	14.04	0.16	0.5599	0.0014
120s	1.1768	0.0071	22.84	0.26	0.4545	0.0022
360s	1.112	0.011	19.14	0.33	0.4616	0.0029

The KAM map and the statistical KAM data of the printed samples after tensile tests are shown in Fig.4-21 and Fig.4-22, respectively, and the KAM fitting parameters are shown in Tab.4-6.

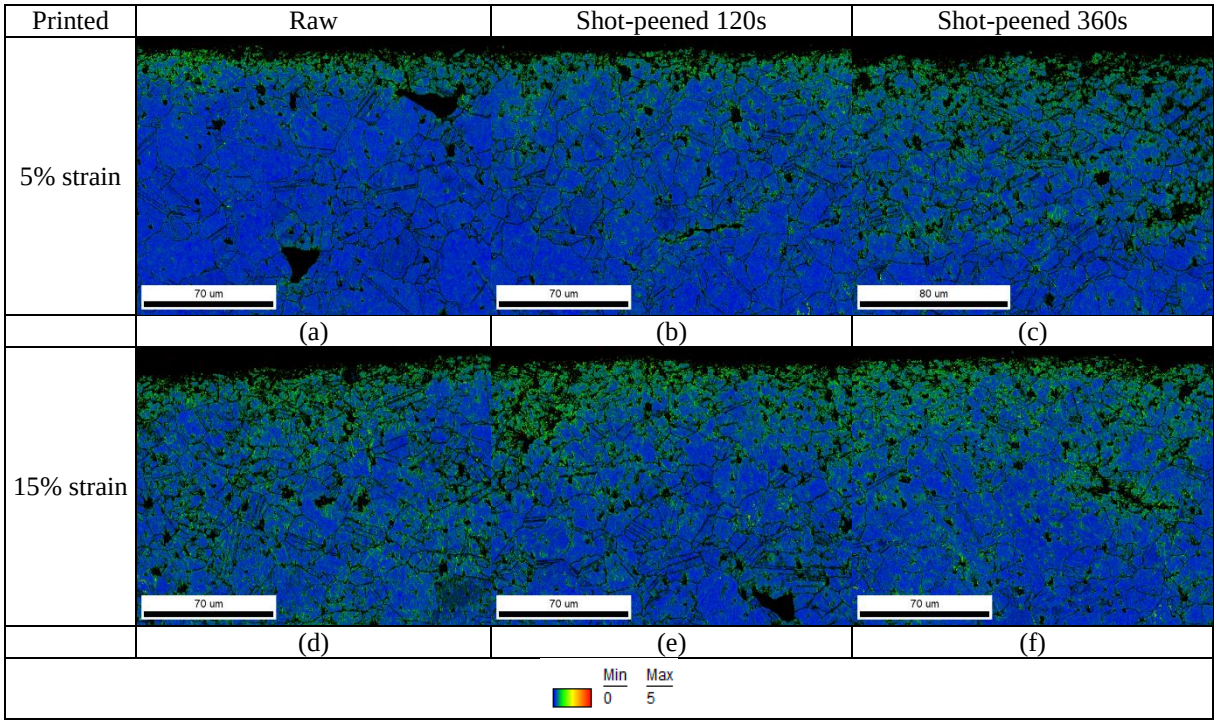

Fig.4-21 KAM map with Confidence index grey scale of printed samples (a) MF-Raw-5% strain (b) MF-120s-5% strain (c) MF-360s-5% strain (d) MF-Raw-15% strain (e) MF-120s-15% strain and (f) MF-360s-15% strain

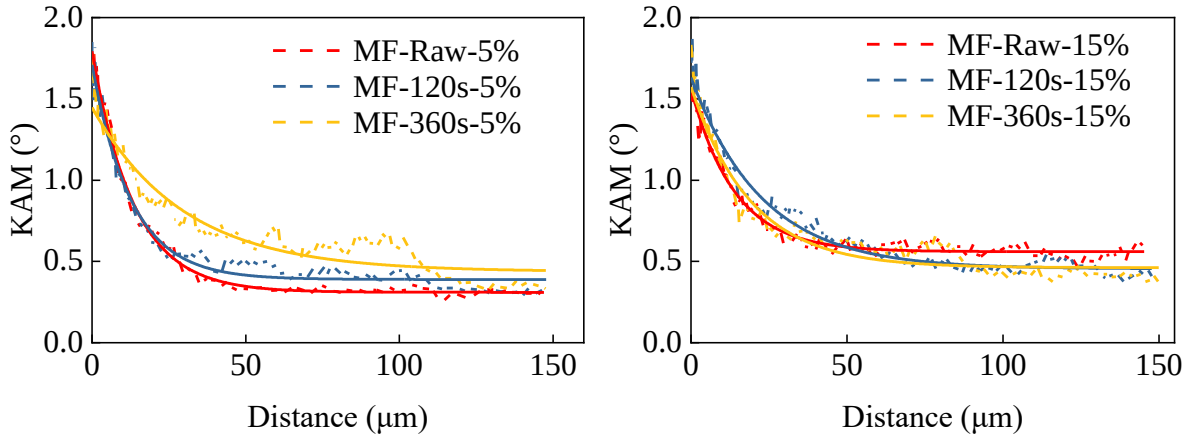

Fig.4-22 The statistical KAM data of printed samples after a tensile strain of (a) 5% (b) 15%

Similarly, the effect of different shot peening time can still be observed in the samples with a tensile strain 5%. It can be seen in Fig.4-22(a) that the depth of the layer affected by the machining for the raw material is around 40 μm, which is deeper than that of cold rolled samples. Meanwhile, the affected layer depths for shot peening 120s and 360s are around 39 μm and 90 μm respectively, which is also deeper than that of cold rolled samples. Fig.4-22(b) illustrates that the different effect in shot peening times could not be observed for the sample with a tensile strain of 15%, which is similar with the results of cold rolled samples. As shown in Fig.4-21(b-f), the misorientation that occurred during the tensile test is mainly distributed around the pores, which is different from the cold rolled samples. This is probably due to the stress concentration generated around the pores during the tensile test that leads to a severe deformation near the edge [149]. Furthermore, the stress concentration near the pores may also be a possible explanation for the observation that the shot peened samples fracture earlier than the non-shot peened sample as shown in Fig.4-6(d). Tensile residual stresses also occur in the interior of the shot peened sample. Due to the combination of tensile residual stress and stress concentration, the cracks are more easily initiated at the pores, which lead to an earlier fracture.

It can also be seen in Fig.4-22(a) that some significant drops of the KAM profile are observed for the shot peened printed materials, such as the yellow and blue curves at 100 μm (Similar phenomenon can be found in the cyclic tests, shown in Fig.4-39). The possible reason may be the not perfectly homogeneous structure of the printed material and insufficient amount of data in the scanning area. For instance, as mentioned above, the misorientation caused during the tensile test is mainly distributed around the pores, thus the existence of the pores in the scanning area will lead to a higher misorientation value at that position.

4.3.5. Analysis of nanoindentation on longitudinal section

The nanoindentation tests on the longitudinal section of the tensile and cyclic tests were performed on FT-I04 Femto-Indenter (Femto Tools, Switzerland), in order to obtain the hardness map of the section. All measurements were conducted with a Berkovich indenter and the CSM method, with an indentation depth of 1 μm. The measurement range is 400 μm×800

μm, with a distance of 20 μm between each indentation position. Taking the CR-360s-8% strain sample as an example, the hardness map obtained from indentation is shown in Fig.4-23. It is evident that the hardness of resin is quite lower than our samples. The gradient of hardness from shot peened surface can be observed on the map.

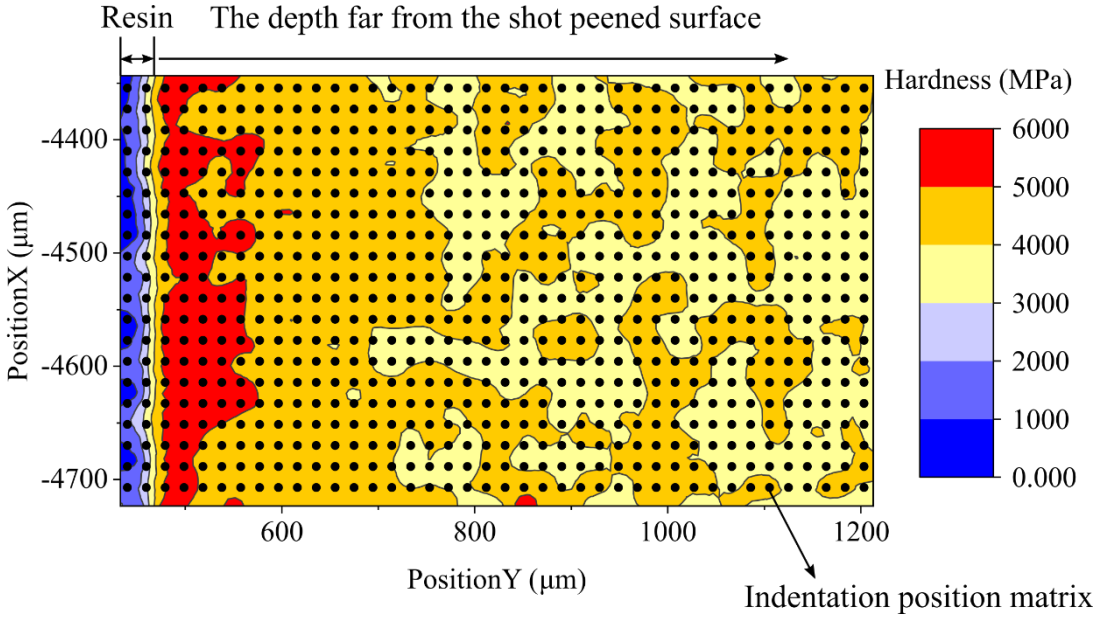

Fig.4-23 The hardness map of CR-360s-8% strain sample

Two types of fits can be performed on nanoindentation response curves. The first type uses all the indentation data for the fit. The second type uses the average responses of the 20 tests at the same distance from the shot peened surface, which is also the profile shown in Chapter 3 to represent the trend of indentation responses. The data of the tests in the resin was removed when fitting the function. The fitting results are shown in Fig.4-24.

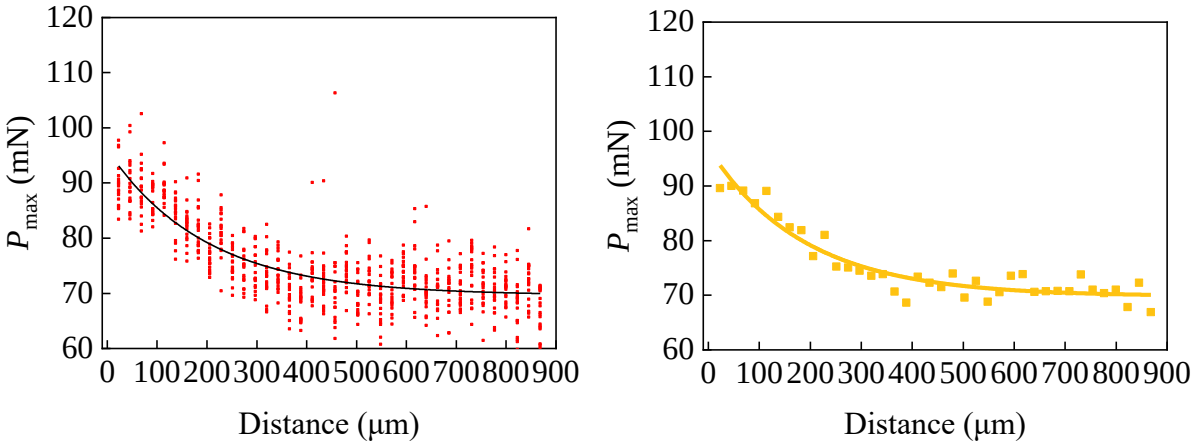

Fig.4-24 Two different fittings of CR-360s-8% strain sample (a) Fit with all indentation data (b) Fit with the average data

The parameters obtained by these two fits are shown in Tab.4-7. It can be seen that the two results are consistent with each other, which indicates that both kinds of fits can be used to

represent the trend of the response. However, the uncertainty is slightly smaller when all the data are fitted without performing an average beforehand.

Tab.4-7 Nanoindentation fitting parameters of tensile cold rolled samples

Fit with all indentation data						
P_{max}						
	A (mN)	$u(A)$ (mN)	t (μm)	$u(t)$ (μm)	y_0 (mN)	$u(y_0)$ (mN)
CR-360s-8% strain	26.34	0.77	198	13	69.64	0.37
Fit with the average data						
P_{max}						
	A (mN)	$u(A)$ (mN)	t (μm)	$u(t)$ (μm)	y_0 (mN)	$u(y_0)$ (mN)
CR-360s-8% strain	27.0	1.9	189	26	69.81	0.77

Therefore, the average responses are used to represent the response trend in the following analysis. The average responses and their variations for the cold rolled samples along the distance from the shot peened surface are shown in Fig.4-25. Due to the different trends observed on S for cold rolled samples and printed samples (presented in next section), a simple horizontal line fitted with the data beyond 300 μm is used to represent the average response for the bulk material. The fitted parameters are listed in Tab.4-8.

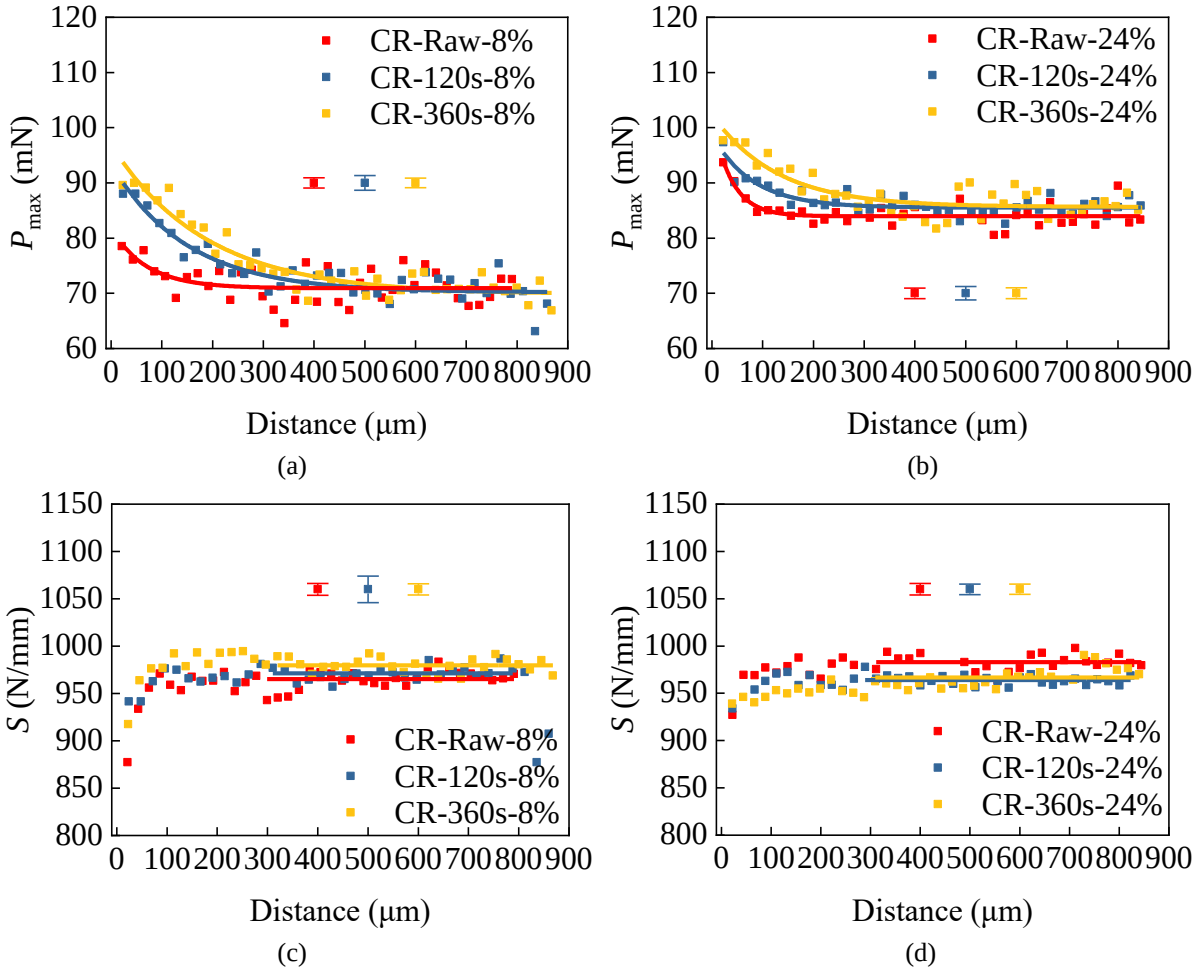

Fig.4-25 The average responses of cold rolled samples along the distance from the shot peened surface (a) P_{max} for 8% tension strain (b) P_{max} for 24% tension strain (c) S for 8% tension strain (d) S for 24% tension strain. Three points besides the curves are represented to show the average error bar of each set.

(Continued on the next page)

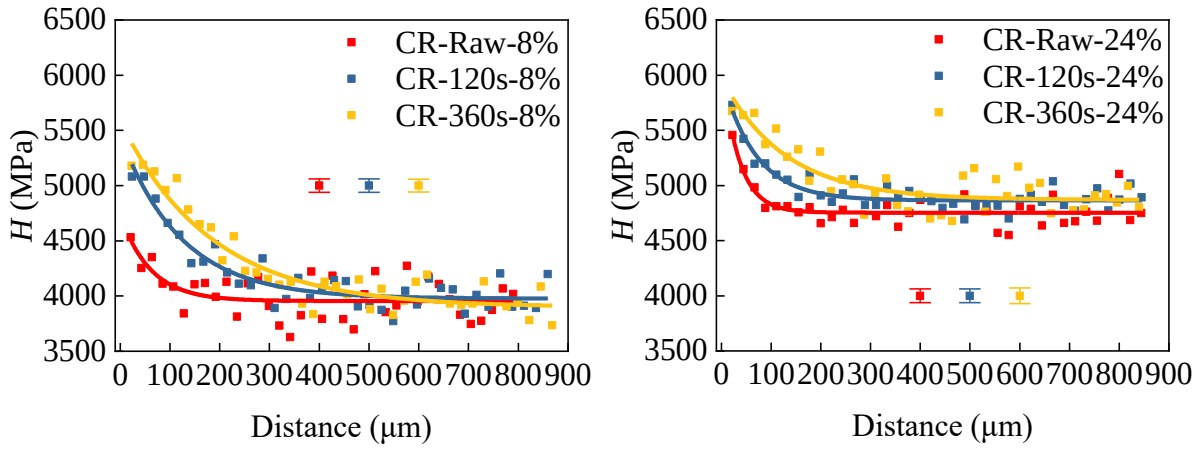

(e) (f)

Fig.4-25 The average responses of cold rolled samples along the distance from the shot peened surface (e) *H* for 8% tension strain (f) *H* for 24% tension strain. Three points besides the curves are represented to show the average error bar of each set.

(Continued)

One thing should be clarified. The matrix of indentation test positions is shown in Fig.4-23. Each point in Fig.4-25 represents the average response of 20 tests at the same distance, i.e., the tests in the same column in Fig.4-23. Accordingly, there is a dispersion for each point. The variation bars shown in Fig.4-25 are the average deviation for all the average responses along the depth, which can represent the average variation for all indentation tests in the matrix.

Fig.4-25(a) and (b) show P_{max} versus the distance from the surface. A higher P_{max} is observed near the shot peened surface, and then decreases to a stable level. This is consistent with the observations presented in Chapter 3 and in this chapter for KAM results. For the cold rolled raw sample with 8% tension strain, the gradient of P_{max} may be due to machining, for which the affected depth is around 210 μm (taken to 3 t, where t is the decay rate parameter in Tab.4-8). Shot peening results in a higher P_{max} near the surface. The value of P_{max} near the surface and the affected depth increase with the shot peening time. Everything is similar for the samples with 24% tensile strain. However, it could be noted that the affected depth decreases, no matter for raw samples or shot peened sample. This indicates that the residual stresses are relaxed with the increasing tension strain.

Fig.4-25(c) and (d) show *S* versus the distance from the surface. A lower *S* is observed near the shot peened surface, and then *S* increases to a stable level, which is also consistent with the results presented in Chapter 3. For samples with 8% tension strain, shot peening can increase the value of *S* near the surface. The affected depth for all three samples is around 150 μm, which is shallower than the depths on P_{max} and *H*. For samples with 24% tension strain, the difference caused by shot peening on *S* no longer exists.

Fig.4-25(e) and (f) show *H* versus the distance from surface. It is obvious that the effect of shot peening on *H* and P_{max} are quite similar: the gradient and the affected depths are similar, which indicates that *H* is mainly determined by P_{max}, while the projected contact area A_c does not play a major role.

Tab.4-8 Nanoindentation fitting parameters of cold rolled samples after tensile straining for different shot peening states

CR-8%						
P_{max}						
	A (mN)	$u(A)$ (mN)	t (μm)	$u(t)$ (μm)	y_0 (mN)	$u(y_0)$ (mN)
Raw	10.8	4.4	70	40	70.92	0.59
120s	23.2	1.8	150	22	70.18	0.59
360s	27.0	1.9	189	26	69.81	0.77
S						
	A (N/mm)	$u(A)$ (N/mm)	t (μm)	$u(t)$ (μm)	y_0 (N/mm)	$u(y_0)$ (N/mm)
Raw					965.1	2.1
120s					971.1	1.6
360s					979.7	1.6
H						
	A (MPa)	$u(A)$ (MPa)	t (μm)	$u(t)$ (μm)	y_0 (MPa)	$u(y_0)$ (MPa)
Raw	783	304	61	30	3955	34
120s	1477	137	123	18	3977	32
360s	1679	104	184	24	3898	44
CR-24%						
P_{max}						
	A (mN)	$u(A)$ (mN)	t (μm)	$u(t)$ (μm)	y_0 (mN)	$u(y_0)$ (mN)
Raw	18.0	5.5	38	12	83.96	0.34
120s	13.0	2.1	81	18	85.5	0.3
360s	16.7	2.3	127	29	85.7	0.59
S						
	A (N/mm)	$u(A)$ (N/mm)	t (μm)	$u(t)$ (μm)	y_0 (N/mm)	$u(y_0)$ (N/mm)
Raw					983.0	1.8
120s					964.1	1.0
360s					966.6	2.1
H						
	A (MPa)	$u(A)$ (MPa)	t (μm)	$u(t)$ (μm)	y_0 (MPa)	$u(y_0)$ (MPa)
Raw	1351	387	35	10	4753	21
120s	1124	142	52	11	4864	17
360s	1103	146	128	29	4870	38

Tab.4-9 Nanoindentation fitting parameters of printed samples after tensile straining for different shot-peening states

MF-5%						
P_{max}						
	A (mN)	$u(A)$ (mN)	t (μm)	$u(t)$ (μm)	y_0 (mN)	$u(y_0)$ (mN)
Raw	36.1	8.9	33.4	8.7	55.76	0.49
120s	32.1	2.6	121	17	57.22	0.69
360s	36.6	2.6	161	23	55.2	1.0

S						
	A (N/mm)	*u*(*A*) (N/mm)	*t* (μm)	*u*(*t*) (μm)	y_0 (N/mm)	*u*(y_0) (N/mm)
Raw					913.2	7.0
120s					928.7	5.0
360s					911.3	9.1
H						
	A (MPa)	*u*(*A*) (MPa)	*t* (μm)	*u*(*t*) (μm)	y_0 (MPa)	*u*(y_0) (MPa)
Raw	2188	466	31.0	6.8	3090	23
120s	1855	151	117	16	3195	38
360s	2077	131	148	18	3091	45
MF-15%						
P_{max}						
	A (mN)	*u*(*A*) (mN)	*t* (μm)	*u*(*t*) (μm)	y_0 (mN)	*u*(y_0) (mN)
Raw	41	28	21	12	64.55	0.75
120s	26.3	3.1	128	25	62.33	0.83
360s	31.7	2.4	123	17	60.65	0.71
S						
	A (N/mm)	*u*(*A*) (N/mm)	*t* (μm)	*u*(*t*) (μm)	y_0 (N/mm)	*u*(y_0) (N/mm)
Raw					899.5	7.8
120s					919.5	5.5
360s					896.9	4.8
H						
	A (MPa)	*u*(*A*) (MPa)	*t* (μm)	*u*(*t*) (μm)	y_0 (MPa)	*u*(y_0) (MPa)
Raw	2511	37	21.0	9.5	3636	37
120s	1616	194	106	19	3532	41
360s	1855	141	125	17	3379	42

The average indentation responses of printed samples along the distance from the shot peened surface are shown in Fig.4-26. The fitting parameters are listed in Tab.4-9.

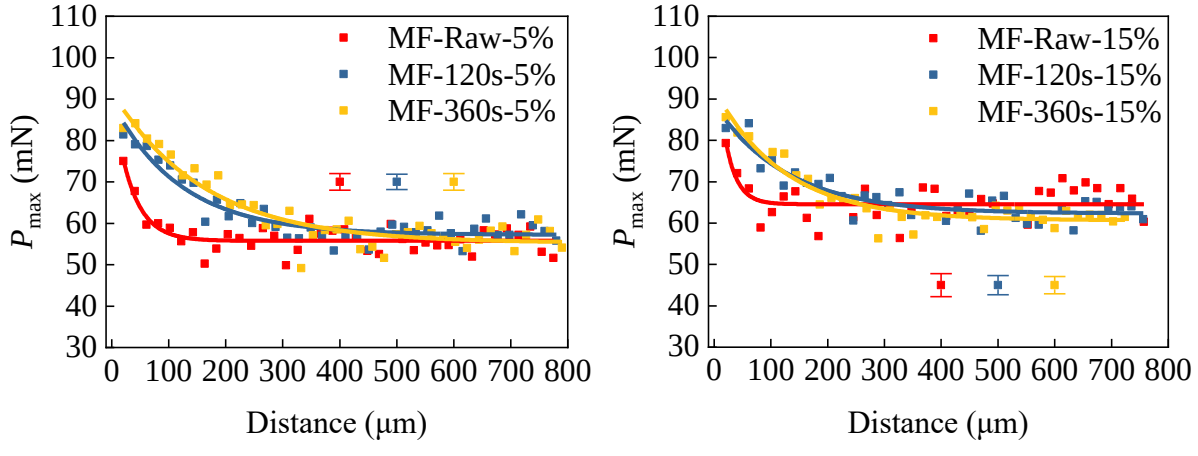

(a) (b)

Fig.4-26 The average responses of printed samples along the distance from the shot peened surface (a) P_{max} for 5% tension strain (b) P_{max} for 15% tension strain

(Continued on the next page)

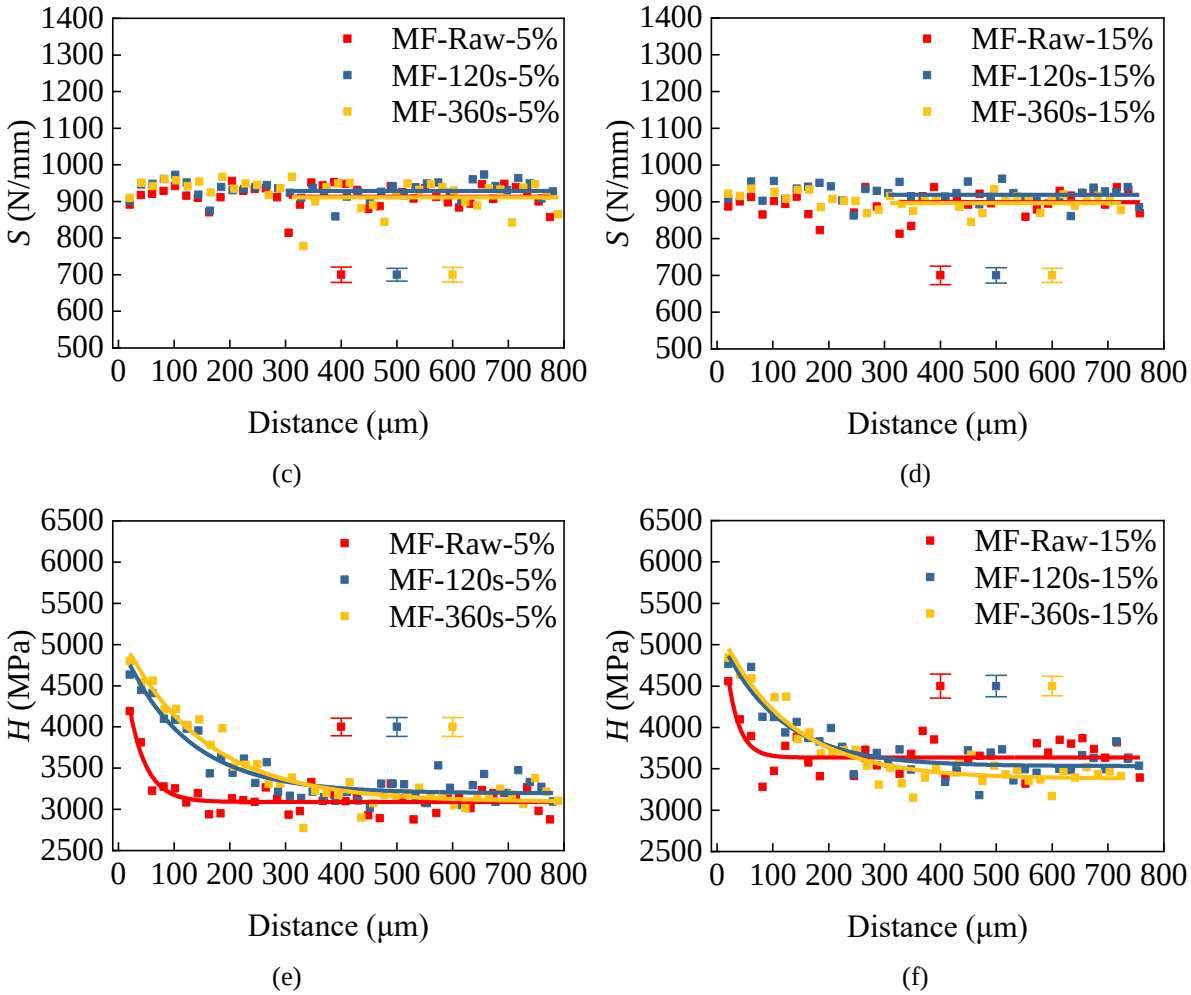

Fig.4-26 The average responses of printed samples along the distance from the shot peened surface (c) *S* for 5% tension strain (d) *S* for 15% tension strain (e) *H* for 5% tension strain (f) *H* for 15% tension strain (Continued)

Fig.4-26(a) and (b) show the average P_{max} versus the distance from the surface. Similarly to the cold rolled samples, shot peened samples have the higher P_{max} near the surface and the deeper affected depth. For samples with 5% tensile strain, the affected depth of P_{max} for the raw material due to machining is around 100 μm, and the affected depths for the shot peened samples 120s and 360s are 360 μm and 480 μm respectively. However, the influence of tensile strain level on printed samples is not as significant as that on cold rolled samples. When the strain level increases to 15%, the affected layer depth decreases but the change is smaller than the change observed on cold rolled sample. The decrease also indicates the relaxation of residual stress.

Fig.4-26(c) and (d) show the *S* profile. Unlike the cold rolled material, the printed material exhibits a constant *S* along the depth, regardless of whether shot peening has been applied or not, and regardless of the tensile strain level (a slight decrease can be observed with the naked eye on some of the Fig.4-25(c) and (d) and the Fig.4-26(c) and (d) but it is difficult to quantify objectively through a fitting or other means). This phenomenon is surprising. No matter considering the simulation results, or the edge effect mentioned in Chapter 3 (indentation position is close to the resin), the *S* value near shot peened surface should be lower. Further

investigation should be performed in future research. For instance, it is advisable to conduct indentation experiments in the depth direction away from the shot-peened surface. Furthermore, the interval between each indentation position along the depth direction should be smaller in order to obtain more detailed information about *S*.

Fig.4-26(e) and (f) show the *H* profile. Similarly to the cold rolled samples, the trend of *H* under different material state and tension strain level are similar to the trend of P_{max}.

Fig.4-27 shows the trend for the bulk material under different tensile level. It can be seen that P_{max} for bulk material increases with the tensile strain, while the samples subjected to higher tension strain exhibit a higher level of cumulative plastic strain. Besides, it is obvious that for the printed material, P_{max} in the bulk for the raw specimen is higher than that for the shot peened 120s sample, and it is the lowest for the shot peened 360s sample. This corresponds to the actual tensile strain level that they have. As shown in Fig.4-6(d), the raw material can be stretched to 15%, whereas the shot peened 120s sample and the shot peened 360s sample can only be stretched to 13% and 9% respectively.

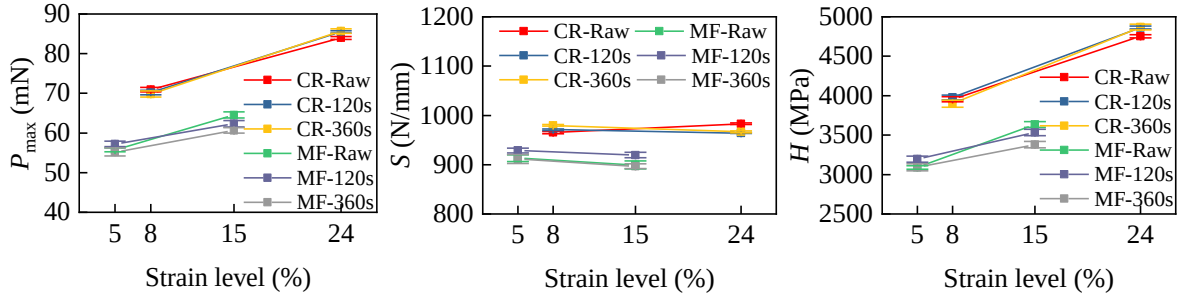

Fig.4-27 The average responses for tensile bulk material under different strain level (a) P_{max} (b) *S* (c) *H*

For the printed material, *S* in the bulk decreases slightly. However, *S* in the bulk stays nearly constant for cold rolled samples when the tensile strain level increases from 8% to 24%. This is different from the simulation results shown in Chapter 3. A possible reason for the discrepancy could be that *S* is almost saturated for the lower tensile strain. Another possible reason for the discrepancy might be that in the simulations, the assumptions that $b = \gamma$ are not suitable for the materials in this chapter. In addition, the inverse method uses the indentation responses only at one indention depth, i.e., the responses at only one representative strain. Using the results of a spherical indenter and different indentation depths to perform the inversion method may provide better results.

Furthermore, as mentioned above, the trend of *H* is similar with P_{max}. *H* for bulk material also increases with the tensile strain.

4.4. Cyclic test

4.4.1. The cyclic curves and key parameters

The cyclic tests ($R_\varepsilon = 0$) were also performed on Instron 8950 250 kN universal testing machine (Instron, UK). Two strain amplitudes, $\Delta\varepsilon/2 = 0.8\%$ (corresponding to a maximum strain of 1.6%) and $\Delta\varepsilon/2 = 0.4\%$ (corresponding to a maximum strain of 0.8%), are selected.

Similarly, the complete relaxation of residual stresses is expected to be observed after the high strain level, whereas the partial relaxation of residual stresses is expected to be observed after the low strain level.

The tests are stopped after the 10th cycle. Strain control was utilized with a rate of 1×10^{-3}/s to achieve the specified strain level, controlled with an extensometer and using a triangle signal. The cyclic curves of cold rolled and printed sample are shown in Fig.4-28 and Fig.4-29.

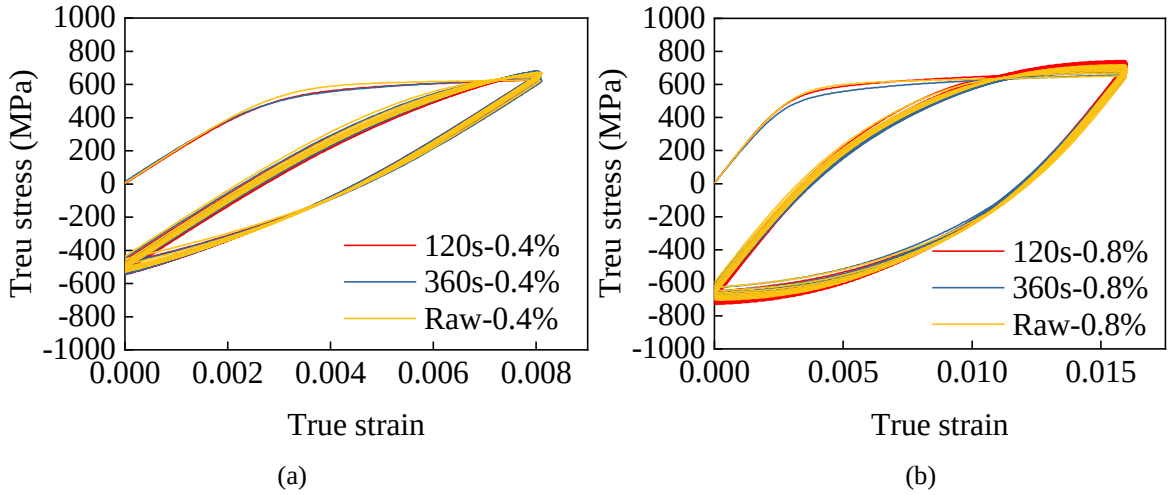

Fig.4-28 Cyclic curves of cold rolled sample (a) $\Delta\varepsilon/2 = 0.4\%$ (b) $\Delta\varepsilon/2 = 0.8\%$

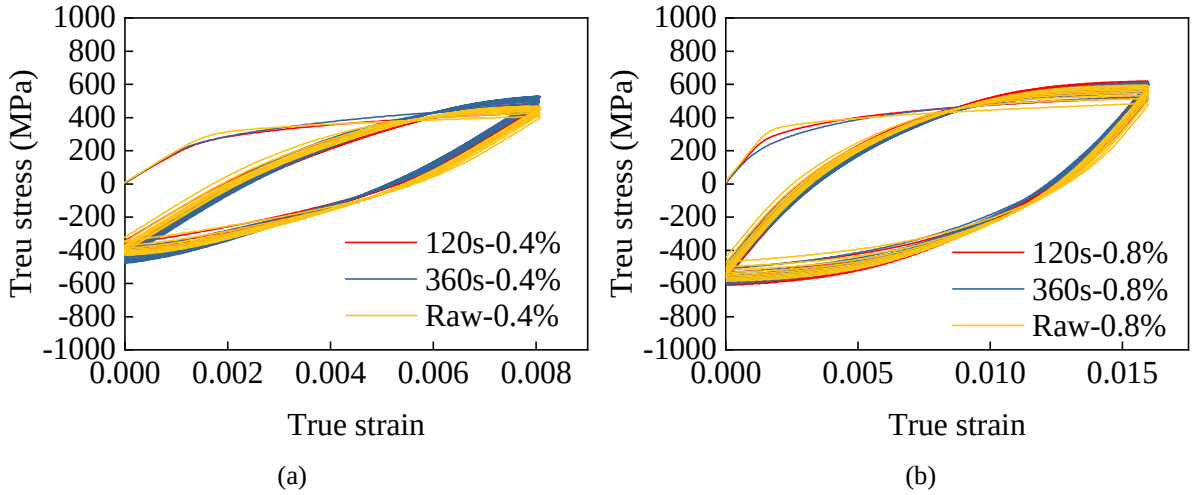

Fig.4-29 Cyclic curves of printed sample (a) $\Delta\varepsilon/2 = 0.4\%$ (b) $\Delta\varepsilon/2 = 0.8\%$

Fig.4-30 to Fig.4-34 show the five key parameters describing the cyclic tests versus the cumulative plastic strain: maximum stress, minimum stress, stress amplitude, mean stress and plastic strain amplitude.

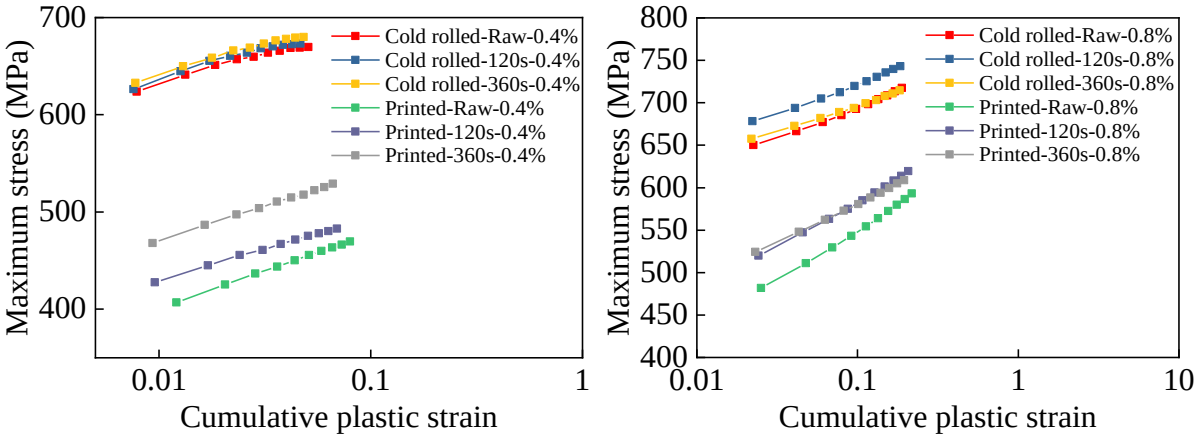

(a) (b)

Fig.4-30 Maximum stress versus cumulative plastic strain (a) $\Delta\varepsilon/2 = 0.4\%$ (b) $\Delta\varepsilon/2 = 0.8\%$

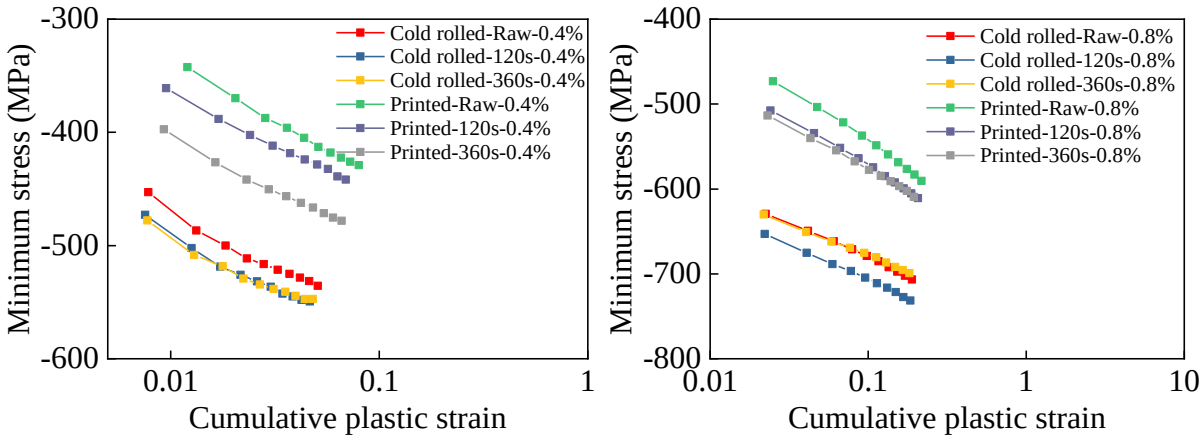

(a) (b)

Fig.4-31 Minimum stress versus cumulative plastic strain (a) $\Delta\varepsilon/2 = 0.4\%$ (b) $\Delta\varepsilon/2 = 0.8\%$

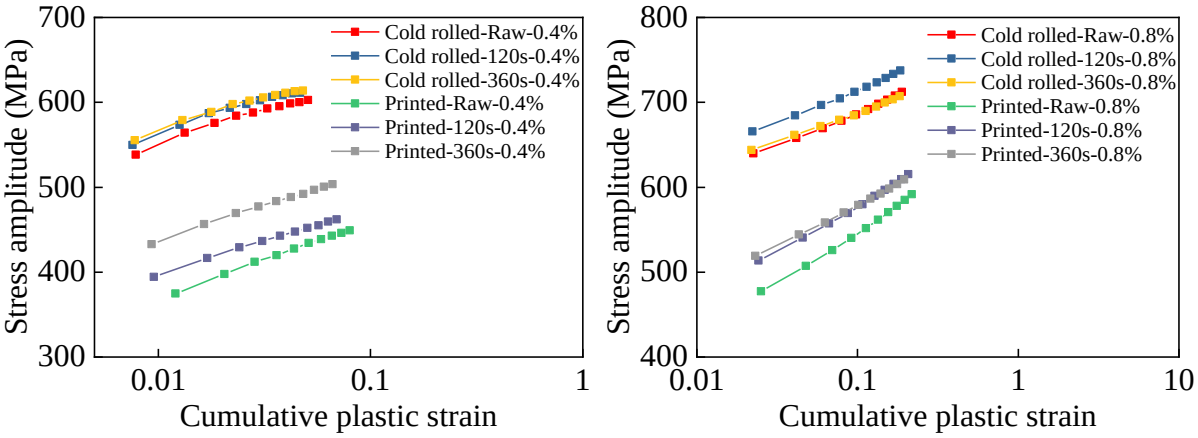

(a) (b)

Fig.4-32 Stress amplitude versus cumulative plastic strain (a) $\Delta\varepsilon/2 = 0.4\%$ (b) $\Delta\varepsilon/2 = 0.8\%$

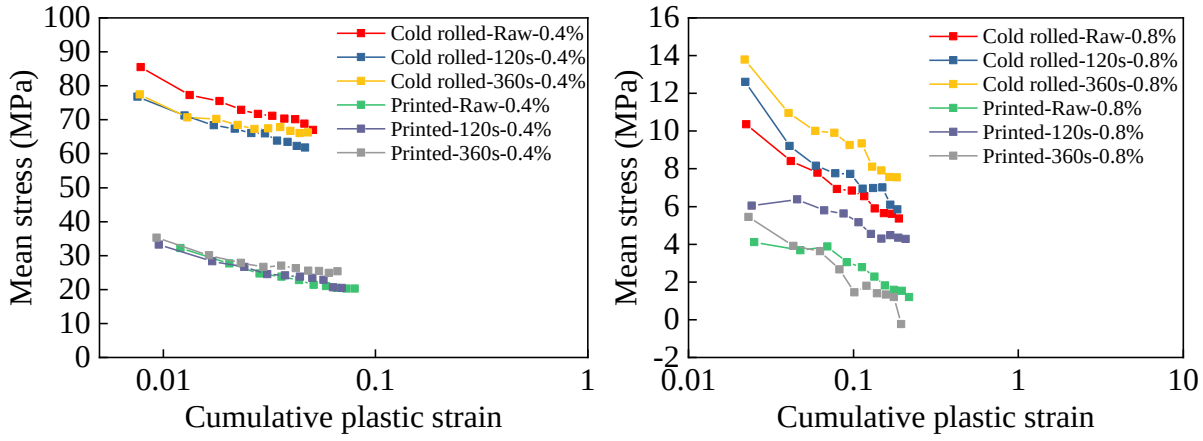

(a) (b)

Fig.4-33 Mean stress versus cumulative plastic strain (a) $\Delta\varepsilon/2 = 0.4\%$ (b) $\Delta\varepsilon/2 = 0.8\%$

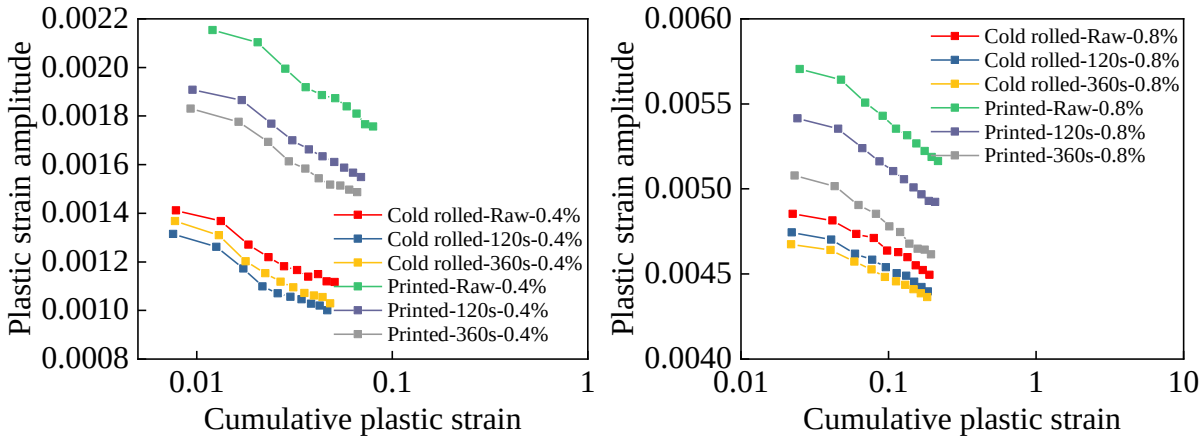

(a) (b)

Fig.4-34 Plastic strain amplitude versus cumulative plastic strain (a) $\Delta\varepsilon/2 = 0.4\%$ (b) $\Delta\varepsilon/2 = 0.8\%$

For both cold rolled and printed materials, the stress amplitude increases with the number of cycles which corresponds to a cyclic hardening. Correspondingly, the plastic strain amplitude is observed to decrease with the number of cycles and both materials tend towards adaptation or even towards elastic adaptation. However, the number of cycles is not sufficient to predict what will be the stabilized state. This implies that both materials work harden at the selected two strain levels in the 10 cycles. A higher strain level results in a lower mean stress while a lower strain level results in a higher mean stress [150]. For an amplitude of 0.4%, a slower relaxation of mean stress is observed at each cycle.

4.4.2. Analysis of the surface mechanical state by X-Ray diffraction

Fig.4-35 and Fig.4-36 show the surface residual stress state for cold rolled and printed samples before and after cyclic tests. It can be observed that the surface axial residual stresses are relaxed after 10 cycles for both strain levels. Concerning the hoop residual stress, the relaxation is observed only at the 0.8% strain level. However, for both cases, the relaxation is not yet complete, and some residual stress remains in the material.

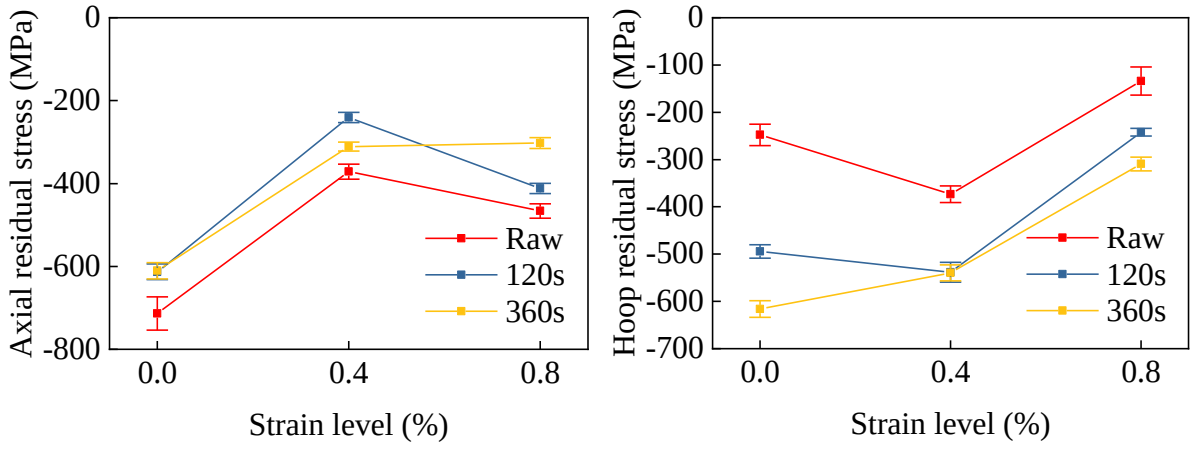

(a) (b)

Fig.4-35 Surface residual stress of cold rolled sample before and after 10 cycles (a) Axial residual stress (b) Hoop residual stress

(For the residual stress for no cyclic tests, the average value of the two samples is taken)

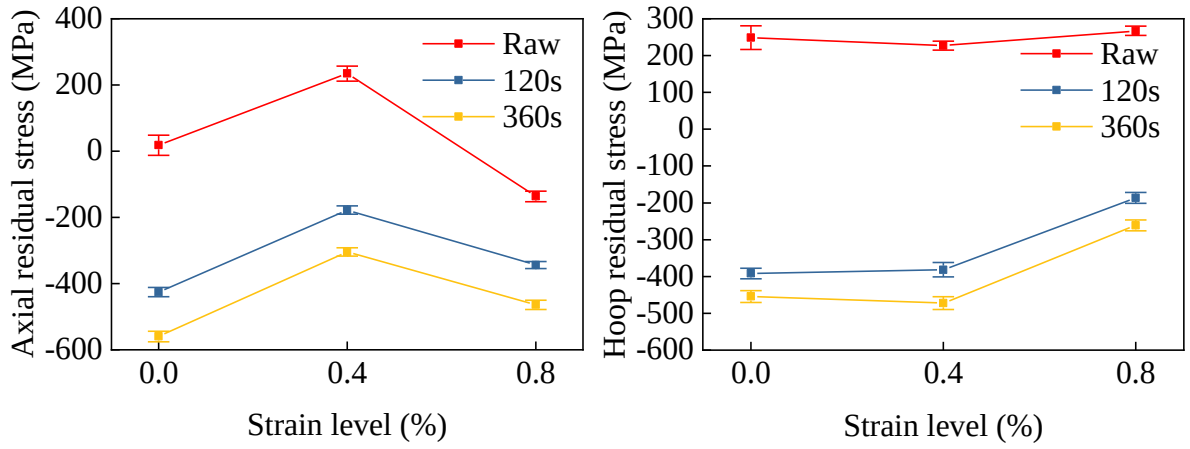

(a) (b)

Fig.4-36 Surface residual stress of printed sample before and after 10 cycles (a) Axial residual stress (b) Hoop residual stress

(For the residual stress for no cyclic tests, the average value of the two samples is taken)

Fig.4-37 show the surface peak width of cold rolled and printed samples before and after cyclic test. It can be seen that the surface peak width stays almost constant when the strain level is 0.4%. However, a decrease of surface peak width is observed in the case of 0.8% strain level. The peak width indicates cyclic softening. However, in the previous section it was shown that the stress amplitude increased, indicating cyclic hardening. This apparent contraction can be explained by the fact that the experimental stress amplitude concerns the whole cross section of the sample, while the X-ray diffraction concerns the surface (about 5 μm). Similarly, the surface peak widths here are also affected by the initial machining of the specimens. Due to shot peening or machining (for raw samples), the dislocation density at the surface is much higher than in the bulk. Since peak widths are sensitive to dislocation density and dislocation structure [151], it is likely that cyclic loading has induced reorganization of the dislocations in the surface layers. The peak width variation of the bulk, which was not affected by machining or shot peening may be different.

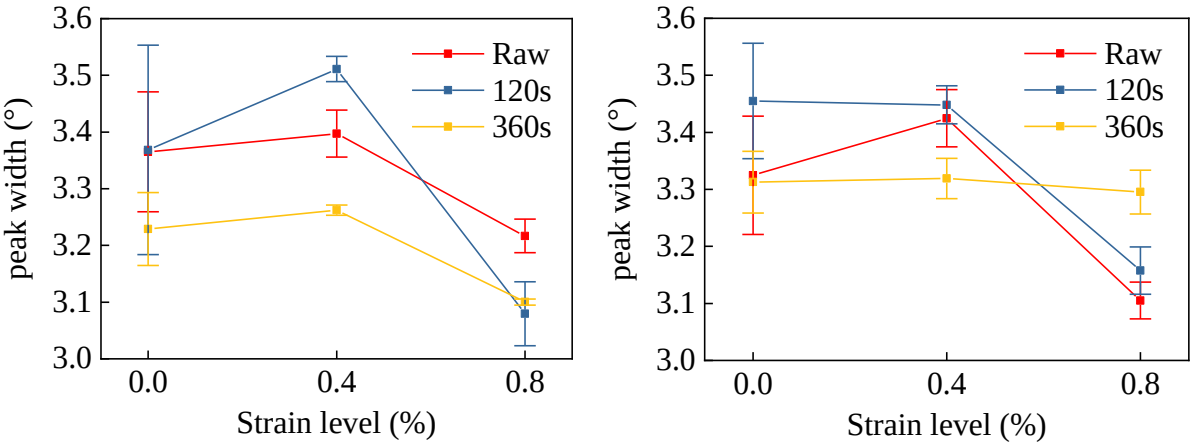

Fig.4-37 Surface peak width of (a) cold rolled sample (b) printed sample before and after cyclic test (Only the peak widths in axial direction, for the peak values of no cyclic test, the average value of the two samples was taken)

4.4.3. Analysis of dislocation evolution at longitudinal section

The statistical KAM data for cold rolled samples after 10 cycles is shown in Fig.4-38, and the fitting parameters are shown in Fig.4-10.

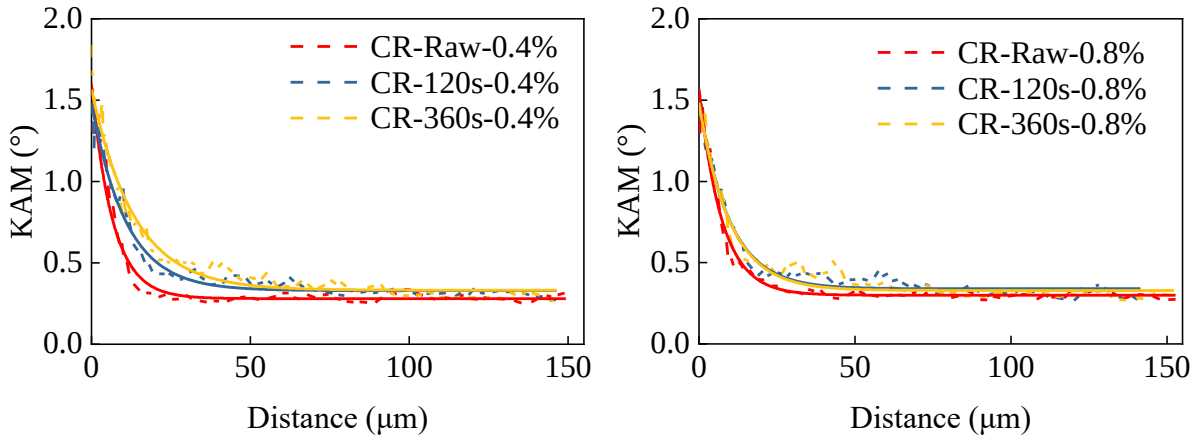

(a) (b)

Fig.4-38 The statistical KAM data of cold rolled samples after 10 cycles (a) $\Delta/2 = 0.4\%$ (b) $\Delta/2 = 0.8\%$

In the case of 0.4% strain level, the affected depth for raw material due to machining is around $3t \approx 20$ μm, which is deeper than that for raw material after 8% strain with the tensile test (around $3t \approx 8$ μm). In addition, the depth of the affected layer for shot peening 120s and 360s sample is around $3t \approx 33$ μm and 40 μm, respectively. When the strain level increases to 0.8%, the affected layer depth for shot peened samples caused by shot peening decreases while the affected layer depth for raw material caused by machining increases. Therefore, the differences of the affected layer depth between the raw material and shot peened samples is diminished, which are around $3t \approx 22$ μm, 29 μm and 30 μm respectively.

Tab.4-10 KAM fitting parameters of the cold rolled samples after 10 cycles at strain level of 0.4% or 0.8%

CR-0.4%						
	A (mN)	$u(A)$ (mN)	t (μm)	$u(t)$ (μm)	y_0 (mN)	$u(y_0)$ (mN)
Raw	1.320	0.011	6.625	0.080	0.2803	0.0013
120s	1.1544	0.0083	10.84	0.12	0.3297	0.0014
360s	1.2334	0.0092	13.48	0.16	0.3322	0.0018
CR-0.8%						
	A (mN)	$u(A)$ (mN)	t (μm)	$u(t)$ (μm)	y_0 (mN)	$u(y_0)$ (mN)
Raw	1.2699	0.0076	7.307	0.066	0.29950	0.00094
120s	1.143	0.010	9.80	0.13	0.3394	0.0016
360s	1.154	0.012	9.89	0.16	0.3290	0.0018

The statistical KAM data for printed samples under cyclic tests is shown in Fig.4-39, and the fitting parameters are shown in Tab.4-11. In the case of 0.4% strain level, the affected layer depths for raw material due to machining is around $3t \approx 30$ μm, which is deeper than that for cold rolled material (around 20 μm). This corresponds to the observation in tensile test, which means that the printed material is easier to be affected by the surface treatment process (such as machining and shot peening) compared to the cold rolled material. In addition, the depth of the affected layer for shot peening 120s and 360s sample is around $3t \approx 57$ μm and 69 μm, respectively. In the case of 0.8% strain level, different with the cold rolled samples, the affected layer depth of raw material, shot peened 120s sample and shot peened 360s sample increases. The difference of affected layer depth caused by two shot peening times remains clear.

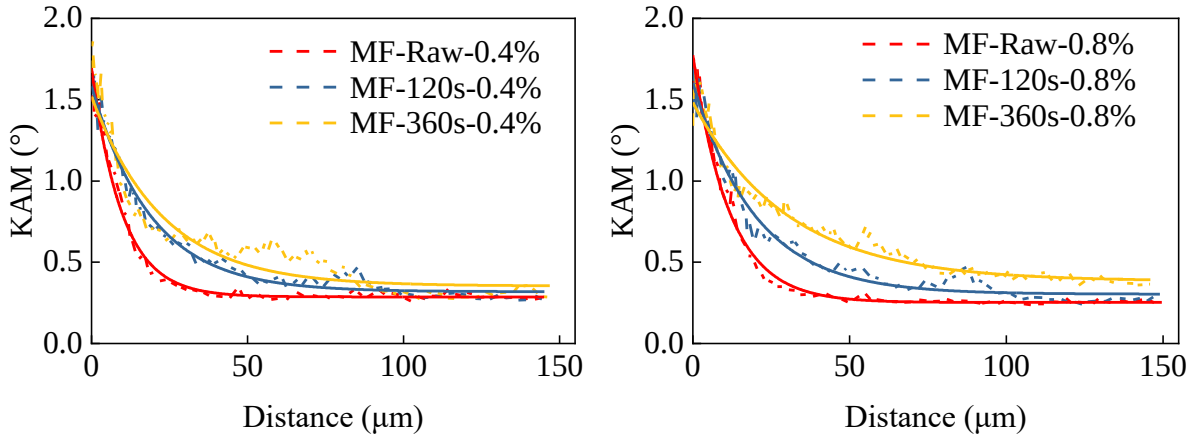

(a) (b)

Fig.4-39 The statistical KAM data of printed samples after 10 cycles (a) $\Delta\varepsilon/2 = 0.4\%$ (b) $\Delta\varepsilon/2 = 0.8\%$

Tab.4-11 KAM fitting parameters of printed samples after 10 cycles at strain level of 0.4% or 0.8%

MF-0.4%						
	A (mN)	$u(A)$ (mN)	t (μm)	$u(t)$ (μm)	y_0 (mN)	$u(y_0)$ (mN)
Raw	1.4081	0.0069	9.744	0.073	0.2867	0.0011
120s	1.2635	0.0072	19.04	0.19	0.3184	0.0019
360s	1.166	0.014	22.67	0.52	0.3535	0.0045

MF-0.8%						
	A (mN)	$u(A)$ (mN)	t (μm)	$u(t)$ (μm)	y_0 (mN)	$u(y_0)$ (mN)
Raw	1.5224	0.0065	11.661	0.079	0.2523	0.0011
120s	1.2994	0.0083	20.07	0.23	0.3033	0.0022
360s	1.0993	0.0067	30.30	0.41	0.3827	0.0031

Furthermore, it can be seen that the dislocation evolution under tensile test and cyclic test are not the same. Taking the cold rolled sample as an example, the average bulk KAM value after cyclic tests and tensile tests are shown in Fig.4-40. The trend of printed samples is similar with that of the cold rolled samples.

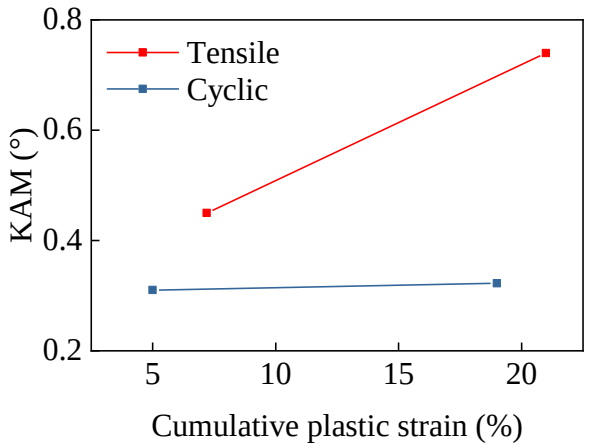

Fig.4-40 The average bulk KAM value of cold rolled samples after tensile and cyclic tests. The KAM values are the average value of raw material, shot peened 120s material and shot peened 360s material

The cumulative plastic strain after 10 cycles with 0.4% strain level and 0.8% strain level is 5% and 19% respectively. While the cumulative plastic strain after tensile test with 8% strain level and 24% strain level is 7.2% and 21% respectively. The bulk KAM values increase with the cumulative plastic strain under tensile test whereas the bulk KAM values stay as constant under cyclic test. Moreover, in the case of the cyclic test at 0.8%, the cyclic cumulative plastic strain is higher than that in tensile test with 8% strain level. However, the bulk KAM value of cyclic test (around 0.3°) is quite lower than that of tensile test (around 0.45°). Just like the difference that was observed between calibration on a tensile test and results on shot peening (Fig. 3.35, showing the difference between nanoindentation and X-ray diffraction), these results show that a calibration of KAM versus plastic strain cannot not be absolute but depends on the loading path (uniaxial vs non-proportional, monotonic vs cyclic).

4.4.4. Analysis of nanoindentation on longitudinal section

The average responses of cold rolled samples along the distance from the shot peened surface after cyclic tests are shown in Fig.4-41.

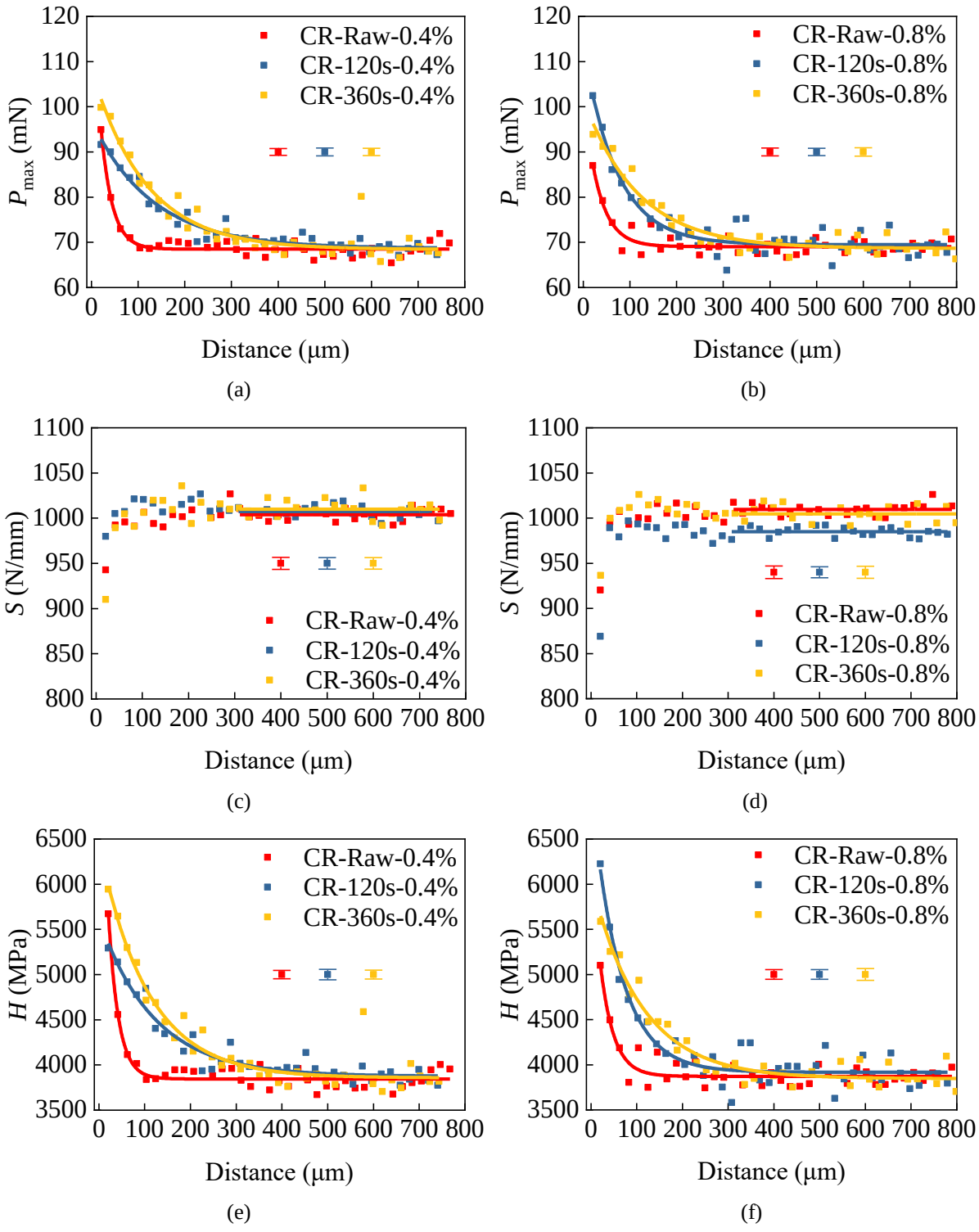

Fig.4-41 The average responses of cold rolled samples along the distance from the shot peened surface (a) P_{max} for 0.4% strain level (b) P_{max} for 0.8% strain level (c) S for 0.4% strain level (d) S for 0.8% strain level (e) H for 0.4% strain level (f) H for 0.8% strain level

The trends are also fitted with an exponential decay function. Similarly, the data for S beyond 300 μm is used to represent the average response for bulk material. The fitting parameters are shown in Tab.4-12.

It can be seen in Fig.4-41 that the trend of indentation responses is similar to the observation in tensile test. Specifically, the shot peened samples have a deeper affected layer

and a higher P_{max} and H. H is mainly determined by P_{max} thus these two variables have a similar profile along the depth. The drop of S value near the surface also exists in these two cases. In addition, there is no difference in the affected layer depth of S for the two shot peened conditions. The affected layer is less than 100 μm, which is lower than that in the tensile test.

For the 0.8% strain level, the sample shot peened for 120s has the maximum P_{max} and H, and the minimum S, which is not as expected. However, this is consistent with the trend shown in Fig.4-32, which indicates that the 120s shot peened sample has the highest stress amplitude. This indicated that the material property for shot peened 120s sample is different from others.

The affected layer depth of P_{max} for raw material ($3t$) caused by machining at two strain levels are around 70 μm and 100 μm respectively. The affected layer depths for two shot peened samples at the 0.4% strain level are around 390 μm and 345 μm respectively, whereas the affected depths at 0.8% strain level are only around 220 μm and 350 μm respectively. Taking the cold rolled sample with 0.4% strain level (shot peened 120s) as an example. The normalized P_{max} and KAM values (Values standardized to between 0 and 1) along the distance away from the sample surface are shown in Fig.4-42. It can be clearly seen from the figure that the affected depth of misorientation, i.e. the work hardening, tends to be stable at around 33 μm ($3t$, with fitting parameters, t = 10.84, shown in Fig.4-10. However, the affected depth on P_{max} is quite deeper than the work hardening. It is known that P_{max} is affected by both work hardening and residual stress. Therefore, it can be concluded that the affected P_{max} in the distance beyond 33 μm is only affected by residual stress.

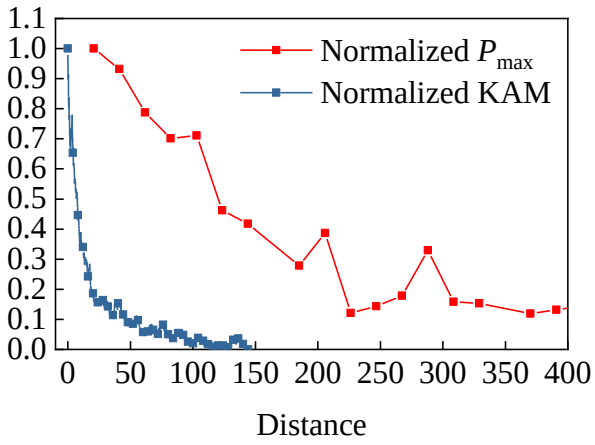

Fig.4-42 The normalized P_{max} and KAM values along the distance away from the sample surface

The affected layer depth of P_{max} decreases from 390 μm to 220 μm for shot peened 120s sample, which means that residual stress relaxation is more significant at the 0.8% strain level than at the 0.4% strain level. However, no obvious difference is observed for shot peened 360s samples.

Tab.4-12 Nanoindentation fitting parameters of the cold rolled samples after 10 cycles at strain level of 0.4% or 0.8%

CR-0.4%						
	P_{max}					
	A (mN)	$u(A)$ (mN)	t (μm)	$u(t)$ (μm)	y_0 (mN)	$u(y_0)$ (mN)
Raw	61.9	8.3	24.4	3.0	68.49	0.28
120s	28.3	1.5	131	13	68.70	0.47
360s	68.4	2.7	115	13	68.43	0.69
	S					
	A (N/mm)	$u(A)$ (N/mm)	t (μm)	$u(t)$ (μm)	y_0 (N/mm)	$u(y_0)$ (N/mm)
Raw					1004.0	1.3
120s					1007.5	1.5
360s					1010.0	2.0
	H					
	A (MPa)	$u(A)$ (MPa)	t (μm)	$u(t)$ (μm)	y_0 (MPa)	$u(y_0)$ (MPa)
Raw	4632	600	22	2.5	3845	17
120s	1741	104	121	13	3875	30
360s	2569	170	107	12	3857	40
CR-0.8%						
	P_{max}					
	A (mN)	$u(A)$ (mN)	t (μm)	$u(t)$ (μm)	y_0 (mN)	$u(y_0)$ (mN)
Raw	34.03	6.1	32.7	6.2	69.05	0.33
120s	43.7	3.8	72.2	8.7	69.49	0.54
360s	33.0	2.1	117	13	68.66	0.57
	S					
	A (N/mm)	$u(A)$ (N/mm)	t (μm)	$u(t)$ (μm)	y_0 (N/mm)	$u(y_0)$ (N/mm)
Raw					1009.7	1.3
120s					984.8	1.1
360s					1004.6	2.1
	H					
	A (MPa)	$u(A)$ (MPa)	t (μm)	$u(t)$ (μm)	y_0 (MPa)	$u(y_0)$ (MPa)
Raw	2499	441	29.3	5.2	3872	20
120s	3118	262	62.6	6.9	3917	32
360s	2175	130	111	11	3847	33

Tab.4-13 Nanoindentation fitting parameters of the printed samples after 10 cycles at strain level of 0.4% or 0.8%

MF-0.4%						
	P_{max}					
	A (mN)	$u(A)$ (mN)	t (μm)	$u(t)$ (μm)	y_0 (mN)	$u(y_0)$ (mN)
Raw	59.3	7.0	32.3	4.0	57.45	0.39
120s	46.2	2.6	129	13	57.96	0.79
360s	56.1	3.4	159	20	54.8	1.5
	S					
	A (N/mm)	$u(A)$ (N/mm)	t (μm)	$u(t)$ (μm)	y_0 (N/mm)	$u(y_0)$ (N/mm)
Raw					965.2	3.7
120s					967.7	6.2
360s					935.0	9.1
	H					
	A (MPa)	$u(A)$ (MPa)	t (μm)	$u(t)$ (μm)	y_0 (MPa)	$u(y_0)$ (MPa)
Raw	3935	510	29.7	3.9	3260	25
120s	3102	147	111.9	9.0	3313	37
360s	3318	171	158	17	3135	73

MF-0.8%						
P_{max}						
	A (mN)	$u(A)$ (mN)	t (μm)	$u(t)$ (μm)	y_0 (mN)	$u(y_0)$ (mN)
Raw	52.4	7.9	39.1	6.6	59.74	0.55
120s	38.3	2.4	159	21	57.96	0.98
360s	54.6	3.1	139	15	58.7	1.0
S						
	A (N/mm)	$u(A)$ (N/mm)	t (μm)	$u(t)$ (μm)	y_0 (N/mm)	$u(y_0)$ (N/mm)
Raw					930.8	8.2
120s					941.0	6.9
360s					905.1	6.5
H						
	A (MPa)	$u(A)$ (MPa)	t (μm)	$u(t)$ (μm)	y_0 (MPa)	$u(y_0)$ (MPa)
Raw	3768	399	32.8	3.7	3438	22
120s	2248	151	150	20	3329	57
360s	3302	157	135	12	3381	50

The average responses of the printed samples along the distance from the shot peened surface are shown in Fig.4-43. The fitting parameters are shown in Tab.4-13.

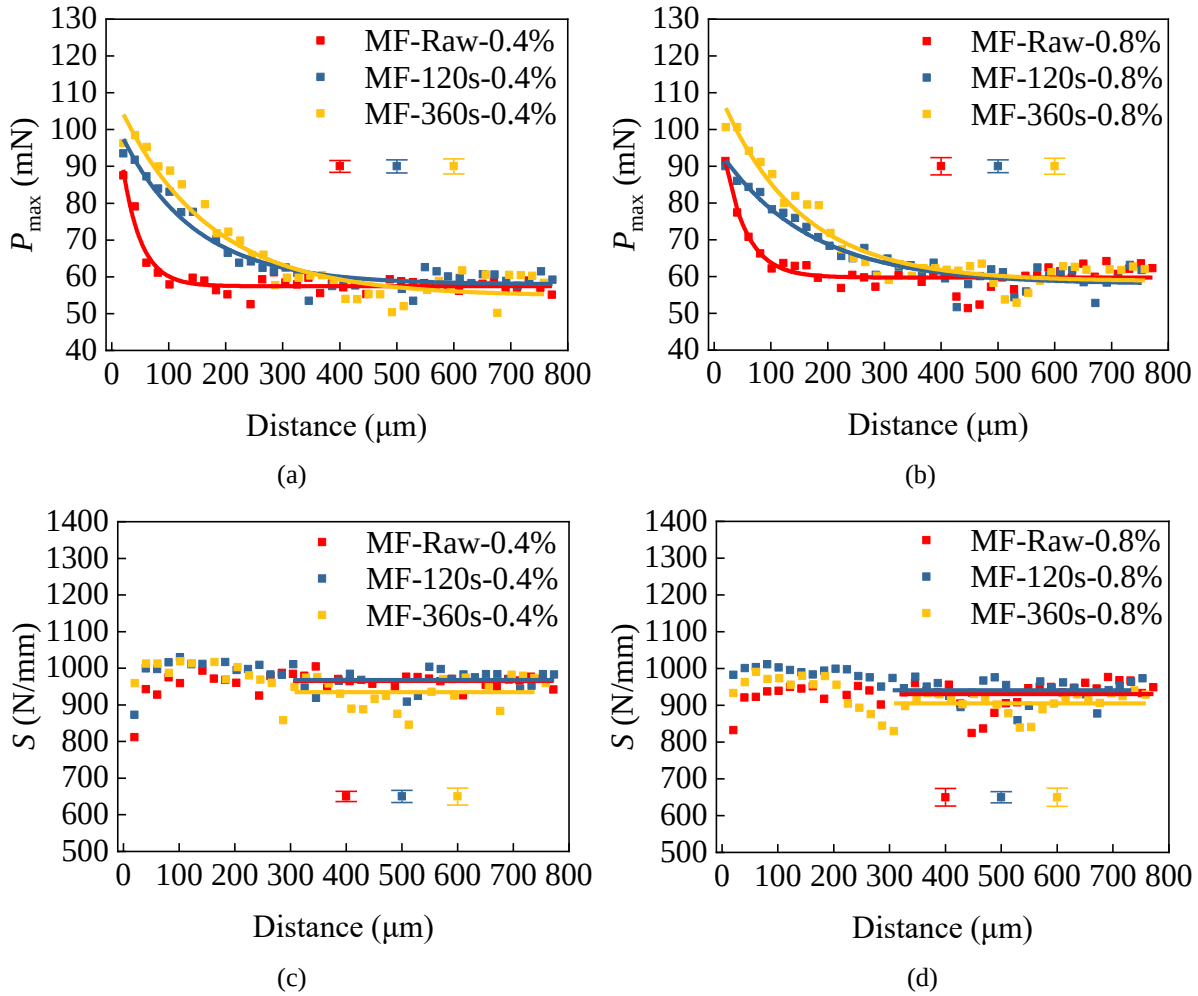

Fig.4-43 The average responses of the printed samples along the distance from the shot peened surface (a) P_{max} for 0.4% strain level (b) P_{max} for 0.8% strain level (c) S for 0.4% strain level (d) S for 0.8% strain level

(Continued on the next page)

The affected layer depths of P_{max} for the two shot peened samples at 0.4% strain level are around 390 μm and 480 μm respectively, which is deeper than for cold rolled samples. After

10 cycles with 0.8% strain level, the affected layer depths for the two shot peened samples are around 480 μm and 420 μm respectively.

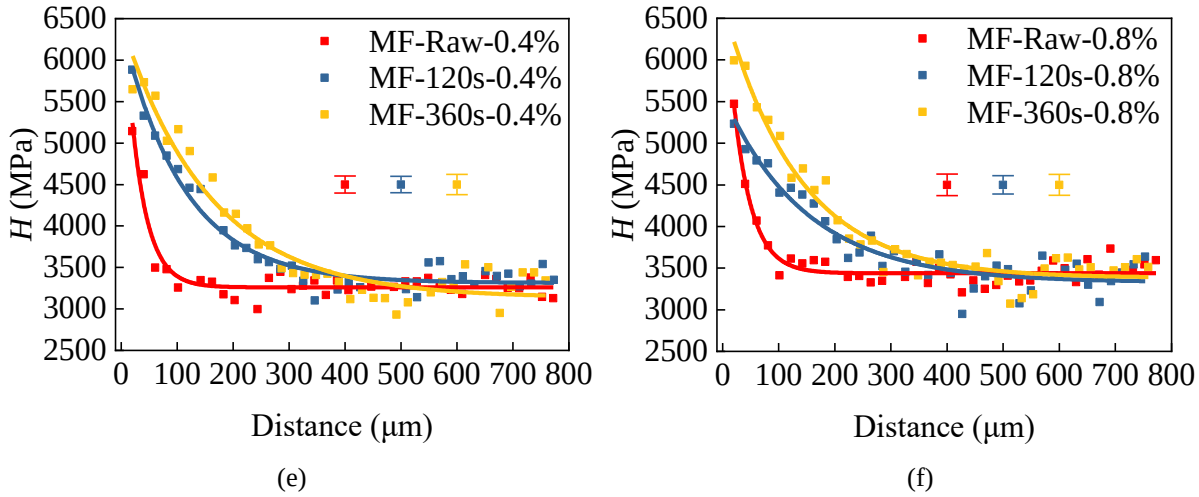

(e) (f)

Fig.4-43 The average responses of the printed samples along the distance from the shot peened surface (e) *H* for 0.4% strain level (f) *H* for 0.8% strain level

(Continued)

In addition, the longer shot peening time still results in a higher degree of work hardening, as shown in Fig.4-39. Therefore, in the combined effect of residual stress and work hardening, the differences between the profiles (P_{max} and *H*) near the surface, upon the distance of 100 μm is more significant than the cold rolled sample shown in Fig.4-41.

Similarly, the slight decrease of affected layer depths of P_{max} (from 480 μm to 420 μm) for shot peened 360s indicates that the residual stress relaxation is more significant at 0.8% strain level than at 0.4% strain level. However, no obvious difference is observed for shot peened 120s samples.

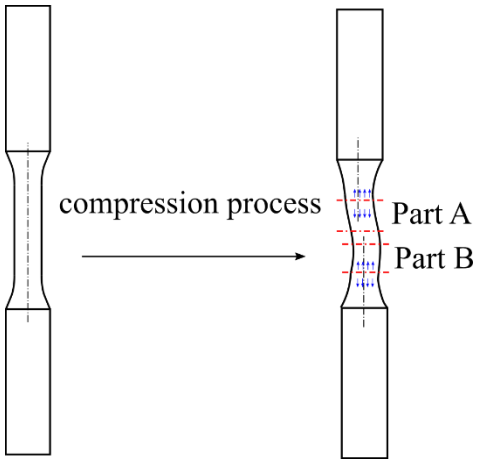

Fig.4-44 The buckling in cyclic test (The schematic is an exaggeration of the buckling)

A more significant residual stress relaxation should be observed under the 0.8% strain level, which is the strain level that has the higher cyclic amplitude. However, for the shot peened 360s cold rolled sample and shot peened 120s printed sample, the difference on residual stress relaxation under two strain levels is not observed. A possible reason may be due to buckling. A slight buckling was observed during the cyclic tests, as shown in Fig.4-44. This buckling exhibited a form that differed from that of a common slender rod. Therefore, it can be assumed

that the macro deformation is still in the global tensile direction, as indicated by the blue arrows in Fig.4-44. However, nanoindentation is a technique providing local properties, which can be affected by the complex deformation path due to the buckling. For instance, the small cylinders Part A and Part B cut off from the sample will have different nanoindentation responses.

Moreover, Fig.4-45 shows the trend for cyclic bulk material under different tension level. The cumulative plastic strain of the cold rolled samples at 0.4% and 0.8% strain levels is approximately 0.05 and 0.19, respectively. Whereas the cumulative plastic strain of the printed samples at 0.4% and 0.8% strain levels is approximately 0.07 and 0.21, respectively.

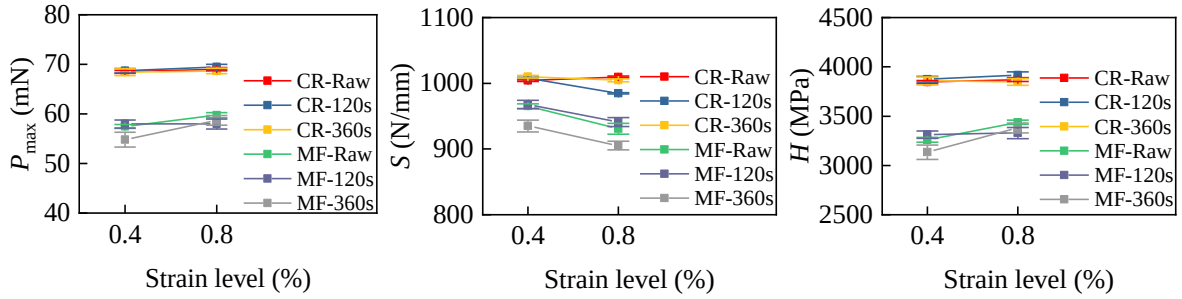

Fig.4-45 The average responses for cyclic bulk material under different strain level (a) P_{max} (b) S (c) H

There is a significant increase on the cumulative plastic strain. However, the significant increase of the cumulative plastic strain does not result in the increase of the P_{max} and H of the bulk material. This also implies that the evolutions observed in the cyclic test and the monotonic tensile tests are not identical. Besides, S remains stable for the cold rolled sample and shows a slight decrease for the printed sample.

4.5. Conclusion

Due to its good strength, ductility, corrosion resistance and high temperature performance, Inconel 625 alloy is widely used in engineering field. A series of mechanical and characterization tests on the printed and commercial cold rolled Inconel 625 treated by two different shot peening times was presented in this chapter.

The printed Inconel 625 was built as a cylinder and subsequently machined to the designed sample geometry. No difference in the elastic modulus between the printed and cold rolled material was observed. However, the plastic behavior differs significantly. The cold rolled material has a higher ultimate tensile stress, elongation rate and yield stress at 0.2% plastic strain, with the values of 1469 MPa, 42% and 630 MPa, respectively, compared to the printed material, which has the values of 1077 MPa, 27% and 368 MPa, respectively. Besides, necking was observed for the cold rolled material, while fracture occurred instantly for the printed material. The IPF indicates that the grain size of the printed samples is larger than for the cold rolled samples. In addition, for the cold rolled material, some recrystallized grains are observed due to segregation during the cold rolling and annealing process; for printed material, a notable degree of porosity was observed.

These two materials were shot peened with two treatment times, 120s and 360s. Subsequently, monotonic tensile tests and cyclic tests were performed on these samples. For the monotonic tensile test, 8% and 24% were selected for the cold rolled samples, and 5% and 15% were selected for printed material. In which, the higher strain level is approximately half of the ultimate tensile strain and the lower strain level is one-third of the high level. $\Delta\varepsilon/2 = 0.4\%$ and $\Delta\varepsilon/2 = 0.8\%$ were selected for the cyclic tests, with R_ε equals 0 and the tests were stopped after 10 cycles.

The tensile stress-strain curves indicate that the shot peening process does not affect the elastic properties. However, the elastic-plastic transition region is affected by the shot peening process. The 0.2% yield stress of shot-peened cold rolled samples is lower than that of the raw material, whereas the yield stress of printed sample is found to be constant in comparison to the raw material. In the fully plastic region, the stress of shot peened cold rolled sample increases slightly, however the increase is more significant for the shot peened printed sample. In addition, shot peening leads to an earlier fracture for the printed sample, for which the fracture occurs at around 13% strain for the shot peened 120s sample and 9% strain for the shot peened 360s sample. The KAM maps show that the misorientation that occurred during the tensile test is mainly distributed around the pores. Thus, the combined effect of positive residual stress in the bulk material and stress concentration near the pores results in the earlier fracture. The cyclic stress-strain curve indicates that both materials were hardened during cyclic tests. Besides, mean stress relaxation also occurs.

A compressive axial residual stress was observed for the non-shot peened cold rolled sample, which is affected by machining. Meanwhile, compressive residual stress also exists in the shot peened samples. After tensile tests, tensile residual stress was observed for both cold rolled and printed samples, which is due to the incompatible strains between the shot peened zone and core zone. After cyclic tests, the residual stress relaxation occurs. However, the relaxation is not complete and some residual stress remains in the material. In the tensile test, the surface peak widths of cold rolled sample increase with the tensile strain, while the surface peak widths for printed samples remain constant. In the cyclic test, for both two materials, the surface peak widths remain constant at 0.4% strain level and a decrease was observed at 0.8% strain level. It is likely that the relaxation is due to the reorganization of dislocations in the surface layers. Moreover, all the peak widths shown in this chapter are all already affected by the machining. A further investigation of the peak width, carried out in the absence of machining effect, will provide information regarding the change in peak width under tensile and cyclic tests.

The KAM map shows the dislocation distribution in the samples. The map indicates that machining does introduce work hardening to the material, but the depth of the affected layer is shallower than that of the shot peened layer. For both cold rolled and printed samples, the effect of shot peening remains after the low strain level tensile test, i.e., the longer shot peening time results in a deeper affected layer and a higher degree of misorientation. The difference between the two shot peening conditions no longer exists after the high strain level tensile test. The

misorientation caused by the large plastic deformation tends to play the major role. Similar phenomenon was also observed for the cold rolled sample in cyclic tests. However, for printed samples, the difference of affected layer depth cause by two shot peening times can also remain after the 0.8% strain level cyclic test. Moreover, it was observed that the affected layer of work hardening is shallower than 100 μm.

The responses of nanoindentation could reflect the residual stress and work hardening evolution during the tensile test and cyclic test. It was observed that the profile of P_{max} and H for all the samples are quite similar, which indicates that, for this material, H is mainly determined by P_{max}, and the projected contact area does play a major role. Corresponding with the KAM profile, no matter for tensile test or cyclic test, the effect of shot peening remains after the low strain level test. The longer shot peening time results in a higher P_{max} value and a deeper affected layer depth. For both materials, the affected depth decreases after the high strain level test. In cyclic test, for the shot peened 120s cold rolled samples and shot peened 360s printed samples, the affected layer of P_{max} after the 0.8% strain level is shallower than that after the 0.4% strain level. This indicates a more significant residual stress relaxation under 0.8% strain level.

S profiles show a different trend in the tests. A drop of S value close to the surface was observed for most samples under tensile test and cyclic test, which is consistent with the observations in Chapter 3. However, it could be seen that for printed sample under tensile test, S value stays constant along the distance, which cannot be explained by neither the simulation results in Chapter 3 nor by the edge effect. A further investigation that carries more nanoindentation tests near the shot peened surface could give us more information.

The responses of the bulk material represent the change of the material under the tensile and cyclic test. For tensile test, P_{max} and H for all the samples increase with the cumulative plastic strain. However, for cyclic test, the increase of cumulative plastic strain does result in a significant increase of P_{max} and H. This reflects that material evolution in tensile test and cyclic test are different.

Chapter 5
Conclusions and perspectives

5.1. Overview of the thesis

Shot peening is an effective method for enhancing the fatigue performance of materials, as it can introduce compressive residual stress to a specific depth of the material. Additionally, shot peening can also induce work hardening. Both residual stress and work hardening can influence the material fatigue performance. This coupling makes it challenging to conduct in-depth investigations. Two issues are mainly focused on in this thesis. The first issue is to develop a method to characterize residual stresses and work hardening simultaneously. The second issue is to investigate the evolution of residual stress and work hardening during the monotonic tensile test and cyclic test. This investigation used several mature characterization techniques, i.e., X-ray diffraction (XRD), Electron backscatter diffraction (EBSD) and Instrument indentation technique, in order to have a comprehensive view on the evolution of residual stress and work hardening.

First, some techniques that could be used in residual stress or work hardening characterization were introduced in Chapter 1. For residual stress measurement, X-ray diffraction method is a quite mature technique to measure the residual stress using lattice spacing. Work hardening can be represented by the dislocation density. Therefore, the characterization of work hardening is considered, in the frame of the present work, equivalent to the characterization of dislocation densities and arrangement. EBSD technique uses CCD camera to collect the Kikuchi patterns which formed by the diffracted backscattered electrons. The Kikuchi patterns can be indexed and thus provide information about the grain orientations. The density of geometrically necessary dislocations (GND) can be represented by the misorientation within a given area, which is called as Kernel Average Misorientation (KAM). Thus, EBSD allows quantitative characterization of dislocations. However, EBSD is not able to characterize the residual stress state. The X-ray diffraction peak broadening is affected by dislocation density and arrangement, which shows the potential of characterizing work hardening. However, the characterization needs a sufficient number of diffraction peaks, and it is merely an empirical approach for estimating work hardening. Instrument indentation technique is sensitive to both residual stress and work hardening. Consequently, in this thesis, instrument indentation technique is used to develop the method for residual stress and work hardening characterization simultaneously.

Then, a series of simulation studies in order to propose the method to characterize the residual stress and work hardening were carried in Chapter 2. Simulation results show that a 2D axisymmetric finite element model can be used for simulation as long as only residual stress

and cumulative plastic strain are introduced. The effect of shot peening backstress on nanoindentation is investigated following. The shot peening backstress profile was obtained from the shot peening simulation. Results show that the shot peening backstress has a similar distribution with residual stress. The equivalent backstress is proposed to study its effects as only deviatoric part of the backstress tensor can affect the indentation responses. Results indicate that the backstress component characterized by a slow evolution rate has the most significant influence on responses. Even at a shot speed of 70 m/s, which is significantly higher than the typical practical speeds (for ultrasonic shot peening), the effect of backstress is smaller and can be neglected compared with the effect of residual stress and cumulative plastic strain. Thus, the proposed method only considers residual stress and work hardening, in which work hardening is represented as cumulative plastic strain. The Response surface function method aims to construct the functions of normalized responses and to solve them in order to obtain the value of residual stress and cumulative plastic strain. Moreover, the method was verified numerically using two different materials. Furthermore, the simulation results indicate that the relaxation of residual stresses occurs when the sample is cut off during sample preparation, which may have an influence when applying the method.

Next, an attempt was made to apply the proposed Response surface function method in practice, as presented in Chapter 3. Two pieces of Inconel 625 were shot peened, with one being measured by X-ray diffraction and another one being preparation for indentation. The measurement results obtained from X-ray diffraction indicate that the maximum compressive residual stress is approximately -600 MPa, and the compressive residual stress can extend to a depth of 500 μm. Meanwhile, the surface cumulative plastic strain is approximately 17%, and the influenced depth can extend to around 300 μm. The sample for indentation test was cut into four pieces and one of them was used for performing indentation on the cross section. Results show that indentation responses, such as the maximum load P_{max} and hardness H, have higher values near the shot peened surface due to the combined effect of strain hardening and compressive residual stress. The contact stiffness S shows an opposite trend, which exhibits lower values near shot peened surface. A possible reason could be the edge effect. Therefore, a correction was applied to remove this effect.

In order to apply the proposed method, the material constitutive behavior parameters should be known. It was found that the material behavior between the subsequent cycles and the tensile section of the first cycle are different. Thus, two sets of material parameters were employed, in which one set of parameters fits the tensile section of the first cycle and another set of parameters fits the subsequent cycles. However, there is a notable difference between the simulation and experimental results for both sets of parameters. Therefore, an inverse analysis technique was used to optimize the material parameters. In the optimization process, it is assumed that the kinematic hardening part has only one backstress component, which has the same evolution rate with the isotropic component. Optimization results indicate that the optimized parameters exhibit good fitness on the experimental and simulated P-h curve. However, the simulated monotonic tensile curve of optimized parameters exhibits a notable

difference with the experimental curve. This difference may be due to the asymmetry in tension and compression properties, or the selection strategy of the hardening model. Despite is difficult to fully explain the discrepancy between the experiment monotonic true stress-true strain curve and the curve simulated using the optimized parameters, we have decided to continue our work with the optimized parameters in this thesis.

Once the material behavior parameters are obtained, the responses surface function method was then applied. Results indicate that the solved profile shows a clear gradient along the shot peening direction. The three combinations of normalized response lead to a similar profile. A significant difference was observed between the profiles solved by Responses surface function method and the profiles measured by X-ray diffraction. For the difference on residual stress, it can be due to stress relaxation during cutting and layer removal during electrolytic polishing. Meanwhile, for the difference on cumulative plastic strain, the difference may be attributed to surface hardening caused by polishing, as well as the different loading paths between the monotonic tensile test and shot peening. Above all, though there is a difference between the profile obtained by the proposed method through indentation technique and the profile measured by X-ray diffraction, the proposed method still demonstrated its feasibility, indicating its potential for practical application.

Finally, the experiments in order to observe the evolution of residual stress and work hardening during monotonic tensile test and cyclic test were presented in Chapter 4. Two kinds of Inconel 625 were investigated in this thesis. One is the commercial cold rolled Inconel 625 and another one is the printed Inconel 625 through Atomic Diffusion Additive Manufacturing (ADAM) process. The two kinds of Inconel 625 exhibit the same elastic modulus. However, the ultimate tensile stress, elongation rate and 0.2% yield stress of printed Inconel 625 are lower than the cold rolled Inconel 625. Besides, no necking was observed for the printed material. A notable degree of porosity was observed for the printed material. Its grain size is higher than the cold rolled sample. Then, the two materials were shot peened for 120s and 360s. For the monotonic test, the tensile cold rolled samples were stretched to 8% and 24%, and the printed samples were stretched to 5% and 15%. For the cyclic test, both cold rolled and printed samples were performed 10 cycles with the strain level of 0.4% and 0.8%.

A positive residual stress was observed for both the cold rolled and printed samples on the shot peened surface after tensile test. We listed 8 possible cases of the surface mechanical evolution state after the tensile test. From the 8 cases, it can be concluded that the positive residual stress is due to the inhomogeneity of the material properties between the shot peened zone and core zone. After the cyclic test, the surface residual stress relaxation occurs but the relaxation is not complete and there are still some residual stresses that remain in the material. In the tensile test, the peak width of the surface of the cold rolled samples increased with the tensile strain, whereas the peak width of the surface of the printed samples remained constant. In the cyclic test, the surface peak widths of both materials remained constant at the 0.4% strain level, and a relaxation was observed at the 0.8% strain level. It is likely that the relaxation is due to the reorganization of dislocations in the surface layers. Moreover, at low tensile strain

levels in tensile test, it can be seen that shot peening can introduce high degree of misorientation. The longer the shot peening time, the higher the misorientation level. However, the difference in the depths affected by different shot peening times on the misorientation no longer exists after the high-level tensile strain test. The misorientation caused by the large plastic deformation during the tensile test tends to play the major role. A similar phenomenon was observed in the cyclic test. Nevertheless, the difference of affected layer depth caused by two shot peening times on misorientation remains after the high strain level cyclic test for the printed samples.

Nanoindentation responses also reflect the effect of shot peening and work hardening. It was observed that P_{max} and H have a higher value near the shot peened surface and then decrease to a stable level. Besides, the profile of P_{max} and H are quite similar, which means that for this material, H is mainly determined by P_{max}, the projected contact area does not play a major role. Meanwhile, the affected layer depth of P_{max} is deeper than the affected layer depth of misorientation (i.e. work hardening). P_{max} is affected by both work hardening and residual stress. Therefore, the change in the affected layer depth of P_{max} (beyond the work hardening influence depth) reflects residual stress relaxation. In the cyclic tests, for the shot peened 120s cold rolled samples and shot peened 360s printed samples, the affected layer of P_{max} after the 0.8% strain level is shallower than that after the 0.4% strain level. This indicates a more significant residual stress relaxation under 0.8% strain level.

5.2. The major conclusions of the thesis

- The shot peening backstress profile was firstly obtained from the shot peening simulation. Results show that shot peening backstress has a similar distribution as residual stress.
- The effect of shot peening backstress on indentation responses was investigated with finite element simulations. The results indicate that the backstress, which has a slow evolution rate, has the most significant influence on indentation responses. However, compared to the effect of residual stress or cumulative plastic strain, the influence of backstress can be neglected.
- A Response Surface Function method was proposed to characterize the residual stress and cumulative plastic strain. The normalized response surfaces (P_{max}/P_{0max}, S/S_0 and H/H_0) can be obtained from a series of simulations with the known level of residual stress and cumulative plastic strain. Moreover, the normalized response surfaces can be fit with polynomial functions. Subsequently, with the normalized responses obtained experiment, the residual stress and cumulative plastic strain profile can be obtained by solving two of the three functions.
- The residual stress redistribution after the cutting during the sample preparation process was investigated by finite element simulation. Results indicate that with the exception of the relaxation of σ_{yy}, which is the stress perpendicular to the cutting surface, the σ_{xx}, which is the stress on the cutting surface, is also released. Moreover, σ_{zz}, which is the stress along the shot peening direction, occurs during this process.

- The mechanical state under monotonic tensile test and 10 cycles cyclic test of two kinds of shot peened Inconel 625 was characterized by X-ray diffraction, Instrument indentation technique and Electron backscatter diffraction. A more significant residual stress relaxation was observed under the high strain level. Meanwhile, it was found that the difference of work hardening caused by two shot peening treatment times cannot be observed under the high strain level.

5.3. Perspectives

The main conclusions of this thesis are summarized above. However, when we analyzed the results, we found that there were still some interesting things can be investigated in the future.

As previously stated, the difference between the simulated monotonic tensile curve of optimized parameters and the experimental curve may be attributed to the asymmetry in tension and compression properties or to the selection strategy of the hardening model. For further investigations, more than one backstress could be applied in the kinematic hardening component and make b and γ as two individual variables.

Besides, more experimental indentation curves can be used to improve the accuracy of the inverse optimization method. Due to the specific characteristics of the spherical indenter, the tests at different indentation depths have different representative strains. Consequently, additional indentation tests with different representative strains could more accurately reflect the material properties. This approach will probably allow for more accurate optimization.

In addition, the fitted material behavior parameters presented in this thesis are derived from the monotonic tensile test curve or cyclic curves. However, the loading path during the indentation process is more like compression rather than tension. Consequently, the stress-strain curves derived from compression tests or cyclic tests initiated from compression may lead to the more accurately fitted parameters.

In the cyclic test, only surface residual stress and peak width were investigated. However, the measured information from the shot peened surface cannot correspond perfectly to the indentation response. In addition, the surface peak width is affected by machining, which makes it challenging to observe the actual variation in peak width caused by mechanical tests. Therefore, it could be interesting to conduct XRD measurement not only on the surface. The profile of residual stress and peak width along the distance away from the shot peened surface can provide a more detailed illustration of their evolution. Additionally, the measured profile can be compared with the nanoindentation response profile, thereby enabling a more comprehensive understanding of the influence of residual stress or work hardening on indentation responses. Meanwhile, the peak width in the deep layer is not affected by machining, which can provide the actual its variation during the mechanical tests.

The S profiles show different trends in this thesis. For some cases, S exhibits a lower value near shot peened surface. However, for printed material, especially in the tensile test, S value stays constant along the depth. This phenomenon is not totally explained in this thesis. In

order to investigate this phenomenon, more nanoindentation tests near the shot peened surface and obtaining more *S* values near the shot peened surface could give us more information.

In addition, it should be noted that, as presented in Section 2.4, after cutting process, σ_{zz} component appears. The trace of the stress tensor after cutting is not simply σ_{xx}; rather, it is the sum of σ_{zz} and the relaxed σ_{xx}, which results in a different hydrostatic stress state. The further influence of the different hydrostatic stress states after cutting process can be investigated in the future.

Appendix

A.1. The indentation unloading process with combined hardening behavior

It is obvious that only elastic deformation occurs during the indentation unloading process when the isotropic hardening behavior is used in the simulation. However, a different phenomenon has been observed for the indentation simulations with combined hardening behavior (in particular, kinematic hardening component is included). For instance, Fig.A-1 show the contour of the unloading process using the optimized parameters shown in Tab.3-7, Chapter3 (Spherical indenter, which radius equals to 10 μm), in which the red color indicates that the material is yield.

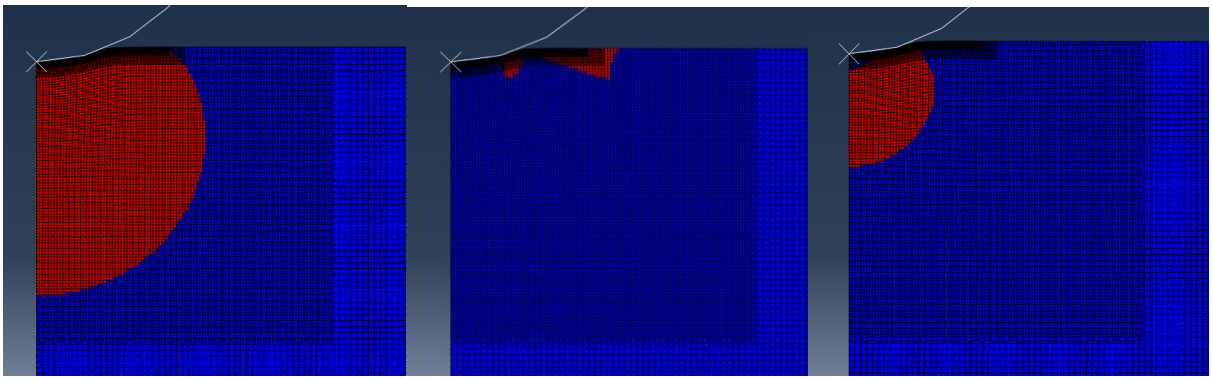

(a) (b) (c)

Fig.A-1 The contour of the indentation unloading process. Red color indicates the yield of material (a) The end of indentation loading (b) Unloading process - where the load is approximately 40% of the P_{max} (c) Unloading process - where the load is approximately 10% of the P_{max}

As illustrated in Fig.A-1(b) and (c), material yield occurs during the unloading process, which can influence the calculation of stiffness. When the load decreases to approximately 40% of the P_{max}, the yield region is relatively small in comparison to the yield region observed at the end of loading, as shown in Fig.A-1(a). Therefore, the influence of this phenomenon on the calculation of stiffness can be ignored. However, when the unloading process continues to a point where the load is approximately 10% of the P_{max}, as shown in Fig.A-1(c), it becomes evident that the yield region is of considerable significance. This is why we stated in Chapter 1 to use unloading data ranging from 40-95% of the maximum load to calculate stiffness.

Moreover, the simulation shown above is under the state without any introduced residual stress and work hardening. It is predictable that when additional mechanical field is introduced to the material, the yielding state will be different. The details of the influence of yielding during the unloading process can be further investigated.

A.2. The effect of backstress on indentation responses using the optimized parameters

The results in Chapter 2 indicate that the backstress with a slow evolution rate can affect indentation responses. The optimized parameters presented above also have a slow evolution rate. Therefore, we first examine the effect of backstress on indentation responses of the optimized material parameters through the simulations.

Fig.A-2 shows the equivalent backstress under different shot peening parameters. The optimized material parameters exhibit negative equivalent backstress values, which increase with shot speed increases but remain relatively constant with the changes in coverage rate. This trend is consistent with the findings in Chapter 2. However, the equivalent stress is approximately -150 MPa when the shot speed exceeds 30m/s, and approximately -100 MPa when the shot speed is around 10 m/s (which is close to the actual shot speed).

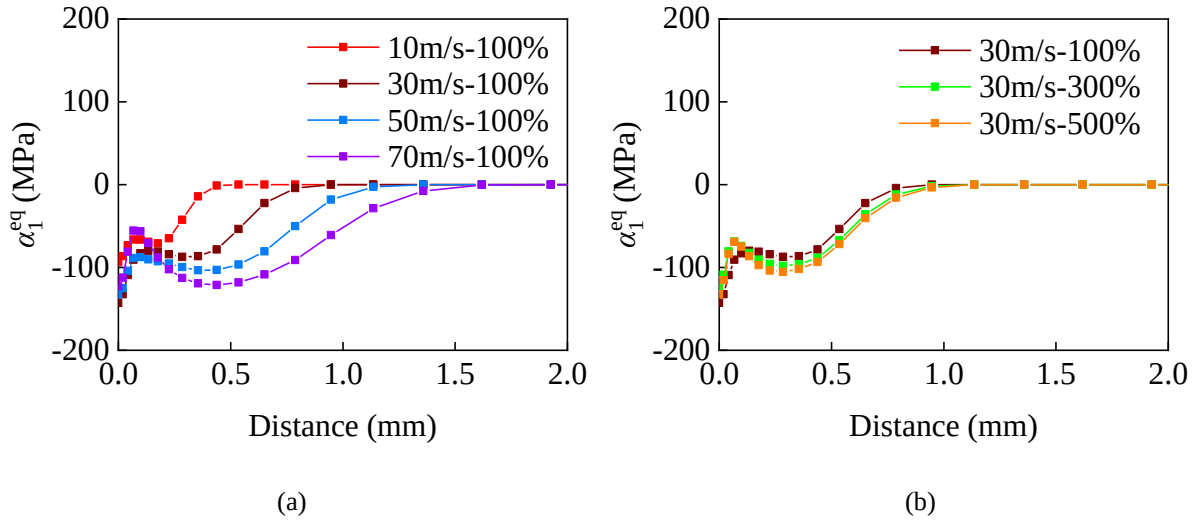

(a) (b)

Fig.A-2 The equivalent backstress distribution under (a) different shot speed and (b) different coverage rate

Fig.A-3 shows the normalized indentation responses with different equivalent backstresses. Similarly, a line of α_1^{eq} equals to -100MPa is plotted in the figure. The result shows that the higher positive or negative equivalent backstress do have a significant influence on the indentation responses. However, considering the actual shot speed (around 10 m/s) in our case, the differences affected by equivalent backstress are only around 1.2% (P_{max}) and 0.5% (S). Comparing experiment normalized responses shown in Fig.3-12 (In which the maximum difference of P_{max} and S is around 15% and 10% respectively) and the simulated normalized responses with cumulative plastic strain or residual stress shown in Fig.3-26 (In which the variation range for P_{max}, S and H are 0 - 36%, -7% - 4% and 0 - 43% respectively), it is still assumed that the effect of backstress can be ignored in this thesis.

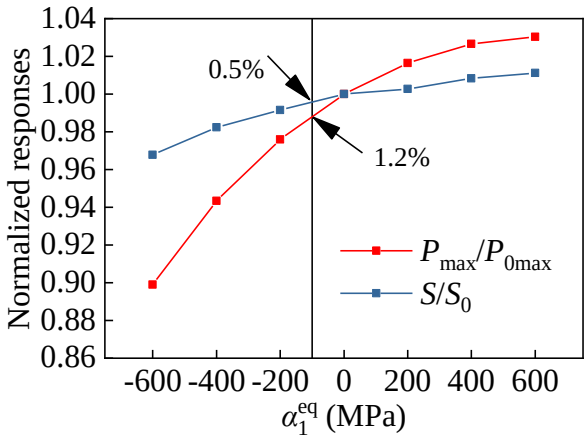

Fig.A-3 The indentation responses with equivalent backstresses

Résumé en français

1. Introduction

Le grenaillage constitue une technique de traitement de surface éprouvée visant à renforcer les propriétés mécaniques des matériaux par l'introduction d'une couche de contraintes résiduelles de compression. Par ailleurs, les déformations plastiques induites par les impacts successifs favorisent également l'écrouissage à la surface du matériau. Cette combinaison contribue à retarder efficacement l'amorçage et la propagation des fissures de fatigue, principalement localisées en surface.

Les contraintes résiduelles et le durcissement par déformation plastique influencent de manière significative les performances en fatigue des matériaux. Toutefois, dans la majorité des cas, les effets des deux phénomènes sont intriqués et l'écrouissage peut, suivant les cas, jouer un rôle positif ou négatif. Pour analyser de manière distincte le rôle de ces deux phénomènes durant les cycles de fatigue, une caractérisation individuelle est requise. Cette démarche permet de suivre leur évolution et de concevoir des spécimens adaptés afin d'optimiser les performances en fatigue en fonction de leurs propriétés spécifiques. La technique d'indentation instrumentée, sensible aux contraintes résiduelles et au durcissement, offre la possibilité d'effectuer une caractérisation simultanée des deux paramètres.

Cette thèse poursuit deux objectifs principaux. Le premier consiste à développer une méthode de caractérisation des contraintes résiduelles et du durcissement par déformation en utilisant la technique de nanoindentation. Le second vise à comparer les comportements en traction et en fatigue cyclique de l'Inconel 625, sous forme commerciale et imprimée en 3D par le procédé ADAM (Atomic Diffusion Additive Manufacturing), soumis à diverses intensités de grenaillage.

2. Caractérisation numérique de l'écrouissage et des contraintes résiduelles avec indentation

Une série d'études de simulation a été réalisée dans ce chapitre afin de proposer une méthode de caractérisation des contraintes résiduelles et du durcissement par déformation (écrouissage). Les résultats de simulation indiquent qu'un modèle d'éléments finis axisymétrique en 2D peut être utilisé, à condition que seules la contrainte résiduelle et la déformation plastique cumulée soient prises en compte.

L'effet de la contrainte interne ('backstress' en anglais), liée à l'écrouissage cinématique induit par le grenaillage, sur les réponses de nanoindentation a été examiné en premier lieu. Le profil de contrainte interne, obtenu par simulation, présente une distribution similaire à celle des contraintes résiduelles. Une notion de contrainte interne équivalente a été proposée pour

évaluer ses effets, étant donné que seule la composante déviatorique du tenseur de contrainte interne influence les réponses en indentation. Les simulations montrent que la composante caractérisée par une faible vitesse d'évolution a l'impact le plus significatif sur les réponses. Même à une vitesse de grenaillage élevée (70 m/s), bien supérieure aux vitesses pratiques couramment utilisées dans le grenaillage par ultrasons, l'effet de la contrainte interne reste négligeable par rapport à celui des contraintes résiduelles et de la déformation plastique cumulée.

Ainsi, la méthode proposée se concentre uniquement sur les contraintes résiduelles et l'écrouissage, représenté par la déformation plastique cumulée. Une méthode basée sur une surface de réponse a été développée pour construire des fonctions de réponse normalisées, permettant d'estimer les valeurs des contraintes résiduelles et de la déformation plastique cumulée. Cette approche a été validée numériquement à l'aide de deux matériaux différents.

En outre, les simulations révèlent qu'une relaxation des contraintes résiduelles peut survenir lors de la découpe des échantillons pendant leur préparation, ce qui peut influencer significativement les résultats lors de l'application de la méthode.

3. Caractérisation expérimentale de l'écrouissage et des contraintes résiduelles

La méthode proposée a été mise en œuvre dans ce chapitre à travers l'étude de deux pièces en Inconel 625 grenaillées. L'une des pièces a été analysée par diffraction des rayons X, tandis que l'autre a été préparée pour l'indentation. Les résultats obtenus par diffraction des rayons X montrent que la contrainte résiduelle de compression maximale atteint environ -600 MPa, avec une profondeur d'influence pouvant s'étendre jusqu'à 500 μm. Parallèlement, la déformation plastique cumulée à la surface est d'environ 17 %, et l'influence de cette déformation s'étend jusqu'à environ 300 μm. L'échantillon destiné à l'essai d'indentation a été découpé en quatre morceaux, dont un a été utilisé pour effectuer l'indentation sur la section transversale. Les résultats montrent que les réponses à l'indentation, telles que la charge maximale (P_{max}) et la dureté (H), sont plus élevées près de la surface grenaillée, ce qui résulte de l'effet combiné de l'écrouissage et de la contrainte résiduelle de compression. En revanche, la rigidité de contact (S) présente une tendance opposée, avec des valeurs plus faibles près de la surface grenaillée, probablement en raison de l'effet de bord. Une correction a donc été appliquée pour éliminer cet effet.

Pour appliquer la méthode proposée, les paramètres du comportement constitutif du matériau doivent être connus. Il a été observé que le comportement du matériau entre les cycles suivants et la section de traction du premier cycle diffère. Ainsi, deux ensembles de paramètres ont été utilisés : l'un pour la partie de traction du premier cycle et l'autre pour les cycles suivants. Cependant, des divergences notables ont été observées entre les résultats de simulation et les résultats expérimentaux pour les deux ensembles de paramètres. Par conséquent, une analyse inverse a été employée pour optimiser ces paramètres vis-à-vis de la réponse en indentation. Dans le processus d'optimisation, il est supposé que la partie de durcissement cinématique

présente une unique composante de contrainte interne, évoluant au même rythme que la composante isotrope. Les résultats d'optimisation montrent que les paramètres ajustés s'accordent bien avec la courbe expérimentale et simulée *P-h*. Cependant, la courbe de traction monotone simulée avec les paramètres optimisés diffère de manière notable de la courbe expérimentale, une différence qui pourrait être attribuée à l'asymétrie des propriétés en traction et en compression, ou à la stratégie de sélection du modèle de durcissement. Bien qu'il reste difficile d'expliquer entièrement l'écart entre la courbe contrainte-déformation expérimentale et la courbe simulée avec les paramètres optimisés, il a été décidé de poursuivre l'étude avec ces paramètres optimisés dans le cadre de cette thèse.

Une fois les paramètres de comportement du matériau déterminés, la méthode de la surface de réponse a été appliquée. Les résultats indiquent que le profil obtenu présente un gradient clair le long de la direction du grenaillage, avec trois combinaisons de réponses normalisées produisant un profil similaire. Une différence significative a été observée entre les profils obtenus par la méthode de la fonction de surface des réponses et ceux mesurés par diffraction des rayons X. Cette différence concernant la contrainte résiduelle pourrait résulter de la relaxation des contraintes pendant la découpe et de l'élimination de la couche de surface lors du polissage électrolytique. En ce qui concerne la différence de déformation plastique cumulée, celle-ci pourrait être due au durcissement de surface causé par le polissage, ainsi qu'aux différences de trajets de chargement entre l'essai de traction monotone et le grenaillage. Néanmoins, bien qu'une différence existe entre le profil obtenu par la méthode proposée via la technique d'indentation et celui mesuré par diffraction des rayons X, cette méthode a démontré sa faisabilité, suggérant ainsi son potentiel pour des applications pratiques.

4. Caractérisation des propriétés mécaniques sous essai cyclique et essai de traction monotone

Ce chapitre présente les expériences menées pour observer l'évolution des contraintes résiduelles et de l'écrouissage lors d'essais de traction monotone et de déformation cyclique. Deux types d'Inconel 625 ont été étudiés dans cette thèse : l'Inconel 625 laminé à froid commercial et l'Inconel 625 fabriqué par le procédé de fabrication additive par diffusion atomique (ADAM). Bien que les deux matériaux possèdent un module d'élasticité identique, les propriétés mécaniques de l'Inconel 625 imprimé, notamment la contrainte de traction ultime, la limite d'élasticité à 0.2% et l'allongement à rupture, sont inférieures à celles de l'Inconel 625 laminé à froid. De plus, aucune striction n'a été observée dans le matériau imprimé, lequel présente un degré notable de porosité et une taille de grain supérieure à celle de l'échantillon laminé à froid.

Les deux matériaux ont été soumis à un traitement de grenaillage pendant 120 et 360 secondes. Dans le cadre des essais monotones, les échantillons laminés à froid ont été étirés à 8% et 24%, tandis que les échantillons imprimés ont été étirés à 5% et 15%. Concernant les essais cycliques, les échantillons laminés à froid et imprimés ont subi 10 cycles avec des amplitudes de déformation de 0.4% et 0.8%.

Après l'essai de traction, une contrainte résiduelle positive a été observée à la surface grenaillée des échantillons des deux types de matériau. Huit scénarios possibles concernant l'évolution de l'état mécanique de la surface après l'essai de traction ont été identifiés, et les résultats indiquent que la contrainte résiduelle positive résulte de l'inhomogénéité des propriétés du matériau entre la zone grenaillée et la zone centrale. Suite à l'essai cyclique, une relaxation partielle de la contrainte résiduelle a été observée, bien que des contraintes résiduelles demeurent dans le matériau.

Dans le cadre de l'essai de traction, la largeur des pics de diffraction observés sur la surface des échantillons laminés à froid augmente avec la déformation, tandis que celle des échantillons imprimés reste constante. Pour les essais cycliques, les largeurs des pics des deux matériaux demeurent constantes à un niveau de déformation de 0.4%, avec une relaxation apparente à un niveau de déformation de 0.8%. Cette relaxation semble être liée à la réorganisation des dislocations au sein des couches superficielles du matériau. En outre, à de faibles niveaux de déformation de traction, le grenaillage induit un degré élevé de désorientation. Il a été observé qu'une augmentation du temps de grenaillage conduit à un accroissement de la désorientation. Toutefois, après des essais de traction à haut niveau de déformation plastique, la différence dans la profondeur d'impact de différents temps de grenaillage sur la désorientation devient négligeable.

Un phénomène similaire a été observé lors des essais cycliques. Toutefois, après des essais cycliques à de hauts niveaux de déformation pour les échantillons imprimés, la différence dans la profondeur de la couche affectée par différents temps de grenaillage persiste, indiquant que l'effet de la désorientation reste plus prononcé après des cycles à fort niveau de déformation.

Les réponses obtenues par nanoindentation ont également permis d'évaluer les effets du grenaillage et de l'écrouissage. Il a été observé que la charge maximale (P_{max}) et la dureté (H) sont plus élevées près de la surface grenaillée et diminuent ensuite jusqu'à un niveau stable. Les profils de P_{max} et de H sont très similaires, suggérant que, pour ce matériau, la dureté (H) est principalement déterminée par P_{max}, et que la zone de contact projetée n'influence pas de manière significative la réponse. La profondeur de la couche affectée par P_{max} est supérieure à celle associée à la désorientation (écrouissage). Étant donné que P_{max} est influencée à la fois par l'écrouissage et les contraintes résiduelles, les variations dans la profondeur de la couche affectée, au-delà de la profondeur d'influence de l'écrouissage, permettent d'évaluer la relaxation des contraintes résiduelles. Dans les essais cycliques, pour les échantillons laminés à froid grenaillés pendant 120 secondes et les échantillons imprimés grenaillés pendant 360 secondes, la profondeur de la couche affectée (observée à l'aide de P_{max}) après un niveau de déformation de 0.8% est inférieure à celle observée après un niveau de déformation de 0.4%, ce qui traduit une relaxation plus importante des contraintes résiduelles à 0.8% de déformation.

5. Conclusion

Le profil de la contrainte interne (liée à l'écrouissage cinématique) de grenaillage a été d'abord déterminé à partir de simulations numériques de grenaillage. Les résultats de ces simulations ont montré que la distribution de la contrainte interne est similaire à celle de la

contrainte résiduelle, suggérant ainsi un impact comparable de ces deux types de contraintes sur le comportement mécanique du matériau traité.

L'effet de la contrainte interne de grenaillage sur les réponses d'indentation a été étudié via des simulations par éléments finis. Les résultats indiquent que cette contrainte interne, dont la vitesse d'évolution est relativement lente, exerce une influence significative sur les réponses d'indentation. Cependant, comparée à l'effet de la contrainte résiduelle ou de l'écrouissage, l'influence de la contrainte interne est négligeable et peut être ignorée dans les simulations visant à modéliser le comportement du matériau sous indentation.

Une méthode basée sur la fonction de surface de réponse a été proposée pour caractériser la contrainte résiduelle et l'écrouissage. Les surfaces de réponse normalisées, telles que P_{max}/P_{0max}, S/S_0 et H/H_0, peuvent être obtenues à partir d'une série de simulations réalisées à partir des niveaux connus de contrainte résiduelle et de déformation plastique cumulative. Ces surfaces peuvent ensuite être ajustées à l'aide de fonctions polynomiales. En intégrant les réponses normalisées obtenues expérimentalement, il est possible de résoudre deux des trois fonctions pour obtenir les profils de contrainte résiduelle et de déformation plastique cumulée du matériau.

La redistribution des contraintes résiduelles après la découpe, lors de la préparation de l'échantillon, a été étudiée par simulation par éléments finis. Les résultats indiquent que, à l'exception de la relaxation de la contrainte (perpendiculaire à la surface de coupe), la contrainte σ_{xx}, qui est parallèle à la surface de coupe, subit également une relaxation. De plus, une relaxation de la contrainte σ_{zz}, le long de la direction du grenaillage, se produit également pendant ce processus. Il est également important de prendre en compte l’effet de proximité de la surface sur la réponse en indentation.

L'état mécanique des échantillons d'Inconel 625 laminé à froid et imprimé par fabrication additive, grenaillés selon deux durées différentes, a été caractérisé à l'aide de techniques telles que la diffraction des rayons X, l'indentation instrumentée et l’EBSD (Electron Back-Scattering Diffraction). Une relaxation plus importante des contraintes résiduelles a été observée sous des niveaux de contrainte élevés. En outre, il a été noté qu'à ces niveaux de contrainte élevés, la différence d'écrouissage entre les deux durées de grenaillage n'était plus perceptible, suggérant que les effets du grenaillage sur l'écrouissage sont moins significatifs sous de telles conditions de charge.

References

[1] Faksa, L., Daves, W., Ecker, W., Klünsner, T., Tkadletz, M. and Czettl, C., 2019. Effect of shot peening on residual stresses and crack closure in CVD coated hard metal cutting inserts. International Journal of Refractory Metals and Hard Materials, 82, pp.174-182.

[2] Suresh, S., 1998. Fatigue of materials. Cambridge university press.

[3] Gurney, T.R., 1979. Fatigue of welded structures. CUP Archive.

[4] Ballio, G. and Castiglioni, C.A., 1995. A unified approach for the design of steel structures under low and/or high cycle fatigue. Journal of Constructional Steel Research, 34(1), pp.75-101.

[5] Kandil, F.A., Lord, J.D., Fry, A.T. and Grant, P.V., 2001. A review of residual stress measurement methods-a guide to technique selection.

[6] Hauk, V., 1997. Structural and residual stress analysis by nondestructive methods: Evaluation-Application-Assessment. Elsevier.

[7] Clarebrough, L.M. and Hargreaves, M.E., 1959. Work hardening of metals. Progress in Metal Physics, 8, pp.1-103.

[8] Koehler, J.S., 1952. The nature of work-hardening. Physical Review, 86(1), p.52.

[9] Mouritz, A.P., 2012. Introduction to aerospace materials. Elsevier.

[10] Schijve, J., 1976. The effect of pre-strain on fatigue crack growth and crack closure. Engineering Fracture Mechanics, 8(4), pp.575-581.

[11] Al-Rubaie, K.S., Barroso, E.K. and Godefroid, L.B., 2006. Fatigue crack growth analysis of pre-strained 7475–T7351 aluminum alloy. International Journal of Fatigue, 28(8), pp.934-942.

[12] Klumpp, A., Maier, S., Chen, H., Fotouhi, M., Schneider, R., Dietrich, S., Lang, K.H. and Schulze, V., 2018. Influence of work-hardening on fatigue crack growth, effective threshold and crack opening behavior in the nickel-based superalloy Inconel 718. International Journal of Fatigue, 116, pp.257-267.

[13] Bauchau, O.A. and Craig, J.I., 2009. Structural analysis: with applications to aerospace structures (Vol. 163). Springer Science & Business Media.

[14] Hashmi, M.S.J., 2016. Comprehensive materials finishing. Elsevier.

[15] Abdelbary, A. and Chang, L., 2023. Principles of engineering tribology: fundamentals and applications. Elsevier.

[16] Mattson, R.L. and Coleman Jr, W.S., 1954. Effect of shot-peening variables and residual stresses on the fatigue life of leaf-spring specimens. SAE Transactions, pp.546-556.

[17] Zhuang, W.Z. and Halford, G.R., 2001. Investigation of residual stress relaxation under cyclic load. International journal of fatigue, 23, pp.31-37.

[18] Leguinagoicoa, N., Albizuri, J. and Larranaga, A., 2022. Fatigue improvement and residual stress relaxation of shot-peened alloy steel DIN 34CrNiMo6 under axial loading. International Journal of Fatigue, 162, p.107006.

[19] Maleki, E., Farrahi, G.H., Reza Kashyzadeh, K., Unal, O., Gugaliano, M. and Bagherifard, S., 2021. Effects of conventional and severe shot peening on residual stress and fatigue strength of steel AISI 1060 and residual stress relaxation due to fatigue loading: Experimental and numerical simulation. Metals and Materials International, 27, pp.2575-2591.

[20] Kim, J.C., Cheong, S.K. and Noguchi, H., 2013. Residual stress relaxation and low-and high-cycle fatigue behavior of shot-peened medium-carbon steel. International Journal of Fatigue, 56, pp.114-122.

[21] Hao, H., Ye, D., Chen, Y., Feng, M. and Liu, J., 2015. A study on the mean stress relaxation behavior of 2124-T851 aluminum alloy during low-cycle fatigue at different strain ratios. Materials & Design, 67, pp.272-279.

[22] Koh, S.K. and Stephens, R.I., 1991. Mean stress effects on low cycle fatigue for a high strength steel. Fatigue & Fracture of Engineering Materials & Structures, 14(4), pp.413-428.

[23] Arcari, A., De Vita, R. and Dowling, N.E., 2009. Mean stress relaxation during cyclic straining of high strength aluminum alloys. International Journal of Fatigue, 31(11-12), pp.1742-1750.

[24] Sandor, B.I., 1972. Fundamentals of cyclic stress and strain. The University of Wisconsin Press, Madison.

[25] Wang, K., Jing, H., Xu, L., Han, Y., Zhao, L. and Song, K., 2021. Cyclic response and dislocation evolution of a nickel-based superalloy under low cycle fatigue deformation. Materials Science and Engineering: A, 814, p.141225.

[26] Nip, K.H., Gardner, L., Davies, C.M. and Elghazouli, A.Y., 2010. Extremely low cycle fatigue tests on structural carbon steel and stainless steel. Journal of constructional steel research, 66(1), pp.96-110.

[27] Antolovich, S.D., 2015. Microstructural aspects of fatigue in Ni-base superalloys. Philosophical Transactions of the Royal Society A: Mathematical, Physical and Engineering Sciences, 373(2038), p.20140128.

[28] Pineau, A. and Antolovich, S.D., 2009. High temperature fatigue of nickel-base superalloys - a review with special emphasis on deformation modes and oxidation. Engineering failure analysis, 16(8), pp.2668-2697.

[29] Zhang, P., Zhu, Q., Hu, C., Wang, C.J., Chen, G. and Qin, H.Y., 2015. Cyclic deformation behavior of a nickel-base superalloy under fatigue loading. Materials & Design, 69, pp.12-21.

[30] Srinivasan, V.S., Sandhya, R., Rao, K.B.S., Mannan, S.L. and Raghavan, K.S., 1991. Effects of temperature on the low cycle fatigue behaviour of nitrogen alloyed type 316L stainless steel. International journal of fatigue, 13(6), pp.471-478.

[31] Antolovich, S.D., Rosa, E. and Pineau, A., 1981. Low cycle fatigue of René 77 at elevated temperatures. Materials Science and Engineering, 47(1), pp.47-57.

[32] Mathar, J., 1934. Determination of initial stresses by measuring the deformations around drilled holes. Transactions of the American Society of Mechanical Engineers, 56(3), pp.249-254.

[33] Misra, A. and Peterson, H.A., 1981. Examination of the ring method for determination of residual stresses: In this method, a ring is cut around the point where residual stresses are to be determined. Calibration is done by using a specimen with a known residual-stress distribution. Experimental Mechanics, 21, pp.268-272.

[34] Treuting, R.G. and Read Jr, W.T., 1951. A mechanical determination of biaxial residual stress in sheet materials. Journal of applied physics, 22(2), pp.130-134.

[35] Olson, M.D., DeWald, A.T., Prime, M.B. and Hill, M.R., 2015. Estimation of uncertainty for contour method residual stress measurements. Experimental Mechanics, 55, pp.577-585.

[36] Jiang, G., Haiyang, F., Bo, P. and Renke, K., 2021. Recent progress of residual stress measurement methods: A review. Chinese Journal of Aeronautics, 34(2), pp.54-78.

[37] He, B.B., 2018. Two-dimensional X-ray Diffraction. John Wiley & Sons.

[38] Hutchings, M.T., Withers, P.J., Holden, T.M. and Lorentzen, T., 2005. Introduction to the characterization of residual stress by neutron diffraction. CRC press.

[39] François, M., Dionnet, B., Sprauel, J.M. and Nardou, F., 1995. The influence of cylindrical geometry on X-ray stress tensor analysis. I. General formulation. Journal of applied crystallography, 28(6), pp.761-767.

[40] Ashby, M.F., 1970. The deformation of plastically non-homogeneous materials. The Philosophical Magazine: A Journal of Theoretical Experimental and Applied Physics, 21(170), pp.399-424.

[41] Vespucci, S., Winkelmann, A., Naresh-Kumar, G., Mingard, K.P., Maneuski, D., Edwards, P.R., Day, A.P., O'Shea, V. and Trager-Cowan, C., 2015. Digital direct electron imaging of energy-filtered electron backscatter diffraction patterns. Physical Review B, 92(20), p.205301.

[42] Kubin, L.P. and Mortensen, A., 2003. Geometrically necessary dislocations and strain-gradient plasticity: a few critical issues. Scripta materialia, 48(2), pp.119-125.

[43] Nye, J.F., 1953. Some geometrical relations in dislocated crystals. Acta metallurgica, 1(2), pp.153-162.

[44] Field, D.P., Trivedi, P.B., Wright, S.I. and Kumar, M., 2005. Analysis of local orientation gradients in deformed single crystals. Ultramicroscopy, 103(1), pp.33-39.

[45] Zhu, L., Fan, X., Xiao, L., Ji, H. and Guo, J., 2023. Influence of shot peening on the microstructure and high-temperature tensile properties of a powder metallurgy Ni-based superalloy. Journal of Materials Science, 58(6), pp.2838-2852.

[46] Sarkar, S. and Das, R., 2018. Shape effect on the elastic properties of Ag nanocrystals. Micro & Nano Letters, 13(3), pp.312-315.

[47] Murugesan, S., Kuppusami, P., Mohandas, E. and Vijayalakshmi, M., 2012. X-ray diffraction Rietveld analysis of cold worked austenitic stainless steel. Materials Letters, 67(1), pp.173-176.

[48] Williamson, G.K. and Hall, W.H., 1953. X-ray line broadening from filed aluminium and wolfram. Acta metallurgica, 1(1), pp.22-31.

[49] Gallet, J., Perez, M., Guillou, R., Ernould, C., Le Bourlot, C., Langlois, C., Beausir, B., Bouzy, E., Chaise, T. and Cazottes, S., 2023. Experimental measurement of dislocation density in metallic materials: a quantitative comparison between measurements techniques (XRD, R-ECCI, HR-EBSD, TEM). Materials Characterization, 199, p.112842.

[50] Prevéy, P.S., 1987, April. The measurement of subsurface residual stress and cold work distributions in nickel base alloys. In ASM's conference on residual stress in design, process and materials selection, pp.11-20.

[51] Oliver, W.C. and Pharr, G.M., 1992. An improved technique for determining hardness and elastic modulus using load and displacement sensing indentation experiments. Journal of materials research, 7(6), pp.1564-1583.

[52] Sen, I. and Kumar, S.S., 2021. Characterizing stress-strain behavior of materials through nanoindentation. In Elasticity of materials. IntechOpen.

[53] Li, X. and Bhushan, B., 2002. A review of nanoindentation continuous stiffness measurement technique and its applications. Materials characterization, 48(1), pp.11-36.

[54] Tsui, T.Y., Oliver, W.C. and Pharr, G.M., 1996. Influences of stress on the measurement of mechanical properties using nanoindentation: Part I. Experimental studies in an aluminum alloy. Journal of Materials Research, 11(3), pp.752-759.

[55] Bolshakov, A., Oliver, W.C. and Pharr, G.M., 1996. Influences of stress on the measurement of mechanical properties using nanoindentation: Part II. Finite element simulations. Journal of Materials Research, 11(3), pp.760-768.

[56] Giannakopoulos, A.E., 2003. The influence of initial elastic surface stresses on instrumented sharp indentation. J. Appl. Mech., 70(5), pp.638-643.

[57] Suresh, S. and Giannakopoulos, A.E., 1998. A new method for estimating residual stresses by instrumented sharp indentation. Acta materialia, 46(16), pp.5755-5767.

[58] Carlsson, S. and Larsson, P.L., 2001. On the determination of residual stress and strain fields by sharp indentation testing.: Part I: theoretical and numerical analysis. Acta materialia, 49(12), pp.2179-2191.

[59] Carlsson, S. and Larsson, P.L., 2001. On the determination of residual stress and strain fields by sharp indentation testing.: Part II: experimental investigation. Acta Materialia, 49(12), pp.2193-2203.

[60] Chen, X., Yan, J. and Karlsson, A.M., 2006. On the determination of residual stress and mechanical properties by indentation. Materials Science and Engineering: A, 416(1-2), pp.139-149.

[61] Liu X, Cai, L and Chen, H, 2022. Residual stress indentation model based on material equivalence. Chinese Journal of Aeronautics, 35(8), pp.304-313.

[62] Lee, Y.H. and Kwon, D., 2003. Measurement of residual-stress effect by nanoindentation on elastically strained (100) W. Scripta Materialia, 49(5), pp.459-465.

[63] Sakharova, N.A., Prates, P.A., Oliveira, M.C., Fernandes, J.V. and Antunes, J.M., 2012. A Simple Method for Estimation of Residual Stresses by Depth‐Sensing Indentation. Strain, 48(1), pp.75-87.

[64] Pham, T.H. and Kim, S.E., 2017. Determination of equi-biaxial residual stress and plastic properties in structural steel using instrumented indentation. Materials Science and Engineering: A, 688, pp.352-363.

[65] Peng, G., Lu, Z., Ma, Y., Feng, Y., Huan, Y. and Zhang, T., 2018. Spherical indentation method for estimating equibiaxial residual stress and elastic-plastic properties of metals simultaneously. Journal of Materials Research, 33(8), pp.884-897.

[66] Ahn, S.M., Park, S.Y., Kim, Y.C., Lee, K.S. and Kim, J.Y., 2015. Surface residual stress in soda-lime glass evaluated using instrumented spherical indentation testing. Journal of materials science, 50, pp.7752-7759.

[67] Greco, A., Sgambitterra, E., Guagliano, M. and Furgiuele, F., 2024. Measurement of laser shock peening induced residual stress by nanoindentation and comparison with XRD technique. Journal of Materials Research and Technology, 30, pp.5701-5710.

[68] Greco, A., Sgambitterra, E., Furgiuele, F. and Furfari, D., 2023. A Novel Method to Measure Equi-Biaxial Residual Stress by Nanoindentation. Experimental Mechanics, 63(9), pp.1493-1508.

[69] Yuan, L., Yuan, W. and Wang, G., 2020. Effects of residual stress on the hardness of elastoplastic material under spherical indentation. Journal of Applied Mechanics, 87(5), p.051004.

[70] Taljat, B. and Pharr, G.M., 1999. Measurement of residual stresses by load and depth sensing spherical indentation. MRS Online Proceedings Library (OPL), 594, p.519.

[71] Swadener, J.G., Taljat, B. and Pharr, G.M., 2001. Measurement of residual stress by load and depth sensing indentation with spherical indenters. Journal of Materials Research, 16(7), pp.2091-2102.

[72] Wang, Z., Deng, L. and Zhao, J., 2018. A novel method to extract the equi-biaxial residual stress and mechanical properties of metal materials by continuous spherical indentation test. Materials Research Express, 6(3), p.036512.

[73] Wang, Z., Deng, L. and Zhao, J., 2019. Estimation of residual stress of metal material without plastic plateau by using continuous spherical indentation. International Journal of Pressure Vessels and Piping, 172, pp.373-378.

[74] Li, Y.G., Kanouté, P. and François, M., 2013. Influence of residual stress and work hardening on instrumented indentation. Matériaux & Techniques, 101(3), p.306.

[75] Idriss, M., Bartier, O., Mauvoisin, G. and Hernot, X., 2021. A phenomenological study of the influence of the hardening type on the indentation F-h cyclic curve. International Journal of Mechanical Sciences, 197, p.106336.

[76] Thom, C.A., Hansen, L.N., Breithaupt, T., Goldsby, D.L. and Kumamoto, K.M., 2022. Backstresses in geologic materials quantified by nanoindentation load-drop experiments. Philosophical Magazine, 102(19), pp.1974-1988.

[77] Westbrook, J.H. and Peyer, H.C., 1973. The science of hardness testing and its research applications. (No Title).

[78] Tabor, D., 1951, The hardness of metals, Clarendon, Oxford, UK..

[79] Gale, J.D. and Achuthan, A., 2014. The effect of work-hardening and pile-up on nanoindentation measurements. Journal of materials science, 49, pp.5066-5075.

[80] Gorsler, F.W., 1985. High-speed machining of aircraft engine alloys. American Society for Metals, pp.57-67.

[81] Paulonis, D.F., Oblak, J.M. and Duvall, D.S., 1969. Precipitation in Nickel-base Alloy 718. Pratt and Whitney Aircraft, Middletown.

[82] Liu, X., Fan, J., Zhang, P., Cao, K., Wang, Z., Chen, F., Liu, D., Tang, B., Kou, H. and Li, J., 2023. Influence of heat treatment on Inconel 625 superalloy sheet: carbides, γ", δ phase precipitation and tensile deformation behavior. Journal of Alloys and Compounds, 930, p.167522.

[83] Chemkhi, M., Djouda, J.M., Bouaziz, M.A., Kauffmann, J., Hild, F. and Retraint, D., 2021. Effects of Mechanical Post-Treatments on Additive Manufactured 17-4PH Stainless Steel Produced by Bound Powder Extrusion. Procedia CIRP, 104, pp.957-961.

[84] Yang, F., Dong, L., Hu, X., Zhou, X., Xie, Z. and Fang, F., 2020. Effect of solution treatment temperature upon the microstructure and mechanical properties of hot rolled Inconel 625 alloy. Journal of materials science, 55(13), pp.5613-5626.

[85] Sukumaran, A., Gupta, R.K. and Anil Kumar, V., 2017. Effect of heat treatment parameters on the microstructure and properties of Inconel-625 superalloy. Journal of Materials Engineering and Performance, 26, pp.3048-3057.

[86] Liu, D., Zhang, X., Qin, X. and Ding, Y., 2017. High-temperature mechanical properties of Inconel-625: role of carbides and delta phase. Materials Science and Technology, 33(14), pp.1610-1617.

[87] Armstrong, P.J. and Frederick, C.O., 1966. A mathematical representation of the multiaxial Bauschinger effect. Berkeley, CA: Berkeley Nuclear Laboratories.

[88] Chaboche, J.L., 1986. Time-independent constitutive theories for cyclic plasticity. International Journal of plasticity, 2(2), pp.149-188.

[89] Voce, E., 1948. The relationship between stress and strain for homogeneous deformation. Journal of the Institute of Metals, 74, pp.537-562.

[90] Bowden, F.P. and Freitag, E.H., 1958. The friction of solids at very high speeds I. Metal on metal; II. Metal on diamond. Proceedings of the Royal Society of London. Series A. Mathematical and Physical Sciences, 248(1254), pp.350-367.

[91] Li, Y.G., 2015, Shot-peening and low-cycle fatigue of titanium alloys: instrumented indentation and X-ray diffraction, PhD, Université de Technologie de Troyes.

[92] Guruprasad, P.J., Carter, W.J. and Benzerga, A.A., 2008. A discrete dislocation analysis of the Bauschinger effect in microcrystals. Acta Materialia, 56(19), pp.5477-5491.

[93] Boyer, V., 2017, Modélisation du grenaillage d'un alliage de nickel avec prise en compte de l'écrouissage et de la microstructure, PhD, Université de Technologie de Troyes.

[94] Daoud, M., Kubler, R., Bemou, A., Osmond, P. and Polette, A., 2021. Prediction of residual stress fields after shot-peening of TRIP780 steel with second-order and artificial neural network models based on multi-impact finite element simulations. Journal of Manufacturing Processes, 72, pp.529-543.

[95] Johnson W., 1972, Impact strength of materials, London, UK: Edward Arnold Publishers, Ltd.

[96] Gariépy, A., Bridier, F., Hoseini, M., Bocher, P., Perron, C. and Lévesque, M., 2013. Experimental and numerical investigation of material heterogeneity in shot peened aluminium alloy AA2024-T351. Surface and Coatings Technology, 219, pp.15-30.

[97] Song, C., Yang, C., Hu, S. and Yin, F., 2023. Numerical modeling of ultrasonic shot peening with an accurate impact velocity. Journal of Manufacturing Processes, 101, pp.982-989.

[98] Qin, Z., Li, B., Chen, T., Chen, C., Chen, R., Ma, H., Xue, H., Yao, C. and Tan, L., 2023. Comparative study of the effects of conventional shot peening and ultrasonic shot peening on very high cycle fatigue properties of GH4169 superalloy. International Journal of Fatigue, 175, p.107799.

[99] Simulia, D., 2016, ABAQUS documentation.

[100] Bartier, O., Hernot, X., Mauvoisin, G. and Moussa, C., 2013. Comparaison entre les déformations représentatives de l'indentation Vickers et de l'indentation sphérique. Matériaux & Techniques, 101(3), p.303.

[101] Moussa, C., Hernot, X., Bartier, O., Delattre, G. and Mauvoisin, G., 2014. Evaluation of the tensile properties of a material through spherical indentation: definition of an average representative strain and a confidence domain. Journal of Materials Science, 49, pp.592-603.

[102] Wu, J., Liu, H., Wei, P., Lin, Q. and Zhou, S., 2020. Effect of shot peening coverage on residual stress and surface roughness of 18CrNiMo7-6 steel. International Journal of Mechanical Sciences, 183, p.105785.

[103] Badreddine, J., Rouhaud, E., Micoulaut, M., Retraint, D., Remy, S., François, M., Viot, P., Doubre-Baboeuf, G., Le Saunier, D. and Desfontaine, V., 2011. Simulation and experimental approach for shot velocity evaluation in ultrasonic shot peening. Mechanics & Industry, 12(3), pp.223-229.

[104] Iturbe, A., Giraud, E., Hormaetxe, E., Garay, A., Germain, G., Ostolaza, K. and Arrazola, P.J., 2017. Mechanical characterization and modelling of Inconel 718 material behavior for machining process assessment. Materials Science and Engineering: A, 682, pp.441-453.

[105] Lee, S., Yu, K., Huh, H., Kolman, R. and Arnoult, X., 2022. Dynamic hardening of AISI 304 steel at a wide range of strain rates and its application to shot peening simulation. Metals, 12(3), p.403.

[106] Li, Y.G., Kanouté, P. and François, M., 2014. Characterization of residual stresses and accumulated plastic strain induced by shot peening through simulation of instrumented indentation. Advanced Materials Research, 996, pp.367-372.

[107] American Society for Testing and Materials, 2004. Standard Practice for Strain-controlled Fatigue Testing[1]. ASTM International.

[108] François, M., 2008. Unified description for the geometry of X-ray stress analysis: proposal for a consistent approach. Journal of Applied Crystallography, 41(1), pp.44-55.

[109] Wu, Y., Guelorget, B., Sun, Z., Deturche, R. and Retraint, D., 2019. Characterization of gradient properties generated by SMAT for a biomedical grade 316L stainless steel. Materials Characterization, 155, p.109788.

[110] Jakes, J.E., Frihart, C.R., Beecher, J.F., Moon, R.J. and Stone, D.S., 2008. Experimental method to account for structural compliance in nanoindentation measurements. Journal of Materials Research, 23(4), pp.1113-1127.

[111] Zhu, Y., Kang, G. and Yu, C., 2017. A finite cyclic elasto-plastic constitutive model to improve the description of cyclic stress-strain hysteresis loops. International Journal of Plasticity, 95, pp.191-215.

[112] Smaga, M., Walther, F. and Eifler, D., 2010. Monotonic and Cyclic Deformation Behaviour of the SiC Particle‐Reinforced Aluminium Matrix Composite AMC225xe. Advanced Engineering Materials, 12(4), pp.262-268.

[113] Lee, J.H., Lee, H., Hyun, H.C. and Kim, M., 2010. Numerical approaches and experimental verification of the conical indentation techniques for residual stress evaluation. Journal of Materials Research, 25(11), pp.2212-2223.

[114] SridharBabu, B., Kumaraswamy, A. and AnjaneyaPrasad, B., 2013. Numerical analysis of effect of friction on mechanical properties of Ti-6Al-4VAlloy through Nanoindentation. Procedia Engineering, 64, pp.1048-1055.

[115] Adam, C.J. and Swain, M.V., 2011. The effect of friction on indenter force and pile-up in numerical simulations of bone nanoindentation. Journal of the mechanical behavior of biomedical materials, 4(7), pp.1554-1558.

[116] Liu, M., Tieu, A.K., Lu, C., Zhu, H. and Deng, G., 2014. A crystal plasticity study of the effect of friction on the evolution of texture and mechanical behaviour in the nano-indentation of an aluminium single crystal. Computational materials science, 81, pp.30-38.

[117] Deng, G.Y., Tieu, A.K., Su, L.H., Zhu, H.T., Zhu, Q., Zamri, W.F.H. and Kong, C., 2019. Characterizing deformation behaviour of an oxidized high speed steel: Effects of nanoindentation depth, friction and oxide scale porosity. International Journal of Mechanical Sciences, 155, pp.267-285.

[118] Fleck, N.A., Muller, G.M., Ashby, M.F. and Hutchinson, J.W., 1994. Strain gradient plasticity: theory and experiment. Acta Metallurgica et materialia, 42(2), pp.475-487.

[119] Stölken, J.S. and Evans, A.G., 1998. A microbend test method for measuring the plasticity length scale. Acta Materialia, 46(14), pp.5109-5115.

[120] Durst, K., Backes, B., Franke, O. and Göken, M., 2006. Indentation size effect in metallic materials: Modeling strength from pop-in to macroscopic hardness using geometrically necessary dislocations. Acta Materialia, 54(9), pp.2547-2555.

[121] Durst, K., Franke, O., Böhner, A. and Göken, M., 2007. Indentation size effect in Ni–Fe solid solutions. Acta materialia, 55(20), pp.6825-6833.

[122] Idriss, M., Bartier, O., Mauvoisin, G. and Hernot, X., 2019. Determining the stress level of monotonic plastically pre-hardened metal sheets using the spherical instrumented indentation technique. Journal of Mechanical Science and Technology, 33, pp.183-195.

[123] N'Jock, M.Y., Roudet, F., Idriss, M., Bartier, O. and Chicot, D., 2016. Work-of-indentation coupled to contact stiffness for calculating elastic modulus by instrumented indentation. Mechanics of Materials, 94, pp.170-179.

[124] Dong, C., Yu, J., Xu, L., Xia, Z. and Zhang, Q., 2020. Tension-compression asymmetry of bilayer Ni/Ni3Al affected by dislocation formation–decomposition and twinning size. Materials Express, 10(2), pp.165-176.

[125] Ezz, S.S., Pope, D.P. and Paidar, V., 1982. The tension/compression flow stress asymmetry in Ni3 (Al, Nb) single crystals. Acta Metallurgica, 30(5), pp.921-926.

[126] Leidermark, D., Moverare, J.J., Simonsson, K., Sjöström, S. and Johansson, S., 2009. Room temperature yield behaviour of a single-crystal nickel-base superalloy with tension/compression asymmetry. Computational materials science, 47(2), pp.366-372.

[127] Wen, Z., Pei, H., Wang, B., Zhang, D. and Yue, Z., 2016. The tension/compression asymmetry of a high γ′ volume fraction nickel-based single-crystal superalloy. Materials at High Temperatures, 33(1), pp.68-74.

[128] Sondhi, S.K., Dyson, B.F. and McLean, M., 2004. Tension–compression creep asymmetry in a turbine disc superalloy: roles of internal stress and thermal ageing. Acta materialia, 52(7), pp.1761-1772.

[129] Ghorbanpour, S., Alam, M.E., Ferreri, N.C., Kumar, A., McWilliams, B.A., Vogel, S.C., Bicknell, J., Beyerlein, I.J. and Knezevic, M., 2020. Experimental characterization and crystal plasticity modeling of anisotropy, tension-compression asymmetry, and texture evolution of additively manufactured Inconel 718 at room and elevated temperatures. International Journal of Plasticity, 125, pp.63-79.

[130] OriginLab®, Algorithms (Smooth), https://www.originlab.com/doc/Origin-Help/Smooth-Algorithm.

[131] Markforged Inc., The Markforged Metal Additive Manufacturing Process, https://markforged.com/resources/learn/design-for-additive-manufacturing-metals.

[132] Yan, H., Zhu, P., Chen, Z., Zhang, H., Zhang, Y. and Zhang, Y., 2022. Effect of shot peening on the surface properties and wear behavior of heavy-duty-axle gear steels. Journal of Materials Research and Technology, 17, pp.22-32.

[133] Wu, J., Liu, H., Wei, P., Zhu, C. and Lin, Q., 2020. Effect of shot peening coverage on hardness, residual stress and surface morphology of carburized rollers. Surface and Coatings Technology, 384, p.125273.

[134] Lin, Q., Liu, H., Zhu, C. and Parker, R.G., 2019. Investigation on the effect of shot peening coverage on the surface integrity. Applied Surface Science, 489, pp.66-72.

[135] Arifvianto, B., Mahardika, M., Dewo, P., Iswanto, P.T. and Salim, U.A., 2011. Effect of surface mechanical attrition treatment (SMAT) on microhardness, surface roughness and wettability of AISI 316L. Materials Chemistry and Physics, 125(3), pp.418-426.

[136] Marteau, J., Bigerelle, M., Mazeran, P.E. and Bouvier, S., 2015. Relation between roughness and processing conditions of AISI 316L stainless steel treated by ultrasonic shot peening. Tribology International, 82, pp.319-329.

[137] Arifvianto, B. and Mahardika, M., 2012. Effects of surface mechanical attrition treatment (SMAT) on a rough surface of AISI 316L stainless steel. Applied Surface Science, 258(10), pp.4538-4543.

[138] Li, Y., Retraint, D., Gao, P., Xue, H., Gao, T. and Sun, Z., 2022. Effect of surface mechanical attrition treatment on torsional fatigue properties of a 7075 aluminum alloy. Metals, 12(5), p.785.

[139] Gao, T., Sun, Z., Xue, H. and Retraint, D., 2020. Effect of surface mechanical attrition treatment on high cycle and very high cycle fatigue of a 7075-T6 aluminium alloy. International Journal of Fatigue, 139, p.105798.

[140] James, M.R., 1987. Relaxation of residual stresses an overview. Pergamon Press, Advances in Surface Treatments. Technology--Applications--Effects, 4, pp.349-365.

[141] Zhu, W., Zhao, F., Yin, S., Liu, Y. and Yang, R., 2021. Effect of tensile deformation on residual stress of GH4169 alloy. Materials, 14(7), p.1773.

[142] He, Y., Mehdi, M., Sanjari, M., Hilinski, E.J., Kestens, L.A.I. and Edrisy, A., 2019, August. Quasi in-situ EBSD characterization of the evolution of microtexture and microstructure in non-oriented electrical steels during cold rolling and annealing. In Journal of Physics: Conference Series (Vol. 1270, No. 1, p. 012001). IOP Publishing.

[143] Gupta, A., Khatirkar, R.K., Dandekar, T., Jha, J.S. and Mishra, S., 2019. Recrystallization behavior of a cold rolled Ti-15V-3Sn-3Cr-3Al alloy. Journal of Materials Research, 34(18), pp.3082-3092.

[144] Akessa, A.D., Tucho, W.M., Lemu, H.G. and Grønsund, J., 2022. Investigations of the microstructure and mechanical properties of 17-4 PH ss printed using a MarkForged metal X. Materials, 15(19), p.6898.

[145] Wei, X., Behm, I., Winkler, T., Scharf, S., Li, X. and Bähr, R., 2022. Experimental study on metal parts under variable 3D printing and sintering orientations using bronze/PLA hybrid filament coupled with fused filament fabrication. Materials, 15(15), p.5333.

[146] Al-Maharma, A.Y., Patil, S.P. and Markert, B., 2020. Effects of porosity on the mechanical properties of additively manufactured components: a critical review. Materials Research Express, 7(12), p.122001.

[147] Gussev, M.N. and Leonard, K.J., 2019. In situ SEM-EBSD analysis of plastic deformation mechanisms in neutron-irradiated austenitic steel. Journal of Nuclear Materials, 517, pp.45-56.

[148] Wang, H., Niu, H., Wu, H., Li, R. and Fan, G., 2022. Tensile Test Coupled with an EBSD Study of a GH4169 Ring Rolled Product. Materials, 15(8), p.2891.

[149] Jeon, J.M., Park, J.M., Yu, J.H., Kim, J.G., Seong, Y., Park, S.H. and Kim, H.S., 2019. Effects of microstructure and internal defects on mechanical anisotropy and asymmetry of selective laser-melted 316L austenitic stainless steel. Materials Science and Engineering: A, 763, p.138152.

[150] Zhang, J., Li, W., Dai, H., Liu, N. and Lin, J., 2020. Study on the elastic-plastic correlation of low-cycle fatigue for variable asymmetric loadings. Materials, 13(11), p.2451.

[151] Ungár, T., 2001. Dislocation densities, arrangements and character from X-ray diffraction experiments. Materials Science and Engineering: A, 309, pp.14-22.

Hui CHEN

Doctorat : Matériaux, Mécanique, Optique et Nanotechnologie

Année 2024

Influence des contraintes résiduelles et de l'écrouissage sur le comportement de l'Inconel 625 grenaillé

Le grenaillage est un traitement de surface qui améliore la performance en fatigue d'un matériau en introduisant simultanément des contraintes résiduelles de compression et un écrouissage. Afin d'étudier l'influence du grenaillage pendant les cycles de fatigue, la caractérisation des contraintes résiduelles et de l'écrouissage, ainsi que leur évolution lors des essais monotones et cycliques sont étudiées. La méthode des surfaces de réponse est proposée pour caractériser simultanément les contraintes résiduelles et l'écrouissage en utilisant la technique de nanoindentation. L'effet de l'écrouissage cinématique induit par le grenaillage sur l'indentation est étudié. Les résultats indiquent que, par rapport à l'effet des contraintes résiduelles et de la déformation plastique cumulée, l'effet de l'écrouissage cinématique peut être négligé. Par conséquent, l'écrouissage est représenté par la déformation plastique cumulée. Les surfaces de réponses peuvent être construite à travers une série de simulations. En utilisant deux surfaces, les valeurs de contraintes résiduelles et de déformation plastique cumulée peuvent être obtenues. L'évolution des contraintes résiduelles et de l'écrouissage sur deux types d'Inconel 625 grenaillés est étudiée. Un essai de traction monotone et un essai cyclique de 10 cycles sont réalisés sur les échantillons, grenaillés pour deux durées de traitement. La diffraction des rayons X, la nanoindentation et l'EBSD sont employées pour caractériser l'évolution des contraintes résiduelles et de l'écrouissage.

Mots clés : grenaillage de précontrainte – éléments finis, méthode des – contraintes résiduelles – écrouissage – rayons X, diffraction – nanoindentation.

Influence of Residual Stress and Work Hardening on the Tensile and Cyclic Behavior of Shot-peened Inconel 625

Shot peening is a mechanical surface treatment that can improve the fatigue performance of a material as it introduces compressive residual stress and work hardening simultaneously. To study the influence of shot peening during fatigue cycles, the method of characterizing residual stress and work hardening, as well as their evolution during monotonic and cyclic tests is investigated in this thesis. The Response Surface Function method is proposed to characterize residual stress and work hardening simultaneously using instrumented indentation technique. The effects of shot peening backstress on indentation response are investigated. Results indicate that, compared to the effect of residual stress and cumulative plastic strain, the effect of backstress can be neglected. Therefore, the work hardening is represented by cumulative plastic strain in the proposed method. The response surface function can be built through a series of finite element simulations. By solving two response surface functions, the residual stress and cumulative plastic strain values can be obtained.The evolution of residual stress and work hardening on two kinds of shot peened Inconel 625 alloy are investigated in this thesis. One is a cold rolled alloy, and another one is an additively manufactured alloy. Monotonic tensile tests and 10 cycles cyclic tests are conducted on the samples, which are shot peened by two treatment times. X-ray diffraction, nanoindentation and Electron backscattered diffraction are employed to characterize the evolution of residual stress and work hardening.

Keywords: shot peening – finite element method – residual stresses – strain hardening – X-ray, diffraction – nanoindentation.

Thèse réalisée en partenariat entre :